Conceptual Models of the Climate

2003 Program of Study
Non-Newtonian Geophysical Fluid Dynamics

Course Lectures
Fellows Project Reports

WHOI-2004-03

Conceptual Models of the Climate
2003 Program of Study:
Non-Newtonian Geophysical Fluid Dynamics

by

Neil J. Balmforth, Director
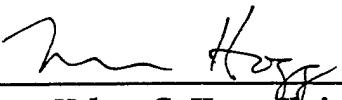## John Hinch, Principal Lecturer

February 2004

Technical Report

Approved for public release; distribution unlimited.

Approved for Distribution:

Nelson G. Hogg, Chair

Department of Physical Oceanography

Preface

Non-Newtonian GFD was the theme of the 2003 Geophysical Fluid Dynamics Summer Study Program. Professor John Hinch (University of Cambridge) gave the principal lectures, which amounted to a thorough introduction to the fluid dynamical foundation of the subject. As usual, the principal lectures were followed by a variety of seminars, covering a wide range of fields, some non-Newtonian, others not.

One newer enterprise this summer was the introduction of a special GFD lecture, intended for a more general audience. This summer's lecture was given by Andy Woods (BP Professor, University of Cambridge), on the general subject of "Volcano Mechanics". Andy presented material covering the current thinking on the geological processes at work in volcanoes, and ideas on how we might model the phenomena from a theoretical perspective. The talk was held in Redfield Auditorium and was attended by almost fifty people, drawing in members of the Oceanographic Institution and the local community, in addition to the program participants. The talk was followed by an enjoyable reception.

This year's Fellows meshed together fairly well. The Fellows' exploits included some notable successes on the softball field (against both the other WHOI teams and the staff team at the summer's close). Their academic accomplishments can be viewed elsewhere in this volume.

Jean-Luc Thiffeault must be thanked for his tireless service of the computers. I also thank Shreyas Mandre for his important contributions in creating this volume. Regarding the every day scientific and educational aspects of the program, special acknowledgements go to Oliver Buhler, Claudia Cenedese, Jean-Luc Thiffeault and George Veronis, and to Keith Bradley for his assistance in the Lab.

The program continues to be indebted to the W.H.O.I. Academic Programs Office, who once more provided a perfect atmosphere in which to run the program. This year Janet Fields stepped down as the administrator of the program, and her place in the cottage was competently filled by Jeanne Fleming and Penny Foster. However, all three helped to ensure that the summer ran smoothly.

Neil J. Balmforth
26th August 2003

TABLE OF CONTENTS

iii

2003 GFD FELLOWS, STAFF AND VISITORS

Fellows

Amit Apte	University of Texas at Austin
Neil Burrell	University of Colorado-Boulder
Junjun Liu	California Institute of Technology
Joel W. Miller	Cambridge University
Julia Mullarney	Res. School of Earth Sci., Australian National University
Anshuman Roy	University of Michigan
Alison Rust	University of Oregon
Andrew Thompson	Scripps Institution of Oceanography, UCSD
Christopher L. Wolfe	Oregon State University

Staff and Visitors

James L. Anderson	Stevens Institute of Technology
Neil J. Balmforth	University of California, Santa Cruz
Andrew Belmonte	Penn State University
Andrew Bernoff	Harvey Mudd College
Gregory Buck	Saint Anselm College
John Bush	Massachusetts Institute of Technology
Colm-cille P. Caulfield	University of California, San Diego
Eric P. Chassignet	University of Miami
Stephen W. Childress	New York University
Charles Doering	University of Michigan
Pascale Garaud	University of Cambridge
Louis N. Howard	Florida State Univ./Massachusetts Institute of Technology
Daniel Joseph	University of Minnesota
Joseph B. Keller	Stanford University
Norman R. Lebovitz	University of Chicago
Jennifer A. MacKinnon	Scripps
Willem V.R. Malkus	Massachusetts Institute of Technology
Philip J. Morrison	University of Texas at Austin
Claes G. Rooth	University of Miami
Alexander V. Soloviev	NOVA Southeastern University
Andrew M. Soward	University of Exeter
Edward A. Spiegel	Columbia University
Jean-Luc Thiffeault	Imperial College
George Veronis	Yale University
Jie Yu	Duke University

2003 Participants

Standing (left to right): Stephen Childress, Alison Rust. Lou Ting, Joseph Keller, Shreyas Mandre, Lakshminarayanan Mahadevan, Andrew Belmonte, Claes Rooth, Amala Mahadevan

Seated on porch (left to right): Evstati Evstatiev (standing), Oliver Buhler, Charles Doering, Misha Chertkov, Alexander Soloviev, Jean-Luc Thiffeault, George Veronis, Shilpa Ghadge, Christopher Wolfe, Amit Apte, Anshuman Roy, Neil Burrell

Seated on ground (left to right): Penny Foster, JunJun Liu, Neil Balmforth, Joel Miller, Pascal Garaud, Julia Mullarney, Andrew Thompson, Jennifer Mackinnon

2003 Principal Lecturer John Hinch

GFD 2003 Lecture Schedule

Monday, June 16

    10:00 am   John Hinch, University of Cambridge, United Kingdom
                                 Phenomena and Rheometry

    2:00 pm   John Hinch
                                 Constitutive Equations

Tuesday, June 17

    10:00 am   John Hinch
                                 Simple Flow Calculations

Wednesday, June 18

    10:00 am   John Hinch
                                 Experiments and Computing

    3:00 pm   John Hinch
                                 Micostructural Studies for Rheology

Thursday, June 19

    10:00 am   John Hinch
                                 Simple Relaxation and Yield Problems

    3:00 pm   John Hinch
                                 Instabilities

Friday, June 20

    10:00 am   John Hinch
                                 Strong Flows

    3:00 pm   John Hinch
                                 The Success and Failure of Oldroyd-B (inc converging flows)

Monday, June 23

    10:30 am   Jean-Luc Thiffeault, Imperial College, United Kingdom
                                 Turbulent Polymers

    2:00 pm   John A. Whitehead, Physical Oceanography Department, WHOI
                                 Discrete Jumps and Oscillations in Temperature – Salinity Driven Laboratory Experiments

Tuesday, June 24

    10:30 am   John Wettlaufer, Yale University
                               Flow of Unfrozen Water

    3:00 pm   Physical Oceanography Department Seminar
                               Location – Clark 507

Wednesday, June 25

    10:30 am   Linda Smolka, Duke University
                               Filament Dynamics of Non-Newtonian Fluids in Extensional Flows

    3:00 pm   Philip Morrison, University of Texas at Austin
                               Fluctuations in Inhomogeneous Systems using Statistical Mechanics

    5:30 PM   Project Discussions

Thursday, June 26

    10:30 am   Oliver Buhler, New York University

                               Vortices in a Tea Cup

Friday, June 27

    10:00 am   Claudia Cenedese, Physical Oceanography Department, WHOI
                               A Laboratory Model of Thermocline Depth and Exchange Fluxes Across Circumpolar Front

---

Week of June 30 – July 4, 2003

Monday, June 30

    10:00 am   Daniel Joseph, University of Minnesota
                               Non-Newtonian Fluids I

Tuesday, July 1

    10:30 am   Daniel Joseph
                               Non-Newtonian Fluids II

Wednesday, July 2

    10:30 am   Norman Lebovitz, University of Chicago
                               Fission Theory Primed

Thursday, July 3

    10:30 am   Joseph B. Keller, Stanford University
                               Water Waves

Friday, July 4

NO LECTURE – DUE TO INDEPENDENCE DAY HOLIDAY

Week of July 7 – 11, 2003

Monday, July 7
    10:30 am   Slava Solomatov, New Mexico State University
                              Mantle Convection with Realistic Rheologies

    3:00 pm   Andrew Fowler, Oxford University, United Kingdom
                              Ice Sheets

Tuesday, July 8
    10:30 am   Lakshminarayanan Mahadevan, Univ. of Cambridge, United Kingdom
                              The Pseudo-Elasticity of Newtonian Fluids

Wednesday, July 9
    10:00 am   Gregory Buck, Saint Anselm College
                              Natural Entanglements: Geometry, Topology and a Phase Transition

Thursday, July 10
    10:30 am   Greg Hirth, Geology & Geophysics Department, WHOI
                              Non-Newtonian Viscous Deformation of the Earth's Mantle

    3:00 pm   Ross Griffiths, Australian National University
                              Solidification in Shear Flows

Friday, July 11
    10:30 am   Alan Rempel, Yale University
                              Freezing Dirt: The Fluid Mechanics of Frost Heave

---

Week of July 14 – 18, 2003

Monday, July 14
    10:30 am   Amala Mahadevan, University of Cambridge, United Kingdom
                              Spatial Heterogeneity at the Sea Surface

Tuesday, July 15
    10:30 am   Informal Discussion
                              Horizontal Convection – Turbulent or Non-Turbulent?

Wednesday, July 16
    10:30 am   Jean-Luc Thiffeault
                                Mixing in a Simple Map

Thursday, July 17
    10:30 am   Oliver Buhler, New York University
                                  Wave Scattering and Remote Recoil

    3:00 pm   Edward Spiegel, Columbia University
                                  The Content of Shape

Friday, July 18
    10:30 am   NO LECTURE

    3:00 pm   John Bush, Massachusetts Institute of Technology
                                  Water Walking Insects

Week of July 21 – 25, 2003

Monday, July 21
    10:30 am   Charles Doering, University of Michigan
                                  The Stochastic Fisher-Kolmogorov-Petrovsky-Piscanov Equation, Interacting Particles and Duality

    3:00 pm   NO LECTURE

Tuesday, July 22
    10:30 am   Alexander Soloviev, NOVA Southeastern University
                                  Horizontal Mixing in the Western Pacific Warm Pool as a Nonlinear Diffusion Process

    3:00 pm   NO LECTURE

Wednesday, July 23
    10:30 am   Misha Chertkov, Los Alamos National Laboratory
                                  Phenomenology of Rayleigh Taylor Turbulence

    3:00 pm   NO LECTURE

Thursday, July 24
    10:30 am   Steve Childress, New York University
                                  Experiments on Flapping Flight as a Symmetry Breaking Bifurcation

    3:00 pm   Jennifer MacKinnon, University of California, San Diego
                                  Missing Mixing or Missing Physics: the Nonlinear Evolution of Internal Gravity Waves over Rough Topography

Friday, July 25
      10:30 am   Andrew Belmonte, Penn State University
                                       Introduction to the Dynamics of Wormlike Micellar Fluids

      3:00 pm   Andrew Belmonte, Penn State University
                                         Instabilities of Viscoelastic Free Surfaces

---

Week of July 28 – August 1, 2003

Monday, July 28
      10:30 am   Ian Frigaard, University of British Columbia
                                       Viscoplastic Fluids

      3:00 pm   Amy Shen, Washington University
                                         Coating Dynamics with Complex Fluids

Tuesday, July 29
      10:30 am   Ian Frigaard, University of British Columbia
                                       Stability of Multi-Layer Viscoplastic Flows

      3:00 pm   NO LECTURE

Wednesday, July 30
      10:30 am   Pascale Garaud, University of Cambridge, United Kingdom
                                       Dusty Acretion Disks

      3:00 pm   NO LECTURE

Thursday, July 31
      10:30 am   Chiang Mei, Massachusetts Institute of Technology
                                       Slow Flows of Mud Down a Channel or a Conical Surface

      3:00 pm   NO LECTURE

Friday, August 1
      10:30 am   Joe Pedlosky, Physical Oceanography Department, WHOI
                                     Rossby Basin Modes and their Instabilities

      3:00 pm   NO LECTURE

Monday, August 4
       10:30 am   Colm-cille Caufield, University of California, San Diego
                                           The Consequences of Stress: Rigorous Bounds for Environmental Flows

       3:00 pm   Antonello Provenzale, Instituto de Cosmogeofisica
                                           Patterns of Blown Sand

Tuesday, August 5
       10:30 am   George Field, Harvard University
                                           Dynamo Theory and Magnetic Helicity

       3:00 pm   NO LECTURE

Wednesday, August 6
       10:30 am   Gordon Ogilvie, University of Cambridge, United Kingdom
                                           The Visco-Elastic/MHD Connection

       3:00 pm   Andrew Woods, University of Cambridge, United Kingdom
                                         Gravity Currents in Porous Media

Thursday, August 7
       10:30 am   Yoel Forterre, Universite de Provence, France
                                         Long-surface Wave Instability in Dry Granular Flows

       3:00 pm   Shreyas Mandre, University of California, Santa Cruz
                                         Dynamics of Roll Waves

Friday, August 8
       10:30 am   Richard Craster, Imperial College, United King
                                         Evolving and Cooling Domes of Lava

       3:00 pm   George Haller, Massachusetts Institute of Technology
                                         Kinematic Theory of Unsteady Separation

Monday, August 11
       10:30 am   NO LECTURE

       3:00 pm   NO LECTURE

Tuesday, August 12
  10:30 am   NO LECTURE

  3:00 pm   NO LECTURE

Wednesday, August 13
  10:30 am   NO LECTURE

  3:00 pm   NO LECTURE

Thursday, August 14
  5:00 pm   Andrew Woods, BP Professor, University of Cambridge, UK
                           Volcano Mechanics – A public lecture at Redfield Auditorium,
                           reception to follow

Friday, August 15
  10:30 am   NO LECTURE

  3:00 pm   NO LECTURE

Week of August 18 – 22, 2003 – Fellows' Lectures

Monday, August 18
  10:30 am   NO LECTURE

  3:00 pm   NO LECTURE

Tuesday, August 19
  10:30 am   Christopher Wolfe, Oregon State University
                           Eddy Formation over Variable Topography

  2:00 pm   Andrew Thompson, Scripps Institution of Oceanography
                           Diffusively Driven Overturning from a Stable Density Gradient

  3:15 pm   Amit Apte, University of Texas at Austin
                           Wave-Mean-Flow Interaction in Oldroyd-B Fluid

Wednesday, August 20
  10:00 am   Anshuman Roy, University of Michigan
                           Viscoelastic Catenary

11:15 am	Neil Burrell, University of Colorado, Boulder *1 ¾ Layer Quasigeostrophic Equations*
2:15 pm	Julia Mullarney, Research School of Earth Sciences, Australian National University *Laboratory Experiments on Non-Linear Rossby Adjustment in a Channel*
3:30 pm	Alison Rust, University of Oregon *Volcanic Tremor*
Thursday, August 21 **10:30 am**	JunJun Liu, California Institute of Technology *Stability of Viscoplastic Flow*
11:15 am	Joel Miller, Cambridge, University, United Kingdom *Elastic Critical Layers*
Thursday, August 22 **10:30 am**	NO LECTURE
3:00 pm	NO LECTURE

Lecture 1: Introduction

E. J. Hinch

Non-Newtonian fluids occur commonly in our world. These fluids, such as toothpaste, saliva, oils, mud and lava, exhibit a number of behaviors that are different from Newtonian fluids and have a number of additional material properties. In general, these differences arise because the fluid has a microstructure that influences the flow. In section 2, we will present a collection of some of the interesting phenomena arising from flow nonlinearities, the inhibition of stretching, elastic effects and normal stresses. In section 3 we will discuss a variety of devices for measuring material properties, a process known as *rheometry*.

1 Fluid Mechanical Preliminaries

The equations of motion for an incompressible fluid of unit density are (for details and derivation see any text on fluid mechanics, e.g. [1])

$$\frac{\partial \mathbf{u}}{\partial t} + (\mathbf{u} \cdot \nabla)\,\mathbf{u} = \nabla \cdot \mathbf{S} + \mathbf{F} \tag{1}$$

$$\nabla \cdot \mathbf{u} = 0 \tag{2}$$

where $\mathbf{u}$ is the velocity, $\mathbf{S}$ is the total stress tensor and $\mathbf{F}$ are the body forces. It is customary to divide the total stress into an isotropic part and a *deviatoric* part as in

$$\mathbf{S} = -p\mathbf{I} + \boldsymbol{\sigma} \tag{3}$$

where $\operatorname{tr}\boldsymbol{\sigma} = 0$. These equations are closed only if we can relate the deviatoric stress to the velocity field (the pressure field satisfies the incompressibility condition). It is common to look for local models where the stress depends only on the local gradients of the flow: $\boldsymbol{\sigma} = \boldsymbol{\sigma}\,(\mathbf{E})$ where $\mathbf{E}$ is the *rate of strain tensor*

$$\mathbf{E} = \frac{1}{2}\left(\nabla \mathbf{u} + \nabla \mathbf{u}^T\right), \tag{4}$$

the symmetric part of the the velocity gradient tensor.

The trace-free requirement on $\boldsymbol{\sigma}$ and the physical requirement of symmetry $\boldsymbol{\sigma} = \boldsymbol{\sigma}^T$ means that there are only 5 independent components of the deviatoric stress: 3 shear stresses (the off-diagonal elements) and 2 normal stress differences (the diagonal elements constrained to sum to 0). These two normal stress differences are

$$N_1 = \sigma_{xx} - \sigma_{yy} \tag{5}$$

$$N_2 = \sigma_{zz} - \sigma_{yy}. \tag{6}$$

1

Throughout this series of notes we will frequently refer to two model flow types: *Simple shear* and *Uni-axial extension*. In simple shear the velocity profile is $\mathbf{u} = \dot{\gamma}\,(y, 0, 0)$ where $\dot{\gamma}$ is the *shear rate*. The rate of strain tensor in this case is

$$\mathbf{E} = \begin{pmatrix} 0 & \dot{\gamma} & 0 \\ \dot{\gamma} & 0 & 0 \\ 0 & 0 & 0 \end{pmatrix}.$$

For uni-axial extension, $\mathbf{u} = \dot{\epsilon}\,(x, -y/2, -z/2)$ with rate of strain tensor

$$\mathbf{E} = \dot{\epsilon} \begin{pmatrix} 1 & 0 & 0 \\ 0 & -1/2 & 0 \\ 0 & 0 & -1/2 \end{pmatrix},$$

where $\dot{\epsilon}$ is the magnitude of the strain. Note that $\dot{\gamma}$ and $\dot{\epsilon}$ are both scalars, whereas $\mathbf{E}$ is a tensor.

2 Phenomena

2.1 Non-linear Flow

In the simple example of flow down a pipe at low Reynolds numbers, the flow rate in Newtonian fluids increases linearly with the applied pressure drop (see figure 1). Any fluids which deviate from this relation are then non-Newtonian. These fluids can be further classified depending on how this relation changes, relative to the Newtonian example. *Shear thinning* fluids become less viscous with increasing shear rates and so have larger than linear growth with pressure-drop in the flow rate. The microstructures of such materials are smashed up at higher shear. This results in lower viscosities, hence the fluid flows more easily. *Shear thickening* fluids become more viscous with increasing shear rate and hence have less than linear flow rates. Shear thickening behavior is less common and generally arises in fluids that have a highly regular microstructure at rest. When the fluid begins to move, the microstructural components jam against each other, thickening the fluid thus preventing movement. Finally there are *yield* fluids for which there is no flow below a certain critical pressure drop. Some common yield fluids are ketchup, toothpaste, silicate-rich lava and mud. The viscous properties of all of these fluids are strongly dependent on temperature and pressure.

2.2 Inhibition of Stretching

Another phenomenon associated with some non-Newtonian fluids is a dramatic resistance to stretching of fluid elements compared to Newtonian fluids. Typically, the force required to stretch the fluid is ~ 1000 times greater than that required to shear it. Measurements of the *extensional viscosity*, the resistance of the fluid to stretching motions, show large variations in behavior depending on the type of flow (see figure 2).

The high extensional viscosities present in these fluids give rise to a multitude of consequences. Bubbles rising in these fluids form cusps at the downstream end, thus avoiding the large stretching flow out of a rear stagnation point (see figure 3). A similar effect in
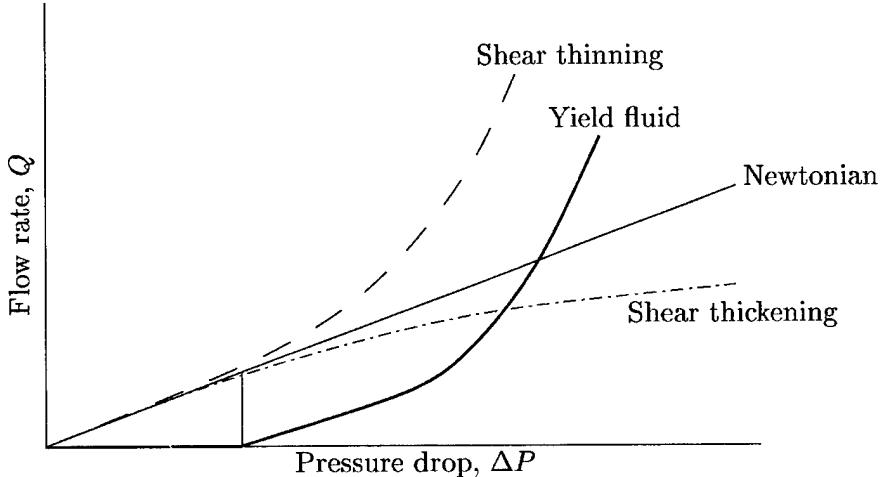
Figure 1: Flow rate as a function of pressure drop for flow down a pipe.

jets inhibits the ejection of spray. The formation of droplets is a highly straining event that occurs at the pinching off of a parcel of fluid. In a fluid containing a few parts per million of high molecular weight polymers, this effect is inhibited by the high extensional viscosity (see figure 4). This lack of spray formation could provide a beneficial effect for fire hoses and in aircraft fuel by preventing potentially explosive mists of droplets from forming.

The inhibition of stretching by high extensional viscosities is also thought to be important in the process of turbulent drag reduction. Addition of very small amounts of high molecular weight polymers to turbulent fluid flows can dramatically reduce the amount of drag in pipe flows. Drag reductions of 50% are possible with polymer concentrations of 10 parts per million (ppm) and as much as an order of magnitude reduction with concentrations of only 500 ppm. This reduction is not well understood and is a much-debated issue in current research. One hypothesis is as follows: drag in turbulent flows is largely due to turbulent bursting events which transport low momentum fluid from near the walls into the interior of the pipe. These bursts are highly straining flows and so are less frequent with the addition of polymers and the attendant increase in extensional viscosity. Such reductions in drag can be critical for oil pipelines (the trans-Alaskan pipeline) and ancient municipal sewer systems. (In Bristol, so great was the drag reduction after a rainfall that a hydrodynamic shock wave was formed in the sewer system and propagated down the network blowing off manhole covers as it passed.)

Conversely, non-Newtonian effects can be detrimental for some industrial processes, for example through the formation of upstream vortices (see section 6 from Lecture 3). Consider flow from a reservoir out a hole: as seen in figure 5, Newtonian fluids flow toward the hole from the entire reservoir while non-Newtonian fluids can form recirculating vortices upstream. These upstream vortices are industrially important in the processing of polymers because fluid that stays in the tank for longer can be significantly degraded (e.g. by a longer exposure to heating), and hence can lead to the production of inconsistent materials. These upstream vortices are caused by high extensional viscosity in the following way: the stretching of fluid elements is proportional to the width of the cone through which fluid flows
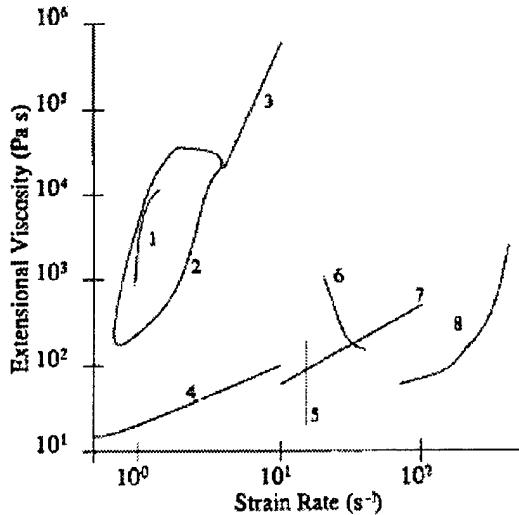
3

Figure 2: Extensional viscosity measurements for the M1 Boger fluid from (1) open siphon, (2) spinline, (3) contraction flow, (4) opposing jets, (5) falling drop, (6) falling bob, (7) contraction flow, (8) contraction flow [from [2]].

into the hole. For non-Newtonian fluids shear is preferential to stretching and a narrower cone of extensional flow forms at the cost of recirculating vortices ([3]). On the other hand, for Newtonian fluids the cone of fluid flowing out through the hole fills the entire container.

2.3 Elastic Effects

Many non-Newtonian fluids are called visco-elastic because they exhibit a variety of elastic effects in which straining of the fluid can store energy. A dramatic example is shown in figure 6 which shows the cutting of visco-elastic liquid as it is poured. The lower portion of the fluid falls as expected, however the upper portion rebounds upward into the container from which it is being poured. Another interesting effect is the open (tubeless) siphon, in which fluid is drawn up over the wall of the upper container by elastic forces from the descending fluid (see figure 7). Finally in flow out of an orifice, non-Newtonian fluids show an expansion of the stream of fluid known as *die swell* (see figure 8). This expansion is caused by the release of elastic energy stored in the fluid as it is stretched in the outlet tube. This tension causes a vertical rebounds after the fluid leaves the tube and because of incompressibility the stream must expand in the transverse direction.

2.4 Normal Stress Effects

Our final category of non-Newtonian effects contains those caused by stresses normal to shear flow. These effects can be viewed as being due to tension in the streamlines of the flow. For example, there can be dramatic effects on the distribution of particles in shear flows. In simple shear there is aggregation of particles. The tension present in the curved streamlines surrounding two particles produces a net force on the particles that pushes

4
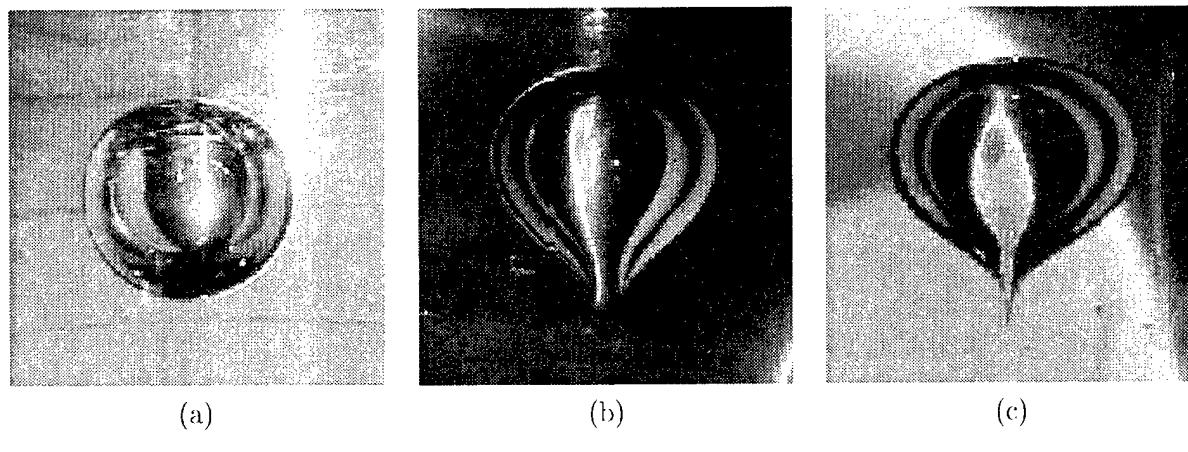
Figure 3: Photographs of air bubles in (a) a newtonian fluid (b-c) a non-newtonian fluid (front and side view). Notice the asymmetry.
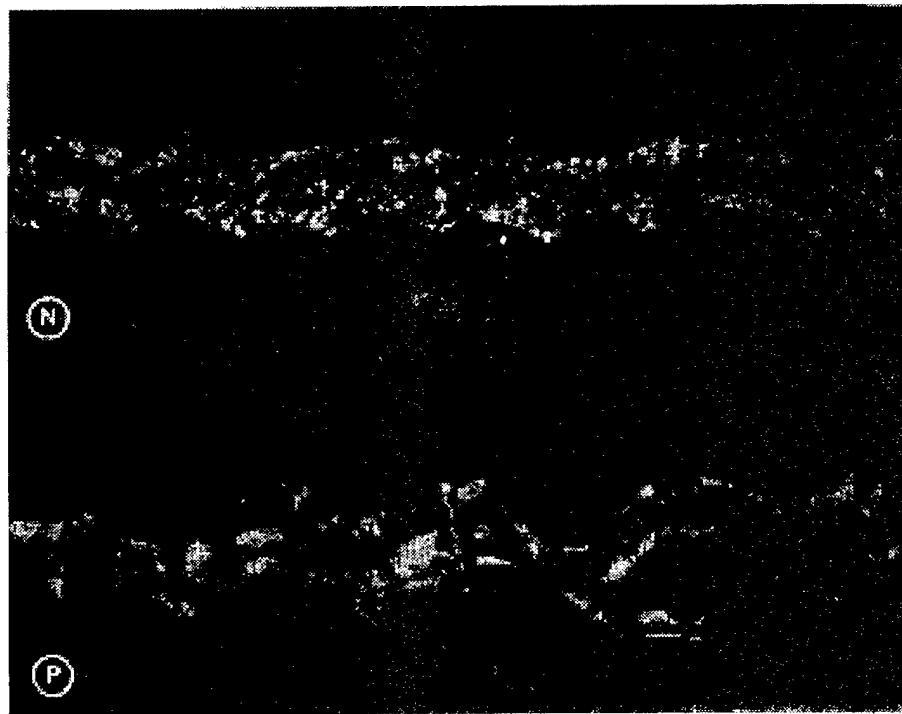

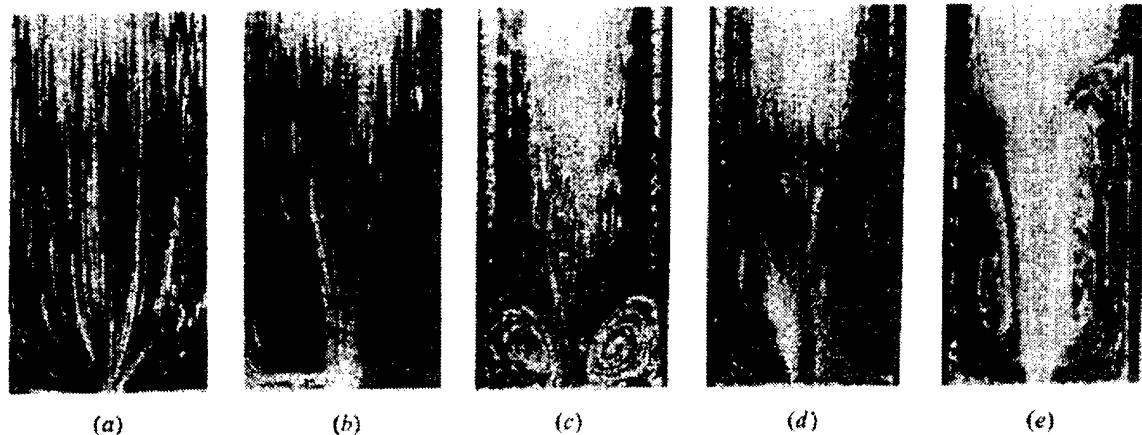Figure 4: Photograph of high-speed jets for pure water and 200 ppm polyethyleneoxide in water.

5

Figure 5: Streamlines of flow out a hole for (a) glycerin, $De = 0$ and (b-e) i for 1.67% aqueous polyacrylamide solution, $De = 0.2, 1, 3$ and 8.

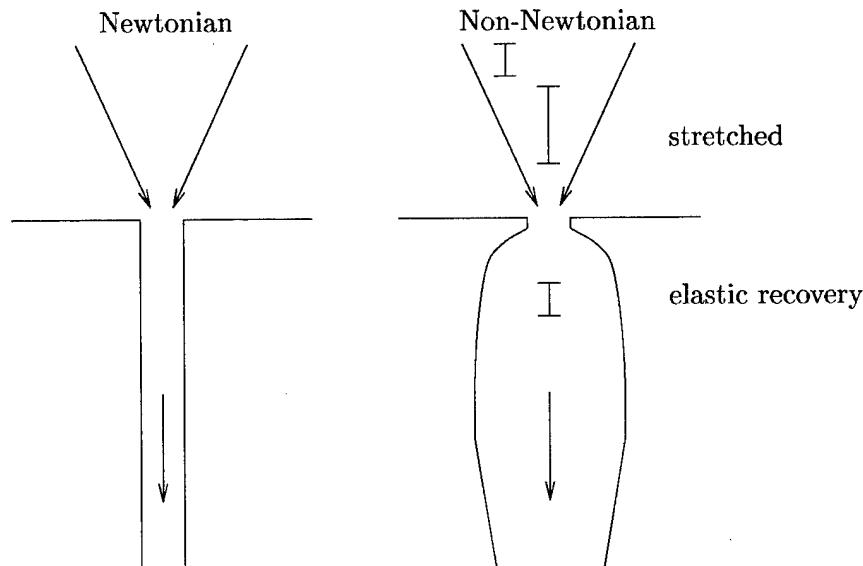Figure 6: Aluminum soap solution cut in midstream

Figure 7: Schematic of the open-siphon effect

Figure 8: Schematic of the die swell effect for Newtonian and non-Newtonian fluids

them together (figure 9) with a cumulative effect as shown in figure 10. A similar effect is the migration of particles to the center of a pipe. The parabolic velocity profile gives a non-uniform shear that is higher near the walls of the pipe than in the center. This makes the tension in the streamlines greater near the wall and thus applies a net force which causes particles to migrate towards the center as in figure 11.
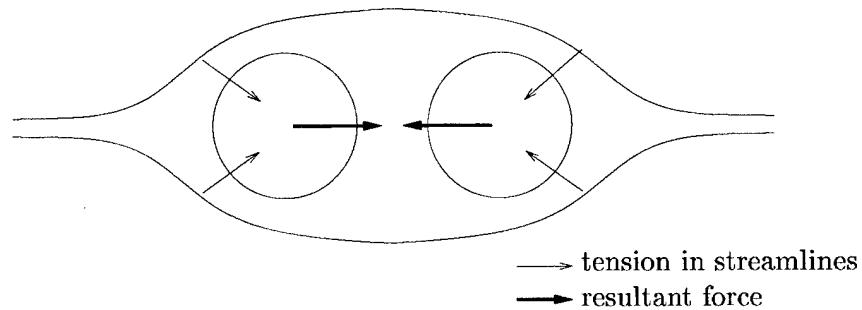
Figure 9: Balance of forces for two particles in a simple shear.

A final example of the effect of normal stresses is that of a spinning rod in a bath of fluid. For low rates of rotation, a Newtonian fluid will have a flat (or slightly depressed) free surface. For comparable rates of rotation in the non-Newtonian fluid, we see an upwards deflection in the free surface, which is higher in the center (see section 4 from Lecture 3). The shear caused by the rotating rod creates tension in the circular streamlines. This "hoop" stress balances the hydrostatic pressure of a column of fluid above it, allowing the fluid to "climb" the rod as in figure 12.
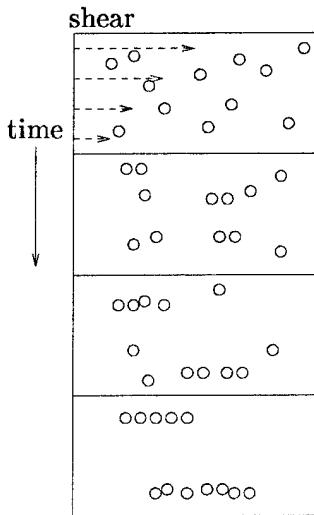
Figure 10: Particle aggregation in sheared polymer solution [after [4]].

	shear rate	tension in streamlines	particle motion
	high	high	
	low	low	
	high	high	

Figure 11: Migration of particles to centerline in a non-Newtonian pipe flow.

3 Rheometry

Rheometry is the study of material properties of fluids including shear viscosities, extensional viscosities and normal stresses as well as the dependence of those properties on temperature and pressure. In this section we discuss the definitions of these properties and the mechanisms used to measure them.

3.1 Simple Shear Devices

There are many ways to generate a shear flow in the laboratory that allow us to measure fluid properties. One of the simplest is shown in figure 13. The fluid lies between two parallel plates with the top plate free to move under an applied force and the bottom plate held fixed. This method works for fluids, such as heavy tars, which are sufficiently viscous so they do not flow out of the sides. The top plate is dragged at constant velocity v across the fluid and feels a force F. The area of the plates is A and their separation is h. The shear rate across the layer is

$$\dot{\gamma} = \frac{v}{h}.$$
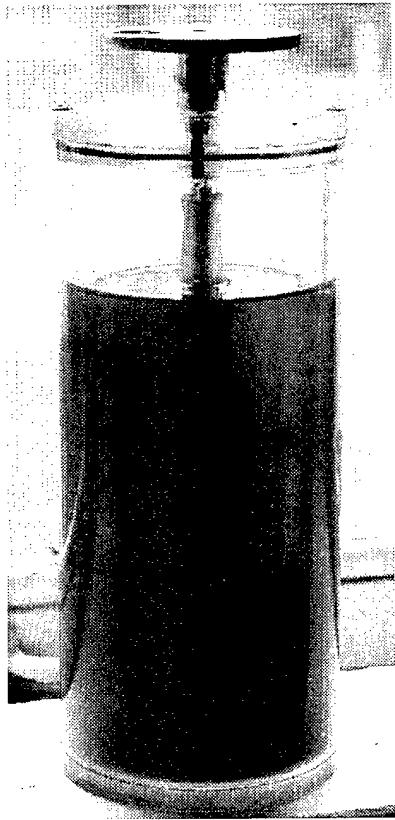
Figure 12: A photograph of the rod climbing effect. The device consisted of a rod immersed in the lower, darker fluid. As the rod is rotated, normal stresses cause a fluid column to rise near the rod.

Possible values of this shear rate range from $\dot{\gamma} \approx 10^{-5}\,\mathrm{s}^{-1}$ for fine particles sedimenting, $\dot{\gamma} \approx 10^1\,\mathrm{s}^{-1}$ for food being chewed and as high as $\dot{\gamma} \approx 10^7\,\mathrm{s}$ in lubrication shear flows. The tangential shear stress is

$$\sigma_{xy} = \frac{F}{A}.$$

and the shear viscosity μ is given by the ratio of these two quantities,

$$\mu = \frac{\sigma_{xy}}{\dot{\gamma}} = \frac{Fh}{Av}.$$

Typical values of μ for non-Newtonian fluids are quite large. for example polymer melts have $\mu \approx 10^3\,\mathrm{Pa\,s}$ and molten glass has $\mu \approx 10^{12}\,\mathrm{Pa\,s}$ (for water $\mu = 10^{-3}\,\mathrm{Pa\,s}$). Shear-thinning materials often have approximate power law dependence with shear viscosity as a function of shear rate, that is

$$\mu(\dot{\gamma}) = k\dot{\gamma}^{n-1}, \qquad \text{for } n < 1. \tag{7}$$

For molten polymers $n \approx 0.6$, toothpaste has $n \approx 0.3$ and grease has $n \approx 0.1$.

A variety of other devices exist for measuring shear viscosities and these are summarized below (figure 14). The capillary tube rheometer is used for measurements on low viscosity
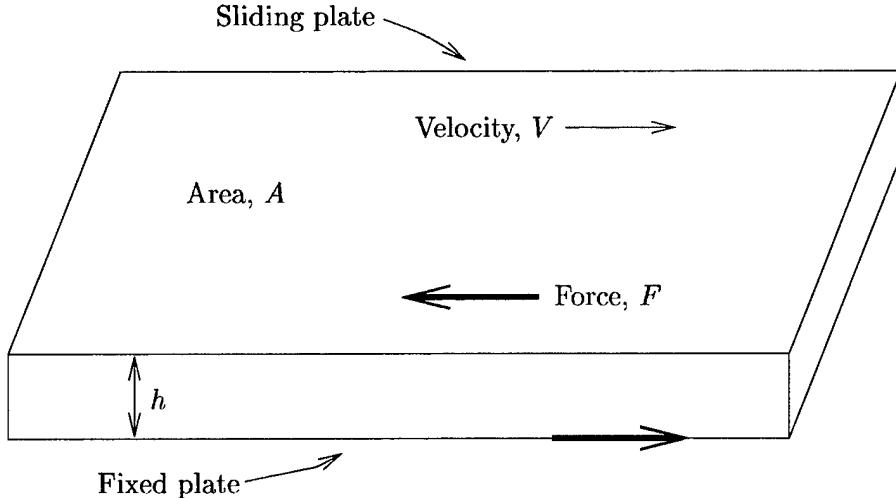
9

Figure 13: Device for measuring simple shear

liquids with high shear rates. The Couette device is used for flows which have very low Reynolds numbers and so does not suffer from any inertial instability. However, a defect of these two devices is that the shear rate is not uniform throughout the device hence it is not clear what value of $\dot{\gamma}$ is being measured. The cone-and-plate rheometer is designed so that the shear rate is independent of position for small angles $\alpha \approx 2°$ (figure 14). Sample rheometric data are shown in figure 15. The plateau at low shear rates, with power law behavior above a critical value is characteristic of non-Newtonian fluids (see section 3.7).

3.2 Normal Stresses

The normal stresses (the first normal stress due conceptually to the tension in the streamlines) can be measured using the cone-and-plate device described earlier. Tension in the streamlines produces an axial thrust pushing the cone and plate apart with a force which can be measured (see figure 14). With the same device, the second normal stress can be found by measuring the distribution of pressure over the surface of the cone or, if the first normal stress is known, it can be computed from the axial thrust on two rotating parallel plates. A final apparatus for measuring the second normal stress is Tanner's tilted trough, in which non-Newtonian fluid flows down an inclined trough. The free surface is curved due to the influence of the second normal stress and this bowing can be measured with an optical device.

3.3 Oscillatory Rheometry

Rheometers of the parallel plate and cone-and-plate varieties often have the capability to do small amplitude oscillatory shear tests. These tests involve the application of a sinusoidal stress (or strain) to the upper plate or cone of the rheometer. The resulting strain (or stress) can be resolved into components that are in phase with the input (elastic response) and $\frac{\pi}{2}$ out of phase with the input (viscous response). From these data a complex modulus,
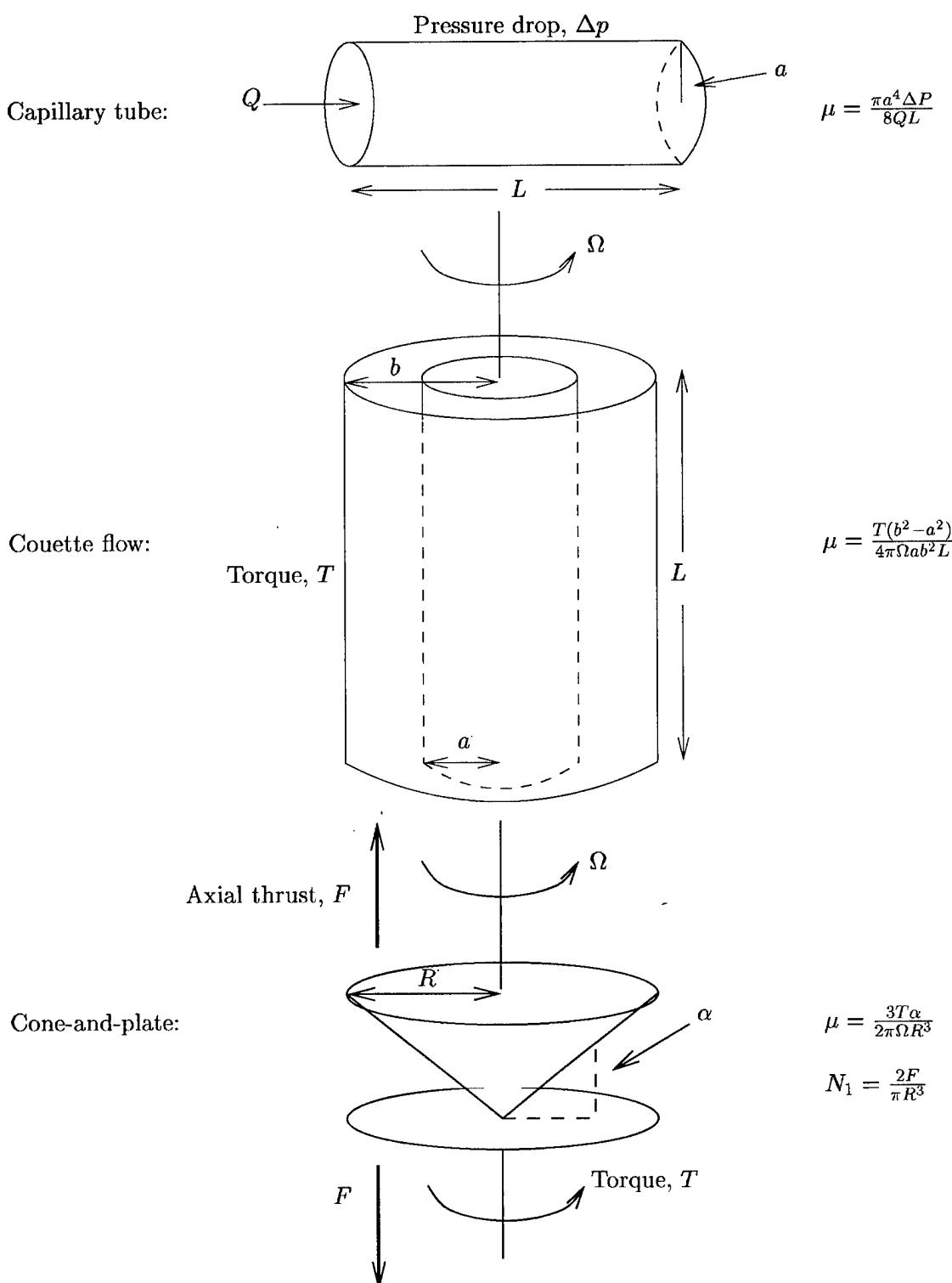
10

Capillary tube:

Pressure drop, Δp

Q → a L

$$\mu = \frac{\pi a^4 \Delta P}{8QL}$$

Ω

Couette flow:

b

Torque, T L

a

$$\mu = \frac{T(b^2 - a^2)}{4\pi \Omega a b^2 L}$$

Axial thrust, F Ω

Cone-and-plate:

R α

$$\mu = \frac{3T\alpha}{2\pi \Omega R^3}$$

$$N_1 = \frac{2F}{\pi R^3}$$

F Torque, T

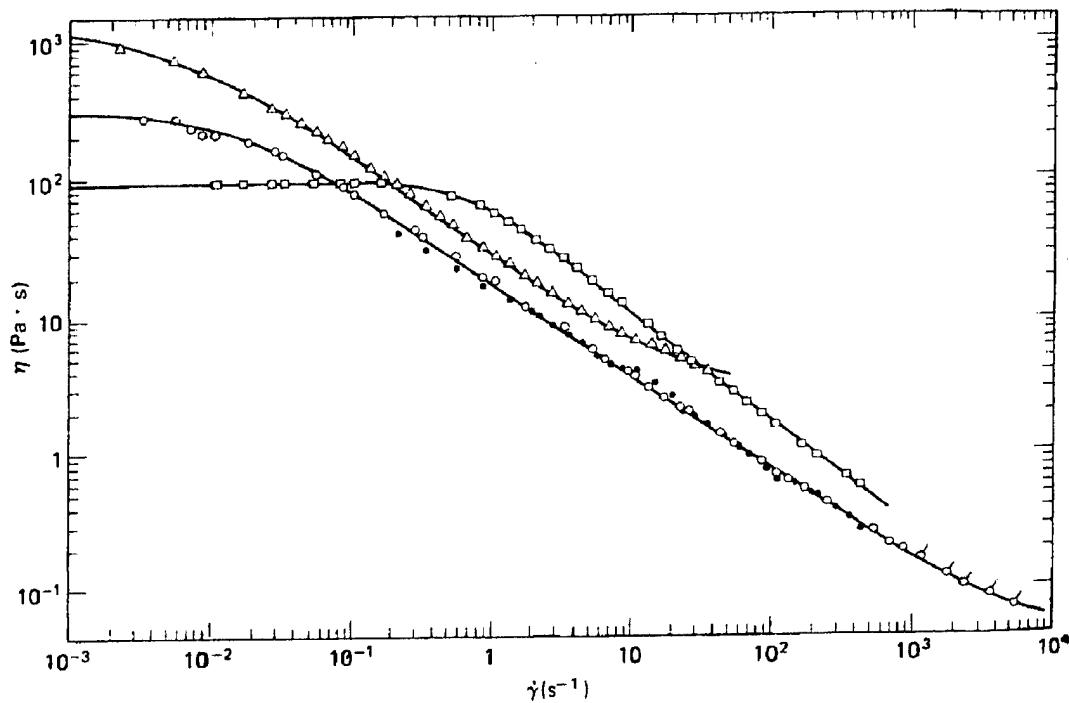Figure 14: Illustration of devices for measuring shear viscosities. The vertical scale in the cone-and-plate illustration is exaggerated.

11

Figure 15: Dependence of viscosity on shear rate for two polymer solutions (○ and △) and an aluminum soap solution (□). All data were taken at 298 K.

12

G^*, is determined as a function of frequency.

$$G^* = G' + iG'',$$ (8)

where G' (storage modulus) and G'' (loss modulus) give information on energy storage and energy dissipation in the flow, respectively. For a perfectly elastic solid, $G'' = 0$ and $G' = G$, the elastic modulus. For a Newtonian fluid, $G' = 0$ and $\mu = \frac{G''}{\omega}$, where ω is the frequency.

3.4 Extensional Viscosity

For the uni-axial extensional flow, we can define the extensional viscosity as,

$$\mu_{ext} = \frac{\sigma_{xx} - \frac{1}{2}\sigma_{yy} - \frac{1}{2}\sigma_{zz}}{3\dot{\epsilon}},$$ (9)

where σ_{xx}, σ_{yy} and σ_{zz} are the diagonal components of the stress tensor. Unfortunately, in the laboratory this steady straining flow cannot be maintained indefinitely. An approximation to this flow is the spinline experiment (figure 16) where, at every point in the flow, there is one straining direction, in this case the x-direction, and two contracting directions. (for further details see section 7 from Lecture 3 and 1 frpm Lecture 8). Using a similar approximation to that used in section 3.1 we can compute an average stress by dividing the tension T by the area A and an average shear from the velocity gradient $\nabla u \approx (v_2 - v_1)/L$. Then the extensional viscosity is given by

$$\mu_{ext} \approx \frac{TL}{A(v_2 - v_1)}.$$ (10)

Other devices to measure extensional viscosity include the filament stretching rheometer and the Moscow rheometer. The filament stretching rheometer works by placing a fluid between two plates which are pulled apart rapidly (2 m within a second) at a constant strain rate and the applied force on the bottom plate is measured. The Moscow rheometer allows surface tension to squeeze a filament of fluid and measures the rate of thinning. The "Worthington jet" could also be used as a possible method to measure the inhibition of stretching: a solid sphere is dropped into a fluid, as it breaks the surface a cavity forms and the filling of this cavity creates an upwards jet. In non-Newtonian fluids the extensional viscosity retards the motion of the drop and the rebound of the surface [5]. Theory to describe the correlation between the maximum height of this jet and the extensional viscosity has yet to be developed. Other devices to measure extensional viscosity include flow between four rollers or opposed jets, film blowing and Meissner's film on an expanding square grid.

3.5 Temperature, concentration and molecular weight scaling

Material properties depend on a variety of parameters, including the concentration and molecular weights of the polymers and also temperature. Using an appropriate choice of non-dimensional parameters the data may be collapsed to give a power-law dependence for viscosity as a function of shear rate. Figure 17 shows a plot of the non-dimensional reduced viscocity and reduced shear rate, which are defined as
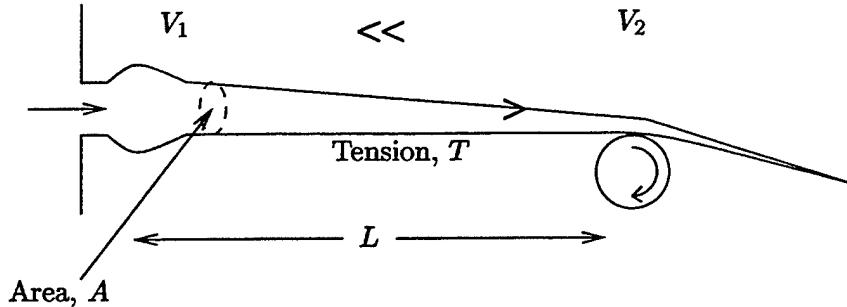
Figure 16: Spinline apparatus for measuring extensional viscosity

$$\mu_r = \mu\left(\dot{\gamma}, T\right) \frac{\mu\left(0, T_*\right)}{\mu\left(0, T\right)}, \tag{11}$$

$$\dot{\gamma}_r = \dot{\gamma}\frac{\mu\left(0, T\right)}{\mu\left(0, T_*\right)} \frac{T_* \rho_*}{T \rho}, \tag{12}$$

where T_* and ρ_* are a reference temperature and density, respectively. Similarly, figure 18 shows a plot of dimensionless viscosity against dimensionless shear rate for a series of solutions with different concentrations of polymers. Figure 19 shows the power law dependence of viscosity on molecular weight. In the dilute regime, (lower molecular weights) the dependence is linear and in the entangled regime (higher molecular weights) the viscosity is proportional to the molecular weight to the (empirically determined) 3.4 power. The significance of these scalings is that the rheological properties can be determined at a reference condition and then extrapolated to other conditions.

3.6 Cox-Merz rule

The Cox-Merz rule is an empirical rule which states that the dependence of the steady shear viscosity on the shear rate can be estimated from the dynamic viscocity (see section 3.3) as a function of frequency as the two curves are approximately identical (figure 20). This has important practical applications as it is easier to acquire data over a wide range of oscillation frequencies. We force a fluid periodically with frequency ω so that the strain $\gamma(t) = \gamma e^{i\omega t}$ and write the resulting stress as

$$\sigma(t) = G^*(\omega)\gamma(t) = \left(G' + iG''\right)\gamma e^{i\omega t},$$

where G^* is a complex elastic modulus. We can also write

$$\sigma(t) = \mu^*\dot{\gamma}(t) = \left(\mu' + i\mu''\right)i\omega\gamma e^{i\omega t}$$

for a complex viscosity μ^*. The Cox-Merz rule states that $\mu = |\mu^*|$ and $N_1 = 2G'$.

3.7 Non-dimensional Parameters

All materials have a relaxation time τ, the time required to return to its base state after being perturbed, for instance by stretching. This timescale can be seen in figure 3 as the
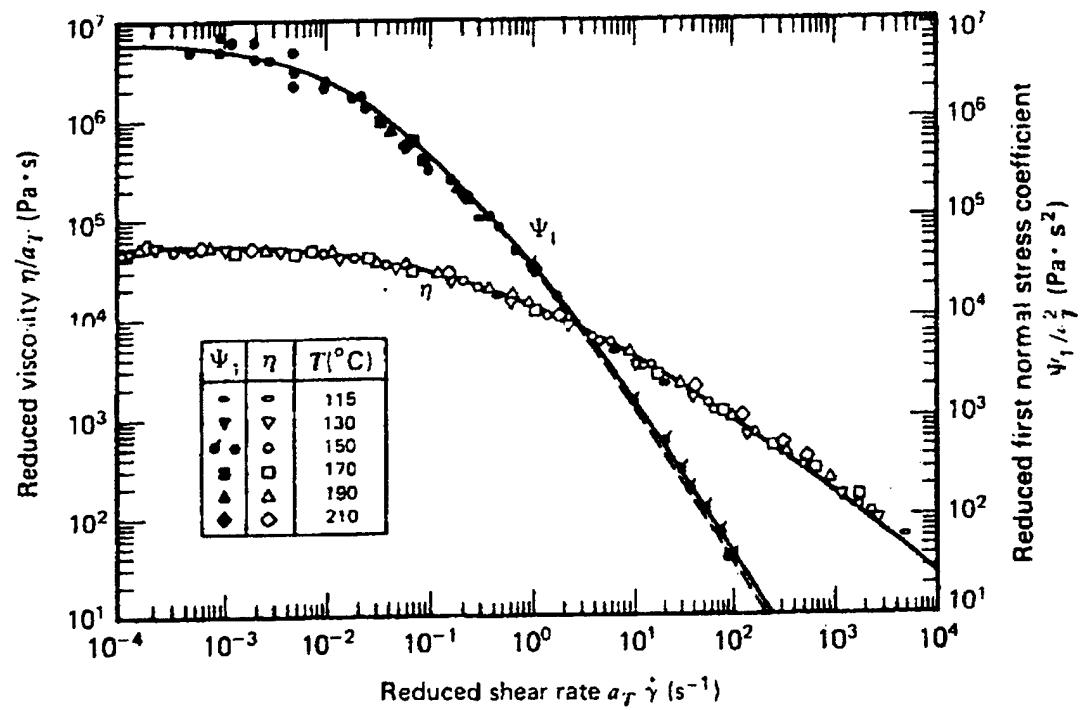
Figure 17: Dimensionless viscosity and first normal stress difference plotted against dimensionless shear rate for a variety of temperatures.
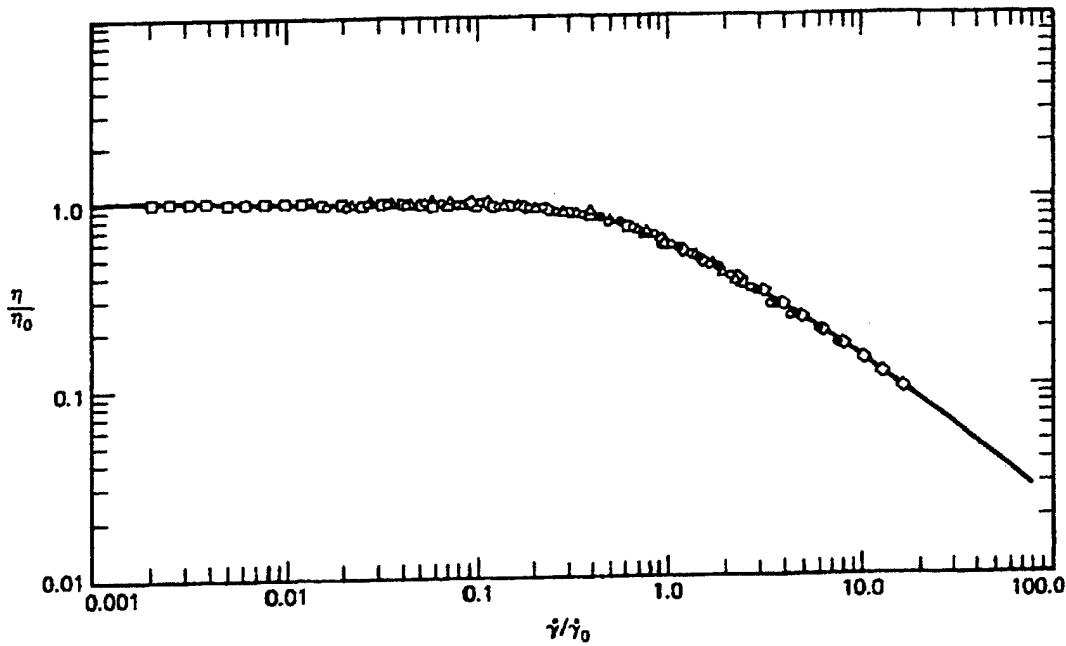
Figure 18: Dimensionless viscosity plotted against dimensionless shear rate for a series of solutions with different solution concentrations.

reciprocal of the shear rate at which the graph of viscosity versus shear rate begins to turn over. In non-Newtonian fluid flow the ratio of the timescales of deformation and relaxation is important. Two important non-dimensional parameters that express this quantity are the Weissenberg number and the Deborah number. The Weissenberg number is a measure of the strength of the shear rate and is defined by

$$Wi = \dot{\gamma}\tau.$$

The Deborah number is the ratio of the characteristic time-scale of the flow to the relaxation time,

$$De = \frac{U\tau}{L}.$$

Note that the Deborah and Weissenberg numbers are often the same (but not always) and either can be used to quantify the importance of relaxation in the fluid. For $De \ll 1$ the material relaxes relatively quickly and it behaves like a viscous fluid. Conversely, when $De \gg 1$ the fluid does not relax on the timescale of the flow and so acts like an elastic solid.

Notes by Neil Burrell and Julia Mullarney

References

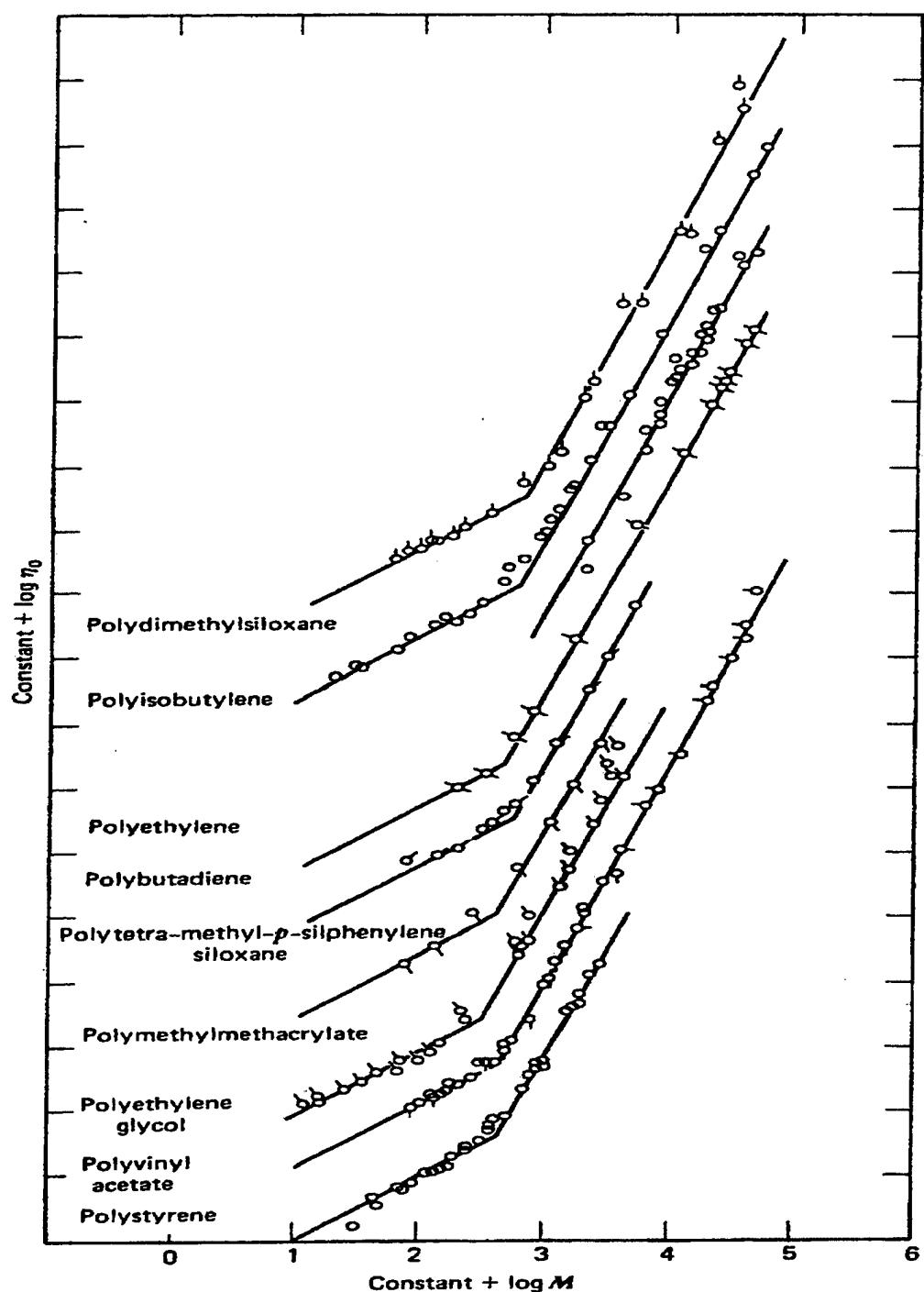[1] G. Batchelor, *An Introduction to fluid dynamics* (Cambridge University Press, Cambridge, 1967).

16

Figure 19: Viscosity versus molecular weight for a variety of polymers.
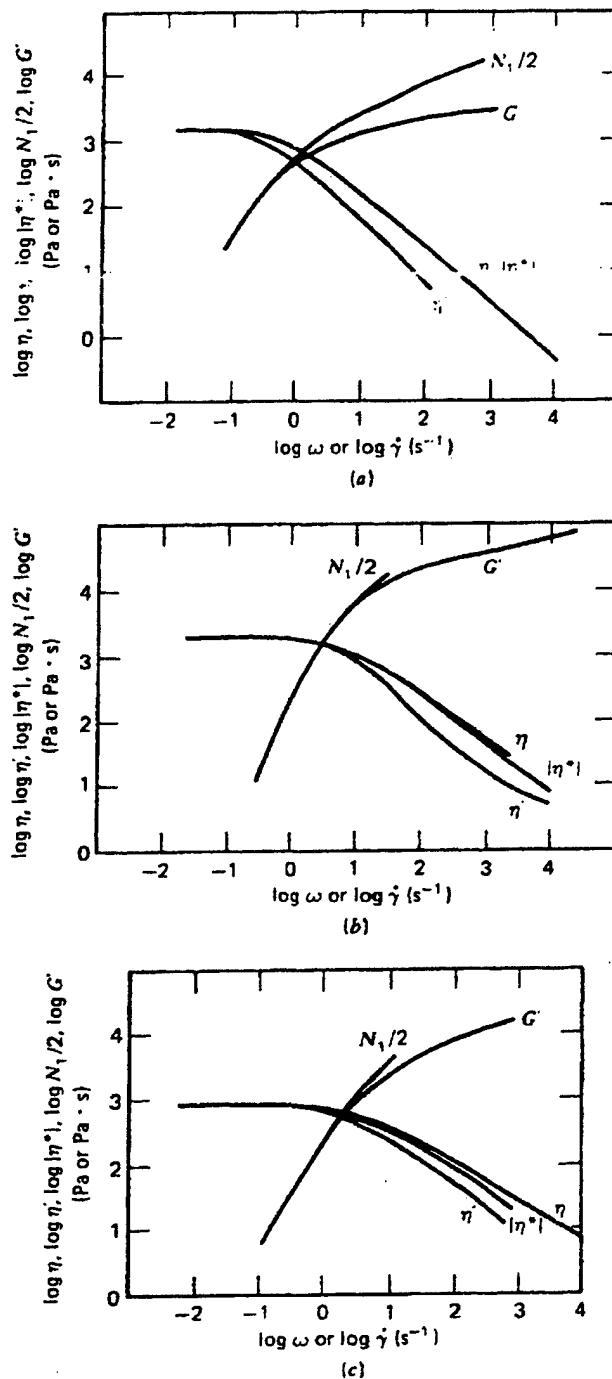
17

Figure 20: Illustration of the Cox-Merz rule. The curves compare properties under steady shear to their oscillating equivalents.

18

[2] R. Keiller, "Modelling of the extensional flow of the m1 fluid with the oldroyd equation," Journal of Non-Newtonian Fluid Mechanics **42**, 49 (1992).

[3] J. R. P. Szabo and E. Hinch, "Start-up of flow of a fene-fluid through a 4:1:4 constriction in a tube," Journal of Non-Newtonian Fluid Mechanics **72**, 73 (1997).

[4] R. D. J. Michele, R. Pätzold, "Alignment and aggregation effects in suspensions of spheres in non-newtonian media," Rheological Acta **16**, 317 (1977).

[5] J.-M. Cheny and K. Walters, "Rheological influences on the splashing experiment," Journal of Non-Newtonian Fluid Mechanics **86**, 185 (1999).

Lecture 2: Constitutive Relations

E. J. Hinch

1 Introduction

This lecture discusses equations of motion for non-Newtonian fluids. Any fluid must satisfy conservation of momentum

$$\rho \frac{D\boldsymbol{u}}{Dt} = -\nabla p + \nabla \cdot \sigma + \rho \boldsymbol{g} \tag{1}$$

where ρ is the density of the fluid, $\boldsymbol{u}$ is the velocity field, p is the pressure and σ is the deviatoric stress tensor (the trace-free component of the stress).[1] We can absorb the body force $\rho \boldsymbol{g}$ into a modified pressure, and in turn we can absorb the modified pressure into the stress giving $\rho \frac{D\boldsymbol{u}}{Dt} = \nabla \cdot \sigma$. Much of the modeling in non-Newtonian fluids concentrates on finding a constitutive relation between σ and the flow velocity distribution.

The fluids we use are incompressible unless stated otherwise, so we have assumed

$$\nabla \cdot \boldsymbol{u} = 0.$$

In many practical applications of non-Newtonian fluids inertia is also negligible. So we will often use the Stokes equations:

$$\nabla \cdot \sigma = 0.$$

2 Phenomenological

2.1 Simple materials

In a simple material the stress σ depends on the deformation and the rate of deformation. To understand this relationship we begin by considering how the fluid deforms. Using a Lagrangian fluid description we follow a fluid particle in the flow. The flow $\boldsymbol{u}$ maps a material element to a new position $\boldsymbol{x}$ that depends on its initial position $\boldsymbol{X}$

$$\boldsymbol{X} \to \boldsymbol{x}(\boldsymbol{X}, t).$$

If we follow a material line element, $\delta\boldsymbol{X}$, it is stretched and rotated in the flow according to

$$\delta\boldsymbol{X} \to \delta\boldsymbol{x} = \mathsf{A} \cdot \delta\boldsymbol{X}, \qquad \mathsf{A}_{iJ} = \frac{\partial x_i}{\partial X_J}.$$

---

[1] In these notes σ is used for either the stress or just the deviatoric stress. It is usually obvious from the context.

We assume that the system is local and causal. That is, the stress at a material point depends only on the history of that material point, and the stress cannot depend on future time. This gives a functional for stress

$$\sigma(t) = \sigma\{A(\tau)\}_{\tau \leq t}. \tag{2}$$

We now adopt the assumption of *material frame indifference* which states that our constitutive equation should not depend on the translation, rotation or acceleration of the frame of reference. Except in extreme cases this should be a good approximation. Thus, we should get the same result if we calculate our stress before or after rotating the frame of reference.

Consider a change of frame of reference given by

$$x' = Q(t)x + a(t), \tag{3}$$

with $Q(t)$ a rotation matrix and a a translation vector. The stress in the new frame of reference is given by

$$\sigma' = \sigma\{Q(\tau)\, A(\tau)\, Q^T(0)\}_{\tau \leq t}$$
$$\equiv Q(t)\, \sigma\{A(\tau)\}_{\tau \leq t}\, Q^T(t).$$

We require $\sigma\{A\}$ to obey this identity for all $Q(t)$.

2.1.1 Perfectly Elastic Materials

A perfectly elastic material responds instantaneously to an applied stress. All that matters is the present strain which depends only on the present position and the relaxed position. The history of how it arrived into its current position does not matter. The functional $\sigma\{A(t)\}$ becomes a function $\sigma(A)$.

We can decompose the deformation tensor A into a rotation tensor R and a stretch tensor U such that

$$A = R \cdot U \quad \text{with} \quad R^T R = I \quad \text{and} \quad U^2 = A^T A. \tag{4}$$

Then setting $Q \equiv R^T$ in *material frame indifference* gives

$$\sigma\{A\} = R^T(t)\, f(U(t))\, R(t), \tag{5}$$

thus reducing the problem to determining the unknown function $f(U)$. It is convenient to express the constitutive law in erms of the potential energy $w(U)$ instead of the function f. The principal of frame indifference leads to the constitutive law. For an elastic material that is isotropic in its rest state, and has potential energy w for elastic deformations, this gives

$$\sigma = \frac{1}{\gamma} \frac{\partial w}{\partial \alpha} AA^T - \frac{1}{\gamma} \frac{\partial w}{\partial \beta} A^{-T}A^{-1} \tag{6}$$

where $\alpha = \frac{1}{2}(\lambda_1^2 + \lambda_2^2 + \lambda_3^2)$, $\beta = \frac{1}{2}(\lambda_1^{-2} + \lambda_2^{-2} + \lambda_3^{-2})$ and $\gamma = \lambda_1^2 \lambda_2^2 \lambda_3^2$ (=1 if incompressible), and λ_n^2 are the eigenvalues of $A^T A$

2.2 Time derivative problem

In a new reference frame the stress is given by

$$\sigma' = Q\sigma Q^T$$

and so

$$\dot{\sigma}' = Q\dot{\sigma}Q^T + \dot{Q}\sigma Q^T + Q\sigma\dot{Q}^T.$$

Thus the transformation from $\dot{\sigma}$ to $\dot{\sigma}'$ does not follow the same relation as the transformation from σ to σ'. We will try to find some other derivative that does.

The new flow velocity is

$$u' = Qu + \dot{Q}x + \dot{a}$$

and the velocity gradient is

$$\frac{\partial u'}{\partial x'} = Q\frac{\partial u}{\partial x}Q^T + \dot{Q}Q^T. \tag{7}$$

The velocity gradient can be separated into symmetric (strain rate) and antisymmetric (vorticity) parts The transformed strain rate is $E' = QEQ^T$ and the transformed vorticity is $\Omega' = Q\Omega Q^T + \dot{Q}Q^T$.

Putting these elements together we can show that the co-rotational (Jaumann [1, 2]) time derivative

$$\overset{\circ}{\sigma} \equiv \frac{D\sigma}{Dt} - \Omega \cdot \sigma + \sigma \cdot \Omega \tag{8}$$

has transformation

$$\overset{\circ}{\sigma'} = Q \overset{\circ}{\sigma} Q^T,$$

(where $\overset{\circ}{\sigma'}$ denotes the co-roational derivative of the stress in the new frame of reference,) as does the co-deformational (Oldroyd [3] or upper convected) derivative

$$\overset{\triangledown}{\sigma} \equiv \frac{D\sigma}{Dt} - \nabla u^T \cdot \sigma - \sigma \cdot \nabla u. \tag{9}$$

Note $\overset{\circ}{I} = 0$ but $\overset{\triangledown}{I} \neq 0$.

The co-rotational time derivative is the rate of change as observed while rotating and translating with the fluid. The co-deformational derivative is the rate of change as observed while deforming and translating with the fluid.

3   Exact approximations

3.1   Linear viscoelasticity

Linear viscoelasticity is valid in the limit where $A^T A \approx I$. The most general form of the history-dependent linear constitutive law is

$$\sigma(t) = R(t) \int_0^\infty G(s) \left(A^T A\right)^{\cdot} (t-s)ds\, R^T(t). \tag{10}$$

22

This is a co-rotational time integral. $G(s)$ represents the elastic memory. It is the Fourier transform of the frequency dependent elastic modulus $G^*(w)$ defined in section 3.3 of Lecture 1. For a Newtonian fluid $G(s) = \delta(s)$ and for an elastic solid, $G(s) = 1$.

For simple shear with shear rate $\dot{\gamma}$

$$\sigma(t) = \int_0^\infty G(s)\dot{\gamma}(t-s)ds \tag{11}$$

and since for steady shear $\dot{\gamma}$ is constant, the steady shear viscosity is given by $\int_0^\infty G(s)ds$.

3.2 Second order fluid

The second order fluid is derived through a retarded motion expansion and is valid for slow, weak flows. Considerable care must be used because this model can have instabilities in regimes where it doesn't apply (*e.g.*, high frequency), and these regimes can arise from poorly chosen boundary conditions.

The stress is Newtonian with small terms added:

$$\sigma = -p\mathsf{I} + 2\mu\mathsf{E} - 2\alpha_1 \overset{\triangledown}{\mathsf{E}} + \alpha_2 \mathsf{E} \cdot \mathsf{E} \tag{12}$$

$$\mu = \int_0^\infty G(s)ds$$

$$\alpha_1 = \int_0^\infty s\,G(s)ds.$$

In simple shear the second order fluid has constant viscosity $\mu = \int_0^\infty G(s)ds$ and normal stress differences $N_1 = \sigma_{yy} - \sigma_{xx} = 2\alpha_1\dot{\gamma}^2$, $N_2 = \sigma_{zz} - \sigma_{yy} = -\frac{1}{4}\alpha_2\dot{\gamma}^2$, where x denotes the flow direction, y is the velocity gradient direction.

In uniaxial extensional flow the viscosity is

$$\mu_{\text{ext}} = \mu + (\alpha_1 + \frac{1}{4}\alpha_2)\dot{\epsilon}, \tag{13}$$

where $\dot{\epsilon}$ is the elongation rate.

4 Semi-empirical models

Many fluids are too non-linear to be described by the linear viscoelastic or slightly non-linear second order models discussed above. For these fluids there are no exact solutions or exact approximations and other models must be considered.

4.1 Generalized Newtonian Fluid

The generalized Newtonian fluid follows the same equations as the Newtonian fluid but the viscosity depends on the shear rate $\dot{\gamma} = \sqrt{2\mathsf{E} : \mathsf{E}}$. As for Newtonian fluids, the stress depends only on the instantaneous flow and not the flow history. The constitutive law is

$$\sigma = -p\mathsf{I} + 2\mu(\dot{\gamma})\mathsf{E}. \tag{14}$$

The generalized Newtonian models were developed to fit experimental data and the form of $\mu(\dot{\gamma})$ is usually derived empirically. Some common expressions used to fit data are:

23

- Power Law [4]

$$\mu(\dot{\gamma}) = k\dot{\gamma}^{n-1},$$ (15)

where k and n are fit parameters.

- Carreau, Yasuda, Cross [5, 6, 7]

$$\mu(\dot{\gamma}) = \mu_\infty + (\mu_0 - \mu_\infty)[1 + (\lambda\dot{\gamma})^a]^{\frac{n-1}{a}}$$ (16)

where μ_0 and μ_∞ are the viscosities at the limits of zero and infinite shear rate, respectively; a, n, and λ are fit parameters.

- Yield fluids: the fluid flows only above some critical stress σ_y.

  - Bingham [8]

  $$\mu = \begin{cases} \infty & \text{if } |\sigma| < \sigma_y \\ \mu_0 + \dfrac{\sigma_y}{\dot{\gamma}} & \text{if } |\sigma| > \sigma_y \end{cases}$$

  - Herschel Bulkley

  $$\mu = \begin{cases} \infty & \text{if } |\sigma| < \sigma_y \\ k\dot{\sigma}^{n-1} + \dfrac{\sigma_y}{\dot{\gamma}} & \text{if } |\sigma| > \sigma_y \end{cases}$$

4.2 The Oldroyd-B and FENE Models

The Oldroyd-B model [3] is one of the simplest models that includes the history of the flow. We use the following equation for the evolution of the deviatoric stress,

$$\sigma + \lambda_1 \overset{\triangledown}{\sigma} = 2\mu(\mathsf{E} + \lambda_2 \overset{\triangledown}{\mathsf{E}}),$$ (17)

where λ_1 is the relaxation time and λ_2 is the retardation time. For a given pressure p, the Oldroyd-B model often appears in an equivalent form for the total stress:

$$\sigma = -p^*\mathsf{I} + 2\mu^*\mathsf{E} + \frac{G}{\tau}\mathsf{A}$$ (18)

$$\overset{\triangledown}{\mathsf{A}} = -\frac{1}{\tau}(\mathsf{A} - \mathsf{I})$$ (19)

where $p^* = p + 2(1 - \lambda_2/\lambda_1)\mu/\lambda_1$, $G = 2(1 - \lambda_2/\lambda_1)\mu$, $\tau = \lambda_1$ and $\mu^* = \lambda_2\mu/\lambda_1$. The Oldroyd-B model reduces to Upper Convective Maxwell (UCM) when $\lambda_2 = 0$ and viscous Newtonian when $\lambda_2 = \lambda_1$.

In simple shear an Oldroyd-B fluid has constant viscosity $\mu = G/2 + \mu^*$ and the normal stresses are

$$N_1 = 2\mu(\lambda_1 - \lambda_2)\dot{\gamma}^2, \qquad N_2 \equiv 0.$$ (20)

The uniaxial extensional viscosity is

$$\mu_{\text{ext}} = \frac{\mu(1 - \lambda_2\dot{\epsilon} - 2\lambda_1\lambda_2\dot{\epsilon}^2)}{(1 - \lambda_2\dot{\epsilon})(1 + \lambda_1\dot{\epsilon})}.$$ (21)
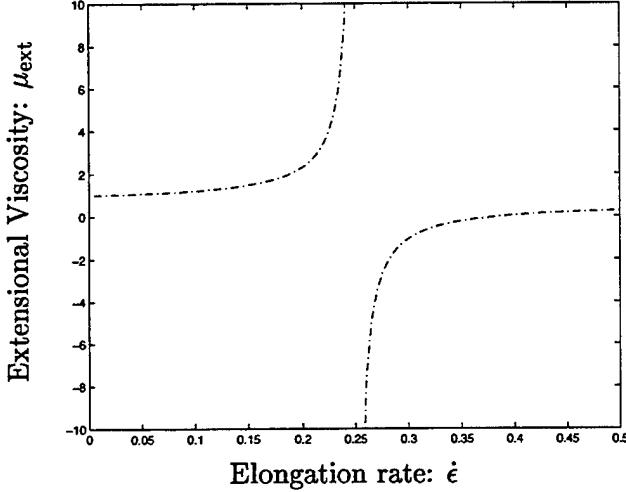
24

Figure 1: The extensional viscosity for $\lambda_1 = 2$, $\lambda_2 = 1$. The extensional viscosity is negative for elongation rates slightly above $1/2\lambda_1$.

This gives negative viscosities at some elongation rates (figure 1) which is unphysical. This happens because the Oldroyd-B model is derived using Hooks Law springs which are infinitely extensible.

The Oldroyd-B model can be reformulated to eliminate the negative viscosity. Assuming that the microstructure is not infinitely extensible, we get

$$\overset{\triangledown}{A} + \frac{f}{\tau}(A - I) = 0 \tag{22}$$

for some function $f(A)$. The stress σ is then

$$\tau = -pI + 2\mu_s E + \frac{Gf}{\tau}(A - I). \tag{23}$$

Occasionally f appears only in Equation (22) and not in (23).

The FENE (finitely extensible nonlinearly elastic) modification keeps A from growing too fast by setting

$$f = \frac{L^2}{L^2 - \text{trace} A}, \tag{24}$$

where L represents a nondimensional length scale for the stretching of the microstructure. The more A stretches, the stiffer it becomes.

4.3 Other Consititutive Equations

Below are a few of the many other costitutive equations, which are derived to match experimental data.

- The White-Metzner model [9] is used for shear-thinning fluids. It is a modified Maxwell model that allows incorporation of experimental data on viscosity as a func-

25

tion of shear rate. The deviatoric stress is given by

$$\sigma + \frac{\mu(\dot{\gamma})}{G} \overset{\triangledown}{\sigma} = 2\mu(\dot{\gamma})\mathsf{E}. \tag{25}$$

The shear thinning viscosity $\mu(\dot{\gamma})$ often follows a power-law.

- The Giesekus model [10] adds quadratic nonlinearity and divides the deviatoric stress into a solvent contribution (σ_s) and a polymer contribution (σ_p).

$$\sigma = \sigma_s + \sigma_p$$
$$\sigma_s = \mu_s\mathsf{E}$$
$$\sigma_p + \lambda_1\overset{\triangledown}{\sigma}_p + \frac{\alpha\lambda_1}{\mu_p}\sigma_p^2 = 2\mu_p\mathsf{E}$$

- The PTT (Phan-Thien-Tanner) model [11] is similar to Giesekus but has a different nonlinear term

$$\sigma = \sigma_s + \sigma_p$$
$$\sigma_s = \mu_s\mathsf{E}$$
$$\sigma_p + \lambda_1\overset{\triangledown}{\sigma}_p + \left[\exp\left(\frac{\lambda_1}{\mu_p}\operatorname{trace}\sigma_p\right) - 1\right]\sigma_p = 2\mu_p\mathsf{E}$$

- The Kay-Bernstein-Kearsly-Zappa (K-BKZ) equation [12] combines linear viscoelasticity and nonlinear elasticity via a memory integral constitutive law:

$$\sigma = \int_0^\infty \dot{G}(s)\left[\frac{\partial w}{\partial \alpha}(\tilde{\mathsf{A}}\tilde{\mathsf{A}}^T - 1) - \frac{\partial w}{\partial \beta}(\tilde{\mathsf{A}}^{-T}\tilde{\mathsf{A}}^{-1} - 1)\right]ds \tag{26}$$

where $\tilde{\mathsf{A}} \equiv \mathsf{A}(t)\mathsf{A}^{-1}(s)$, and w, α and β are as in Section 2.1.1.

In simple shear

$$\mu = \int_0^\infty \dot{G}(s)\left(\frac{\partial w}{\partial \alpha} + \frac{\partial w}{\partial \beta}\right)ds,$$

while in extension

$$\mu_{\text{ext}} = \int_0^\infty \dot{G}(s)\left[\frac{\partial w}{\partial \alpha}(e^{2\dot{\epsilon}s} - e^{-\dot{\epsilon}s}) + \frac{\partial w}{\partial \beta}(e^{\dot{\epsilon}s} - e^{-2\dot{\epsilon}s})\right]ds.$$

The Wagner model [13] is a special case of the K-BKZ model with

$$\frac{\partial w}{\partial \beta} = 0 \ (N_2 = 0) \quad \text{and} \quad \frac{\partial w}{\partial \alpha} = e^{-k\sqrt{\alpha-3+\theta(\beta-\alpha)}}.$$

- One can choose σ_p to be the sum of several components each of which has its own relaxation time. This allows us to introduce multiple relaxation times into most of the above models.

Notes by Joel C. Miller and Alison Rust

References

[1] G. Jaumann, *Grundlagen der Bewegungslehre* (Springer, Leipzig, 1905).

[2] S. Zaremba, "Correlation of dynamic and steady flow viscosities," Bull. Acad. Sci. Cracovie 594 (1903).

[3] J. G. Oldroyd, "On the formulation of rheological equations of state," Proc. Roy. Soc. London **200**, 523 (1950).

[4] de Waele, "Viscometry and plastometry," Oil Color Chem. Assoc. J. **6**, 33 (1923).

[5] P. Carreau, "Rheological equations from molecular network theories," Trans. Soc. Rheol **16**, 99 (1972).

[6] R. A. K. Yasuda and R. Cohen, "Shear-flow properties of concentrated-solutions of linear and star branched polystyrenes," Rheol. Acta **20**, 163 (1981).

[7] M. Cross, "Rheology of non-newtonian fluids: a new flow equation for pseudo-plastic systems," J. Colloid **20**, 417 (1958).

[8] E. C. Bingham, *Fluidity and Plasticity* (McGraw-Hill, New York, 1922).

[9] J. L. White and A. Metzner, "Rheological equations from molecular network theories," J. Appl. Polym. Sci. **7**, 1867 (1963).

[10] H. Giesekus, "A simple constitutive equation for polymer fluids based on the concept of deformation dependent tensorial mobility," J. Non-Newtonian Fluid Mech. **11**, 69 (1982).

[11] N. Phan-Thien and R. I. Tanner, "A new constitutive equation derived from network theory," J. Non-Newtonian Fluid Mech. **2**, 353 (1977).

[12] B. Bernstein, E. A. Kearsley, and L. J. Zapas, "Thermodynamics of perfect elastic fluids," J. Res. Natl. Bur. Stand. **68**, 103 (1964).

[13] M. H. Wagner, "Network theory of polymer melts," Rheol. Acta **18**, 33 (1979).

Lecture 3: Simple Flows

E. J. Hinch

In this lecture, we will study some simple flow phenomena for the non-Newtonian fluid. From analyzing these simple phenomena, we will find that non-Newtonian fluid has many unique properties and can be quite different from the Newtonian fluid in some aspects.

1 Pipe flow of a power-law fluid

The pipe flow of Newtonian fluid has been widely studied and well understood. Here, we will analyze the pipe flow of non-Newtonian fluid and compare the phenomenon with that of the Newtonian fluid.

We consider a cylindrical pipe, where the radius of the pipe is R and the length is L. The pressure drop across the pipe is Δp and the flux of the fluid though the pipe is Q (shown in Figure 1). Also, we assume that the flow in the pipe is steady, uni-directional and uniform in z.

Thus, the axial momentum of the fluid satisfies:

$$0 = -\frac{dp}{dz} + \frac{1}{r}\frac{\partial(r\sigma_{zr})}{\partial r}. \tag{1}$$

Integrate this equation with respect to r and scale $\frac{dp}{dz}$ with $\frac{\Delta p}{L}$, we have:

$$\sigma_{zr} = \frac{r}{R}\sigma_{wall}, \tag{2}$$

where σ_{wall} represents the stress on the wall and is given by $\sigma_{wall} = \frac{\Delta p R}{2L}$. For the power-law fluid, the constitutive equation is:

$$\sigma_{zr} = k\dot{\gamma}^n, \tag{3}$$

Figure 1: Pipe flow

28
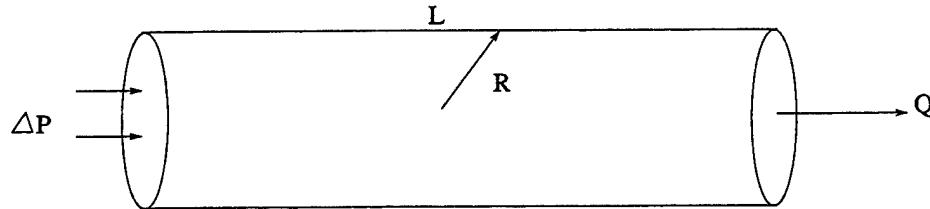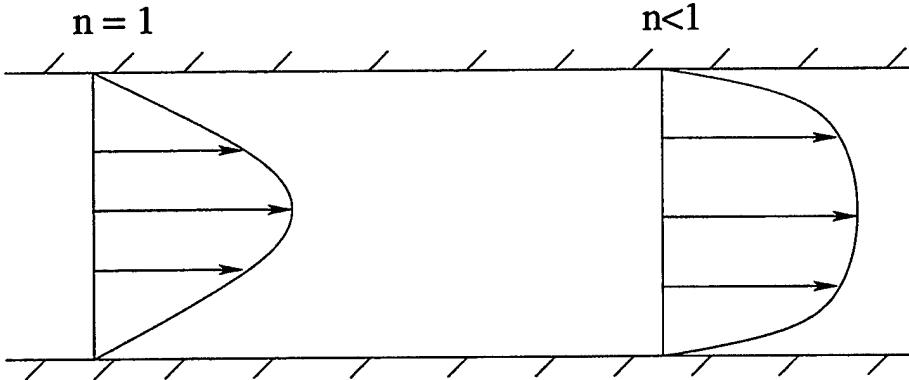
Figure 2: Flow profile

where k is a constant and $\dot{\gamma}$ is the scalar strain rate. For the pipe flow, the strain rate can be expressed as:

$$\dot{\gamma} = -\frac{dw}{dr},\qquad(4)$$

where w is the axial velocity. Substitute the expression for the strain rate into the constitutive equation, then put the constitutive equation into the equation (2); we find

$$-k\left(\frac{dw}{dr}\right)^n = \frac{r}{R}\sigma_{wall}.\qquad(5)$$

Integrate this equation with respect to r; we have:

$$w = \left(\frac{\sigma_w}{kR}\right)^{\frac{1}{n}}\frac{R^{\frac{1}{n}+1} - r^{\frac{1}{n}+1}}{\frac{1}{n}+1}.\qquad(6)$$

For the different choices of n, the relation of the axial velocity to the radius is different(see Fig. 2). For Newtonian flow (Poiseuille flow) with $n = 1$, the structure of the flow is quadratic ($w \propto r^2$). For shear thinning fluid with $n < 1$, the profile of the flow is flatter in the middle and decays faster towards the wall. Near the middle of the pipe, the stress σ is low, and the viscosity μ is high; near the boundary of the pipe, the stress σ is high, and the viscosity μ is low.

The volume flux Q of the flow through the pipe is given by:

$$Q = \int_0^R w2\pi r\,dr = \frac{\pi R^3}{\frac{1}{n}+3}\left(\frac{\Delta PR}{2Lk}\right)^{\frac{1}{n}}.\qquad(7)$$

The volume flux Q of the shear thinning non-Newtonian fluid increases more quickly with pressure gradient than the Newtonian fluid. The flow of a power law fluid along pipe has common applications in wire coating, film draining and drop spreading.

2 Capillary rheometry

In Capillary rheometry, the shear viscosity of a fluid can be determined by shear rate. Assuming the flux through the pipe to be Q and the axial velocity to be w, the flux of the

fluid can be expressed as:

$$Q = \int_0^R w 2\pi r \, dr = w\pi r^2 \big|_0^R - \int_0^R \frac{dw}{dr} \pi r^2 \, dr. \tag{8}$$

Since the axial velocity is zero at the boundary (no slip boundary conditions), then $w\pi r^2 \big|_0^R = 0$. Also, the strain rate $\dot{\gamma}$ can be expressed as $\dot{\gamma} = \frac{dw}{dr}$. Thus,

$$Q = -\int_0^R \dot{\gamma} \pi r^2 \, dr. \tag{9}$$

From the calculation of the flow through the pipe in Section 1, we know that the stress can be expressed as:

$$\sigma_{zr} = \frac{r}{R} \sigma_{wall}. \tag{10}$$

This relation does not depend on the constitutive equation, and the stess σ_{zr} linearly depends on the stress on the wall σ_{wall}. Therefore, the radius can also be expressed as a function of the stress: $r = \frac{R\sigma_{rz}}{\sigma_{wall}}$

Changing the integration variable from the radius r to the stress σ, we may express the flux through the pipe:

$$Q = -\frac{\pi R^3}{\sigma_{wall}^3} \int_0^{\sigma_{wall}} \dot{\gamma}(\sigma) \sigma^2 \, d\sigma. \tag{11}$$

Before the change of variables, the strain rate is a function of the radius, which describes the geometric property of the strain rate. After the change the variable, the strain rate is a function of the stress, which describes the material property of the strain rate. If we differentiate the above equation with respect to the stress on the wall σ_{wall}, we have:

$$\dot{\gamma}_{wall} = -\frac{1}{\sigma_{wall}^2} \frac{d}{d\sigma_{wall}} \left(\frac{\sigma_{wall}^3 Q}{\pi R^3} \right) = -\frac{1}{\pi R^3} \left(3Q + \sigma_{wall} \frac{dQ}{d\sigma_{wall}} \right). \tag{12}$$

Since the stress on the wall σ_w is linearly proportional to the pressure gradient Δp, we may simplify this equation as:

$$\dot{\gamma}_{wall} = -\frac{1}{\pi R^3} \left(3 + \frac{d\ln Q}{d\ln \Delta p} \right). \tag{13}$$

Here $\frac{d\ln Q}{d\ln \Delta p}$ is the slope of the $\ln Q$ and $\ln \Delta p$ plot. For a Newtonian flow (Poisseuille fluid), we have $\frac{d\ln Q}{d\ln \Delta p} = 1$. For a shear thinning fluid with $n = 1/4$, the relationship will be: $\frac{d\ln Q}{d\ln \Delta p} = 4$. But for any fluid, by measuring the volume flux through the pipe Q and the pressure gradient Δp, the value of the strain rate on the wall can be calculated from the above equation. Thus the viscosity on the wall can be expressed as:

$$\mu_{wall} = \frac{\sigma_{wall}}{\dot{\gamma}_{wall}} = \frac{\Delta p R}{2L \dot{\gamma}_{wall}}, \tag{14}$$
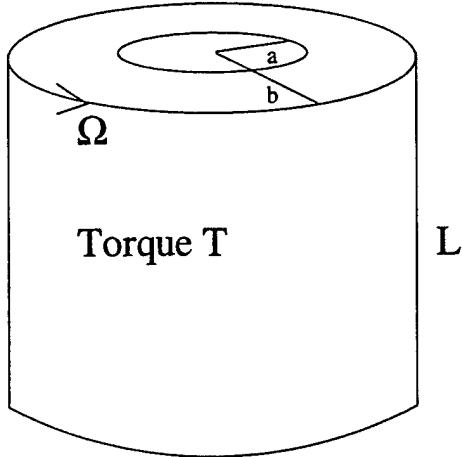
which gives the rheological law.

Figure 3: Couette device

3 Bingham yield fluid in a Couette device

For a Bingham fluid, if the applied stress σ is smaller than the yield stress, the fluid will remains rigid. But if the applied stress σ is larger than the yield stress, the fluid yields and shears. For a Couette device containing Bingham fluid, we assume that the inner radius is a and the outer radius is b and apply a torque T on the outer cylinder (see Figure 3). For an axisymmetric steady flow with velocity field $(0, u_\theta(r), 0)$, conservation of momentum in the θ direction demands that:

$$0 = \frac{1}{r^2} \frac{d}{dr}(r^2 \sigma_{\theta r}).$$

(15)

Integrating this equation with respect to r, we have:

$$\sigma_{r\theta} = \frac{T}{2\pi L r^2}.$$

(16)

The constitutive equation for the Bingham fluid is:

$$\dot{\gamma} = 0 \qquad \text{if } \sigma < \sigma_y$$

(17)

$$\sigma_{r\theta} = \sigma_y + \mu \dot{\gamma} \qquad \text{if } \sigma > \sigma_y,$$

(18)

where σ_y is the yield stress and $\dot{\gamma}$ is the only non-zero component of the strain rate tensor: $\dot{\gamma} = r \frac{d}{dr}\left(\frac{u_\theta}{r}\right)$. Therefore, we could get the yield radius r_y in the device to be:

$$r_y = \sqrt{\frac{T}{2\pi L \sigma_y}}.$$

(19)

Therefore, the different positions for r_y correspond to different flow types of the Bingham fluid in the Couette device:

$$\text{Yield throughout} \quad \text{if } r_y > b,$$

(20)

$$\text{Yield nowhere} \quad \text{if } r_y < a,$$

(21)

$$\text{Intermediate situation} \quad \text{if } a < r_y < b.$$

(22)

31

In the intermediate state, for $a < r_y < b$, the material yields and shears; but for $r_y < r < b$, the material rotates rigidly. Now we will calculate these two regions separately. For $a < r < r_y$, the shear rate is expressed as:

$$\dot\gamma = r\frac{d}{dr}\left(\frac{u_\theta}{r}\right) = \frac{\sigma_y}{\mu}\left(\frac{r_y^2}{r^2} - 1\right).$$

(23)

Integrating this equation with respect to r, we find:

$$\frac{u_\theta}{r} = \frac{\sigma_y}{\mu}\left(\frac{1}{2}\left(\frac{1}{a^2} - \frac{1}{r^2}\right) - \ln\left(\frac{r}{a}\right)\right).$$

(24)

For the region $r_y < r < b$, the solid body rotation can be expressed as:

$$\frac{u_\theta}{r} = \Omega,$$

(25)

where Ω is the constant rotation rate. At $r = r_y$, we match the velocity in these two regions to find that

$$\Omega = \frac{\sigma_y}{\mu}\left(\frac{1}{2}\left(\frac{1}{a^2} - \frac{1}{r^2}\right) - \ln\left(\frac{r}{a}\right)\right).$$

(26)

Since the radius for the yield surface r_y is also a function of the torque T, the angular velocity of the solid body rotation Ω is a function of the applied torque T.

4 Rod climbing of a second order fluid

As we have seen in earlier lectures, a well-documented phenomenon of non-Newtonian fluids is rod climbing. When a rod is rotated in a non-Newtonian fluid, the fluid is forced towards the center instead of being thrown away from the rod as in a Newtonian fluid. In a non-Newtonian fluid, tension in the streamlines, or the hoop stress, has a radial force inward that forces the fluid towards and then up the rod. In this section we determine the free surface of a weakly non-linear second-order fluid caused by a rod of radius a rotating at a frequency Ω in the fluid (figure 4).

The flow is weakly non-linear so to leading order, the fluid behaves like a Newtonian fluid. The velocity, which has only an azimuthal component, is determined from the azimuthal component of the momentum equation,

$$\mu\frac{\partial}{\partial r}\left(\frac{1}{r}\frac{\partial}{\partial r}\left(ru_\theta\right)\right).$$

(27)

Integrating this equation and applying boundary condition of $r = a$ and $r = \infty$ yields

$$u_\theta = \frac{\Omega a^2}{r},$$

(28)

and the strain rate is

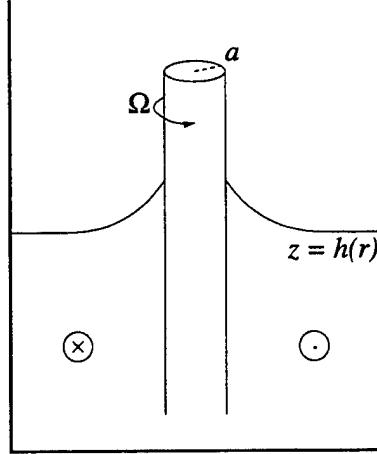$$\dot\gamma = r\frac{d}{dr}\left(\frac{u_\theta}{r}\right) = -\frac{2\Omega a^2}{r^2}.$$

(29)

Figure 4: Geometry of rod climbing problem. A cylinder of radius a is rotating with frequency Ω, which causes a displacement of the free surface which is described by $h(r)$.

The constitutive equation of a second-order fluid is given by

$$\sigma = -pI + 2\mu E - 2\alpha \overset{\triangledown}{E} + \beta E \cdot E, \tag{30}$$

where $\overset{\triangledown}{E}$ is the upper convective derivative of the strain tensor E, and the last two terms of equation (30) are small compared to the others. Then, because $E_{r\theta} = E_{\theta r} = \frac{1}{2}\dot\gamma$, the components of stress are given by

$$\sigma_{\theta r} = \mu\dot\gamma, \tag{31}$$

$$\sigma_{rr} = -p + \frac{1}{4}\beta\dot\gamma^2, \tag{32}$$

$$\sigma_{\theta\theta} = -p + \left(2\alpha + \frac{1}{4}\beta\right)\dot\gamma^2, \tag{33}$$

$$\sigma_{zz} = -p. \tag{34}$$

In order to determine the pressure dependence in the radial direction, we apply the steady state Stokes equation and consider the radial component in cylindrical coordinates to find

$$0 = \frac{\partial \sigma_{rr}}{\partial r} + \frac{\sigma_{rr} - \sigma_{\theta\theta}}{r}, \tag{35}$$

where the last term is the normal stress N_1 or the hoop stress. Using equations (32) and (33) we can write the normal stresses in terms of r. Integrating with respect to r yields

$$\sigma_{rr} + 2\alpha\frac{\Omega^2 a^4}{r^4} = -p + \frac{1}{4}(2\alpha + \beta)\dot\gamma^2 = f(z), \tag{36}$$

where f is an arbitrary function of z. The axial or vertical component of the Stokes equation gives a hydrostatic balance

$$0 = \frac{\partial \sigma_{zz}}{\partial z} + \rho g. \tag{37}$$

33

Integrating with respect to z and applying the boundary condition $p = 0$ at the free surface, $z = h(r)$, we find

$$p = \rho g \left(h(r) - z \right). \tag{38}$$

Finally, we choose $f(z) = \rho g z$ to cancel the z dependence in the pressure to find that the free surface height is described by

$$h(r) = \frac{1}{\rho g} \left(2\alpha + \beta \right) \frac{\Omega^2 a^4}{r^4}. \tag{39}$$

Therefore as long as $2\alpha + \beta > 0$ rod climbing occurs in the fluid. If this term is negative, though, it implies that the fluid is plunging down the rod rather than climbing up the rod. This solution seems unphysical and may be due to an improper force balance or improper definition of the constitutive equation.

5 Unchanged flow field for some second order fluids

In the previous section we have assumed that there is no small non-linear correction to the flow field u_θ as there is in the constitutive equation (30). In this section we sketch how to show that this is a valid assumption for some flows. At the end of the section we will see that the method described here does not necessarily verify an unchanged flow field in the rod climbing problem. The following proof will require the use of the identity,

$$\nabla \cdot \left(\overset{\triangledown}{E} + 4E \cdot E \right) = \frac{D}{Dt} \nabla^2 u + \nabla u \cdot \nabla^2 u + \nabla (E : E). \tag{40}$$

As we only touched on this topic briefly in lecture, we will not prove the identity here, but leave it as an exercise for the interested reader.

We define p_1 and p_2 as the pressure that satisfies the Stokes flow and the pressure related to the non-linear elastic effect, respectively. Then u and p_1 satisfy the equation for Stokes flow,

$$0 = \nabla p_1 + \mu \nabla^2 u. \tag{41}$$

Since u does not have an elastic correction, we must be able to show that u and p_2 satisfy

$$\nabla \cdot \sigma = 0, \tag{42}$$

$$\sigma = -p_2 I + 2\mu E - 2\alpha \overset{\triangledown}{E} - 4\alpha E \cdot E \tag{43}$$

with

$$p_2 = p_1 - \frac{\alpha}{\mu} \frac{D p_1}{Dt} + \alpha E : E. \tag{44}$$

We can show that this is indeed true by using the identity given in (40). (Details are again left for the interested reader). Note that in (43) β has the specific value -4α. Recall that for rod climbing to occur $2\alpha + \beta > 0$, and therefore the method sketched here does not apply to the rod climbing problem. This analysis does show that for some flows, the equations of motion and the constitutive equation are satisfied without a small elastic correction to the flow field u. This holds in planar and uni-directional flows without a restriction on the relationship between α and β.

34

6 Anisotropic converging channel flow of a suspension of rigid rods

The constitutive equation for a suspension of rigid rods is given by

$$\sigma = -pI + 2\mu_{\text{shear}}E + 2\mu_{\text{ext.}}\hat{p}\hat{p}\left(\hat{p}\cdot E \cdot \hat{p}\right), \tag{45}$$

where $\hat{p}$ is the unit vector in the direction of the rods. The shear and extensional viscosities, μ_{shear} and $\mu_{\text{ext.}}$, are constants with $\mu_{\text{ext.}}$ representing an additional viscosity over μ_{shear} in the direction of the rods. In this problem it is assumed that the rods are fixed in the direction of the flow, and we will describe the formation of recirculating eddies (cf. lecture 2) around a point sink.

The flow field is described by a two-dimensional sink flow in the half plane given by

$$\mathbf{u} = \left(\frac{f(\theta)}{r}, 0\right), \qquad \hat{p} = (1,0) \tag{46}$$

in polar coordinates, where the radial direction represents the distance for the point sink and the azimuthal direction varies between 0 and π in the upper half plane. Therefore the velocity is purely in the radial direction and satisfies incompressibility.

Using the constitutive equation given in (45), we can determine the different components of the stress using

$$E_{rr} = \frac{\partial u_r}{\partial r}, \qquad E_{r\theta} = \frac{1}{2r}\frac{\partial u_r}{\partial \theta}, \qquad E_{\theta\theta} = \frac{u_r}{r}. \tag{47}$$

Note that the extensional viscosity only makes a contribution to σ_{rr}, so

$$\sigma_{rr} = -\frac{g(\theta)}{r^2} - 2(\mu_{\text{shear}} + \mu_{\text{ext.}})\frac{f}{r^2}, \tag{48}$$

$$\sigma_{r\theta} = \mu_{\text{shear}}\frac{f'}{r^2}, \tag{49}$$

$$\sigma_{\theta\theta} = -\frac{g(\theta)}{r^2} + 2\mu_{\text{shear}}\frac{f}{r^2}, \tag{50}$$

where $g(\theta)/r^2$ is the pressure, which is an unknown function of θ, and primes here denote differentiation with respect to θ. Now the two unknows, $f(\theta)$ and $g(\theta)$, can solved for by applying the two components of momentum conservation.

Assuming steady state and taking the azimuthal component of the steady Stokes equation $\nabla \cdot \sigma = 0$ (see table in Bird *et al.*),

$$\frac{\partial \sigma_{r\theta}}{\partial r} + \frac{1}{r}\frac{\partial \sigma_{\theta\theta}}{\partial \theta} + 2\frac{\sigma_{r\theta}}{r} = 0. \tag{51}$$

Using equations (49) and (50), this can then be written in terms of f and g by

$$g' = 2\mu_{\text{shear}}f'. \tag{52}$$

Similarly, the radial component of $\nabla \cdot \sigma = 0$ gives

$$\frac{\partial \sigma_{rr}}{\partial r} + \frac{1}{r}\frac{\partial \sigma_{r\theta}}{\partial \theta} + \frac{\sigma_{rr} - \sigma_{\theta\theta}}{r} = 0. \tag{53}$$
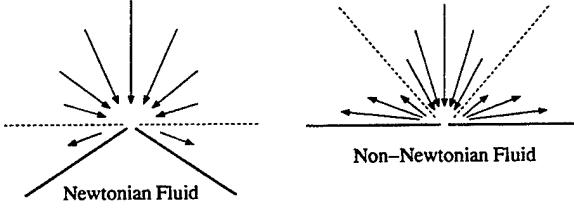
35

Figure 5: Diagrams of point sink converging channel flow. The diagram on the left shows that for a Newtonian fluid, recirculating vortices only appear when the plane is bent past horizontal. Non-Newtonian fluids can generate recirculating vortices even with a flat plate because of the additional extensional viscosity. The streamlines shown here are not valid close to the point sink as the flow is no longer purely radial in this region.

or in terms of f and g

$$f'' + \left(4 + 2\frac{\mu_{\text{ext.}}}{\mu_{\text{shear}}}\right) f = \text{const.} \tag{54}$$

The equation for f is a harmonic oscillator equation. We require that f goes to zero on the boundaries $\theta = 0, \pi$ to satisfy the condition of no slip, and we expect the maximum flow rate to occur in the middle, or $\theta = \pi/2$. For a Newtonian fluid, the additional extensional viscosity $\mu_{\text{ext.}} = 0$ and by applying the no-slip boundary condition we find to within a multiplicative constant that

$$f = 1 - \cos(2\theta), \tag{55}$$

and there are no recirculating eddies. If the plate is bent at an angle larger than π then recirculating eddies are present even in a Newtonian fluid. For a non-Newtonian fluid, $\mu_{\text{ext.}} \neq 0$ and we can solve equation (54) to find,

$$f = \cos\frac{\lambda\pi}{2} - \cos\lambda\left(\theta + \frac{\pi}{2}\right), \tag{56}$$

where $\lambda = sqrt{4 + 2\mu_{\text{shear}}/\mu_{\text{ext.}}}$. In this case there are always recirculating eddies on both sides of the sink (figure 5). Note that these equations approximate the flow far from the sink so that the streamlines are always in the radial direction. Close to the sink the streamlines must turn to form the vortices. From (56) we can see that the angle of the flow into the sink, and thus the size of the vortices, is determined by the ratio $\sqrt{\mu_{\text{shear}}/\mu_{\text{ext.}}}$.

7 Spinning of an Oldroyd B fluid

Finally, the last simple flow we will consider is fiber spinning of an Oldroyd B fluid. The constitutive equation of an Oldroyd B fluid is given by

$$\sigma = -pI + 2\mu E + GA, \tag{57}$$

where GA is the elastic stress, and A is a measure of the deformation of the microstructure. The time dependence of A is described by

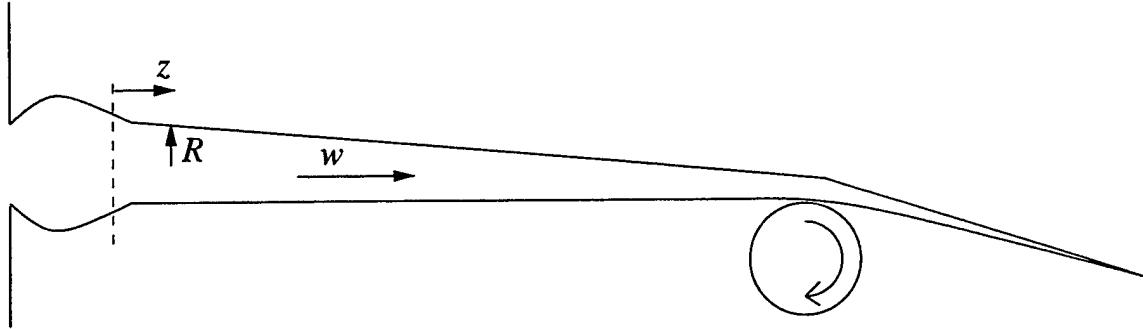$$\frac{DA}{Dt} = A \cdot \nabla U + (\nabla U)^T \cdot A - \frac{1}{\tau}(A - 1). \tag{58}$$

Figure 6: Geometry of fiber spinning of an Oldroyd B fluid. The fluid is pulled from a reservoir by a spinning wheel. After a brief initial transient region, the fluid is pulled into a cylinder whose radius decreases and velocity increases in the direction of positive z.

The first two terms on the right hand side describe the stretching of the microstructure while the last term describes relaxation back to the steady state, $A = 1$, on a time scale τ.

The geometry for this problem is shown in figure 6. Fluid begins in a reservoir, and after a brief initial transient region is pulled out into a cylinder beginning at $z = 0$ by a spinning wheel. The fluid is stretched and accelerated so that the velocity w increases and the radius R decreases moving in the direction of positive z. The flux and tension are both constant and are given by

$$Q = \pi R^2 w \tag{59}$$

and

$$F = \pi R^2 \sigma_{zz} \tag{60}$$

respectively.

Considering the constitutive equation and applying the boundary condition of no radial stress on the free surface $\sigma_{rr} = 0$ (57) gives

$$p = -\mu \frac{dw}{dz} + G A_{rr}. \tag{61}$$

Then, considering the axial component of stress and using the expression for pressure given above, we find

$$\sigma_{zz} = 3\mu \frac{dw}{dz} + G\left(A_{zz} - A_{rr}\right) = \frac{Fw}{Q}, \tag{62}$$

where we have made use of the expressions for the tension and the flux in the cylinder. Finally, from equation (58) the steady state equations for the radial and axial components of the deformation of A can be written as

$$w \frac{dA_{rr}}{dz} = -A_{rr} \frac{dw}{dz} - \frac{1}{\tau}\left(A_{rr} - 1\right) \tag{63}$$

$$w \frac{dA_{zz}}{dz} = 2A_{zz} \frac{dw}{dz} - \frac{1}{\tau}\left(A_{zz} - 1\right). \tag{64}$$

In general, for a given Deborah number, $\text{De} = \tau \frac{dw}{dz}$, the equations above must be solved numerically. However, we will consider two limits where the equations are analytically

37

tractable. In the Newtonian limit of small Deborah number, De $\ll 1$, the two terms on the right hand side of equations (63) and (64) balance to give

$$A_{rr} \sim 1 - \tau\frac{dw}{dz}, \qquad A_{zz} \sim 1 + 2\tau\frac{dw}{dz}. \tag{65}$$

Plugging these expressions for A_{rr} and A_{zz} into (62) gives a simple linear equation

$$3(\mu + G\tau)\frac{dw}{dz} = \frac{Fw}{Q}, \tag{66}$$

which has the solution

$$w(z) = w(0)\exp\left[\frac{Fz}{3Q(\mu + G\tau)}\right]. \tag{67}$$

Therefore in the Newtonian regime the velocity increases exponentially until the elastic limit is reached, in which the relaxation rate is comparable to the shear, or $\tau\frac{dw}{dz} \sim 1$.

In the elastic limit the stretching term in the axial direction dominates radial stretching and viscosity, $\mu\frac{dw}{dz} \ll GA_{rr} \ll GA_{zz}$, and therefore

$$\sigma_{zz} \sim GA_{zz} = \frac{Fw}{Q}. \tag{68}$$

From (64) we have

$$w\frac{dA_{zz}}{dz} = 2A_{zz}\frac{dw}{dz} - \frac{1}{\tau}(A_{zz}) \tag{69}$$

since $A_{zz} \gg 1$. Plugging $A_{zz} = Fw/Q$ into this equation yields a simple linear differential equation which has the solution

$$w = w_1 + \frac{z}{\tau}. \tag{70}$$

Upon reaching the elastic regime the velocity only grows linearly. Numerical results indicate that there is an abrupt change in the dynamics of the thread as the fluid transitions between the Newtonian and elastic regimes. This transition affects not only the velocity, but also the radius of the thread as given from the thread's flux and tension relationships (59) and (60).

Notes by Junjun Liu and Andrew Thompson

Lecture 4: Experiments and Numerics

E. J. Hinch

1 Experiments

In this section we discuss experimental approaches to characterizing materials and assessing the behavior of flowing materials. Standard apparatuses used to determine fluid rheology were described in section 3 of Lecture 1. Here we emphasize practical problems in measuring the rheology of non-Newtonian fluids, the importance of using standard fluids, and methods for observing flow properties.

1.1 Materials

What is a complete rheological description? Measuring the shear viscosity, normal stresses and elastic modulus in shear flow is not sufficient to describe a fluid, as two fluids may be similar in these characteristics and yet have distinct behavior in extensional flow. It is important to document experimental details carefully, including measurement technique, fluid preparation and molecular weight distributions, so that others can reproduce the results. To this end, rheologists study standard fluids. Meissner [1] coordinated a project to examine low density polyethylene fluids. In more recent years, there has been a transition from the use of hot melts to cold solutions as standard fluids for logistical ease.

An example of a modern standard fluid is the M1 ('magic') fluid which consists of 0.244 % polyisobutylene (molecular weight 3.8×10^6 g/mol) and 7% kerosene in polybutene. The M1 fluid is a Boger fluid, that is, one which has a shear viscosity that is approximately independent of shear rate, thus allowing a separation of shear and elastic effects. There is good agreement amongst different shear rheometers in the measurements of shear viscosity of the M1 fluid. However a series of extensional viscosity measurements demonstrates that different measurement techniques can lead to a range of extensional viscosities [2] (up to four orders of magnitude; see figure 2 from Lecture 1. A rational explanation of this phenomenon will be given in Lecture 9.

1.1.1 Practical problems

There are many experimental difficulties in measuring the properties of non-Newtonian fluids. These include:

- Flow instabilites in Couette and cone-and-plate apparatuses can produce a jump in torque that may be erroneously interpreted as an increase in viscosity.
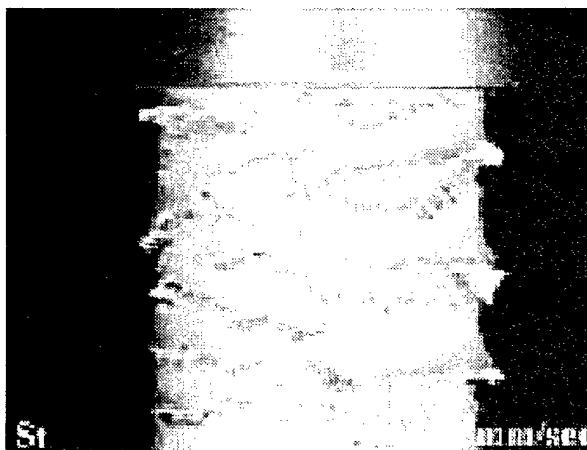
Figure 1: Stick-slip from flow of a mixture of clay powder and oil through a 20 mm diameter steel dye at 13 mm/s [4].

- The no-slip boundary condition at walls is generally assumed but is not always valid (figure 1).

- There can be slipping along internal layers, known as shear banding. Rheometers can be designed to observe this phenomena to avoid misinterpretations.

- Friction from shearing viscous fluids increases temperatures in the fluids, which causes a reduction in fluid viscosity.

- Phase-separation and crystallisation will cause changes in rheological properties. The standard S1 ('silly') fluid (5% polyisobutylene in decalin [3] by weight) has been problematic because it tends to phase separate.

- Degradation of the fluid due to UV radiation, bio-organisms or mechanical breaking of polymers by the flow itself (*e.g.*, figure 2).

1.2 Observations

Standard methods of flow observation include direct visualisation, laser doppler anemometry and particle image velocimetry. Fluid properties and flow characteristics can also be inferred from measurements of fluid fluxes and normal stresses for flow through a simple geometry such as flow through a pipe. There are however complications associated with this technique. There is a large pressure drop at pipe entry, an effect that can be accounted for by using a range of pipe lengths and extrapolating the data to an infinite pipe. Additionally there is an error associated with measuring normal stresses using pressure taps in the walls, because flow past the hole creates normal stresses.

Visualization may be complemented by assessing stresses from flow-induced anisotropy in the optical index of refraction of the fluid (birefringence). When plane-polarized monochromatic light passes through the fluid and then through a second polarizer, the birefringence
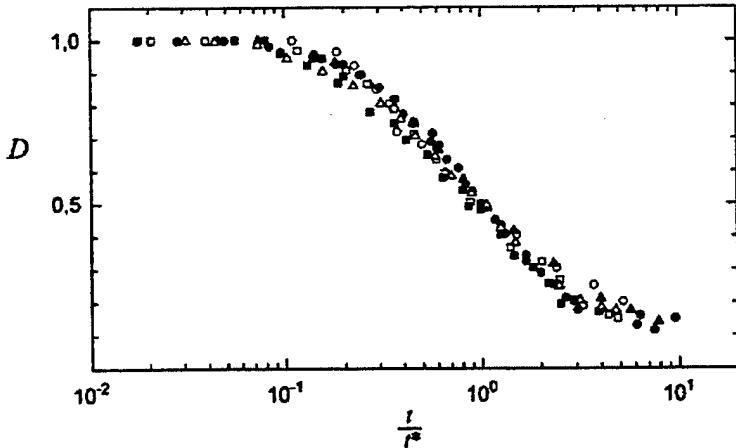
40

Figure 2: Plot showing drag reduction for aqueous PEO solutions with time related to mechanical degredation of polymers. The symbols correspond to experiments at different Reynolds numbers ($2.0 \times 10^{-5} < Re < 18.1 \times 10^{-5}$). t is the residence time of the solution in the flow and t^* is the half-degradation time [5].

of the fluid causes constructive and destructive interference fringes (figure 3) from which stress contours are deduced (figure 4). A linear relationship between stress and index of refraction (n) is sometimes assumed,

$$\sigma = c\Delta n, \tag{1}$$

where c, the stress optical coefficient, is a constant determined from a simple test flow. For qualitative assessment (1) is not required however the quantitative application of this technique depends on the validity of the stress optical law. This law may fail because birefringence measures bond alignment and not the magnitude of the stretching. This is particulary problematic in strong extensional flows.

Failure of the stress-optical law was demonstrated by [7] with simultaneous measurements of birefringence and extensional stress of polymer solutions in a filament stretching rheometer. The data indicate a non-linear relationship between stress and birefringece. Furthermore, stress relaxation was faster than birefringence relaxation, leading to a hysteresis in the stress optical law (figure 5).

2 Numerics

2.1 Discretization

There are three methods of discretisation which are commonly used in the numerical solution of non-Newtonian fluid flow problems. These are finite element, spectral and finite difference methods. Finite element techniques are good for problems with complex geometries, and as solvers for elliptic equations. Spectral methods are very accurate but only work for periodic geometries such as a wavy-wall tube. They are often used for turbulent drag problems. Finite difference methods are relatively simple and are most easily applied to mappable

41

(a) slit wall shear rate = 80 s⁻¹   (b) slit wall shear rate = 255 s⁻¹

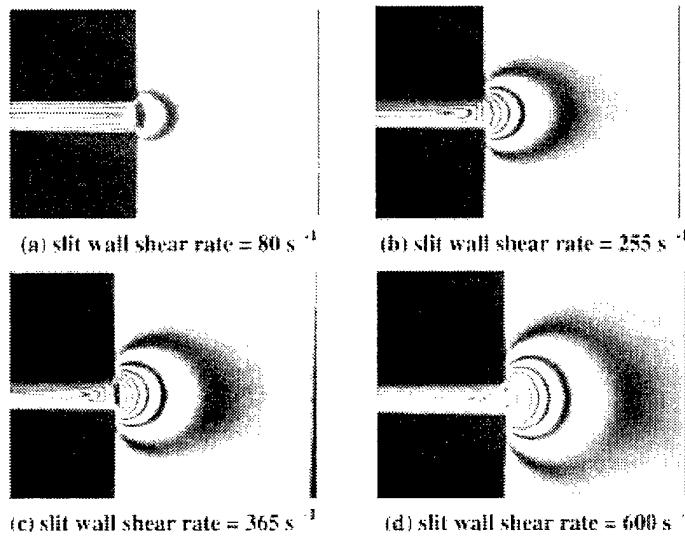(c) slit wall shear rate = 365 s⁻¹   (d) slit wall shear rate = 600 s⁻¹

Figure 3: Photographs of fringe patterns for fluid flowing into a slit for a range of shear rates. Dark fringes are areas of destructive interference and each additional fringe indicates that the slow ray is an additional wavlength behind the fast light ray. From [6]
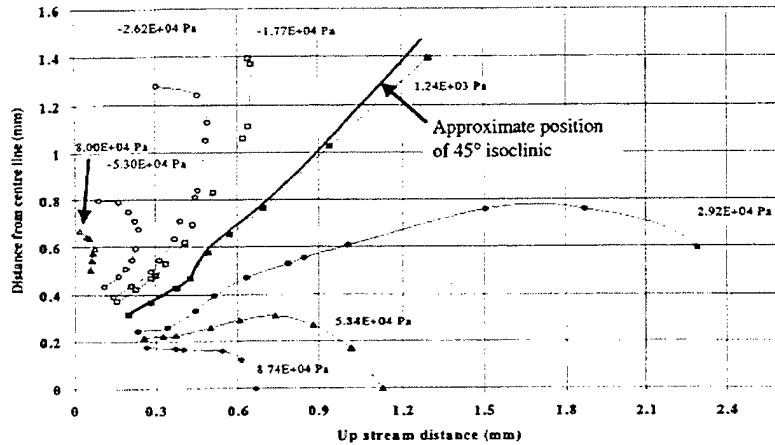

Figure 4: The first normal stress contours corresponding to the flow shown in Figure 3, part (b).
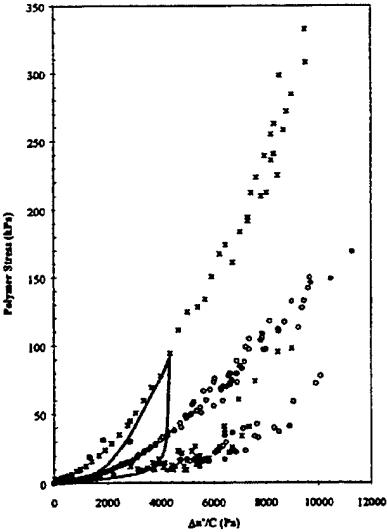
Figure 5: Stress versus birefringence for extensional flow and subsequent relaxation at a range of Weissenberg numbers; asterisk: Wi = 41.7, circle: Wi = 16.8, square: Wi = 2.84, line: conformation dependent FENE model with Wi = 2.84.

geometries (*i.e.*, domains that can be mapped onto a quadrilateral grid). We include only a brief overview of each of these methods. For further details, see *e.g.* [8].

2.1.1 Finite Elements

The domain is divided into a grid of triangular or quadrilateral elements, (note that use of a triangular grid can lead to difficulties with list processing associated with the storing of neighbouring elements). The unknown fields (such as velocity) are represented by a sum (over the elements) of the product of known functions, ϕ_i, and unknown amplitudes, f_i,

$$\mathbf{u}(\mathbf{x}) = \sum^{N} f_i \, \phi_i(\mathbf{x}), \qquad (2)$$

where ϕ_i are referred to as test functions. These summation representations are substituted into the governing equations, and then on projection we have

$$\int \left(\rho \frac{\mathbf{Du}}{\mathbf{Dt}} + \nabla p - \mu \nabla^2 \mathbf{u} - \nabla \cdot \sigma^{elast} \right) \cdot \phi_s(\mathbf{x}) \, dV = 0, \quad \text{for } s = 1, 2, \dots N. \qquad (3)$$

By requiring the above relation to hold, we obtain a set of ordinary differential equations for the functions f_i. These can be solved easily (*e.g.* using a Runge-Kutta scheme) to find the f_i and hence the unknown fields.

2.1.2 Spectral Methods

Similar to the finite element method, the spectral representation of flows is a summation of the product of an unknown amplitude with a known basis function (such as Fourier or

Chebyshev modes) so

$$f(x) = \sum^{N} f_n \, e^{inx}. \tag{4}$$

The elegance of this method lies in the fact that spatial derivatives of (4) become multiplications, which are numerically simple to perform, and the error term in such a representation is exponentially small,

$$f'(x) = \sum^{N} f_n in \, e^{inx} + O(e^{-N}). \tag{5}$$

A disadvantage of this method is that the product of two functions requires summing over cross terms which is computationally expensive,

$$f(x)g(x) = \sum_n^N \sum_k^N f_k \, g_{n-k} e^{inx}. \tag{6}$$

In order to avoid this expense, pseudo-spectral methods are used instead. This method calculates the derivatives using (5) but the product of functions is calculated with the actual function values (using Fast Fourier transforms to switch between the two). To avoid aliasing it is common to remove the top third of the spectrum (for quadratic nonlinearities). Spectral methods are ideal for periodic boundaries but cannot represent discontinuities in the flow very well because the basis functions are smooth.

2.1.3 Finite Difference Methods

Finite difference methods are widely employed in modeling fluid dynamics problems. This method involves a coordinate grid so the labelling and interaction of nodes is straightforward. The equations are generally discretised using a second-order central differencing scheme. For example, the second derivative is approximated by

$$f'' \approx \frac{f(x+h) - 2f(x) + f(x-h)}{h^2}. \tag{7}$$

It is important to note that the discretization process can sometimes lead to errors. For example the finite difference expression for the divergence of radial flow is not the same as the analytical expression,

2.2 Benchmark numerical cases

Solutions from benchmark problems are used for testing numerical codes. Some common examples are shown in figure 6 below.

2.3 Pressure

The pressure in two-dimensional calculations for Newtonian fluids can be avoided by taking the curl of the momentum equation to obtain the vorticity equation. However this is not possible for calculations involving non-Newtonian fluids because all components of the stress tensor are required to give an accurate description of the flow.

44

Sphere in a tube: Dominated by shear

Contraction: Difficult sharp corner

Journal bearing: Good for spectral methods

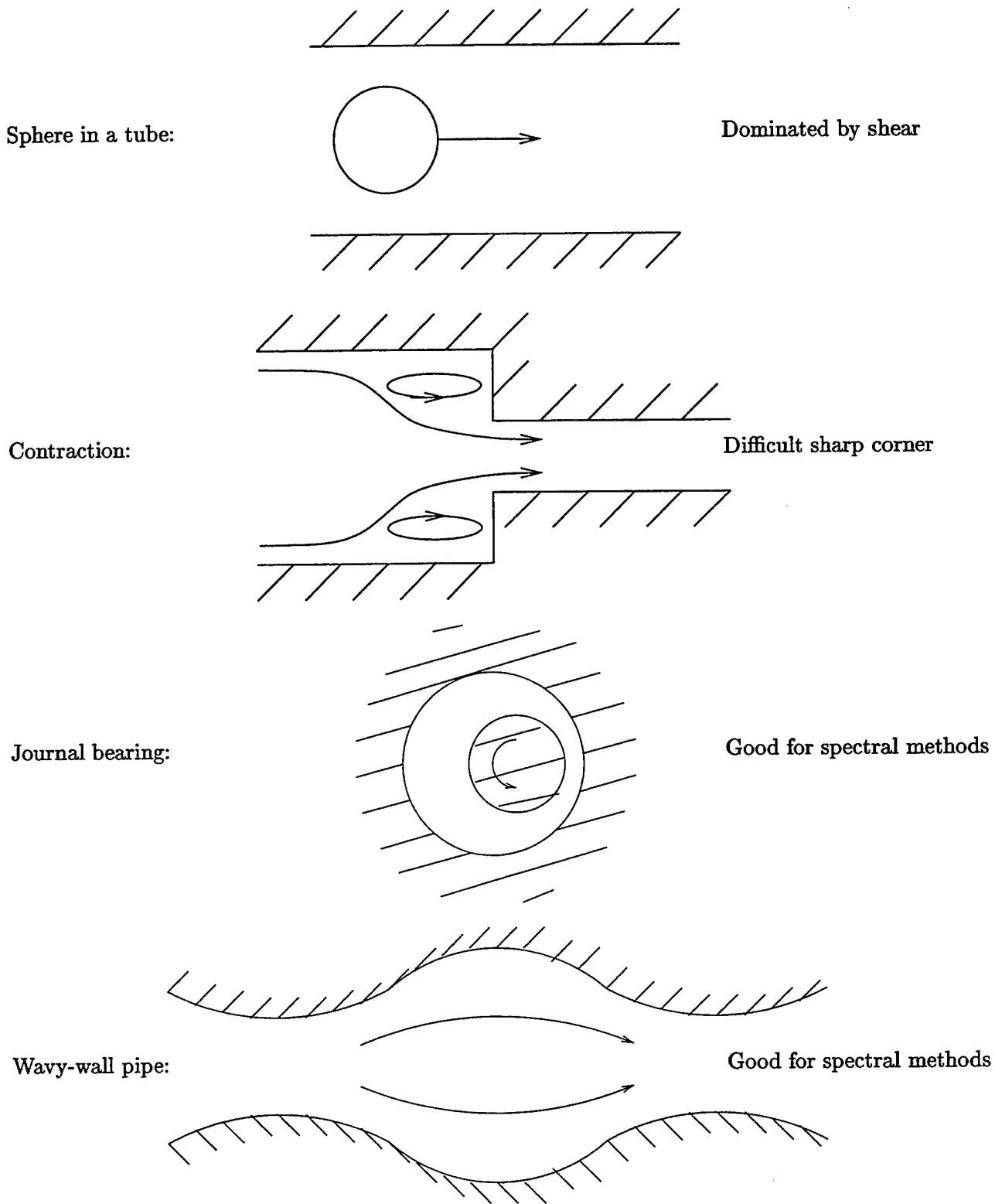Wavy-wall pipe: Good for spectral methods

Figure 6: Benchmark problems for testing numerical code.

2.3.1 Fractional step with pressure projection

Consider the pressure equation (found by taking the divergence of the momentum equation),

$$\nabla^2 p = \nabla \cdot \left[-\rho \frac{D\mathbf{u}}{Dt} + \nabla \cdot (\sigma^{visc} + \sigma^{elast}) \right]. \tag{8}$$

When solving numerically for the pressure, incompressibility is usually satisfied only to within a small error, so that

$$\nabla \cdot \mathbf{u} \approx 0. \tag{9}$$

Over many timesteps these small errors can accumulate, leading to a significant error. This problem can be reduced using a fractional step with pressure projection. This numerical technique (used with finite differencing, finite element and spectral methods) finds an approximate solution $\mathbf{u}^*$ and then makes a correction which removes the error in the incompressibilty condition and guarantees that $\nabla \cdot \mathbf{u} = 0$ exactly.

The fractional step uses $\mathbf{u}^*$ found by solving

$$\frac{\mathbf{u}^* - \mathbf{u}^n}{\Delta t} = -(\rho \mathbf{u} \cdot \nabla \mathbf{u})^n + \nabla \cdot (\sigma^{visc} + \sigma^{elast})^n, \tag{10}$$

with the no-slip boundary condition and then the pressure projection gives the solution for the next timestep,

$$\mathbf{u}^{n+1} = \mathbf{u}^* - \Delta t \nabla p^{n+1}. \tag{11}$$

Note therefore that

$$\nabla \cdot \mathbf{u}^{n+1} = \nabla \cdot \mathbf{u}^* - \Delta t \, \nabla^2 p^{n+1} = \nabla \cdot \mathbf{u}^* - \nabla \cdot \mathbf{u}^* = 0. \tag{12}$$

The disadvantage of this technique is that the no-slip boundary condition is not exactly satisifed by $\mathbf{u}^{n+1}$.

2.3.2 Fractional step with pressure update

The method described above can be refined by using a fractional step with a pressure update. This includes the pressure term explicitly in the calculations, so adjustments are made to the pressure at the previous time, as opposed to recalculating the pressure field at each timestep. This method is much better at handling the boundary conditions and leads to a closer approximation to the no-slip condition.

The velocity at the fractional step, $\mathbf{u}^*$ is given by

$$\frac{\mathbf{u}^* - \mathbf{u}^n}{\Delta t} = -\nabla p^{n-\frac{1}{2}} + \left[-\rho \mathbf{u} \cdot \nabla \mathbf{u} + \nabla \cdot \sigma^{elast} \right]^{n+\frac{1}{2}} + \left[\nabla \cdot \sigma^{visc} \right]^{n+\frac{1}{2}}, \tag{13}$$

where $p^{n-1/2}$ is the pressure at the last step. Then the non-zero divergence of $\mathbf{u}^*$ is given by

$$\nabla \cdot \mathbf{u}^* = \Delta t \, \nabla^2 \delta p^{n+\frac{1}{2}}. \tag{14}$$

The solution (including the pressure field) is then updated by

$$\mathbf{u}^{n+1} = \mathbf{u}^* - \Delta t \, \nabla \delta p^{n+\frac{1}{2}}, \tag{15}$$

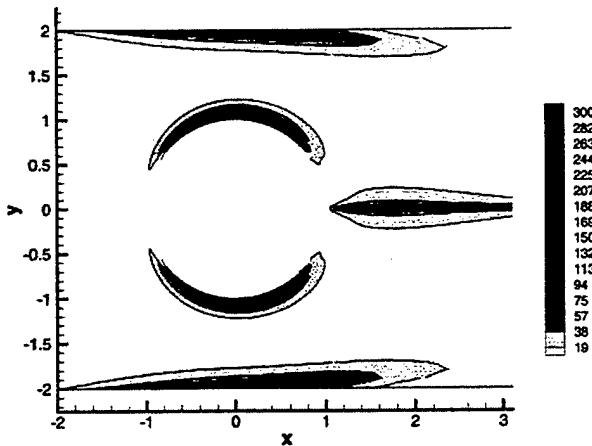$$p^{n+\frac{1}{2}} = p^{n-\frac{1}{2}} + \delta p^{n+\frac{1}{2}}. \tag{16}$$

46

Figure 7: Contours of the configuration tensor component $< QQ >_{xx}$ around a cylinder for flow of an Oldroyd-B fluid through a linear array of cylinders with $De = 1$. From [10].

2.3.3 Staggered grids

Central differencing can lead to spurious pressure modes (oscillations on the scale of the grid). In finite difference techniques these can be avoided by using a staggered grid, in which different fields are held on different points, (e.g. velocities on the midpoints of cells boundaries, shear stresses on the corners and momentum terms at the cell center). However, a staggered grid is not possible with finite element models. This leaves an essential difficulty in such schemes.

2.4 Elliptic and hyperbolic parts

The elliptic pressure equation is relatively easily solved. However the stress equation is a hyperbolic partial differential equation and there is no easy method of solution. With a finite difference code, the method of characteristics can be employed (using the streamlines as the characteristics). An alternative is 'black box magic' such as the code MINMOD, which uses second order discretization over the domain except in the vicinity of shocks where the discretization is first-order. For finite-element methods an upwinding technique can offer a method of solution, however this generates large numerical diffusion. Alternatively a lagrangian grid can be used, so that the grid and the elements defined on it travel along with the flow, such as that employed by [9].

2.5 Numerical Problems

There are a number of problems which develop when computing non-Newtonian flows. Convergence tests are often neglected and numerical instabilities can develop when simulating flows with sharp corners, interfaces between shear layers, and thin layers of high stress (e.g. 7). More grid resolution is needed in these areas, however it is computationally expensive.

A limitation of the Upper Convective Maxwell and Oldroyd-B models is that there appear to be no solutions for large Deborah numbers (high strain rates). For flow past a

47

sphere in a tube, the maximum Deborah numbers are $De_{max} = 2.17$ and $De_{max} = 1.28$ for the UCM and Oldroyd-B models, respectively [11]. At greater than these critical Deborah numbers there is a region in which the extensional viscosity is negative. The FENE model (Finite Extension Nonlinear Elasticity), overcomes this problem and is sucessful up to $De \approx 100$ (see Lecture 2).

Notes by Alison Rust and Julia Mullarney

References

[1] J. Meissner, "Basic parameters, melt rheology, processing and end-use properties of three similar low density polyethylene samples," Pure Appl. Chem. **42**, 553 (1975).

[2] R. A. Keiller, "Modelling of the extensional flow of the m1 fluid with the oldroyd equation," J. Non-Newtonian Fluid Mech. **42**, 49 (1992).

[3] N. E. Hudson and J. Ferguson, "The anomalous shear flow properties of s1," J. Non-Newtonian Fluid Mech. **52**, 105 (1994).

[4] O. L. Kulikov and K. Hornung, "A simple geometrical solution to the surface fracturing problem in extrusion processes," J. Non-Newtonian Fluid Mech. **98**, 107 (2001).

[5] V. N. Kalashnikov, "Degradation accompanying turbulent drag reduction by polymer additives," J. Non-Newtonian Fluid Mech. **103**, 105 (2002).

[6] M. T. Martyn, C. Nakason, and P. D. Coates, "Stress measurements for contraction flows of viscoelastic polymer melts," J. Non-Newtonian Fluid Mech. **91**, 123 (2000).

[7] T. Sridhar, D. A. Nguyen, and G. G. Fuller, "Birefringence and stress growth in uniaxial extension of polymer solutions," J. Non-Newtonian Fluid Mech. **90**, 299 (2000).

[8] R. Peyret and T. D. Taylor, *Computational Methods for Fluid Flow* (Springer-Verlag, New York, 1983).

[9] P. Szabo, J. M. Rallison, and E. J. Hinch, "Start-up of flow of a fene-fluid through a 4:1:4 constriction in a tube," J. Non-Newtonian Fluid Mech. **72**, 73 (1997).

[10] A. E. Caola, Y. L. Joo, R. C. Armstrong, and R. A. Brown, "Highly parallel time integration of viscoelastic flows," J. Non-Newtonian Fluid Mech. **100**, 191 (2001).

[11] Y. Fan, "Limiting behavior of the solutions of a falling sphere in a tube filled with viscoelastic fluids," J. Non-Newtonian Fluid Mech. **110**, 77 (2003).

Lecture 5: Microstructural studies

E. J. Hinch

1   Introduction

These two lectures will describe attempts to derive constitutive equations from "first princi-ples." A large separation of length scales between the flow and the microstructure allows us to approximate the bulk properties of the fluid by averaging over the small scales. We begin by considering microstructure in a Newtonian solvent: first spheres, then other shapes, and finally their deformations and interactions. Moving beyond this approach, we also consider models for isolated or entangled polymers.

2   Separation of length scales

A typical length scale characterizing microstructure is $l \sim 1\,\mu\mathrm{m}$, while the macroscopic length scale, the scale on which the flow varies, is a few orders of magnitude large, e.g., $L \sim 1\,\mathrm{cm}$. The micro scale is large enough that the continuum approximation is valid (it works well down to about $10\,\mathrm{nm}$). However, even though the length scales are separated, the time scales are comparable. Thus, we will use only space-averages (or maybe ensemble averages) but not time-averages. Another assumption is that the microscopic Reynolds number is small:

$$Re_l = \frac{\rho \dot{\gamma} l^2}{\mu} \ll 1.$$

Without this assumption it is possible to have macroscopic boundary layers smaller than the microscopic length scale. Note that the macroscopic Reynolds number $Re_L = (\rho \dot{\gamma} L^2)/\mu$ can be large or small. If Re_L is very large, then the macroscopic length scale (e.g. in boundary layers) can be comparable to the microscopic length scale and the desired separation of scales breaks down.

Our general approach to this two-scale problem has two steps. First we compute the effect of the flow on the microstructure; this is difficult and requires approximations or models. We will delay the discussion of this procedure in detail to the following sections. Once that problem is solved, we can extract the constitutive relation by averaging, which we discuss presently.

There are several ways to do this averaging. One choice, not employed here, is ensemble averaging. Another technique that we will not discuss further is homogenization; this uses asymptotic analysis to achieve the same result. Here we will use volume averaging with a

representative volume V between the micro and macro scales, $l \ll V^{1/3} \ll L$. Averaging the momentum equation and neglecting micro Reynolds stresses we get

$$\bar{\rho}\left[\frac{\partial \bar{\mathbf{u}}}{\partial t} + \bar{\mathbf{u}} \cdot \nabla \bar{\mathbf{u}}\right] = \nabla \cdot \bar{\boldsymbol{\sigma}} + \bar{F}, \tag{1}$$

where $\bar{}$ denotes averaging over V. The stress tensor in the presence of particles in a Newtonian fluid is given by

$$\boldsymbol{\sigma} = -p\boldsymbol{\delta} + 2\mu\boldsymbol{E} + \boldsymbol{\sigma}^+, \tag{2}$$

where $\boldsymbol{\sigma}^+$ is the stress inside the particles, μ is the viscosity of the solvent, $\boldsymbol{E}$ is the rate of strain tensor and p is the pressure. The averages of the latter three quantities are unchanged by the microstructure up to leading order in the small parameter l/L, i.e., $\bar{p} = p + O(l/L)$, etc. Note that for general microstructure we cannot compute $\boldsymbol{\sigma}^+$ but it varies on the micro scales. The average of $\boldsymbol{\sigma}^+$ is

$$\overline{\boldsymbol{\sigma}^+} = \frac{1}{V}\int_V \boldsymbol{\sigma}^+ dV = n\left\langle \int_P \boldsymbol{\sigma}^+ dV\right\rangle, \tag{3}$$

where n is the number density of particles, $\int_P \cdot dV$ is the integral over a particle and $< \cdot >$ is the average over types of particles if needed. If the particles are considered to be rigid, the strain e inside the particle is zero. Neglecting the pressure and micro-gravity, we see that

$$\sigma_{ij}^+ = \partial_k(\sigma_{ik}^+ x_j) - x_j \partial_k \sigma_{ik}^+ = \partial_k(\sigma_{ik}^+ x_j), \tag{4}$$

where $\mathbf{x} = (x_1, x_2, x_3)$ are the space-coordinates. Then the volume integral over the particle reduces to a integral over the surface S:

$$\int_P \boldsymbol{\sigma}^+ dV = \oint_S \boldsymbol{\sigma}^+ \cdot \hat{\mathbf{n}} \mathbf{x} \, dA. \tag{5}$$

Thus, we need to know only the stress on the surface of the particle.

3 Suspension of Rigid Spheres

The simplest case of a microstructure is that of a dilute suspension of inert, rigid spheres. This highly idealized case was studied originally by Einstein in 1906, although his method involved subtracting two divergent integrals to get the right answer! The problem is to solve the Stokes flow around a sphere of radius a with prescribed linear flow far away. We also require that there be no net force and couple. The governing equations are

$$\nabla \cdot \mathbf{u} = 0 \tag{6}$$

$$0 = -\nabla p + \mu\nabla^2 \mathbf{u} \tag{7}$$

for $r > a$ with boundary conditions

$$\mathbf{u} = \mathbf{V} + \boldsymbol{\omega} \times \mathbf{x}, \text{ on } r = a, \tag{8}$$

$$\mathbf{u} = \mathbf{U} + \mathbf{x} \cdot \nabla\mathbf{U}, \, r \to \infty, \tag{9}$$

50

where $\mathbf{U} + \mathbf{x} \cdot \nabla \mathbf{U}$ is the prescribed flow at infinity, ω is the vorticity and $\mathbf{V}$ the velocity on the surface of the particle, to be determined using the force- and couple-free conditions

$$\mathbf{F} = \oint_{r=a} \sigma \cdot \mathbf{n} dA = 0 \tag{10}$$

$$\mathbf{G} = \oint_{r=a} \mathbf{x} \times \sigma \cdot \mathbf{n} dA = 0. \tag{11}$$

We split $\nabla \mathbf{U}$ into symmetric strain rate $\mathbf{E}$ and antisymmetric vorticity Ω, i.e.,

$$\mathbf{x} \cdot \nabla \mathbf{U} = \mathbf{x} \cdot \mathbf{E} + \Omega \times \mathbf{x}.$$

The conditions (10)-(11) imply that the particle translates with the mean flow $\mathbf{V} = \mathbf{U}$ and rotates with the mean vorticity $\omega = \Omega$. The flow field and the pressure field is

$$\mathbf{u} = \mathbf{U} + \Omega \times \mathbf{x} + \mathbf{E} \cdot \mathbf{x} - \mathbf{E} \cdot \mathbf{x} \frac{a^5}{r^5} - \frac{5}{2r^2} \mathbf{x} \cdot \mathbf{E} \cdot \mathbf{x} \left(\frac{a^3}{r^3} - \frac{a^5}{r^5} \right) \mathbf{x} \tag{12}$$

$$p = -5\mu a^3 (\mathbf{x} \cdot E\mathbf{x})/r^5. \tag{13}$$

Evaluating the stress on the surface of the particle

$$\sigma \cdot \mathbf{n}|_{r=a} = \frac{5}{2} \frac{\mu}{a} \mathbf{E} \cdot \mathbf{x} \tag{14}$$

and integrating

$$\oint \sigma \cdot \mathbf{n} dA = 5\mu \mathbf{E} \cdot \frac{4\pi}{3} a^3 \tag{15}$$

gives an average stress

$$\bar{\sigma} = -p\delta + 2\mu\mathbf{E} + 5\mu\mathbf{E}\varphi = -p\delta + 2\mu^*\mathbf{E} \tag{16}$$

where $\varphi = 4\pi n a^3/3$ is the fraction of volume occupied by the spheres and

$$\mu^* = \mu \left(1 + \frac{5}{2}\varphi \right)$$

is the Einstein viscosity due to the presence of the spheres in the liquid. This result does not depend on the type of flow or the size of individual particles, only their volume fraction.

4 Suspension of Rigid Spheroids

Now consider a dilute suspension of rigid particles that are not spherical. The next simplest class of particles are spheroids which are ellipsoids with semi-axes a, b and b. The aspect ratio of the spheroid is $r = a/b$. For $r > 1$, this is a prolate spheroid with the two equal axes being shorter than the unique axis, while for $r < 1$ this is an oblate spheroid with the two equal axes being longer. As in the previous section, in order to determine the effect of these particles on the flow, we will determine the stress contribution of one particle and then average over the number of particles per unit volume to get the macroscopic stress contribution.

	A	B	C
$r \to \infty$	$\dfrac{r^2}{2(\ln 2r - 3/2)}$	$\dfrac{6 \ln 2r - 11}{r^2}$	2
$r \to 0$	$\dfrac{10}{3\pi r}$	$-\dfrac{8}{3\pi r}$	$\dfrac{8}{3\pi r}$

Table 1: Material constants A, B and C for suspensions of rigid spheroids.

Considering Stokes flow around a spheroid we are lead to an evolution equation for a unit vector p in the direction of the axis of symmetry

$$\dot{\mathbf{p}} = \mathbf{\Omega} \times \mathbf{p} + \frac{r^2 - 1}{r^2 + 1} \left[\mathbf{E} \cdot \mathbf{p} - \mathbf{p}(\mathbf{p} \cdot \mathbf{E} \cdot \mathbf{p})\right]$$

where $\dot{()}$ is the material time derivative of $()$ and $\mathbf{\Omega}$ is the vorticity of the flow at infinity. The solution of Stokes flow around a spheroid was obtained by Oberbeck in 1876 [1]. For a given p we can integrate the stress around the boundary of the particle and get an expression for the macroscopic stress due to a volume fraction φ of spheroids

$$\overline{\sigma} = -\overline{p}\delta + 2\mu\mathbf{E} + 2\mu\varphi\left[A\left(\mathbf{p} \cdot \mathbf{E} \cdot \mathbf{p}\right)\mathbf{pp} + B\left(\mathbf{pp} \cdot \mathbf{E} + \mathbf{E} \cdot \mathbf{pp}\right) + C\mathbf{E}\right]$$

with A, B, and C constants depending only on the shape of the particles. For the limits of slender rods and flat disks the values of A, B and C are given in table 1.

In a simple extensional flow, rod-like particles will align with the stretching direction of the flow, the orientation that maximizes dissipation. For disk-like particles the axis of symmetry will align with the compression direction which is also the orientation of that shape that maximizes the dissipation of the flow. For rods and disks (the limits $r \to \infty$ and $r \to 0$) we can compute from this flow an effective extensional viscosity for dilute suspensions. If $\varphi \ll 1$ and $r \gg 1$ then

$$\mu_{\text{ext}}^* = \mu\left(1 + \varphi\frac{r^2}{3(\ln 2r - 3/2)}\right)$$

and if we substitute the definition of $\varphi = 4\pi nab^2/3$ where n is the number of particles per unit volume then we get

$$\mu_{\text{ext}}^* = \mu\left(1 + \frac{4\pi na^3}{9(\ln 2r - 3/2)}\right)$$

which is the same viscosity that we would get from a suspension of rigid spheres of radius a, apart from a factor that varies only logarithmically in r. Since a is the largest dimension of the spheroid, this explains why very small concentrations of polymers which are very long can have large effects on the characteristics of the flow. In the case of disks rather than rods

$$\mu_{\text{ext}}^* = \mu\left(1 + \varphi\frac{10}{3\pi r}\right) = \mu\left(1 + \frac{10nb^3}{a}\right).$$

In a simple shear flow, these spheroidal particles do not approach a steady state, but instead tumble in the flow, spending some time aligned with the flow and then flipping

relatively quickly to the opposite orientation again aligned with the flow. The effective shear viscosities can be computed for rods,

$$\mu^*_{\text{shear}} = \mu \left(1 + \varphi \frac{8}{25} \frac{r}{\ln r}\right),$$

and for disks,

$$\mu^*_{\text{shear}} = \mu \left(1 + \varphi \frac{31}{10}\right),$$

where the exact effective shear viscosities depend on the distribution of all of the particles in the flow over all of the possible tumbling orbits. Even this very simple model of rigid, asymmetric particles can explain a situation where $\mu^*_{\text{shear}} \ll \mu^*_{\text{ext}}$ that is typical of many non-Newtonian fluids (for Newtonian fluids $\mu_{\text{ext}} = 3\mu_{\text{shear}}$). We also see that there are three measures of concentration for the rods:

$$\varphi r^2 = na^3 \qquad \text{for } \mu^*_{ext},$$
$$\varphi r = na^2 b \qquad \text{for } \mu^*_{shear},$$
$$\varphi = nab^2 \qquad \text{for permeability.}$$

One feature of non-Newtonian fluids that cannot be explained by these simple models is the relaxation of the fluid back to a basic state over a particular time-scale. One way to add this feature of relaxation to this model is to allow the rods and disks to execute Brownian motion on a particular time-scale, $1/6D_{\text{rot}}$ given by

$$D_{\text{rot}} = kT \left(8\pi\mu a^3\right)^{-1} \qquad \text{for spheres,}$$
$$D_{\text{rot}} = kT \left(\frac{8\pi\mu a^3}{3(\ln 2r - 3/2)}\right)^{-1} \qquad \text{for rods}$$
$$\text{and } D_{\text{rot}} = kT \left(8\mu b^3/3\right)^{-1}, \qquad \text{for disks.}$$

Then instead of writing down an evolution equation for the orientation vector $\mathbf{p}$, we write down the Fokker-Planck equation for the probability density $\mathcal{P}(\mathbf{p}, t)$

$$\frac{\partial \mathcal{P}}{\partial t} + \nabla \cdot (\dot{\mathbf{p}}\mathcal{P}) = D_{\text{rot}}\nabla^2 \mathcal{P}$$

where $\dot{\mathbf{p}}$ is as before from the deterministic model. Then we can compute an average stress by averaging not only over all of the particles in a volume, but also over the distribution $\mathcal{P}$. If we write $\langle \cdot \rangle = \int_{|p|=1} \cdot \mathcal{P}dp$ then the average stress due to rigid spheroids is

$$\sigma = -p\mathbf{I} + 2\mu\mathbf{E} + 2\mu\varphi\left[A\mathbf{E} : \langle\mathbf{pppp}\rangle + B\left(\mathbf{E} \cdot \langle\mathbf{pp}\rangle + \langle\mathbf{pp}\rangle \cdot \mathbf{E}\right) + C\mathbf{E} + FD_{\text{rot}}\langle\mathbf{pp}\rangle\right],$$

where there is now a new material constant F for the entropic stress ($F = 3r^2/(\ln 2r - 1/2)$ for rods, $F = 12/(\pi r)$ for disks). The equations for $\langle\mathbf{pp}\rangle$ and $\langle\mathbf{pppp}\rangle$ involve even higher order moments leading to an infinity hierarchy of equations. Different closures can be used to solve this problem. Some commonly used closures assume $\langle\mathbf{pppp}\rangle$ to be a function of $\langle\mathbf{pp}\rangle$.

Notes by Neil Burrell and Amit Apte

53

References

[1] H. Oberbeck, "über stationäre flussigkeitsbewegungen mit berücksichtigung der inneren reibung," Crelles Journal **81**, 62 (1876).

Lecture 6: Simple Relaxation and Yield Problems

E. J. Hinch

1 Deformable Microstructure

All of the microstructural elements discussed so far have been rigid. Most real non-Newtonian fluids are composed of deformable bodies, such as liquid drops or flexible polymers. Allowing deformable microstructure dramatically increases the complexity of the problem because the microstructure now has a large number of internal degrees of freedom. We will first consider the case of dilute suspensions where the interactions between the microscopic particles can be ignored.

1.1 Emulsions

One of simplest fluids with a deformable microstructure is an emulsion of immiscible drops in a solvent. Let the emulsion consist of drops of fluid with viscosity μ_{in}, surface tension T, and characteristic radius a suspended in a solvent with viscosity μ_{out} (μ_{out} is the viscosity of the external fluid). The drops are dilute, non-interacting, and do not mix with the exterior fluid.

Suppose that the drop is caught in a purely straining flow with strain rate E. The straining flow exerts a viscous stress $\mu_{\text{out}}E$ that stretches the drop. This stress is counteracted by the drop's surface tension T/a which tends to make the drop spherical. The equilibrium shape is somewhat sausage-like, as shown in Figure 1. If the viscous stress on the drop exceeds its capillary pressure, that is if $\mu_{\text{out}}E > T/a$, the drop will (normally) rupture. Each rupture reduces the size of the drops, which drives up the capillary pressure. This rupturing process will halt when the drops reach the radius

$$a_* = \frac{T}{\mu_{\text{out}}E}.$$ (1)

The size reduction is essentially irreversible since coalescence is usually much slower than the time scale of the exterior flow.

Rupture is difficult if the internal viscosity is too large or too small compared to the external viscosity. If $\mu_{\text{in}} \ll \mu_{\text{out}}$ the drops are too slippery for the exterior flow to have a strong effect. Theoretical and experimental estimates indicate that the drops become long
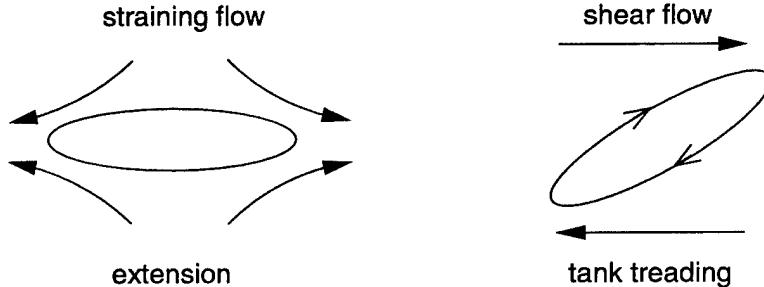
Figure 1: Pre-rupture shapes of drops in an emulsion in straining and shearing flow.

and thin, but do not rupture unless

$$\mu_{out}E > \frac{T}{a}\begin{cases} 0.54\left(\dfrac{\mu_{out}}{\mu_{in}}\right)^{2/3} & \text{simple shear} \\[2mm] 0.14\left(\dfrac{\mu_{out}}{\mu_{in}}\right)^{1/6} & \text{extensional flow} \end{cases} \tag{2}$$

However, mobile surfactants in the drop will give the exterior flow something to grab onto and causes the drops to lose small droplets off their pointed ends. This phenomenon, called 'tip-streaming,' occurs if $\mu_{out}E > 0.56\,T/a$.

In general, the dimensionless capillary number

$$\text{Ca} = \frac{T}{a\mu_{out}E} \tag{3}$$

measures the efficiency of an emulsification process. For simple straining flows and viscosity ratios in the range

$$10^{-2} \lesssim \frac{\mu_{in}}{\mu_{out}} \lesssim 1, \tag{4}$$

the capillary number is near unity, but it can be as large as 20 for viscosity ratios outside this range.

A shear flow will induce internal circulation in the drops. In the limit of very small internal viscosity, all of the external vorticity is taken up by the internal circulation and the envelope will not rotate relative to the external flow (Figure 1). This phenomenon is known as 'tank treading' because the fluid on the drop surface is stationary relative to the fluid just outside the surface, just as a tank's treads are stationary relative to the ground. As the internal viscosity increases, more and more of the external vorticity is taken up by solid body rotation of the drop.

Shear flow will cause extension of the drops just as in straining flow, and the conditions for rupture and the final drop size as similar to the previous case. One crucial difference is that shear flow cannot rupture the drops if $\mu_{in} > 3\mu_{out}$. If this is the case, the drops are so rigid that they just rotate with the exterior vorticity. The drops are still extended by the exterior flow, but before they can rupture they rotate so that they are stretched in the orthogonal direction. Instead of rupturing, the drops are periodically stretched and compressed around their mean shapes.

In order to determine the effect of the drops on the rheology, we have to solve the Stokes problem for both the interior and exterior flow, as well as determine the location of the free surface. This is challenging and not very efficient. To make progress, we consider small ellipsoidal deformations of a spherical drop.

Let the location of the free surface be given by

$$r(\boldsymbol{x}, t) = a(1 + \boldsymbol{x} \cdot \mathsf{A}(t) \cdot \boldsymbol{x} + \cdots), \tag{5}$$

where a is the equilibrium radius of the drop. The leading few terms of the evolution equation for the deformation tensor A in Stokes flow are

$$\frac{D\mathsf{A}}{Dt} - \Omega \cdot \mathsf{A} + \mathsf{A} \cdot \Omega = k_1 \mathsf{E} + k_5 (\mathsf{A} \cdot \mathsf{E} + \mathsf{E} \cdot \mathsf{A}) - \frac{T}{\mu_{\text{out}} a}(k_2 \mathsf{A} + k_6 \mathsf{A} \cdot \mathsf{A} + \cdots) \tag{6}$$

$$\sigma = -p\mathsf{I} + 2\mu_{\text{out}}\mathsf{E} + 2\mu_{\text{out}}\phi \left[k_3 \mathsf{E} + k_7(\mathsf{A} \cdot \mathsf{E} + \mathsf{E} \cdot \mathsf{A}) - \frac{T}{\mu_{\text{out}} a}(k_4 \mathsf{A} + k_8 \mathsf{A} \cdot \mathsf{A} + \cdots) + \cdots \right]. \tag{7}$$

with coefficients k_n that depend on the viscosity ratio $\lambda = \mu_{\text{in}}/\mu_{\text{out}}$. About 16 of the coefficients have been calculated. The first four are

$$k_1 = \frac{5}{2\lambda + 3}, \qquad k_2 = \frac{40(\lambda + 1)}{(2\lambda + 3)(19\lambda + 16)},$$

$$k_3 = \frac{5(\lambda - 1)}{2\lambda + 3}, \qquad k_4 = \frac{4}{2\lambda + 3}.$$

Unfortunately, this theory does not fit the data very well and its restriction to small deformations make it mute on the effect of drop rupture on the rheology.

Experiments and numerical studies have shown that the pre-rupture rheology is characterized by small strain hardening and small shear thinning, with $N_1 > 0$ and $N_2 < 0$. Interestingly, repeated rupture leaves the effective viscosity nearly constant since rupture preserves the volume fraction of the droplets. This is consistent with Einstein's observation that the effective viscosity of a suspension depends only on the volume fraction of the particles and not on their absolute size.

2 Electrical Double Layers

Another deformable microstructure is an electric double layer around a charged colloidal particle. The solvent ions dissociate in presence of charged particles, forming a neutralizing cloud of counter-ions. The thickness of the double layer is given by the Debye length κ^{-1}, where

$$\kappa^2 = \sum_i \frac{n_i Z_i^2 e^2}{\epsilon k T}. \tag{8}$$

Here, $Z_i e$ is the charge on solvent ions of number density n_i and ϵ the dielectric constant. Thus, the colloidal particles act as spheres with a slightly larger radius, contributing a very small increase in the Einstein viscosity. In addition, the flow can distort this cloud but at low concentrations the effect is negligible.
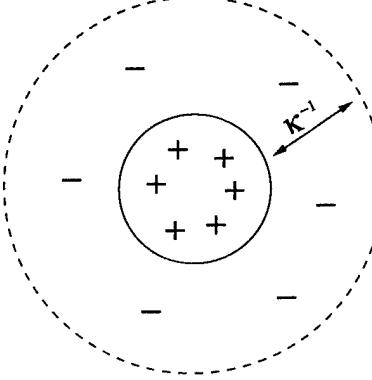
Figure 2: An electric double layer around a charged colloidal particle

3 Interactions

In this section we study the interactions between particles in concentrated solutions. These interactions include excluded volume interactions of rigid spheres and rods as well as deformable drops; electrical and van der Waals interactions.

3.1 Rigid Spheres

For a dilute solution of rigid spheres, only pair interactions (i.e. collisions) are important. At low shear rates, the effect of the collisions is to increase the effective viscosity [1]:

$$\mu^* = \mu(1 + 2.5\varphi + 6.2\varphi^2). \qquad (9)$$

The data from experiments by Saunders verifies the above result [2, 3] as shown in Figure 3. (This is Figure 14.17 from [4].) For purely extensional flows, the coefficient of the φ^2 term is 7.6.

For high concentrations, the experiments show shear thinning by a factor of roughly two. The shear thinning effect increases with the concentration. This is illustrated in Figure 4. (This is Figure 14.3 and 14.4(a) from [4].) The numerical simulations show shear thinning at moderate shear rates and shear thickening at high shear rates. This shear thickening has not been verified experimentally and may be a numerical artifact.

3.2 Electrical Interactions

As discussed previously, electrically charged colloids tend to form a shielding cloud of solution counter-ions whose thickness is given by the Debye length κ^{-1}. This cloud has a profound effect on the dynamics of collisions between colloidal particles. If the approaching particles are separated by a length r much greater than the Debye length, the particles interact like uncharged spheres of slightly augmented radius. Once the particle separation becomes comparable to the Debye length, the colloids begin to feel their mutual electrical repulsion. Their approach is halted at a characteristic distance r_*, determined from

$$6\pi\mu a\dot{\gamma}r_* = \frac{\epsilon\zeta a^2\kappa}{r_*}e^{-\kappa(r_*-a)},$$
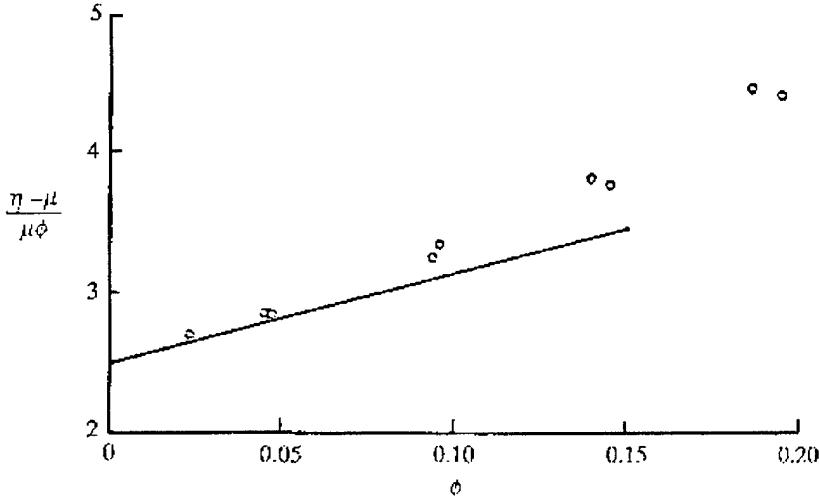
Figure 3: The data from [2, 3] verifying Equation 9

where viscous drag balances interparticle electrical repulsion. Here ζ is the surface charge density of the colloid, and ϵ is the dielectric constant for the solvent.

The effect of the charge particle interactions on the rheology can be calculated in much the same was as for uncharged rigid spheres. The result is an effective viscosity given by

$$\mu^* = \mu \left[1 + 2.5\varphi + 2.8\varphi^2 \left(\frac{r_*}{a} \right)^5 \right].$$

Since r_* is usually greater than a, the coefficient of the φ^2 term is much greater than the 6.2 found for the hydrodynamic interaction between rigid spheres, as illustrated in Figure 5. (This is Figure 14.19 from [4].) Changing the solvent ion concentration can have a large impact on the viscosity by changing the screening length κ^{-1}.

3.3 van der Waals Interactions

Van der Waals interactions allow aggregation of large, extended structures called flocs. Flocs are fractal structures with a typical dimension $d \sim 2.3$, which implies that they are packed more closely than a planar structure but less densely than a solid. If the flocs are small, they will tend to stick together after collisions but large flocs will be destroyed by strong flows. The size R of these flocs can be estimated by the following scaling argument. The number of particles of radius a in a floc is $N = (R/a)^d$ In equilibrium, the viscous forces (given by the Stokes drag formula) will balance the cohesive forces:

$$(6\pi\mu R) (\dot{\gamma}R) = F_b N \frac{a}{R},$$

59
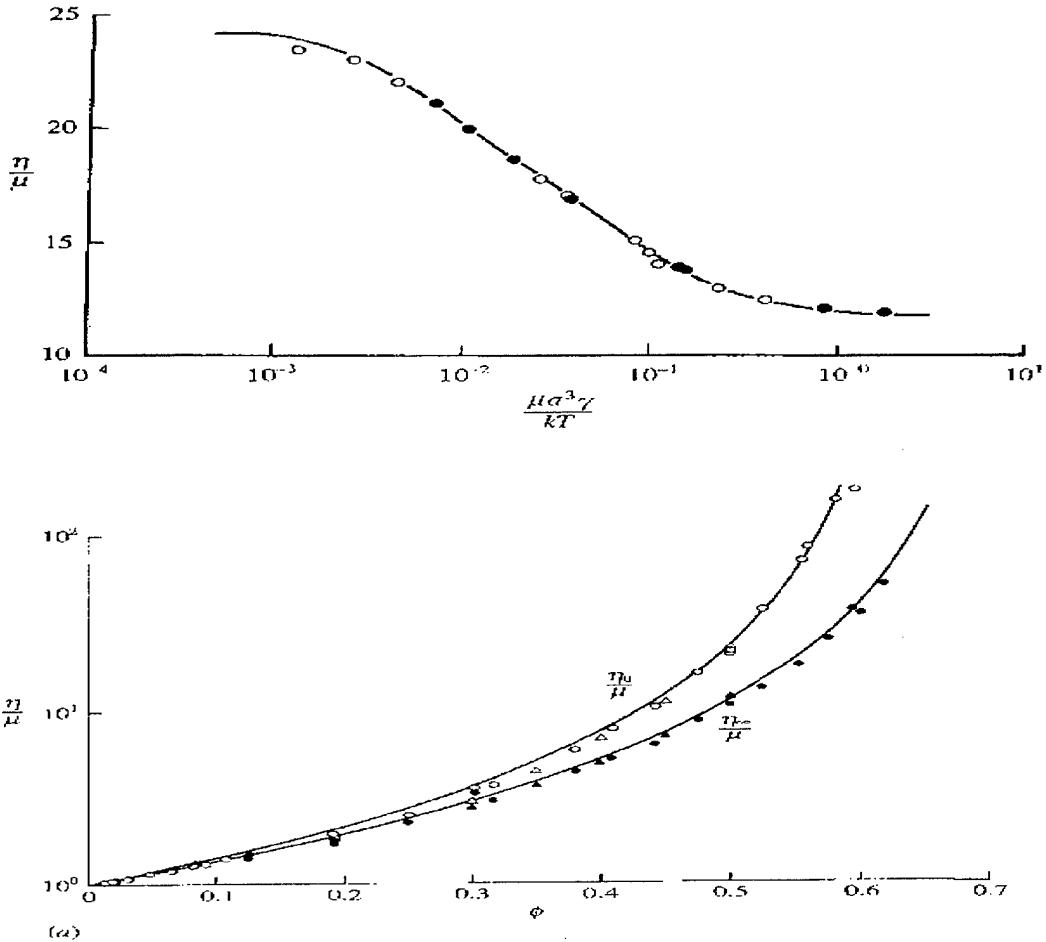
Figure 4: The shear thinning at high concentrations.

where F_b is the bond force and Na/R is the number of bonds per floc. Solving for R/a, we see that the volume fraction of the flocs is

$$\varphi_f = \varphi(R/a)^{3-d} = \varphi \frac{F_b}{6\pi\mu a^2 \dot{\gamma}}.$$

The effective viscosity is simply the Einstein viscosity with φ_f replacing φ. Since $\varphi_f \sim 1/\dot{\gamma}$, suspensions of flocs exhibit strong shear thinning. The expression for φ_f is unbounded as $\dot{\gamma} \to 0$. However, physically, φ_f cannot be greater than one. Thus, at low shear rates the solution gels and has a yield stress $\sim (\varphi F_b/a^2)$.

3.4 Rigid Fibers

In contrast to dilute suspensions of rigid fibers, concentrated solutions cannot pack with random orientation if $\varphi r > 1$ because of topological constraints. (Here $r > 1$ is the aspect ratio of the fiber.) Instead, the fibers spontaneously align - this is called the nematic phase

60
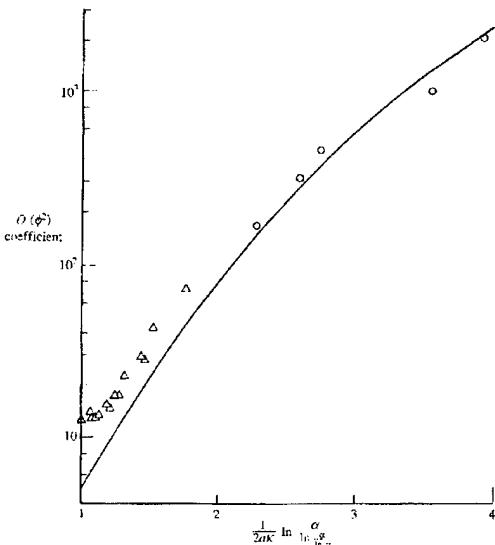
Figure 5: The coefficient of the φ^2 term in the effective viscosity

transition. As discussed in Lecture 5, the shear viscosity depends linearly on the aspect ratio and it can be large only when φr is large and the fibers are aligned. However, the extensional viscosity depends quadratically on the aspect ratio; it can be big even when $\varphi r < 1$ and the fibers are randomly oriented. Since the aspect ratio r of disks is less than 1, they cannot align randomly if $\varphi/r > 1$.

3.5 Drops

When the microstructure is deformable, the geometrical constraints are much less stringent and there is no jamming or locking of particles. During collision, the deformations lead to wider gap between the particles. Additionally, strong flow distorts the drops into cylinders with spherical end caps. These cylinders present a smaller collisional cross-section than a sphere of the same volume. This means that a suspension of drops is effectively 'dilute' even at a concentration of 30%. Because of this, blood works despite its high concentration of red blood cells.

4 Polymer chains

We have discussed microstructure without any internal structure. In the remaining part of the lecture, we will discuss various models for polymers, first for isolated polymers and then for entangled ones.

4.1 Isolated Polymers

The simplest model studied in the '40s is the bead-and-spring model, shown schematically in Figure 6. This model replaces a chain of N bonds each of length b with two spheres of

61
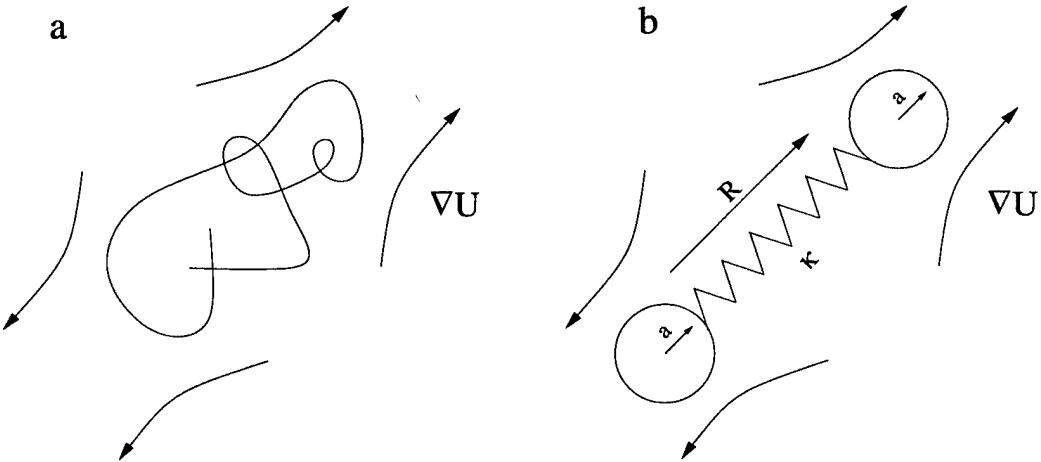
Figure 6: (a) A schematic drawing of polymer being distorted by the flow. (b) The bead-and-spring model to study the isolated polymer chains.

radius a joined by a spring of spring constant κ. Assuming that each bond is undergoing Brownian motion, we obtain the effective spring constant of $\kappa = 3kT/Nb^2$ and sphere radius $a = b\sqrt{(N/6)}$. If we denote by $\mathbf{R}$ the vector joining the two spheres, the Stokes drag on the spheres is $6\pi\mu a(\mathbf{R}\cdot\nabla\mathbf{u} - \dot{\mathbf{R}})$. Equating the drag force with restoring force $-\kappa\mathbf{R}$ of the spring, we obtain the time evolution of $\mathbf{R}$:

$$\dot{\mathbf{R}} = \mathbf{R}\cdot\nabla\mathbf{u} - \frac{1}{2\tau}\mathbf{R}, \qquad \text{where} \qquad \tau = \frac{\sqrt{6}}{\pi}\frac{kT}{\mu\left(N^{1/2}b\right)^3}.$$

The equation for the deformation tensor $\mathbf{A}\propto\mathbf{RR}$ is obtained as

$$\overset{\triangledown}{\mathbf{A}} = \frac{D\mathbf{A}}{Dt} - \mathbf{A}\cdot\nabla\mathbf{u} - (\nabla\mathbf{u})^T\cdot\mathbf{A} = -\frac{1}{\tau}\left(\mathbf{A} - \frac{Na^2}{3}\delta\right).$$

The stress tensor is given by

$$\sigma = -p\delta + 2\mu\mathbf{E} + n\kappa\mathbf{A},$$

where n is the number density of the chains. This is the Oldroyd-B model. In a shear flow, μ is constant, the first normal stress depends quadratically on the strain rate, and the second normal stress is zero. As we noted in the second lecture, this model gives negative extensional viscosity when $\dot{\gamma}\tau > 1/2$ because the model allows the polymers to stretch indefinitely.

There are a number of (boring) refinements to the bead and spring model: Allowing the polymer to have a spectrum of internal modes just leads to a spectrum of relaxation times. Considering polydisperse molecular weight polymers smears out the relaxation time, but does not otherwise modify the model.

An extremely important refinement accounts for the fact that polymers cannot be extended indefinitely—they all have finite length. This is accomplished by modifying the spring force law so that the restoring force goes to infinity when the polymer is maximally

extended. A common form for this force law is

$$F = \frac{kT}{Nb^2} \frac{R}{1 - R^2/L^2},$$

where $L = Nb$ is the total length of the polymer. This modification is called FENE for Finite Extension Nonlinear Elasticity.

Some other refinements are: inclusion of nonlinear bead friction; rotation of beads; nonlinear internal modes.

4.2 Entangled Polymers

A polymer in a concentrated solution is not free to move arbitrarily because neighboring polymer chains impose topological constraints. A class of models called the reptation models, first suggested by de Gennes in 1971[5], focuses on a single polymer which squiggles and squirms around other polymer chains, as shown schematically in Figure 7. Consider the
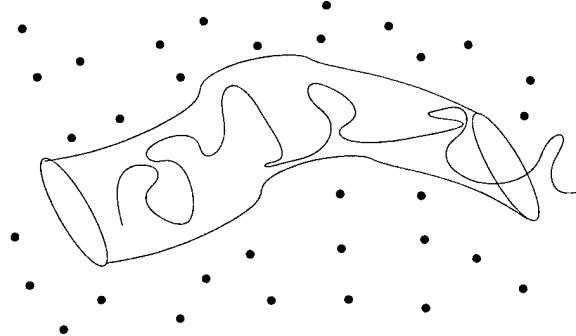
Figure 7: A polymer chain reptating through the tube formed by presence of other polymers

motion of a single polymer, keeping all the others fixed. Assuming that the chain diffuses along its length L with a diffusion constant D proportional to $kT/\mu L$, we see that the diffusion time scale is

$$\tau_d = \frac{L^2}{D}. \tag{10}$$

Since the molecular weight M is proportional to the length, the above equation implies that the diffusion time scale is proportional to M^3. But experiments discussed in Lecture 1 show this power to be 3.4. Attempts to capture this elusive 3.4 have lead to many refinements of this simple model. One of them (the A-BKZ model) considers the deformations with the mean flow of an effective tube containing the polymer [6]. A refinement of this refinement considers the effect of retraction of the polymer, which leads to an effective shrinking of the tube, along with the tube deformation. Another obvious refinement is to allow for the reptation of other polymers. The latter two theories have been combined together to give finally the correct power of 3.4 [7]!

Notes by Amit Apte and Christopher L. Wolfe?

63

References

[1] G. K. Batchelor, "The effect of brownian motion on the bulk stress in a suspension of spherical particles," J. Fluid Mech. **83**, 97 (1977).

[2] W. B. Russel, "A review of the role of colloidal forces in the rheology of suspensions," J. Rheology **24**, 287 (1980).

[3] F. L. Saunders, "Rheological properties of monodisperse latex systems," J. Colloid Sci. **16**, 13 (1961).

[4] W. B. .Russel, D. A. .Saville, and W. R. .Schowalter, *Colloidal Dispersions* (Cambridge University Press, Cambridge, 1989).

[5] P.-G. de Gennes, "Reptation of a polymer chain in the presence of fixed obstacles," Journal of Chemical Physics **55**, 572 (1971).

[6] M. Doi, "Explanation for the 3.4-power law for viscosity of polymeric liquids on the basis of the tube model," Journal of Polymer Science, Polymer Physics Edition **21**, 667 (1983).

[7] J. D. Cloizeaux, "Relaxation and viscosity anomaly of melts made of long entangled polymers - time-dependent reptation," Macromolecules **23**, 4678 (1990).

Lecture 7: Stress Relaxation

E. J. Hinch

1 Introduction

How does a Non-Newtonian fluid behave when under stress? And what happens when the force causing the stress is removed? One would expect that purely elastic solids when combined with viscous fluids would be adequate in modeling Non-Newtonian fluids. However, that is not the case.

As is apparent in figure 1, there is a certain time scale characteristic of Non-Newtonian fluids that is absent when such substances are modeled as a mix of elastic solids and viscous fluids. Accounting for a *relaxation time* of the microstructure and the extra normal streses is essential to the description of such materials.

When a Non-Newtonian fluid is deformed, the instantaneous viscous stress that builds up scales as $\mu_o \dot{\gamma}$, where μ_o is the zero-shear viscosity of the material. If we now suppose that there is a memory time (τ) associated with the microstructure within the material, then the deformation it undergoes for a constant shear rate, $\dot{\gamma}$, would be $\dot{\gamma}\tau$. As in elastic solids, the elastic stress associated with such a deformation would be $G\dot{\gamma}\tau$, where G is the elastic modulus of the material. After the memory time or the relaxation time of the material has elapsed, the stress would reach a steady value which would scale as $(\mu_o + G\tau)\dot{\gamma}$ as seen in figure 1. It is reasonable to think of $(\mu_o + G\tau)$ as an enhanced viscosity. In other words, Non-Newtonian fluids have a characteristic memory time scale which is referred to as the *relaxation time*. When the applied rate of deformation is reduced to zero, these materials relax over their characteristic relaxation time - a constitutive property of each material. This phenomenon is known as stress relaxation.

2 Flow of a non-Newtonian fluid past a rigid sphere

We will now look at the flow of a Non-Newtonian fluid past a sphere. While such a flow can be steady in an Eulerian sense, it might be unsteady in a Lagrangian sense. Arigo *et al*, [1] worked out the FEM simulations of the long wake behind the sphere using the Oldroyd-B model for the microstructure, as shown in figure 2. Note that the wake gets longer as the Deborah number, *De*, increases. This is because as the shear rate is increased, the fluid behind the wake is stretched more and more, therefore requiring a larger distance to relax.

In figure 3, the force required to move the sphere at a constant velocity through the fluid is plotted against Weissenberg number (which for this case may be thought of as the dimensionless shear rate). The force is made dimensionless with the equivalent Stokes
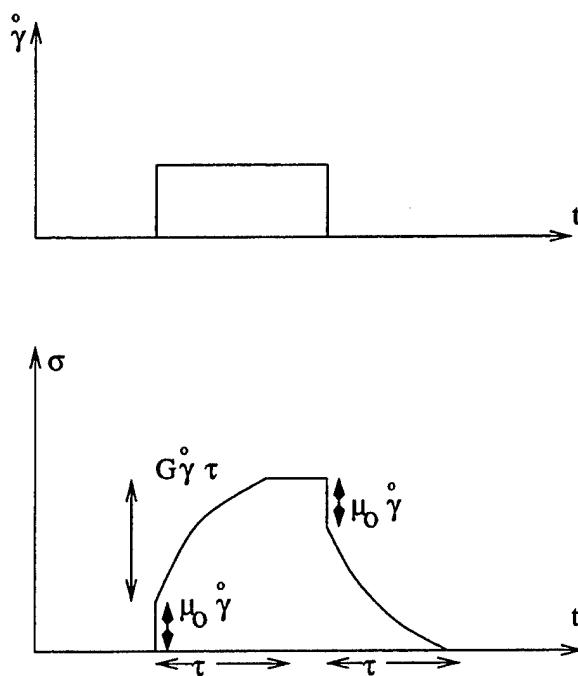
Figure 1: Stress build-up and relaxation in a viscoelastic material due to a step strain rate.
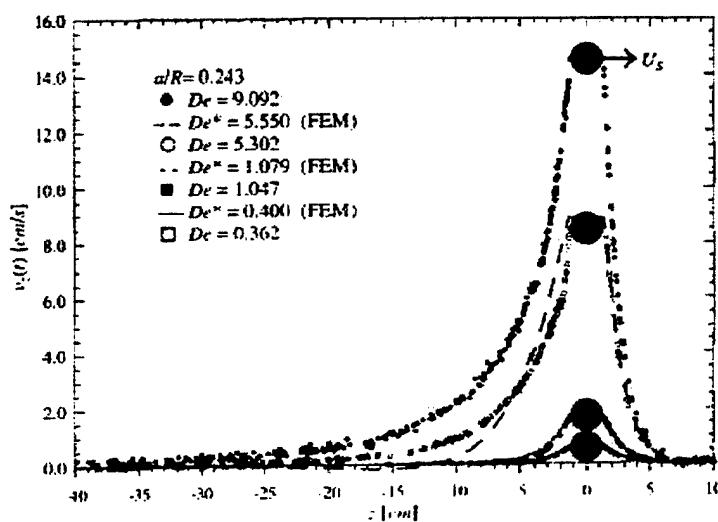

Figure 2: Velocity in the wake of a rigid sphere moving through a non-Newtonian fluid, as a function of the distance from the center of the sphere.
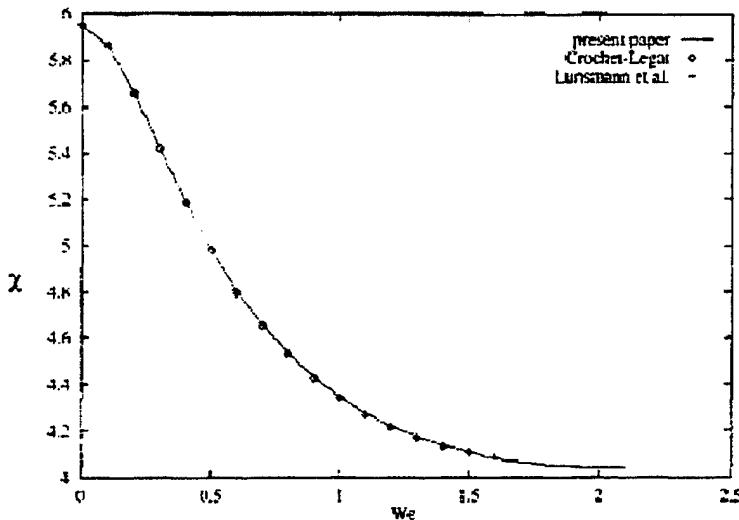
Figure 3: Drag on the sphere, scaled with Stokes drag, plotted against the Weissenberg number.

drag - the force that would have been required to move the sphere at the same velocity in a Newtonian fluid of viscosity $(\mu_o + G\tau)$ [2]. A comparison with the experiments shows that the force required does not decrease as drastically as predicted by the Oldroyd-B calculation [3], as shown in figure 4. The simulations can be brought closer to the experimental observation by calculating the Stokes drag using the zero-shear viscosity of the fluid instead of the deformation enhanced viscosity. This is because, as the sphere is moved faster (up to a limit), the fluid gets less time to deform. Hence the viscosity as seen by the sphere still remains μ_o. Two of the important experimental observations that the Oldroyd-B model fails to predict are the large increase in drag beyond a critical We and the much larger wake seen behind the sphere.

When a sphere moves through a Non-Newtonian fluid, negative wakes are observed. In a negative wake, the fluid in the wake region of a moving sphere starts to move in a direction opposite to that of the sphere. Figure 5 shows a cartoon describing the effect. These negative wakes have been ascribed to the high stresses that the moving sphere introduces in its wake regions as it deforms the microstructure. The stress relaxation of the fluid after the sphere has moved away from a point causes a secondary flow.

Another calculation was done by Harlen [4] using a finite extensible non-linear elastic (FENE-CR) microstructure model proposed by Chilcott and Rallison, a figure from which is shown in figure 6. This simulation demonstrates that the extent of negativity in a wake increases as the extensibility (parameter L in figure) of the microstructure increases.
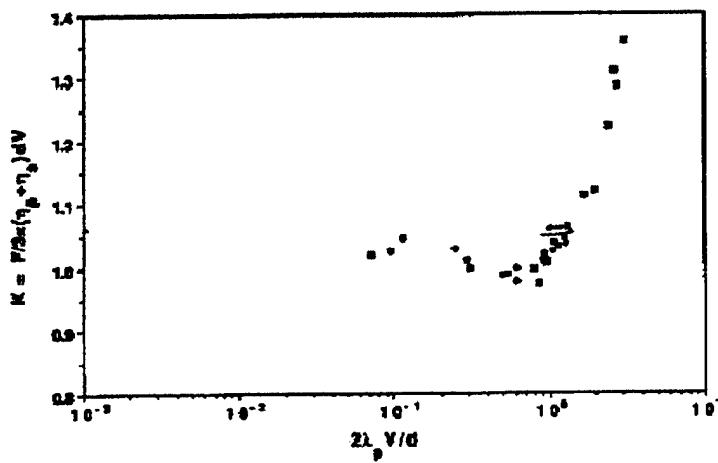
Figure 4: Drag on the sphere plotted against Weissenberg number, measured experimentally.
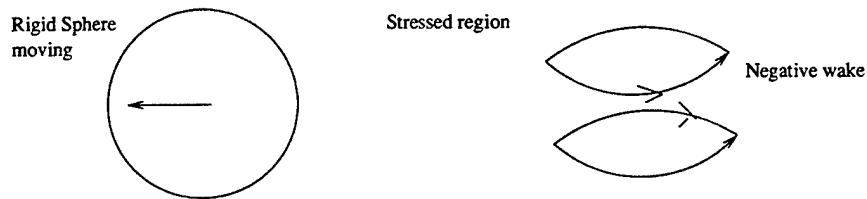
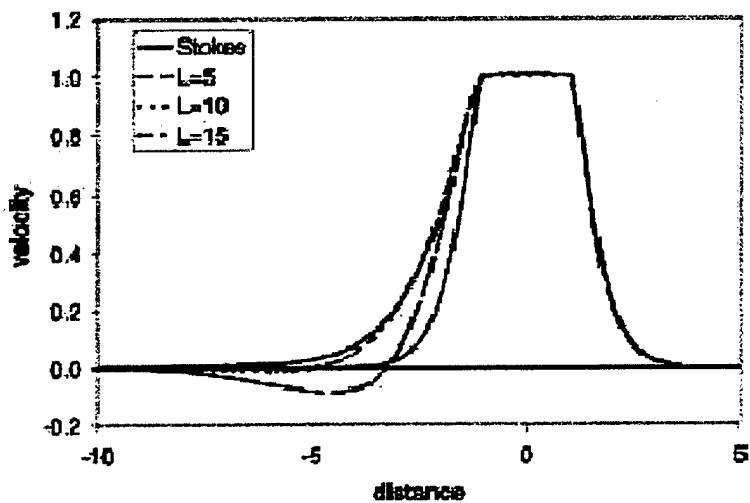Figure 5: Cartoon showing a negative wake region behind the sphere

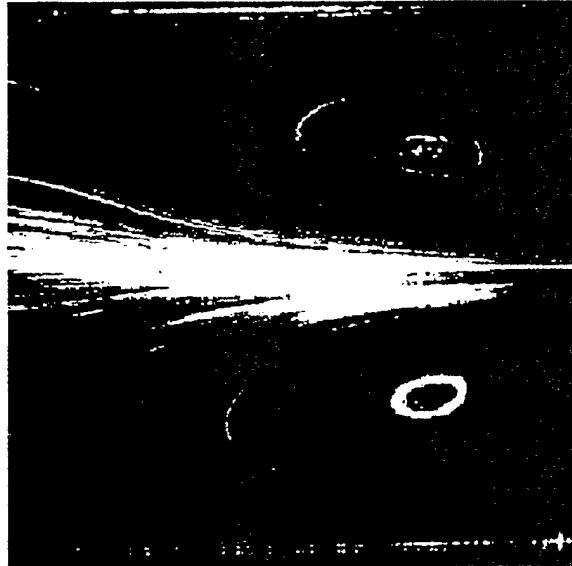Figure 6: The negative wake as seen in FENE-CR calculations.

68

Figure 7: A picture from an experiment, showing the upstream vortex in the contraction flow of a non-Newtonian fluid.

3 Flow of a non-Newtonian fluid through a sudden contraction

Large upstream vortices are observed in Non-Newtonian fluids flowing through a channel contraction as shown by Cartalos and Piau [5] (see figure 7). This is another example of a flow which may be unsteady in the Lagrangian sense while being steady in the Eulerian sense. Oldroyd-B model has been used in the FEM simulations of such flows ([6, 7]). In figure 8, we can see the pressure drop (made dimensionless with the Stokes drag) across the contraction plotted against the Deborah number. This result disagrees with what is observed in experiments (see figure 9) wherein an initial decrease in the pressure drop is followed by a steady climb up to an order of magnitude higher value. Thus Oldroyd-B successfully predicts the initial small decrease in pressure drop until a De of about 5. However, it fails to predict the large upstream vortices and the dramatic increase in pressure drop seen in constraction flows of such fluids. Again, it is better to scale the pressure drop for higher De using μ_o instead of $(\mu_o + G\tau)$ as explained for a sphere moving in a Non-Newtonian fluid.

Arigo, et al. [1] worked out the FEM simulation of a sphere falling down a tube filled with a Non-Newtonian fluid, wherein a constant force was applied to move the sphere. Figure 10 shows the velocity of the sphere as it descends down the tube. Again, Oldroyd-B is the model that has been used in the calculation. In the figure, it is evident that the velocity of the sphere overshoots the Newtonian value during start-up of the fall. This is due to shear-thinning. After reaching a peak, the velocity begins to decrease and becomes less than the Newtonian case after a sufficiently long time. Increasing the Deborah number results in the sphere slowing down more quickly.
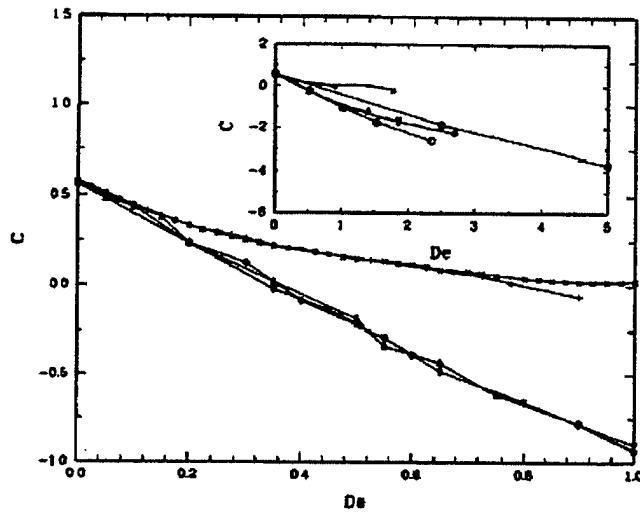
69

Figure 8: Pressure drop across the contraction, calculated using the Oldroyd-B model, plotted against De.
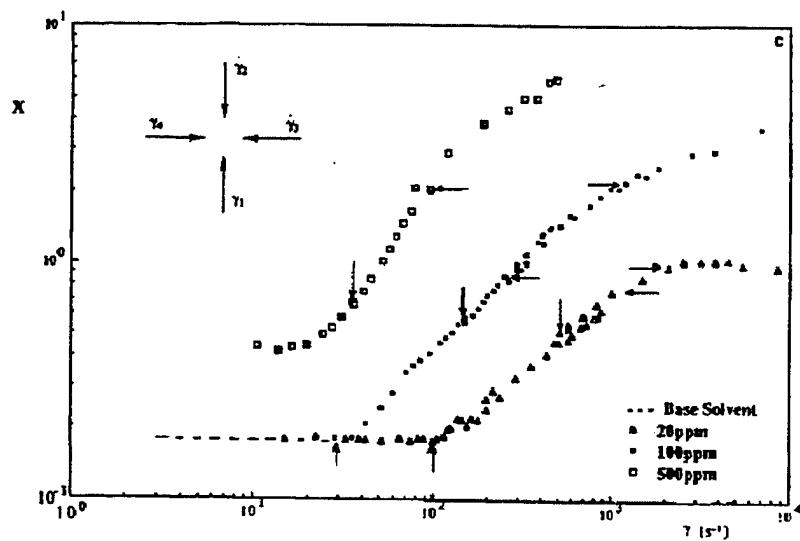

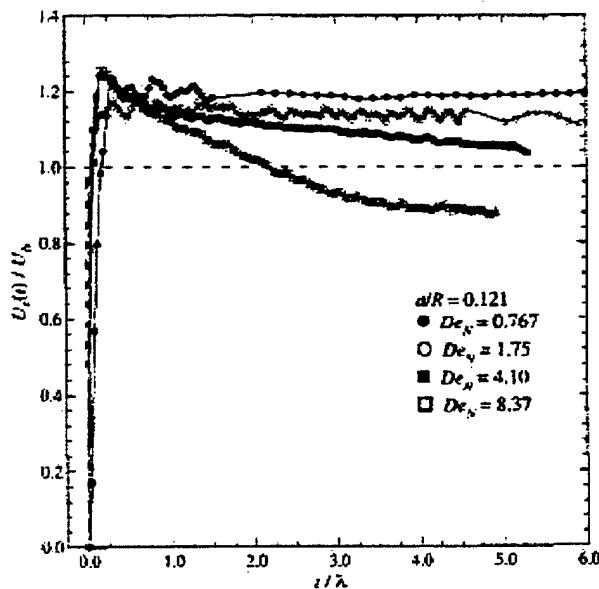Figure 9: Experimental results of pressure drop in a contraction flow plotted against strain rate.

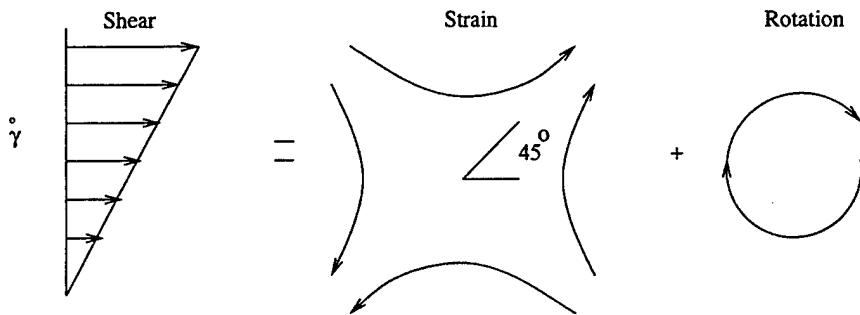Figure 10: Velocity of the sphere plotted against time

Figure 11: Shear flow can be written as a sum of straining and rotation.

3.1 Non-linear deformation

When a Non-Newtonian fluid undergoes a nonlinear deformation, tension in the streamlines develops due to the large relaxation time of the microstructure. This tension in the streamlines results in non-zero normal stresses within the fluid. We can estimate the approximate shear and normal stresses in Non-Newtonian fluid deformed by a simple shear flow in the following manner. The simple shear flow can be decomposed into a purely straining motion with the principal axes oriented at 45° from the axis of shear and a pure rotation as is shown in figure 11.

The straining motion causes a strain of $\dot{\gamma}\tau$ resulting in a shear stress equal to $G\dot{\gamma}\tau$ in the microstructure. Pure rotation then causes the microstructure to align in the direction of the flow, thereby lending it to compression by the straining motion, as shown in figure

71
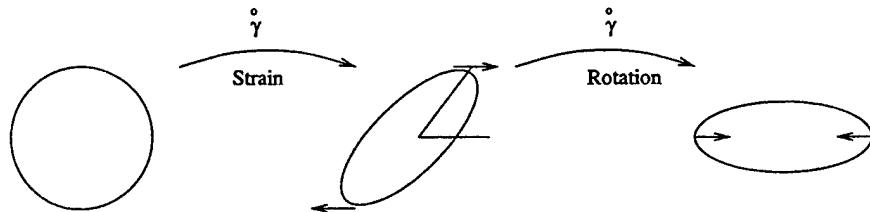
Figure 12: Shear and Normal Stresses in a non-Newtonian fluid.

12. The extent of the compression is $\dot{\gamma}\tau$. Thus

$$\text{Normal Stress} = \text{Shear Stress} \times \dot{\gamma}\tau$$

4 Yield Problems

Some Non-Newtonian fluids undergo a yield behavior when deformed beyond a limit. Such fluids have an associated yield stress beyond which it undergoes a distinct change in flow behavior. Common examples of materials that possess a yield stress are foams, cross-linked gels and pastes. In this lecture we will talk about such materials and then describe some of the common applications of yielding in the transport of small particles as well as the dangers of having a dead zone in sharp corners of channels. We will then proceed to the age-old squeeze film paradox. After that we will talk about what is common between ketchup bottles and oil pipelines.

Kabla & Debregeas [8] has suggested that foams get permanently damaged upon yielding. Therefore, an understanding of the yield behavior of foams is of direct relevance to their efficacy. The figure 13 has been taken from St.Jalmes & Durian [9]. They show how the yielding stress and strain decrease with decreasing volume fraction of gas in a foam. The rheological behavior of an unnamed cross-linked gel is shown in figure ??. Both the degree of cross-linking and the concentration of the polymer molecules forming the gel will determine its yield stress.

Yield stress is an important quantity when walls are being plastered. If the yield stress of the plaster is too large, it will not flow very smoothly - sticking, slipping and bringing into question the self-esteem of the painter. However, if the yield stress is too small, painting the cieling will be an exercise in making the floor dirty because all the plater paste will give in to gravity. The figure ?? shows the yielding behavior of a suspension of 30% Aluminium particles in an unknown solvent. Clearly, the the yielding behavior is strongly governed by the pH of the suspension. An explanation for this is still lacking.

Another interesting effect of yield stress can be seen in the sedimentation of rigid particles in a Bingham fluid. In order for the particle to sediment, the stress due to gravitational force should be higher than the yield stress of the fluid. When that happens, a fluid region is created around the particle that will cause it to cruise through the Bingham fluid and sediment, as can be seen in figure 14. For the case of a spherical particle, there are two stagnation points where the stress is below yield stress. Hence, they remain undeformed and can be treated as solid regions. Detailed calculations for this problem can be found in work by Beris *et al* [10].
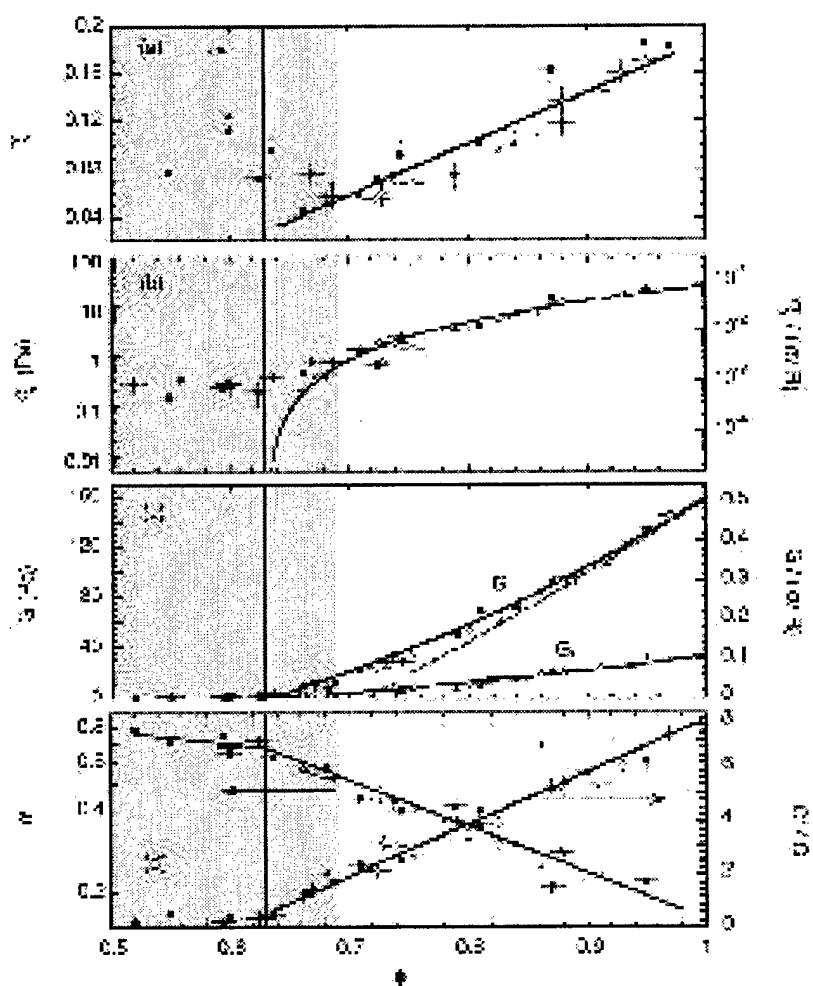
Figure 13: Yield strain and yield stress of a foam Vs. volume fraction of gas.
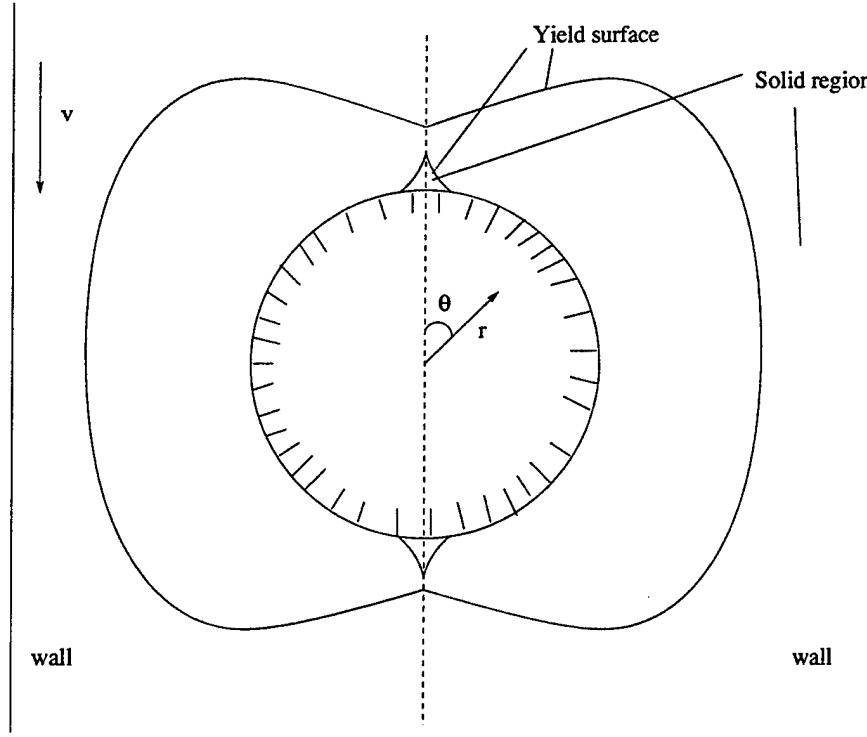
Figure 14: Sedimentation of a sphere in a Bingham fluid.

When a Bingham yield fluid flows through a rectangular channel, the fluid near the corner can remain unyielded as seen in figure 15.

5 Squeeze film paradox

In this section, we will talk about the squeeze film paradox. First, we will describe this paradox. After that, we will address the solution of this problem [11, 12, 13].

As shown in Fig. 16, we consider a film of Bingham fluid described in terms of a Cartesian coordinate system (x, z) in which x is the horizontal and z the vertical. Let the center of the film lie at the origin. If we squeeze the film with the vertical velocity $W/2$ from above and the vertical velocity $-W/2$ from below, the film will move horizontally with the velocity u and vertically with the velocity w (Shown in figure 16). If the effect of gravity is ignored, the momentum equations for the film are:

$$0 = -\frac{\partial p}{\partial x} + \sigma_{xx,x} + \sigma_{xz,z}, \tag{1}$$

$$0 = -\frac{\partial p}{\partial z} + \sigma_{xz,x} + \sigma_{zz,z}. \tag{2}$$
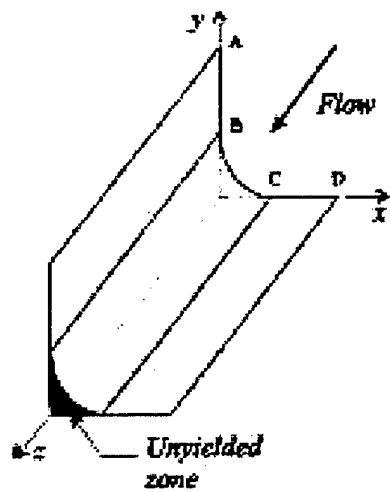
74

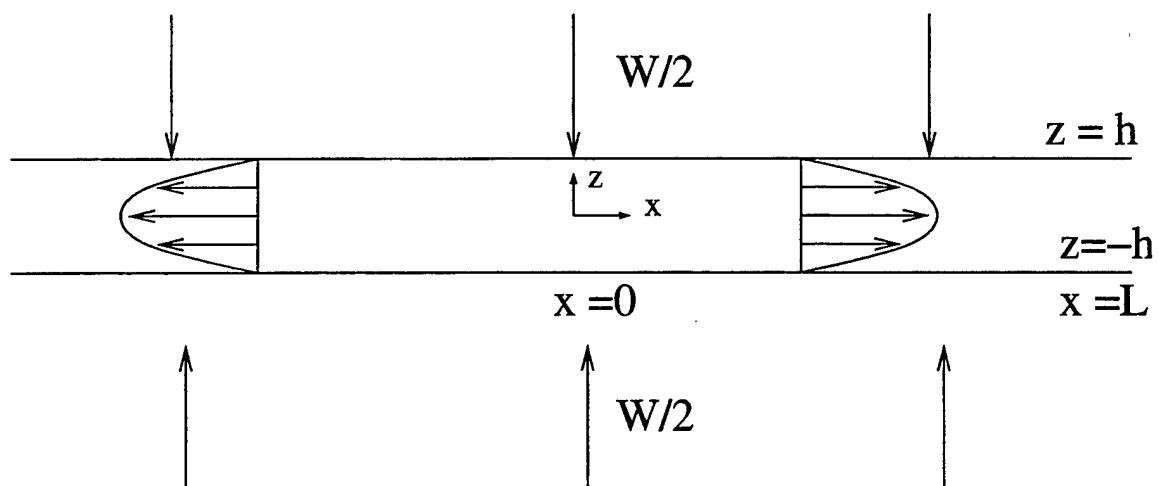Figure 15: Unyielded zone in the corner of a rectangular channel.

Figure 16: Squeezing of the film

For a Bingham fluid, the relationship between the stress and strain rate is

$$\mathbf{E} = \mathbf{0} \quad \text{if } |\sigma| < \sigma_y, \tag{3}$$

$$\sigma = (2\mu + \frac{\sigma_y}{|\mathbf{E}|})\mathbf{E} \quad \text{if } |\sigma| > \sigma_y, \tag{4}$$

where σ_y is the yield stress, $\mathbf{E}$ is the strain rate tensor and σ is the stress tensor. $\mathbf{E}$ can be expressed as:

$$\mathbf{E} = \begin{pmatrix} u_x & \frac{1}{2}(u_z + w_x) \\ \frac{1}{2}(u_z + w_x) & w_z \end{pmatrix}. \tag{5}$$

The second invariant of the strain rate tensor and the stress tensor are: $|\mathbf{E}| = \sqrt{\frac{1}{2}\mathbf{E} : \mathbf{E}}$ and $|\sigma| = \sqrt{\frac{1}{2}\sigma : \sigma}$ respectively. We non-dimensionalize the momentum equation in the following way. Let L be the horizontal length scale, H be the vertical length scale, and W be the scale for the vertical velocity. Then the horizontal velocity u can be scaled as $W\frac{L}{H}$, and strain rate tensor E can be scaled as $\frac{W}{L}$. Also we scale σ_y, σ_{xz} by $\frac{\mu W L}{H^2}$ and σ_{xx}, σ_{zz} by $\frac{\mu W}{H}$, and the presssure p by $\frac{\mu W L^2}{H^2}$. Let $\epsilon = \frac{H}{L}$. Since the horizontal length scale L is much larger than the vertical length scale H, we have $\epsilon \ll 1$, $p \gg (\sigma_y, \sigma_{xz}) \gg (\sigma_{xx}, \sigma_{zz})$. Then the non-dimensionalized equation can be written as:

$$0 = -\frac{\partial p}{\partial x} + \epsilon^2 \sigma_{xx,x} + \sigma_{xz,z}, \tag{6}$$

$$0 = -\frac{1}{\epsilon^2}\frac{\partial p}{\partial z} + \sigma_{xz,x} + \sigma_{zz,z}. \tag{7}$$

To $O(\epsilon^2)$, the momentum equation in the z direction is:

$$\frac{\partial p}{\partial z} = 0. \tag{8}$$

Thus, the pressure is not a function of the height to $O(\epsilon^2)$:

$$p = p(x) + O(\epsilon^2). \tag{9}$$

The non-dimensionlized strain rates are:

$$\mathbf{E} = \begin{pmatrix} \epsilon u_x & \frac{1}{2}(u_z + \epsilon^2 w_x) \\ \frac{1}{2}(u_z + \epsilon^2 w_x) & \epsilon w_z \end{pmatrix}. \tag{10}$$

So the leading order constitutive law will be:

$$u_z = 0 \quad \text{if } |\sigma_{xz}| < \sigma_y, \tag{11}$$

$$\sigma_{xz} = -\sigma_y + \dot{\gamma}u_z \ (\text{in } z > 0) \quad \text{if } |\sigma_{xz}| < \sigma_y, \tag{12}$$

$$\sigma_{xz} = +\sigma_y - \dot{\gamma}u_z \ (\text{in } z < 0) \quad \text{if } |\sigma_{xz}| < \sigma_y. \tag{13}$$

Integrating the momentum equation along the x-direction with respect to z, we find:

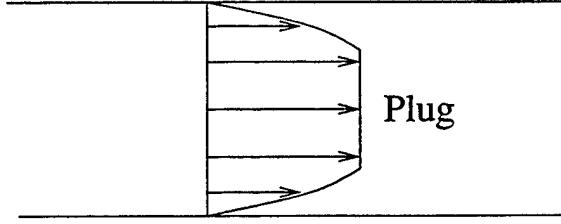$$\sigma_{xz} = \frac{dp}{dx}z + O(\epsilon^2) \tag{14}$$

76

Figure 17: Plug velocity profile in the unyielded region of the film.

By introducing equation (14) into the leading order constitutive law equation(11-13) at the yielding level $z = Y$, we find that:

$$\frac{dp}{dx}Y = -\sigma_y. \tag{15}$$

Hence the yield level Y can be expressed as:

$$Y = \sigma_y / \left(-\frac{dp}{dx}\right). \tag{16}$$

The velocity gradient in the z-direction then becomes:

$$u_z = \begin{cases} 0 & \text{in } 0 \le z \le Y \\ \frac{dp}{dx}(z - Y) & \text{in } Y \le z \le 1. \end{cases} \tag{17}$$

Integrating in z, we obtain the velocity profile as:

$$u = \begin{cases} U & \text{in } 0 \le z \le Y \\ U + \frac{dp}{dx}\frac{1}{2}(z - Y)^2 & \text{in } Y \le z \le 1. \end{cases} \tag{18}$$

When the height z is less than the yield level Y, the fluid in the film will not yield and move with a uniform plug velocity U. When the height z is larger than the yield level Y, the velocity of the fluid in the film increases quadratically with height (See in figure 17).

Assume the non-slip boundary condition:

$$u = 0 \quad \text{at } z = 1. \tag{19}$$

Then match the velocity profile to the non-slip boundary condition; we have:

$$\frac{dp}{dx} = -\frac{2U}{(1 - Y)^2}. \tag{20}$$

Substituting the pressure gradient along the x direction into the velocity profile, we have

$$u = \begin{cases} U & \text{in } 0 \le z \le Y \\ U[1 - \frac{(z-Y)^2}{(1-Y)^2}] & \text{in } Y \le z \le 1. \end{cases} \tag{21}$$

Therefore, we obtain the horizontal velocities of the film at different heights. However, that is not the end of the story. Integrating the horizontal velocity along the z direction, we can obtain the volume flux Q:

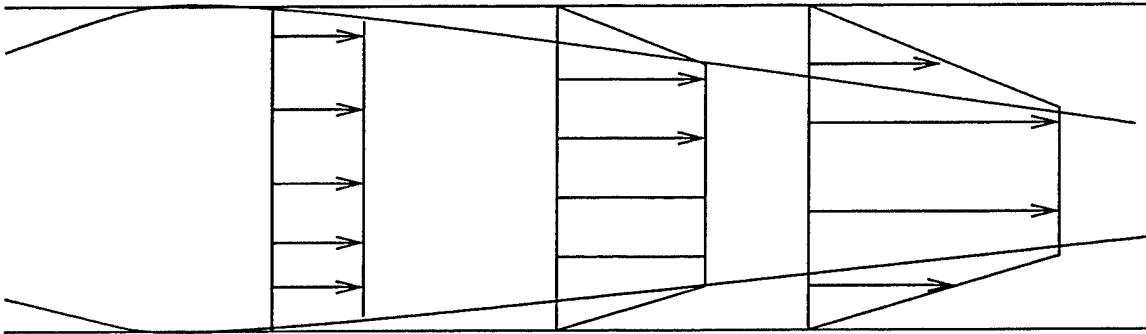$$Q = \int_0^1 u\,dz = U[\frac{2}{3} + \frac{1}{3}Y]. \tag{22}$$

77

Figure 18: The velocity is increasing in the x direction – paradox!

As we squeeze the film, the sum of the horizontal flux Q of the fluid should be equal to the decrease of the fluid volume in the vertical direction per unit time because of the mass conservation:

$$Q = \frac{1}{2}x. \tag{23}$$

Combining the two equations above, we obtain the expression for the plug velocity U.

$$U = \frac{\frac{1}{2}x}{\frac{2}{3} + \frac{1}{3}Y}. \tag{24}$$

Putting this into the expression for the pressure gradient along the x-direction, we have:

$$\frac{dp}{dx} = -\frac{x}{(\frac{2}{3} + \frac{1}{3}Y)(1 - Y)^2}. \tag{25}$$

After substituting the pressure gradient along the x direction into the expression for the yield level, we obtain an equation for the yield level Y:

$$Y = \sigma_y \left(\frac{2}{3} + \frac{1}{3}Y\right)(1 - Y)^2/x. \tag{26}$$

The asymptotic solution of this equation is:

$$Y \sim \begin{cases} 1 - x^{\frac{1}{2}} & \text{in } x \ll 1 \\ \frac{2\sigma_y}{3x} & \text{in } x \gg 1. \end{cases} \tag{27}$$

By introducing the expression for the yield level Y into the equation for the plug velocity U, we find that the plug velocity U is not a constant any more, but varies in the horizontal direction x (See figure 18), which contradicts with the previous conclusion. This is known as the squeeze film paradox.

To resolve the squeeze film paradox, we show how plug velocity U can be a function of x if we assume the stress is actually just above the yield value in the "plug" region: $|\sigma| = \sigma_y + O(\epsilon)$. Now, the stress is given by,

$$\sigma_{xz} = -\sigma_y \frac{z}{Y}, \tag{28}$$

78

Thus $|\sigma| \approx \sigma_y$ if

$$\sigma_{xx} = -\sigma_{zz} = \sigma_y \sqrt{1 - \frac{z^2}{Y^2}} + O(\epsilon). \tag{29}$$

Since the strain rate tensor E is proportional to the stress tensor for the Bingham fluid, the derivative of the horizontal velocity u with respect to z should have first order approximation, $u_z = O(\epsilon)$, and we could assume that the horizontal velocity u can be expanded as $u = U(x) + \epsilon u_1(x, z)$. Then the strain rate tensor can be expressed as:

$$\mathbf{E} = \epsilon \begin{pmatrix} U_x & \frac{1}{2}u_{1z} \\ \frac{1}{2}u_{1z} & -U_x \end{pmatrix}. \tag{30}$$

Therefore the magnitude of the strain rate tensor is: $|\mathbf{E}| = \epsilon \sqrt{\mathbf{U}_x^2 + \frac{1}{4}\mathbf{u}_{1z}^2}$, and we have

$$-\sigma_y \frac{z}{Y} = \sigma_{xz} = \left(2 + \frac{\sigma_y}{\epsilon \sqrt{U_x^2 + \frac{1}{4}u_{1z}^2}} \right) \epsilon \frac{1}{2} u_{1z}. \tag{31}$$

Thus, u_{1z} satisfies:

$$u_{1z} = -\frac{2U_x \frac{z}{Y}}{\sqrt{1 - (\frac{z}{Y})^2}}. \tag{32}$$

This solution is singular as z approches the yielding level Y, requiring a thin transition layer of order $O(\epsilon)$, across which we must match the pseudoplug solution with the earlier solution for the yielding region in order to fully specify the flow. Without going through this refinement, we may still integrate equation (32) to find the velocity connection inside the plug,

$$u_1 = 2U_x Y \sqrt{1 - \left(\frac{z}{Y}\right)^2}. \tag{33}$$

Therefore, the horizontal velocity u varies in the x and the z directions even in the plug region as predicted.

6   Ketchup bottles and oil pipelines

There are great reservoirs underneath the ocean. In the petroleum industry, oil is often pumped through long pipelines to the sea surface. The length of the pipelines is usually 3 km, and the diameter of the pipelines is usually 10cm. When the oil is pumped up out of these reservoirs, the temperature of the oil is high ($\sim 80°C$) and the viscosity of the oil is low. During transport, the cold water in the ocean ($\sim 4°C$) cools the oil. To insulate the pipeline from the ocean water and ease pumping, insulating gel is put between the pipelines. A pratical problem which then occur is that the hot oil pipe will also heat the gel and make the gel expand. People usually build a vacant expansion pipe to contain the expanded gel. After the production stops, the oil pipe cools and gel contracts. The contracted gel is then

recyled. Three questions emerge that need to be answered before the production process: Will the gel convect with the large temperature difference $\Delta T = 80°C$? Can we generate the pressure to pump the oil 3Km in 10 hours without bursting the pipe? How much gel flows out of the expansion pipe in the recycling process?

We address these questions one by one. First, let us consider whether the gel will convect. Before we answer this question, we need to calculate the yield stress of the gel. Lab observations show that a 1mm air bubble does not move in the vertical gel pipe and air bubbles larger than 1mm will move. A balance of buoyant stress and the yield stress of the gel(τ_*) gives the following estimate:

$$\tau_* = \Delta\rho_0 g d = 10 \ Pa, \tag{34}$$

where the $\Delta\rho_0$ is the density difference between the gel and air, and d is the diameter of the bubble. Therefore, the yield stress of the gel is about $10Pa$. Near the surface of the oil pipe the temperature of the gel is around $80°C$, and the temperature of the gel near the cold water is around $4°C$. The temperature difference between the cold gel and the hot gel will therefore be about: $\Delta T \sim 80°C$. The density difference for the gel at these different temperatures is:

$$\frac{\Delta\rho}{\rho} = 10^{-2}. \tag{35}$$

Consequently, there will be a buoyant force on a "bubble" of the heated gel. From Eq. 34, a bubble of diameter D will be held in place by the yield stress if:

$$\tau_* \approx 10Pa > \Delta\rho g D = 10^{-2} \cdot 10 \cdot D, \tag{36}$$

that is, if $D < 10cm$. Since the diameter of the pipe is about 10cm, the gel will not convect.

Now, let us consider whether pumping is feasible. For pumping, the pressure difference across the pipe should exceed the yield stress of the gel along the wall:

$$\pi r^2 \Delta p > 2\pi r L \tau_*, \tag{37}$$

where r is the radius of the pipe, L is the length of the pipe, Δp is the pressure difference across the pipe, and τ_* is the yield stress of the gel. Therefore, we estimate pressure drop per unit length as:

$$\frac{\Delta p}{L} = 200Pa \cdot m^{-1}. \tag{38}$$

Measurement shows that the pressure drop per unit length in the oil pipes is $350Pa m^{-1}$ in the 100m long pipe test. Therefore, the gel will flow. For the 3km long pipe, the total pressure drop will be: $\Delta p = 6bar$. Since the strength of the pipe is about $50bar$, it is also safe for pumping gel to 3Km in 10 hours.

In the hot oil pipe, the gel expands and flows into the special expansion pipe. When the production stops, the pipe cools, and the gel contracts. Does the gel flow out of the expansion pipe? Before answering this question, let us look at a ketchup bottle problem and calculate how much fluid comes out of the ketchup bottle.
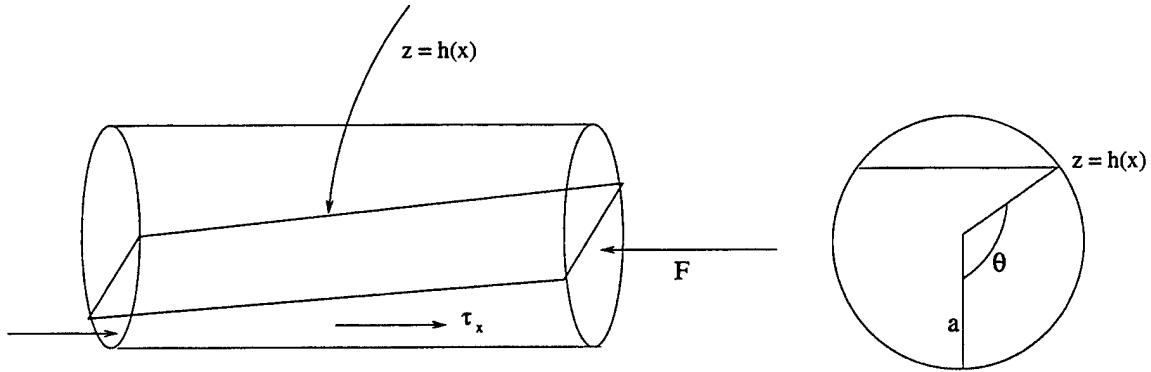
80

Figure 19: The flow of gel inside the expansion pipe is similar to that of ketchup in a bottle.

For an idealized cylindrical ketchup bottle, let x be the distance along the bottle, z be the height of the ketchup in the bottle $z = h(x)$, and A be the cross section of the ketchup in the bottle.

Then the pressure force is:

$$F = \int p \, dA, \tag{39}$$

where p is the hydrostatic pressure produced by the ketchup. Then the gradient of the pressure force along the x direction is:

$$\frac{dF}{dx} = \rho g \frac{dh}{dx} A. \tag{40}$$

In the steady state, the pressure gradient force is balanced by the friction between the ketchup and the wall of the ketchup bottle. The kepchup can flow if the friction stress is larger than the yield stress of the ketchup:

$$\rho g \frac{dh}{dx} A > \tau_* 2 a \theta, \tag{41}$$

where τ_* is the yield stress and $2a\theta$ express the wetted area per unit length, with the angle θ defined as in figure 19. The height of the wetted area can be expressed as $h = a(1 - \cos(\theta))$ and $A = a^2(\theta - \frac{1}{2}\sin(\theta))$. Substituting these two expression into the equation of the pressure gradient force, we get

$$\frac{d\theta}{dx} > \frac{\tau_*}{\rho g a^2} \frac{2\theta}{\sin(\theta)(\theta - \frac{1}{2}\sin(\theta))}. \tag{42}$$

Therefore, flow will continue until the inequality becomes an equality, giving the volume removed from a ketchup bottle:

$$V = a^3 \frac{\rho g a}{\tau_*} 1.69, \tag{43}$$

from a length $a \frac{\rho g a}{\tau_*} 0.85$. This calculation fits well with experiments.

Notes by Junjun Liu and Anshuman Roy

References

[1] M. T. Arigo, D. Rajagopalan, N. Shapley, and G. H. McKinley, "The sedimentation of a sphere through an elastic fluid. part 1. steady motion," Journal of Non-Newtonian Fluid Mechanics **60(2-3)**, 225 (1995).

[2] F. Yuran and M. D. Crochet, "High-order finite element methods for viscoelastic flows," Journal of Non-Newtonian Fluid Mechanics **57(2-3)**, 283 (1995).

[3] V. Tirtaadmadja, P. H. T. Uhlherr, and T. Sridhar, "Creeping motion of spheres in fluid m1," Journal of Non-Newtonian Fluid Mechanics **35(2-3)**, 327 (1990).

[4] O. G. Harlen, "The negative wake behind a sphere sedimenting through a viscoelastic fluid," Journal of Non-Newtonian Fluid Mechanics **108(1-3)**, 411 (2002).

[5] U. Cartalos and J. M. Piau, "Creeping flow regimes of low concentration polymer solutions in thick solvents through an orifice die," Journal of Non-Newtonian Fluid Mechanics **45(2)**, 231 (1992).

[6] B. Debbaut, J. M. Marchal, and M. J. Crochet, "Numerical-simulation of highly viscoelastic flows through an abrupt contraction," Journal of Non-Newtonian Fluid Mechanics **29(1-3)**, 119 (1988).

[7] P. J. Coates., R. C. Armstrong, and R. A. Brown, "Calculation of steady-state viscoelastic flow through axisymmetric contractions with the eeme formulation," Journal of Non-Newtonian Fluid Mechanics **108(1-3)**, 411 (1992).

[8] A. Kabla and G. Debregeas, "Local stress relaxation and shear banding in a dry foam under shear," Physical review letters **90(25)**, Art. No. 258303 (2003).

[9] A. Saint-Jalmes and D. J. Durian, "Vanishing elasticity for wet foams: Equivalence with emulsions and role of polydispersity," Journal of Rheology **43(6)**, 1411 (1999).

[10] A. N. Beris, J. A. Tsamopoulos, R. C. Armstrong, and R. A. Brown, "Creeping motion of a sphere through a bingham plastic," Journal of Fluid Mechanics **158**, 219 (1985).

[11] I. C. Walton and S. H. Bittleston, "The axial-flow of a bingham plastic in a narrow eccentric annulus," Journal of Fluid Mechanics **222**, 39 (1991).

[12] N. J. Balmforth and R. V. Craster, "A consistent thin-layer theory for bingham plastics," Journal of Non-Newtonian Fluid Mechanics **84**, 65 (1999).

[13] S. D. R. Wilson, "Sqeezing flow of a bingham material," Journal of Non-Newtonian Fluid Mechanics **47**, 211 (1993).

Lecture 8:
Instabilities

E. J. Hinch

A large class of fluids flows is never observed in practice even though they are exact solutions to the equations of motion. This is because these flows are unstable to small perturbations that are always present in the environment. Newtonian fluid flows support a vast array of instabilities and it is not surprising that many of these instabilities persist when the Newtonian fluid is replaced by a non-Newtonian fluid. Additionally, there are a number of instabilities which are found only in non-Newtonian fluids.

In this lecture we survey six non-Newtonian flow instabilities. The first, the spinline draw resonance, is an instability of a simple viscous fluid that can be modified by non-Newtonian effects. Sections 2–4 deal with instabilities which depend on non-Newtonian effects for their existence. In section 5, we examine the little understood phenomenon of turbulent drag reduction in a dilute suspension of polymers. Finally, section 6 deals the instabilities of a high speed elastic jet.

1   Spinline Draw Resonance

The manufacture of synthetic fabrics such as nylon and kevlar involves the drawing of polymer melts into thin fibers on a spinline. The geometry of a simple spinline is shown in figure 1. As the draw ratio—the ratio of the velocity of the spindle to the exit velocity of the fluid—is increased, the spun fiber becomes thinner, so the spinning of extremely thin fibers requires large draw ratios. If the draw ratio is increased beyond a critical value,
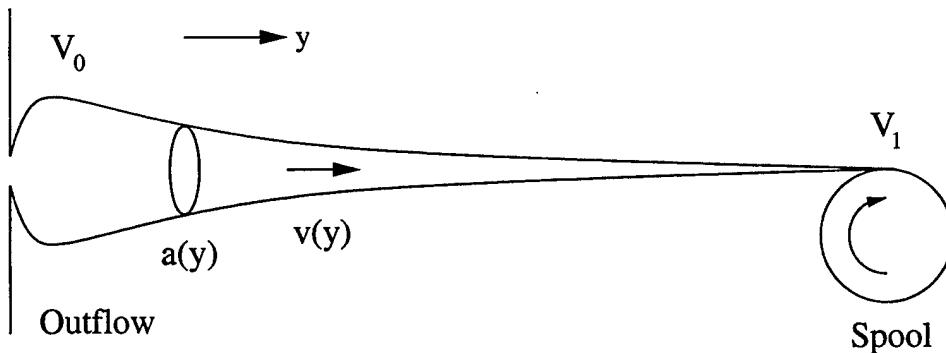

Figure 1: Geometry of a spinline.

the spinline draw resonance sets it. This instability, first described by Christensen [1] and Miller [2], is characterized by sustained periodic oscillations in the cross-sectional area and stress in the spinning polymer strand. While most fibers are spun from non-Newtonian fluids, the spinline draw resonance occurs even in purely Newtonian fluids. We will consider the simpler Newtonian instability first.

The geometry of a simple spinline is shown in figure 1. A steady state can be found by assuming that the cross-sectional area a and velocity v are functions of the streamwise coordinate y only. The continuity equation becomes a conservation equation for area,

$$\frac{\partial}{\partial y}(av) = 0, \tag{1}$$

while the momentum equation is a balance between the viscous force and the (constant) tension T:

$$\frac{T}{a} = \sigma_{yy} = 3\mu\frac{\partial v}{\partial y}. \tag{2}$$

The spinline has length L and boundary conditions

$$\begin{aligned} v(0) &= V_0 \\ v(L) &= V_1. \end{aligned} \tag{3}$$

The solution to equations (1)–(3) is

$$v(y) = V_0\,\mathrm{Dr}^{y/L} \tag{4}$$

$$a(y) = \frac{TL}{3\mu\ln\mathrm{Dr}}\,\mathrm{Dr}^{-y/L}, \tag{5}$$

where the $\mathrm{Dr} = V_1/V_0$ is the draw ratio.

This simple solution is unstable if

$$\mathrm{Dr} > 20.3.$$

Including additional processes can have a dramatic effect on this stability criterion. Inertia, cooling (which increases viscosity), and elastic effects can push the critical draw ratio to $\mathrm{Dr} \approx 10^3$. Surface tension and shear thinning, on the other hand, have a destabilizing influence and can lower the stability threshold to $\mathrm{Dr} \approx 3$. The exact stability threshold in an industrial application is set by a competition between these stabilizing and destabilizing effects.

To understand the mechanism for this instability, imagine a perturbation which causes a thinning of the thread near the spool (at $y = L$). Since the speed of the thread near the spool is fixed, the mass flux onto the spool must decrease, which decreases the total tension in the line. This low tension causes the velocity to decrease throughout the interior of the line. The speed of the thread at the outflow point (at $y = 0$) is similarly fixed, so the line must thicken near the outflow point to conserve mass (figure 2a). This thickened section will eventually propagate down the line to the spool. Once it reaches the spool, the increased mass flux onto the spool will increase the tension in the line, which causes the line to thin at the outflow point (figure 2b).
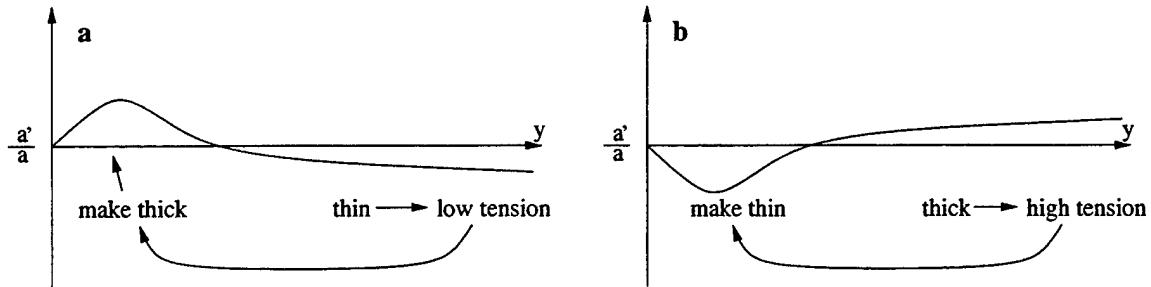
84

Figure 2: Mechanism for spinline draw resonance. (a) Thinning at the spool causes thickening at the outflow point. (b) Thickening at the spool causes thinning at the outflow point.
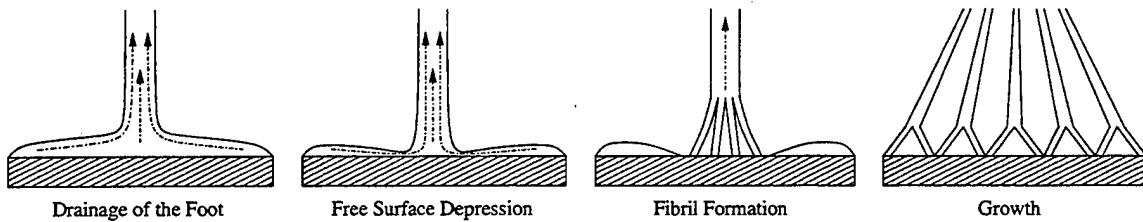

Figure 3: Development of the buckling instability, after Spiegelberg and McKinley's figure 10 [3]. The dash-dot curves represent streamlines.

The amplified feedback combined with the time delay caused by propagation feeds the instability. Above the critical draw ratio, the perturbation can grow to finite size. The system settles down into limit cycles, causing periodic oscillations in the thickness of the spun fiber.

2 Buckling Instability

The 'filament stretching device' is a common experimental device for measuring extensional properties of polymer solutions. In this device— which is described in detail in Lecture 2—a small cylinder of fluid is held between two rigid circular plates which are suddenly separated at a known rate. The extensional properties of the fluid are deduced by measuring the force on the plates as a function of the known strain. In order to obtain a consistent rheological measurement, the strain rate should be approximately constant throughout the extending fluid column. The buckling instability, which occurs on the plates of the filament stretching device, can seriously compromise the utility of the device unless measures are taken to prevent it. This instability was first observed by Spiegelberg and McKinley [3].

Figure 3 illustrates the evolution of the buckling instability. In the initial stages of the experiment, fluid is drained from the 'foot' of the column to feed the extending column. Eventually, the reservoir next to the column is depleted, at which time the foot begins to break up into fibrils. These fibrils migrate to the outer edge of the plate and can themselves develop secondary and tertiary instabilities.

The mechanism for this instability can be simply understood with the paradigm of

85

tension in curved streamlines. As the reservoir at the foot of the column is drained, the streamlines become increasingly more curved. Eventually, the tension in the streamlines is so great it overwhelms the adhesive force holding the column to the plate. This causes the center of the foot to detach from the plate, leaving the fibrils attached to the outer edge. The final configuration has nearly straight streamlines and thus forms a configuration which globally minimizes stored elastic energy. A mathematical investigation of the buckling instability can be found in Kumar and Graham [4].

Recent filament stretching devices have incorporated plates that contract as the filament is stretched. This modification stabilizes the foot of the column and allows consistent measurements of the extensional properties of the fluid [3].

3 Purely Elastic Instability of Curved Streamlines

A common feature of visco-elastic fluids is that instabilities can occur even in the absence of inertia. These are discussed at length in the review article [5]. Many of these occur in situations where the streamlines are curved. Streamlines in shear flow are under tension. If they are curved, this tension creates a *hoop stress*, which can lead to instabilities. The hoop stress acts in a direction opposite to the centrifugal effects, and so the resulting instabilities are clearly distinct from inertial effects.

The most famous example is the Taylor-Couette instability. In a Taylor-Couette device (two concentric rotating cylinders with fluid between them), an instability arises at sufficiently high flow rates. In a Newtonian fluid the instability occurs because of centrifugal effects at sufficiently high Taylor number (the Taylor number $4\frac{\Omega_1 R_1^2 - \Omega_2 R_2^2}{R_2^2 - R_1^2}\frac{\Omega_1 d^4}{\mu^2}$ is the ratio of centrifugal force to viscous force), but in a non-Newtonian fluid an instability can occur at negligible Taylor number (e.g., 10^{-8}). The mechanism creating the instability is the hoop stress generated by the flow which acts oppositely to the expected centrifugal force. This instability was first observed and analyzed by [6, 7, 8]. Further experimental analysis was done by [9] and by a number of other people. For a gap ratio of $\epsilon \equiv (R_2 - R_1)/R_2$, the instability appears to happen when $\epsilon^{1/2}\text{Wi} \approx 8$ (note that $\epsilon^{1/2}\text{Wi} = \sqrt{\text{DeWi}}$).

Numerics suggest that axisymmetric and non-axisymmetric modes can occur, and both are observed in experiments. The instability occurs as a supercritical Hopf bifurcation.

Other flows with curved streamlines can be found in Taylor-Dean, plate-plate or cone and plate geometries. This general class of instabilities has led to the concept of *elastic turbulence* [10], a complicated time-dependent flow with negligible Reynolds number.

4 Instability of coextrusion

Even in flow with straight streamlines instabilities can occur in inertialess flow with elasticity. In core-annular flow of two fluids down a pipe, differences in elastic properties can lead to instability at zero Reynolds number. We consider a pipe with flow in the $\hat{z}$ direction, with one fluid at $r < r_0$ and another at $r_0 < r < R$. At the interface between the two fluids $\sigma \cdot n$ must be continuous. If the elastic properties of the two fluids are different, there will be a discontinuity of the σ_{zz} component because the two fluids have different first normal
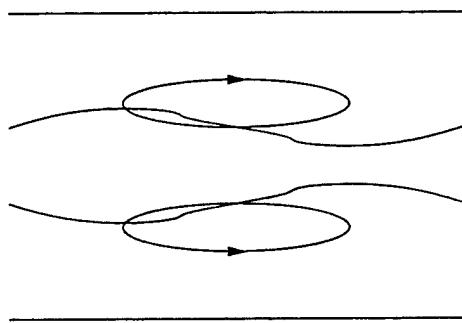
stress differences. However, since n has no component in the $\hat{z}$ component, $\sigma \cdot n$ remains continuous.
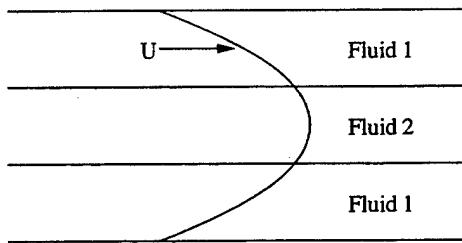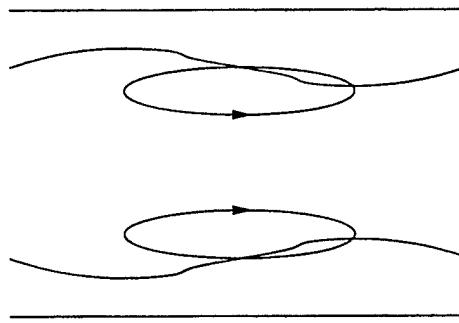

(a) The unperturbed basic flow.
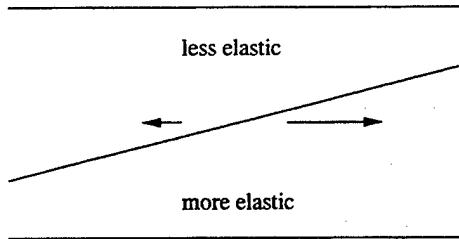
(b) Zooming in on a perturbed interface. Because the fluids have different elasticities, the interface moves to the right.

(c) A small core which is more elastic than the outer fluid. Since the core is small, the recirculation occurs in the outer fluid and enhances the perturbation to the interface

(d) A perturbation with a large core which is more elastic than the outer fluid. Here the recirculation occurs in the core and opposes the perturbation to the interface.

Figure 4: Mechanism of instability: The misalignment of the interface and the base flow creates a perturbation flow. Incompressibility forces the flow to recirculate. The recirculation can either enhance or oppose the perturbation to the interface.

When there is a perturbation to the interface, n is no longer purely radial, so a secondary flow across the interface must develop to keep $\sigma \cdot n$ continous. Physically the more elastic fluid is pulling the less elastic fluid across the curved interface. The secondary flow must have a recirculation by conservation of mass. If the inner fluid takes up a large fraction of the pipe, the recirculation will take place inside the inner fluid. If it takes up a small fraction of the pipe, the recirculation will take place inside the outer fluid. Thus the recirculation will either enhance or stabilize the perturbation, depending on which fluid is more elastic.

This instability was first computed in the longwave limit by [11], and the mechanism was explained by [12]. It was found that if the more elastic fluid occupied less than 32% of the volume the flow would be unstable to long waves, regardless of whether the more elastic fluid was in the core or the annulus.

This instability has been studied in detail in her PhD thesis by Wilson [13]. It was further found that when the discontinuity is smoothed out, the instability can be eliminated [14].

5 Turbulent Drag Reduction

It was noted during the second world war that the addition of a small amount of high molecular weight polymers to gasoline dramatically reduced the effective turbulent viscosity of the flow. Since then it has been shown that drag reduction of a turbulent flow is a general feature of dilute solutions of long polymers. Though it is potentially of extreme industrial value, a detailed explanation of this phenomenon remains elusive. However, a general framework for understanding this effect has emerged.

The action of the polymers is primarily to modify turbulent behavior near the walls. There, wall eddies are formed which transport momentum into the fluid interior which exerts a drag on the flow. The polymer's high resistance to extension makes these eddies wider and less frequent and, consequently, less efficient in transporting momentum away from the walls. Cross-stream fluctuations are suppressed relative to their Newtonian values while alongstream fluctuations are actually enhanced. The traditional explanation for turbulent drag reduction—that the addition of polymers reduces the turbulent intensity of the flow—cannot hold since the turbulent intensity in the bulk of the fluid is unaffected by the presence of polymers. (This explanation follows that in [15].) Figure 5 shows numerical simulations of the effect of polymers on the mean flow and near-wall velocity fluctuations.
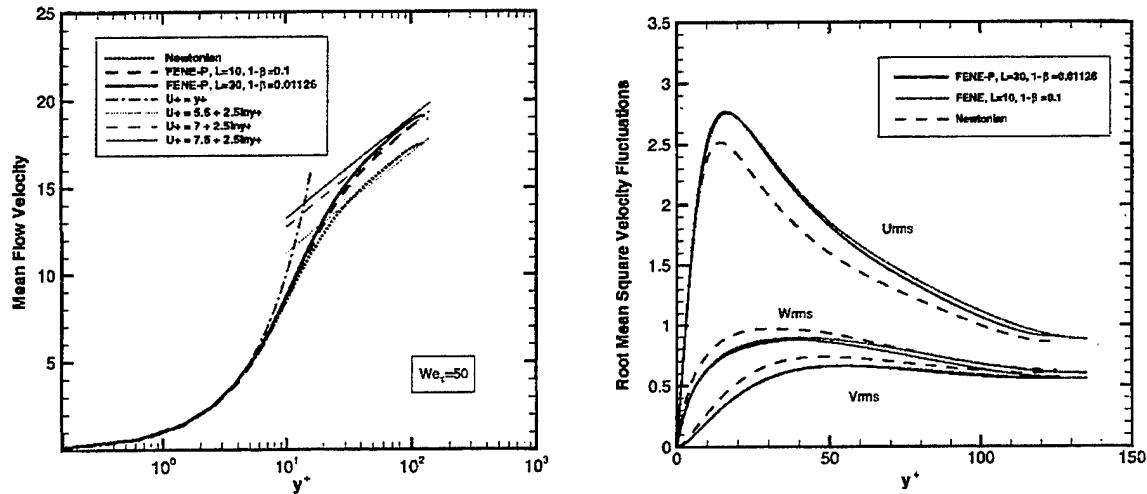

Figure 5: Numerical simulations of turbulence using Newtonian and two different FENE rheologies, from [15]. Left: Mean flow velocity in the log-layer near the wall. Right: RMS velocity fluctuations near the wall. The wall coordinate $y^+ \equiv \nu y / \nu_0$ where ν_0 is the viscosity of fluid and ν is the effictive viscosity.

88

6 Instability of a High Speed Elastic Jet

We now look at an instability which happens at high Reynolds number and high Weissenberg number. We consider a high speed submerged elastic jet [16, 17]. It is well known that a high extensional viscosity helps prevent an elastic jet from breaking up into spray, so elasticity helps stabilize that instability. However, other instabilities can arise. We follow [17] to consider the effect of elasticity using an Oldroyd-B model.

6.1 Governing Equations

The equations of motion are

$$\nabla \cdot U = 0$$

$$\rho \frac{DU}{Dt} = -\nabla P + \mu \nabla^2 U + G \nabla \cdot \mathsf{A}$$

$$\overset{\nabla}{\mathsf{A}} = -\frac{1}{\tau}(\mathsf{A} - \mathsf{I})$$

The basic state has flow in only the x direction. It is steady and rectilinear, so $\frac{D\mathsf{A}}{Dt} = 0$. We get

$$U = (U(y,z), 0, 0)$$

$$\mathsf{A} = \begin{bmatrix} 1 + 2\tau^2(U_y^2 + U_z^2) & \tau U_y & \tau U_z \\ \tau U_y & 1 & 0 \\ \tau U_z & 0 & 1 \end{bmatrix}.$$

We now make the assumption that the Reynolds number is large, $\frac{\rho UL}{\mu + G\tau} \gg 1$, and that the Weissenberg number is large as well, $\frac{U\tau}{L} \gg 1$.

6.2 Linearization

The problem is linearized with lower case letters denoting the perturbation quantities. We denote the components of the perturbed velocity by $u = (u, v, w)$. The linearized equations are

$$u_x + v_y + w_z = 0$$

$$\rho[u_t + Uu_x + vU_y + wU_z] = -p_x + G[a_{11,x} + a_{12,x} + a_{13,z}]$$

$$\rho[v_t + Uv_x] = -p_y + Ga_{12,x}$$

$$\rho[w_t + Uw_x] = -p_z + Ga_{13,x}$$

$$a_{11,t} + Ua_{11,x} + vA_{11,y} + wA_{11,t} = 2A_{11}u_x + 2a_{12}U_y + 2a_{13}U_z$$

$$a_{12,t} + Ua_{12,x} = A_{11}v_x$$

$$a_{13,t} + Ua_{13,x} = A_{11}w_x$$

and we seek a solution proportional to $e^{i\alpha(x-ct)}$ where the wavenumber α is real and the growth rate is αc.

89

We can make progress using different coordinates. We change to streamline displacements. We let η denote the y-displacement of a material particle from its equilibrium position and ζ denote its z-displacement. Then $\frac{D\eta}{Dt} = v$ to first order, but we can express $\frac{D\eta}{Dt}$ to first order as

$$\frac{D\eta}{Dt} = \eta_t + (U \cdot \nabla)\eta$$

$$= \eta_t + (U\frac{\partial}{\partial x})\eta$$

$$= i\alpha(U - c)\eta$$

so $v = i\alpha(U - c)\eta$. A similar analysis can be done for ζ. By incompressibility

$$u = -\eta U_y - \zeta U_z - (U - c)(\eta_y + \zeta_z)$$

and

$$a_{12} = i\alpha\eta A_{11}$$
$$a_{13} = i\alpha\zeta A_{11}$$
$$a_{11} = -2A_{11}(\eta_y + \zeta_z) - (\eta A_{11,y} + \zeta A_{11,z}).$$

We use these to arrive at

$$i\alpha[\rho(U - c)^2 - GA_{11}](\eta_y + \zeta_z) = i\alpha p$$
$$[\rho(U - c)^2 - GA_{11}]\alpha^2\eta = p_y$$
$$[\rho(U - c)^2 - GA_{11}]\alpha^2\zeta = p_z.$$

In planar flow we set $\zeta = 0$ and $\eta = -\phi/(U - c)$ to arrive at an elastic Rayleigh equation

$$\frac{d}{dy}\left([\rho(U - c)^2 - GA_{11}]\frac{d}{dy}\frac{\phi}{U - c}\right) = \alpha^2[\rho(U - c)^2 - GA_{11}]\frac{\phi}{U - c}.$$

This can be expressed in a self-adjoint form, giving a semi-circle theorem [18] which states that the complex wave speed c must lie within a circle centered on $(U_{\max} + U_{\min})/2$ with radius $(U_{\max} - U_{\min})/2$.

We assume that the time-scale of the instability is much less than vorticity diffusion, stress relaxation and shear wave propogation.

6.3 Two-dimensional jet

We consider a two dimensional jet where

$$U(y) = \begin{cases} U_0\left(1 - \frac{y^2}{b^2}\right) & |y| \leq b \\ 0 & |y| > b \end{cases}$$

$$GA_{11} = \begin{cases} \frac{8G\tau^2 U_0^2 y^2}{b^4} & |y| \leq b \\ 0 & |y| > b \end{cases}$$
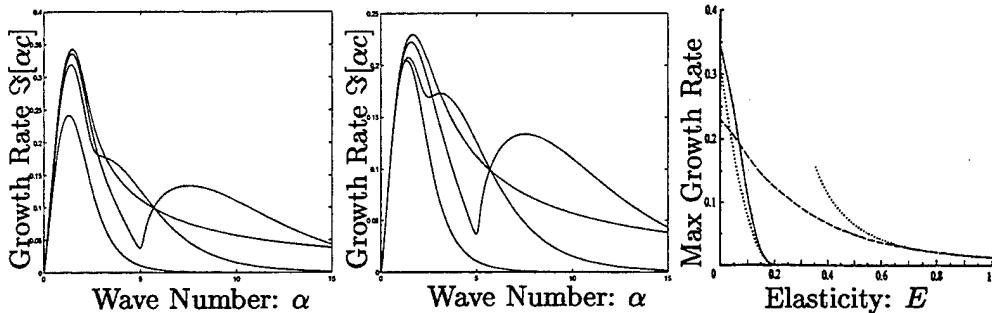
90

We define the elasticity number

$$E = \frac{GA_{11}}{\rho U^2} = \frac{G\tau^2}{\rho b^2}$$

which, remarkably, is independent of the flow rate. Outside the jet we have a potential flow

$$p = e^{\mp \alpha y}$$

$$\eta = \mp \frac{e^{\mp \alpha y}}{\alpha c^2}$$

We look for sinuous and varicose modes to see the effect of the elasticity parameter E on the growth rates.

(a) The growth rate of the instability as a function of k for sinuous disturbances with E equaling 0, 0.0025, 0.01 and 0.05. The highest peak occurs for $E = 0$, and the peak decreases as E increases.	(b) The growth rate of the instability as a function of k for varicose disturbances with E equaling 0, 0.0025, 0.01 and 0.05. The highest peak occurs for $E = 0$, and the peak decreases as E increases.	(c) The maximum growth rate of the 2D jet as a function of the elsaticity for the sinuous mode (continuous curve) and the varicose mode (dashed curve). The dotted curves are asymptotic results for long waves.

Figure 6: Growth rates — Elasticity stabilizes both instabilities. For small (nonzero) E, there appears to be an elastic wave mode at large wavenumber.

As the elasticity approaches 0, there is an unstable mode with moderate growth rate at large α. As E decreases further, the value of α increases. This instability is localized close to the interface, and depends on the discontinuity in shear rates. As the discontinuity in shear rates leads to a jump in normal stresses, this may be similar to the coextrusion instability in origin.

6.4 Conclusions

The elasticity has a stabilizing effect. For a two-dimensional jet, the sinuous mode is no longer unstable when $E \geq 0.2$. The varicose mode remains unstable as E increases, but the maximum growth rate decays to 0.

For an axisymmetric jet, it was shown by Batchelor and Gill [19] that the Newtonian case is stable to varicose perturbations. Adding a small amount of elasticity allows the emergence of an unstable mode for large α. However, as the elasticity increases, this unstable mode is damped and stabilized at $E = 0.228$. The sinuous mode is stabilized at $E = 0.3756$.

Notes by Joel C. Miller and Christopher L. Wolfe

References

[1] R. E. Christensen, "Extrusion coating of polypropylene," Soc. of Pet. Engineers J. **18**, 751 (1962).

[2] J. C. Miller, "Swelling behaviour in extrusion," Soc. of Pet. Engineers Trans. **3**, 134 (1963).

[3] S. Spiegelberg and G. McKinley, "Stress relaxation and elastic decohesion of viscoelastic polymer solutions in extensional flow," J. Non-Newt. Fluid Mech. **67**, 49 (1996).

[4] K. Kumar and M. Graham, "Buckling instabilities in models of viscoelastic free surface flows," J. Non-Newt. Fluid Mech. **89**, 337 (2000).

[5] E. S. G. Shaqfeh, "Purely elastic instabilities in viscometric flows," Annual Review of Fluid Mechanics **31**, 129 (1996).

[6] S. J. Muller, R. G. Larson, and E. S. G. Shaqfeh, "A purely elastic transition in taylor-couette flow," Rheologica Acta **28**, 499 (1989).

[7] R. G. Larson, E. S. G. Shaqfeh, and S. J. Muller, "The effect of fluid rheology on the elastic taylor-couette instability," Journal of Non-Newtonian Fluid Mechanics **51**, 195 (1994).

[8] E. S. G. Shaqfeh, S. J. Muller, and R. G. Larson, "The effects of gap width and dilute solutions properties on the viscoelastic instability," Journal of Fluid Mechanics **235**, 285 (1992).

[9] A. Groisman and V. Steinberg, "Mechanism of elastic instability in taylor-couette flow in polymer solutions: experiment," Physics of Fluids **10**, 2451 (1998).

[10] A. Groisman and V. Steinberg, "Elastic turbulence in a polymer solution flow," Nature **405**, 53 (2000).

[11] K. P. Chen, "Interfacial instability due to elastic stratification in concentric coextrusion of two viscoelastic fluids," Journal of Non-Newtonian Fluid Mechanics **40**, 155 (1991).

[12] E. J. Hinch, O. J. Harris, and J. M. Rallison, "The instability mechanism for two elastic liquids being co-extruded," Journal of Non-Newtonian Fluid Mechanics **43**, 311 (1992).

[13] H. J. Wilson, Ph.D. thesis, Cambridge University, Cambridge, United Kingdom, 1998.

[14] H. J. Wilson and J. M. Rallison, "Instability of channel flow of a shear-thinning white metzner fluid," Journal of Non-Newtonian Fluid Mechanics **87**, 75 (1999).

[15] C. D. Dimitropoulos, R. Sureshhumar, and A. N. Beris, "Direct numerical simulation of viscoelastic turbulent channel flow exhibiting drag reduction: effect of the variation of rheological parameters," J. Non-Newt. Fluid Mech. **79**, 433 (1998).

[16] J. Azaiez and G. M. Homsy, "Linear stability of free shear flow of viscoelastic liquiids," Journal of Fluid Mechanics **268**, 37 (1994).

[17] J. M. Rallison and E. J. Hinch, "Instability of a high-speed submerged elastic jet," Journal of Fluid Mechanics **288**, 311 (1995).

[18] L. N. Howard, "Note on a paper by J. W. Miles," Journal of Fluid Mechanics **10**, 509 (1961).

[19] G. K. Batchelor and A. E. Gill, "Analysis of the stability of axisymmetric jets," Journal of Fluid Mechanics **14**, 529 (1962).

Lecture 9: Strong Flows

E. J. Hinch

1 Birefringent Strand

1.1 Flow of a FENE fluid past a sphere

In the lecture on stress relaxation, we talked about how an Oldroyd-B fluid deforms as it flows past a rigid sphere. We also discussed the two main shortcomings of the Oldroyd-B model as the Deborah number increases, namely the failure to predict the sudden increase in pressure drop after an initial decrease and long wakes. The infinite extensibility of the Oldroyd-B model renders it useless at high Deborah numbers. However, if the Oldroyd-B model is modified into its finitely extensible counterpart also called the FENE (Finitely Extensible Nonlinear Elastic) model, then strong flow phenomena can be successfully predicted.

Figure 1 has been taken from a finite difference calculation [1] for a sphere falling down a cylinder of FENE fluid. Notice the increase in drag force after an initial decrease. The initial decrease in drag until De = 1.3 is captured well by the Oldroyd-B model. Such a decrease occurs due to the elasticity of the microstructure lending itself to the flow and deforming along with it. However, at higher Deborah numbers, the Olroyd-B continues to deform to infinite lengths. The finite extensibility in the FENE model limits the deformation of the microstructure, leading to an extensional viscosity that adds to the drag experienced by the flow. Figure 2 is a plot of the drag force felt by the falling sphere with increasing Wi [2].
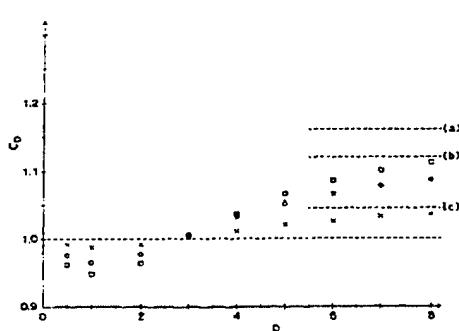

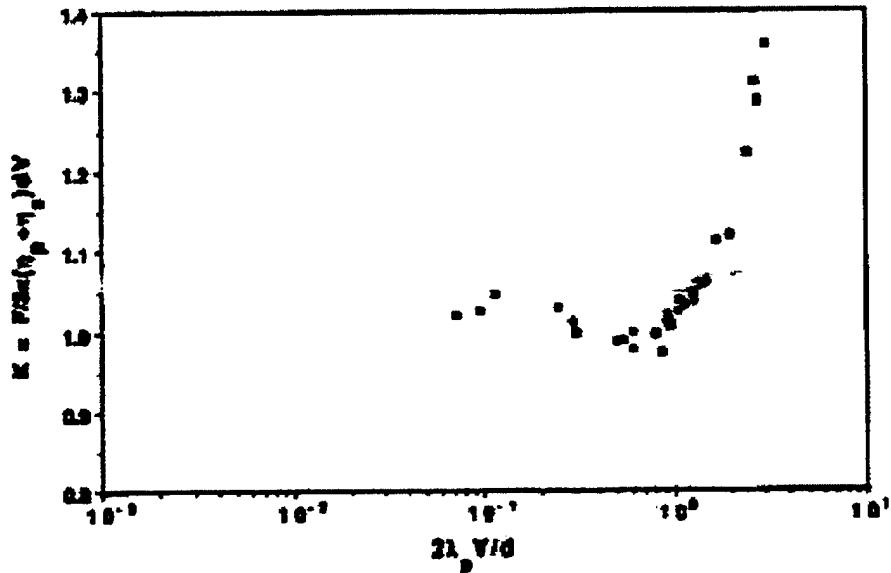Figure 1: Drag on a sphere with FENE fluid flowing past it plotted against De

94

Figure 2: Drag on a sphere in a viscoelastic fluid plotted against Wi, measured experimentally.

It is evident that the Oldroyd-B model does well at small Wi, but fails beyond Wi greater than 1.

FENE calculations also successfully predict the long wake seen in flow past a rigid sphere. The longer-than-Newtonian wake arises because the fluid takes a finite amount of time to relax (relaxation time). The material in the wake is highly stretched due to the strong extensional flow there. Consequently, a large extensional viscosity results that causes increased drag on the sphere above the Newtonian value. It is possible to see these effects by passing polarized light through the medium. As could be predicted from figure 3, very high birefringence is observed in the downstream wake formed by the sphere, especially in the regions close to the center streamline that emanates from the stagnation point. Henceforth, we will refer to this region as the 'birefringent strand', and infer that large stresses occur there.

1.2 Cross-slot flow of a viscoelastic fluid

Figure 4 shows the flow of fluid from two channels that are sucked out by two other channels perpendicular to the inlet channels. The velocity profiles at different sections of the exit channel are shown in figures 5 and 7. The flow is simple extensional by design, and will therefore stretch out the microstructure, leading to a birefringent strand. A careful look at the development of the flow profile gives us some confidence about the effect of the birefringent strand on the flow. It is clear that only after a time of the order of the microstructure relaxation time has elapsed, will the parabolic profile develop.
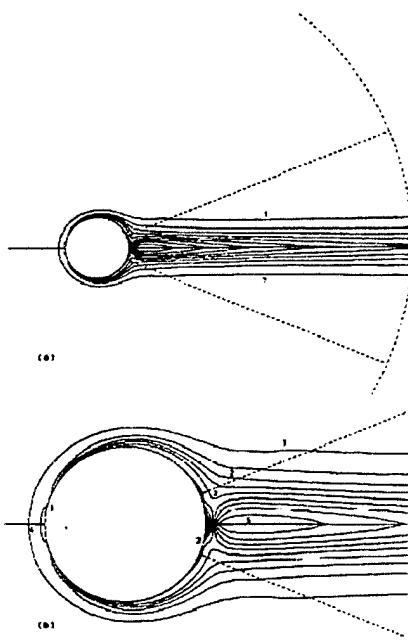
95

Figure 3: Long wake seen in flow of a FENE fluid past a rigid sphere. The contours are of constant $tr(A)$ [1].
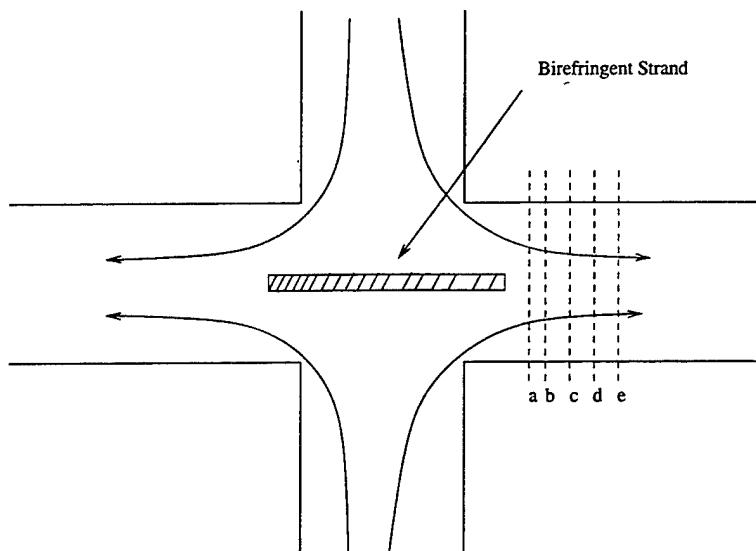

Figure 4: A schematic figure showing the cross-slot flow. The profiles at different positions in the exit channel (a, b, c, d and e) are plotted in the following figure
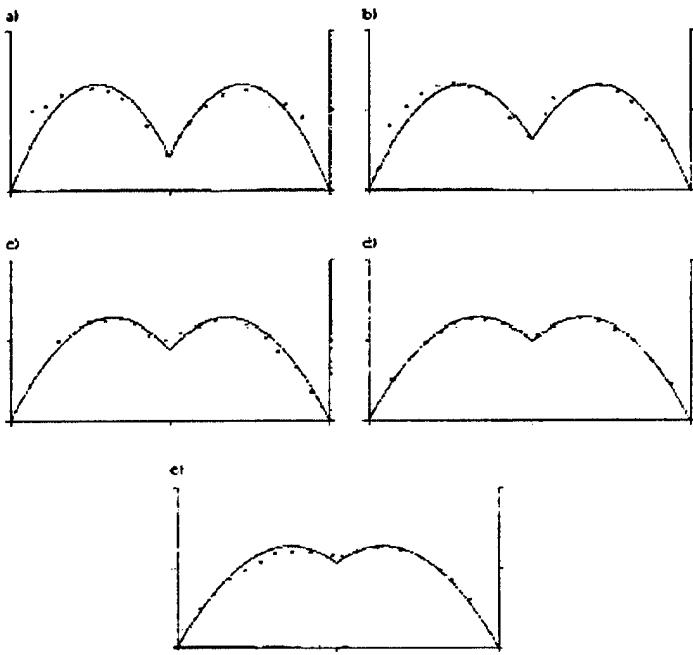
Figure 5: Development of the velocity profile in the exit channel.

This suggests that it is possible to view the birefringent strand in terms of an elastic boundary layer if one views the fluid within this strand as Newtonian but with a very large viscosity equal to the extensional viscosity. In this formulation, the fluid surrounding the strand is imagined to have a constant Newtonian viscosity and the strand is a thin layer of fluid with much higher viscosity.

1.2.1 Analysis of a birefringent strand in an exit channel

The velocity profile in the exit channel is given by

$$u(x,y) = U(x) \frac{a-y}{a} + (Q - U(x)a) \frac{3y(a-y)}{a^2}. \tag{1}$$

Force balance on the birefringent strand results in:

$$\left[\mu \frac{\partial u}{\partial y} \right]_{0-}^{0+} + \frac{\partial}{\partial x} \left(\delta \, \mu_{ext} \frac{\partial U(x)}{\partial x} \right) = 0 \tag{2}$$

where, μ_{ext} is the extensional viscosity in the birefringent strand. From the velocity profile, we have:

$$\left[\mu \frac{\partial u}{\partial y} \right]_{0-}^{0+} = 2\mu \left[-\frac{U(x)}{a} + (Q - U(x)a) \frac{3}{a^2} \right] \tag{3}$$
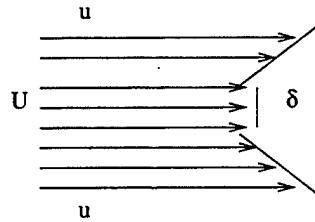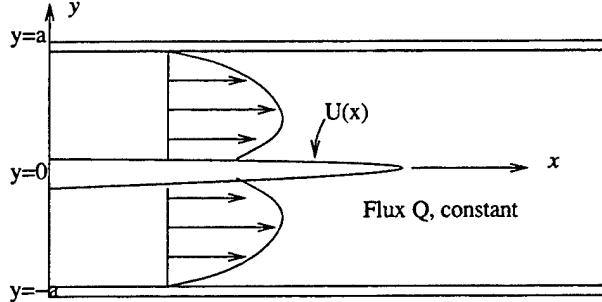
Solving, we obtain

Figure 6: Flow in the exit channel with a birefringent strand

$$U(x) = \frac{3Q}{2a}(1 - e^{-\sqrt{\frac{8\mu}{\delta\mu_{ext}a}}x})$$ (4)

Thus, the velocity along the center streamline starting at the stagnation point increases very rapidly to the steady Newtonian value. It is also possible to calculate the thickness of the thin birefringent strand (a good exercise for the keen reader). Interesting predictions about the thickness of the birefringent strand for a given flow rate can be made using a FENE dumbbell model for the microstructure. Harlen, Hinch and Rallison [3] performed such calculations and realized that, as the flow rate increased, there must be a transition from thin strands to much thicker ones that would look like pipes. This is shown in figure 7.

1.3 Flow of a FENE fluid past a bubble

Another interesting effect of a stagnation point flow is that of a Non-Newtonian fluid past a bubble. Since the bubble is deformable, unlike a rigid sphere, a cusp forms at the stagnation point. Rallison and Malaga (2003). have worked out the calculations for such a flow. They concluded that the curvature at the cusp becomes sharper with increasing extensibility of the microstructure, as shown by the cartoon in figure 8. By definition, extensibility is ratio of the fully stretched length of the microstructure to its equilibrium size. Note that the curvature increases with stretching of the microstructure, which ultimately leads to elimination of the stagnation point—a nonlinear feedback of the microstructure on the flow.
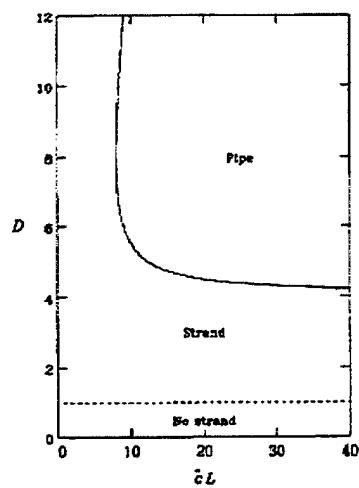
Figure 7: A plot of Deborah number vs concentration of polymer molecules showing the different states of the birefringent strand seen in the numerical calculation.

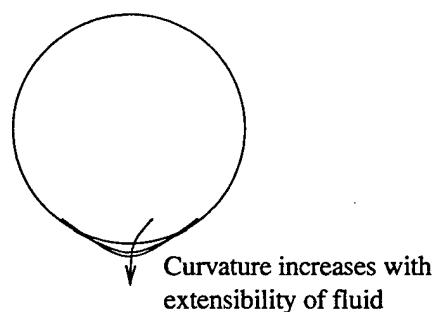Curvature increases with extensibility of fluid
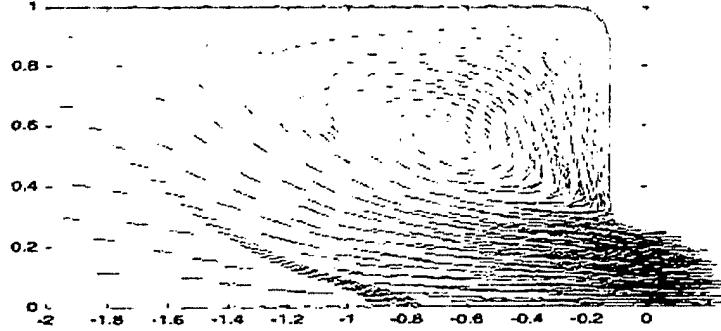
Figure 8: A cartoon of the bubble in a viscoelastic fluid.

Figure 9: Numerical simulation of a contraction flow of a FENE fluid [4]. Non-Newtonian fluids generate corner vortices that are much larger those apparent in Newtonian fluids.

2 Wine glass model of contraction flow

In lecture 3 we considered anisotropic converging channel flow of a suspension of rigid rods. Here we turn our attention to a strong contraction flow of a general anisotropic material. Experiments and numerical simulations have shown that these flows develop large upstream vortices that have a lengthscale greater than a corner vortex observed in a Newtonian fluid. Figure 9 shows a simulation of flow into a contraction [4] where the large corner vortex is apparent. Figure 10 is an image of a similar contraction flow from experiments [5]. The darker regions outside of the inner flow (white region) are the corner vortices.

We consider the wine glass model of contraction flow, which is a toy model [4]. The geometry is shown in figure 11. Initially there is no deformation of the microstructure in the region upstream of the "wine glass." In this upstream region the relaxation rate of the microstructure is greater than the strain rate. As we near the contraction, though, the strain rate increases and will become comparable to the relaxation rate. At this transition, material located in the region $r < r_D$ begins to stretch, where r is the distance from the centerline of the pipe (figure 11). Once the fluid passes into the "bowl" of the wine glass, the polymers continue to stretch as both the flow and strain rate increase. Eventually the polymers become fully stretched at a distance r_L from the centerline. At this point the fluid enters the "stem" of the wine glass and travels towards the contraction which has a radius r_C.

We can now make some progress on this problem using scaling arguments. Within the bowl we can approximate the flow as a point sink flow given by

$$u = \frac{Q}{2\pi r^2}. \tag{5}$$

The point sink flow approximation is valid within the bowl and stem regions. Stretching of the microstructure begins to become important when the relaxation rate is of the same order of magnitude as the strain rate, or in other words, the Weissenberg number is $O(1)$. At this point

$$\frac{1}{\tau} \sim E \sim \frac{\partial u}{\partial r} \tag{6}$$

100
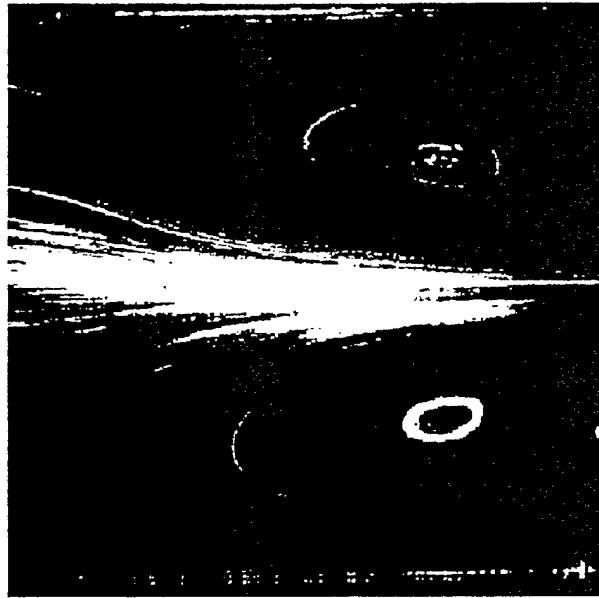
Figure 10: Image of contraction flow from experiments [5]. The white region indicates strong extension flow (the "stem" in the wine glass model), and the corner vortices are the darker regions outside it.

Figure 11: Geometry of the wine glass model of contraction flow [4]. This figure shows half of a pipe with a 4:1 contraction. Flow is into the contraction. The microstructure begins to be stretched once it enters the bowl, and becomes fully stretched when it enters the stem. The maximum radius of the bowl is R_D, the maximum radius of the stem is R_L and the radius of the contraction is R_C.

101

and, from differentiating (5), we determine that stretching begins to be important at

$$r_D \sim (Q\tau)^{1/3}. \tag{7}$$
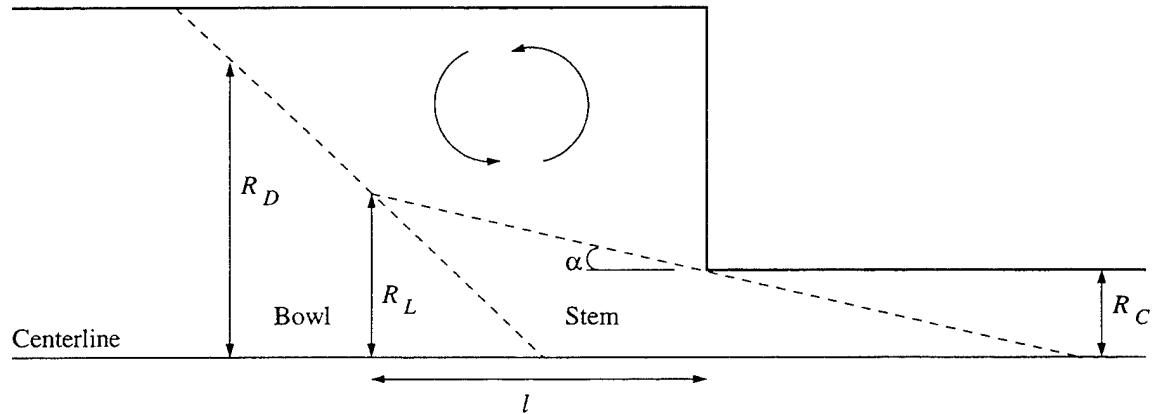
Within the bowl, the strain rate becomes large and dominates the relaxation term. In this region then, the microstructure stretches like fluid line elements. Line element stretching is proportional to the velocity of the flow and since A is the tensor describing the microstructure, we find

$$A \propto u^2 \propto r^{-4}, \tag{8}$$

where we have used the relationship between u and r for a point sink flow.

Upon entering the stem of the wine glass, the microstructure has become fully stretched. In this finite extension regime $A \simeq L^2$. Now assuming an individual polymer begins stretching at a distance r_E from the centerline, A at this point is simply equal to 1. Then using (8) we can consider the two limits of undeformed microstructure ($A = 1$) and fully stretched microstructure ($A = L^2$) to show

$$1 \sim \frac{1}{r_E^4}, \qquad L^2 \sim \frac{1}{r_L^4}, \tag{9}$$

which gives the result that the microstructure becomes fully stretched at

$$r_L = \frac{r_E}{L^{1/2}}. \tag{10}$$

The large vortices that we are interested in viewing occur only if r_E falls within the region where the strain rate is larger than the relaxation rate. Or in other words, the polymers can only become fully stretched if $r_E = L^{1/2} r_L < r_D$. Note also that this model makes sense only if r_D lies within the upstream pipe. Now applying this constraint and noting that the Deborah number for this flow is given by

$$\mathrm{De} = \frac{Q\tau}{r_C}, \tag{11}$$

we find that the microstructure can become fully stretched only if we exceed a critical Deborah number,

$$\mathrm{De} > \mathrm{De_{crit.}} = L^{3/2}. \tag{12}$$

In determining $\mathrm{De_{crit.}}$ we have assumed that $r_L \simeq r_C$, which is true if we assume the cone angle α is small.

Once the material is fully stretched we have an extensional viscosity μ_{ext} that is much larger than the shear viscosity, μ_{shear}, and the momentum balance is between the high extensional viscosity in the stem and the high shear in the recirculating vortices. This balance can be written as

$$\mu_{\mathrm{ext}} \frac{\partial^2 u}{\partial r^2} \simeq \mu_{\mathrm{shear}} \frac{1}{r^2} \frac{\partial^2 u}{\partial \theta^2}. \tag{13}$$

As in the problem we discussed in section 6 from Lecture 3, for converging channel flow, the dependence in the θ direction has a sinusoidal character, where the θ direction is in the
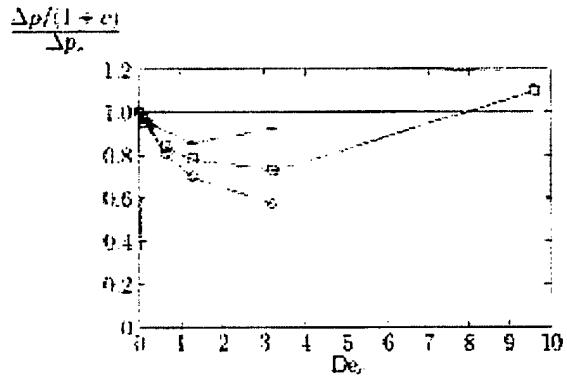
$$\frac{\Delta p/(1+c)}{\Delta p_r}$$

Figure 12: Numerical simulation of pressure drop as a function of Deborah number for an Oldroyd B fluid (Szabo *et al.* 1997). As the Deborah number increases, the microstructure is stretched and the pressure drop decreases. There is some evidence for increasing pressure drop at high De.

direction of the cone angle α. Assuming a separable solution for equation (13), we find that the r-independent solution has a sinusoidal dependence with an argument of $\left(\sqrt{\frac{\mu_{\text{ext}}}{\mu_{\text{shear}}}}\theta\right)$. Therefore the angle of the stem is given by

$$\alpha \sim \sqrt{\frac{\mu_{\text{shear}}}{\mu_{\text{ext}}}}, \tag{14}$$

from which we can see that as long as $\mu_{\text{ext}} \gg \mu_{\text{shear}}$, our assumption of small cone angle is valid. The length of the cone l can be found using trigonometry, $\tan \alpha = (r_L - r_C)/l$, which with the small angle approximation gives

$$l = \frac{r_L - r_C}{\alpha} = r_C \left(\text{De}^{\frac{1}{3}} L^{-\frac{1}{2}} - 1\right)\sqrt{\frac{G\tau L^2}{\mu}}. \tag{15}$$

Here we have used the fact that $\mu_{\text{ext}} \sim G\tau L^2$ and our previous relationships for r_L and De. It is easy to see from our scaling arguments for the angle α that these vortices are much larger than the corner vortices we would expect to see in a Newtonian fluid. Numerical calculations [4] have shown that these scaling arguments are within 20% of the full numerical calculations. The authors also include numerical models of how the pressure drop varies with increasing Deborah number (figure 12) for an Oldroyd B fluid. As the fluid enters the wine glass and the microstructure is stretched, the pressure drop decreases (cf. turbulent drag reduction). There is also some evidence that at very large Deborah number the pressure drop begins to increase again.

3   Corner singularity

The geometry for flow around a corner singularity is shown in figure 13. For very fast flows around a sharp corner (we will consider a 270° corner), $\nabla u \gg 1/\tau$ or De $\gg 1$. In this
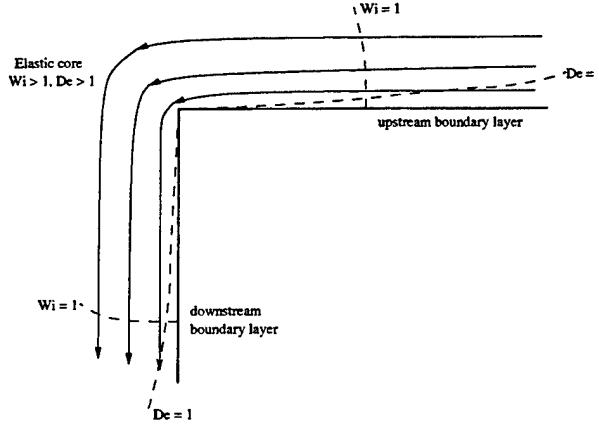
Figure 13: Geometry of flow around a corner singularity. Near the corner, the microstructure is strongly stretched. This region is known as the elastic core. Both upstream and downstream of the corner there will be boundary layers where viscous effects become important (the Deborah number becomes small). Far from the corner the shear is small (the Weissenberg number is small).

case the relaxation of the microstructure is negligible and only the stretching is important. There will be both upstream and downstream boundary layers where the Deborah number is small and viscous effects are imporant. Also, far from the corner, the shear is small so the Weissenberg number becomes small. The transition between these regions are marked with a dashed line in figure 13. The equation for the evolution of the microstructure in the elastic core then becomes

$$\frac{DA}{Dt} = A \cdot \nabla \mathbf{u} + (\nabla \mathbf{u})^T \cdot A \tag{16}$$

where A deforms with the flow. As we discussed briefly in the previous section and in earlier lectures, the microstructure deforms like fluid line elements. This can be written more formally as

$$\frac{d}{dt}\delta l = \delta l \cdot \nabla \mathbf{u}. \tag{17}$$

If we then consider a steady flow, the fact that A will deform like fluid line elements suggests that we look for a solution of the form

$$A = f(\psi)\mathbf{u}\mathbf{u}. \tag{18}$$

Here f is an unknown function which accounts for the fact that the deformation depends on the choice of streamline.

Now when we analyze the momentum equation for these flows, even though the Deborah number is large, the inertial terms are still negligible. Therefore the flow is still Stokes flow except that the stretching of the microstructure GA balances the pressure gradient rather than the viscous forces balancing pressure. Then applying our guess for A and noting that $f(\psi)$ is a scalar function, we can write

$$0 = -\nabla p + G f^{\frac{1}{2}}\mathbf{u} \cdot \nabla f^{\frac{1}{2}}\mathbf{u} \tag{19}$$

104

where we have used incompressibility, $\nabla \cdot \mathbf{u} = 0$. The reason for splitting f in this fashion is that now equation (19) is suggestive of a steady Euler's equation in $f^{1/2}\mathbf{u}$. Indeed, we can write

$$-\nabla p + \frac{1}{2}G\nabla\left(f|\mathbf{u}|^2\right) = 0 \tag{20}$$

and by integrating we get an anti-Bernoulli equation where

$$p - \frac{1}{2}Gf|\mathbf{u}|^2 = \text{const.} \tag{21}$$

along streamlines. This is termed an anti-Bernoulli equation because rather than pressure decreasing with increasing velocity, pressure will increase with increasing velocity. (Theoretically you would need to flip the wings of an airplane upside down to fly in a non-Newtonian fluid!) We can now seek a potential flow solution to (21), assuming the flow is irrotational, and has the form

$$f^{1/2}\mathbf{u} = \nabla\phi. \tag{22}$$

The solution to potential flow around an angle α [6] is

$$\phi = Cr^{\pi/\alpha}\cos\left(\frac{\pi\theta}{\alpha}\right). \tag{23}$$

For our 270° corner with a properly normalized velocity, this gives

$$\phi = \frac{3}{2}r^{\frac{2}{3}}\cos\left(\frac{2}{3}\theta\right). \tag{24}$$

Note that this solution can be obtained by finding the complex potential solution for flow in a half plane and using conformal mapping to transform the flat plate to the desired angle. This now represents the solution for our flow around a corner neglecting the boundary layer effects (i.e. potential flow only satisfies conditions of no normal flow at the boundaries, not the no-slip condition). This also shows that $u \propto \phi/r \propto r^{-1/3}$ and, since $\sigma \propto A \propto u^2$, we find that

$$\sigma \propto r^{-\frac{2}{3}}. \tag{25}$$

At this point, using the definition of the stream function we can write

$$f^{\frac{1}{2}}\mathbf{u} = f^{\frac{1}{2}}(\psi)\nabla \times (0,0,\psi) = f^{\frac{1}{2}}\nabla \times \left(0,0,\frac{3}{2}r^{\frac{2}{3}}\sin\frac{2}{3}\theta\right). \tag{26}$$

Finally, using the fact that f is also a function of ψ, we can write

$$\psi = g\left(r^{\frac{2}{3}}\sin\frac{3}{2}\theta\right), \tag{27}$$

where g is an unknown function. Rather than solving for g, though, we will apply matching between the inner solution and the boundary layer solution.

Before considering the flow in the boundary layer, we first analyze how the microstructure deforms with the fluid. Then as before, we can say that the fluid deforms like a line

element, but also in order to conserve mass, the fluid is squeezed in the direction perpendicular to the stretching,

$$\delta l \propto u \qquad \delta l_\perp \propto \frac{1}{u}. \tag{28}$$

Following the work by Renardy (1994) we can then seek a solution of A in terms of the streamwise coordinates,

$$A = \lambda \mathbf{u}\mathbf{u} + \mu(\mathbf{u}\mathbf{v} + \mathbf{v}\mathbf{u}) + \nu \mathbf{v}\mathbf{v}, \tag{29}$$

where

$$\mathbf{u} = (u, v) \qquad \mathbf{v} = \left(-\frac{v}{u^2 + v^2}, \frac{u}{u^2 + v^2} \right). \tag{30}$$

Note that $\mathbf{u} \cdot \mathbf{v} = 0$ and $|\mathbf{v}| = 1/|\mathbf{u}|$. We then substitute this construction into the upper convective derivative of A assuming that the flow is steady. We now include the effects of relaxation because they will be important in the boundary layer. After an excursion through the land of linear algebra, we find three equations for the unknowns λ, μ and ν,

$$\mathbf{u} \cdot \nabla \lambda = 2\frac{\dot{\gamma}}{u^2}\mu - \frac{1}{\tau}\left(\lambda - \frac{1}{u^2} \right), \tag{31}$$

$$\mathbf{u} \cdot \nabla \mu = \frac{\dot{\gamma}}{u^2}\nu - \frac{1}{\tau}\mu, \tag{32}$$

$$\mathbf{u} \cdot \nabla \nu = -\frac{1}{\tau}\left(\nu - u^2 \right), \tag{33}$$

where the last equation is decoupled from the first two. It is helpful to note that

$$\dot{\gamma} = \mathbf{v} \cdot \left(\nabla \mathbf{u} + \nabla \mathbf{u}^T \right) \cdot \mathbf{u} = -u^2 \nabla \cdot \mathbf{v} \tag{34}$$

from which one can see that the terms that contain $\dot{\gamma}$ in (31) and (32) come from the $(A \cdot \nabla \mathbf{u} + (\nabla \mathbf{u})^T \cdot A)$ terms in the upper convective derivative. For slow flows, the inertia-like terms on the LHS are small, so the balance of the remaining terms gives,

$$\nu \sim u^2 \qquad \mu \sim \gamma \tau \qquad \lambda \sim \frac{1}{u^2} + \frac{2\gamma^2\tau^2}{u^2}. \tag{35}$$

For fast flows, the RHS of (31–33) are approximately zero and therefore λ, μ and ν are constants.

In the boundary layer we can seek a similarity solution in streamline coordinates for the four unknown functions ψ, λ, μ and ν. Setting up this similarity solution is discussed in depth in Rallison and Hinch, 2004. At the conclusion of the analysis, the similarity function for ψ as we approach the outer limit of the boundary layer tends to $\xi^{7/3}$ where ξ is the non-dimensional parameter in the boundary layer. By matching the boundary layer solution to the inner elastic core, we find

$$\psi = Cr^{\frac{14}{9}} \sin^{\frac{7}{3}} \left(\frac{2}{3}\theta \right), \tag{36}$$

where C is an arbitrary constant. Finite element simulations [7] have shown excellent agreement with these results verifying that $u \sim r^{5/9}$ and $\sigma \sim r^{-2/3}$ as shown in figure 14.
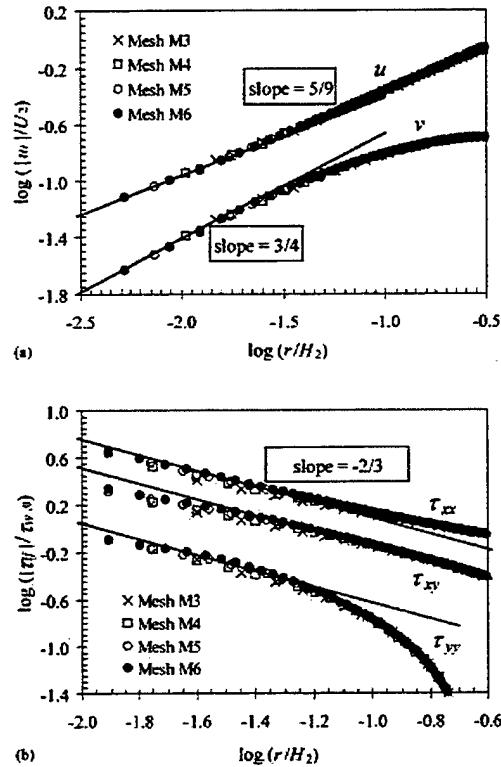
106

Figure 14: Finite element simulations of stress singularity at a sharp (270°) corner [7]. The upper plot shows velocity as a function of distance from the corner in the elastic core while the lower plot shows stress as a function of distance from the corner in the elastic core. The lines are drawn for reference to the power law relationships.
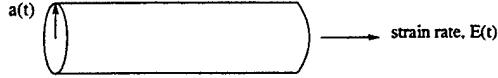
107

Figure 15: A filament being stretched.

4 Elastic stress saturation in a stretching filament

We will now look at the problem of rapid stretching of a filament of an elastic liquid, with a large surface tension. The problem is motivated from the fiber spinning process, in which fibers are drawn rapidly from droplets of viscoelastic liquids.

Let $a(t)$ be the radius of the filament at time t (see figure 15). Also, let the strain rate applied to the filament be $E(t)$. Conservation of mass gives us

$$\dot{a} = -\frac{1}{2} E a \qquad (37)$$

Hoop stress due to surface tension (χ) has the effect of squeezing the filament. Thus, with neglect of the viscous stresses and the elastic stress component, σ_{rr}, conservation of momentum leads to

$$\frac{\chi}{a} = G A_{zz} \qquad (38)$$

where A is the tensor describing the configuration of the microstructure and G is the elastic modulus.

Due to the straining of the filament, the microstructure will get deformed with time. Here we model the microstructure with an Oldroyd-B model, assuming large deformations of the microstructure, and get

$$\begin{aligned}
\dot{A}_{zz} &= 2E A_{zz} - \frac{1}{\tau} A_{zz} \\
&= (2E - \frac{1}{\tau}) A_{zz}, \qquad (39)
\end{aligned}$$

where τ is the relaxation time of the microstructure. Since the surface tension is resisting the stretching of the filament, we need to find out the strain E required to stretch the filament. The strain rate cannot be very large because that would break the filament. Equation of momentum, Eq. 38, gives $A_{zz} \propto \frac{1}{a}$. Using this and Eq. 37, we have $\frac{\dot{A}_{zz}}{A_{zz}} = -\frac{\dot{a}}{a} = \frac{1}{2} E$. We then look at Eq. 39 and solve to get $E = \frac{2}{3} \frac{1}{\tau}$. Conservation of mass (Eq. 37) then gives the variation of filament radius with time as:

$$a(t) = a(0) e^{-\frac{t}{3\tau}}. \qquad (40)$$

The result we have obtained does not compare well with experiments, in the as is shown in figure 16. The experiments were done using S1 fluid by Liang and Mackley [8] and the solid theoretical curves are from the analysis carried out by Entov and Hinch [9] in which they used a spectrum of relaxation times instead of the single relaxation time that we used in our earlier derivation. When a spectrum of relaxation times is used for the microstructure, the solution for the stretching and relaxation of stress is:
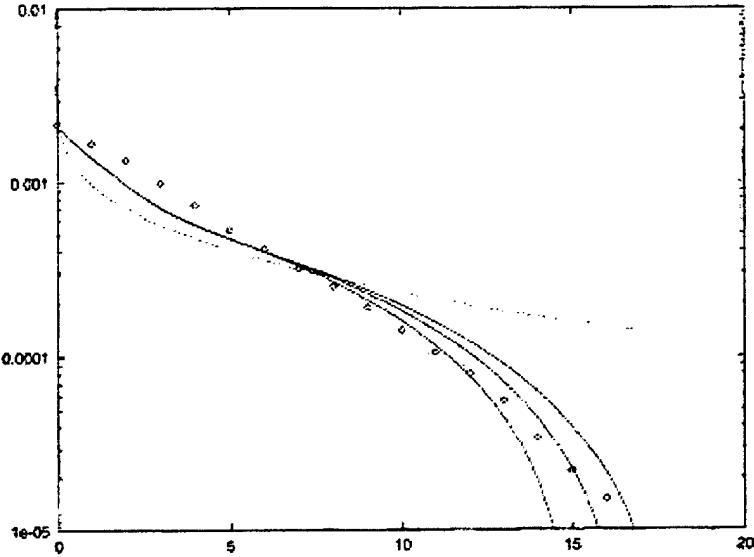
108

Figure 16: Variation of the diameter of an S1 liquid filament (on y-axis) being stretched with time (on x-axis). The dotted line is the theoretical result derived in Eq. 40.

$$A_{zz}^i = \frac{1}{a^4(t)} e^{-t/\tau_i},$$ (41)

where the subscript i represents the relaxation mode.

Hence, the momentum equation becomes

$$\frac{\chi}{a} = \frac{1}{a^4} \sum_i g_i e^{-t/\tau_i}.$$ (42)

Then, the radius of the filament as a function of time is

$$a(t) = \left(\frac{G(t)}{\chi}^{1/3} \right)$$ (43)

where $G(t) = \sum g_i e^{-t/\tau_i}$ is the material stress-relaxation function.

5   Oldroyd-B: Successes and Failures

The Oldroyd-B is one of the simplest and the most frequently used models for the microstructure. Its simplicity lies in the fact that it adds an elasticity G to the fluid and a single relaxation time τ, over and above the Newtonian fluid viscosity, μ_0. Although this model has been successful in explaining some of the viscoelastic phenomena, it has been found to perform poorly when the rate of deformation of the fluid is much larger than the relaxation time of the microstructure.
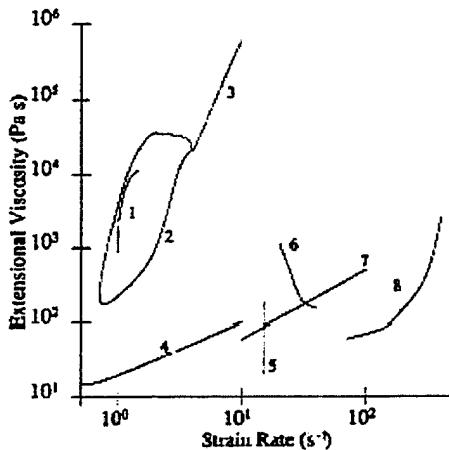
109

Figure 17: Extensional viscosity of an M-1 fluid depends on what device you use to measure it.

Figure 17 demonstrates this problem quite vividly. This is a plot of measurements of extensional viscosity of the same fluid (M1) but in different devices which are represented by different curves labeled 1 through 8. Curve 1 is from an open siphon device, 2 is from a spinline, 3, 7 & 8 are from a contraction flow device, 4 is from an opposing jet, 5 is from a falling drop and 6 is from a falling blob. The other plots in figure 17 are details of some of the measurements made. Notice the large scatter and disagreement in the curves. This raises two questions. First, is extensional viscosity an appropriate quantity to be measured for non-Newtonian fluids or should we be using some other measure for the influence of a largely deformed microstructure on the flow, e.g. elastic constant? Second, will Oldroyd-B be able to capture the effect of largely extended microstructures on the flow?

The answer to the first question is not clear at this time. Using the strain on the microstructure to define the stress with the help of an elastic constant could be one way of going about it. The answer to the second question is that Oldroyd-B fails to describes these effects. For a contraction flow, while Oldroyd-B does predict a small initial decrease in pressure drop, it fails to predict the large increase in pressure drop or the size of upstream vortices seen at higher flow rates. In the case of a fluid flowing past sphere, it rightly predicts the initial decrease in drag but again fails to predict the increase in force and large wake lengths observed at higher flow rates. As a final example, Oldroyd-B gives us the correct time scale for the deformation of capillary filament being stretched, but does not predict any breakage of the filament at very high applied strain rates. From a numerical perspective, the Oldroyd-B model runs into problems for high De, because it suggests that the microstructure can keep stretching to infinite lengths as long as there exists a force to deform it. Consequently, the extensional stresses become negative beyond a critical De. This is obviously unrealistic and we are forced to conclude that more physics is required in the constitutive equation than contained in Oldroyd-B.

The modification to the constitutive equation that has been successfully used and rather swiftly accepted is FENE — Finitely Extensible Non-Linear Elastic microstructure. This
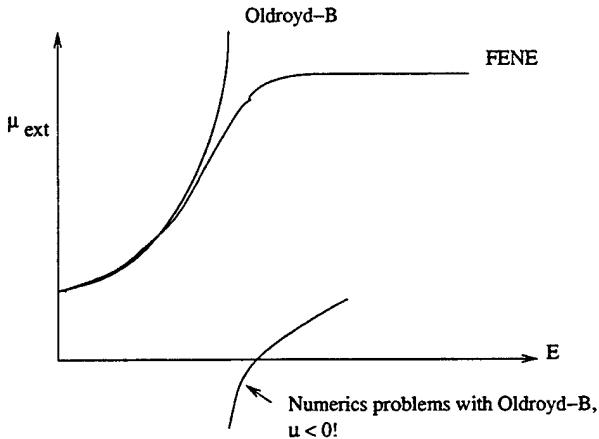
110

Figure 18: The negative viscosity as predicted by Oldroyd-B and the FENE cure to that.

model limits the deformation to a certain length L and retains a large positive value for extensional stresses at high De. It predicts a large pressure drop for strong contraction flows, a large increase in drag for strong flows past a sphere and finally, breakage of the capillary filament when drawn at a large strain rate. Also, for strongly extensional flows in general, the FENE modification predicts $\mu_{ext} \gg \mu_{shear}$. This dramatic anisotropy in viscosity can be of direct consequence to polymer turbulent drag reduction.

In conclusion, we can say that we have begun to get some understanding of both the strong and weak flows of elastic liquids. While the Oldroyd-B model is a good choice for small $De \ll 1$ flows, the FENE model is a clear winner for high $De \gg 1$ flows. Thus Non-Newtonian fluids have unique dynamical signatures that cannot be explained by the superposition of viscous and elastic effects. A general theory for such fluids is still lacking due to the diversity of materials and their characteristic flow behaviors.

Notes by Anshuman Roy and Andrew Thompson

References

[1] M. D. Chilcott and J. M. Rallison, "Creeping flows of dilute polymer solutions past cylinders and spheres," Journal of Non-Newtonian Fluid Mechanics 29(1-3), 381 (1988).

[2] V. Tirtaatmadja, P. H. T. Uhlherr, and T. Sridhar, "Creeping motion of spheres in fluid m1," Journal of Non-Newtonian Fluid Mechanics 35(2-3), 327 (1990).

[3] O. G. Harlen, E. J. Hinch, and J. M. Rallison, "Birefringent pipes - the steady flow of a dilute polymer solution near a stagnation point," Journal of Non-Newtonian Fluid Mechanics 44, 229 (1992).

[4] P. Szabo, J. M. Rallison, and E. J. Hinch, "Start-up of flow of a fene-fluid through a 4:1:4 constriction in a tube," Journal of Non-Newtonian Fluid Mechanics 72, 73 (1997).

[5] U. Cartalos and J. M. Piau, "Creeping flow regimes of low concentration polymer solutions in thick sovents through an orifice die," Journal of Non-Newtonian Fluid Mechanics **45**, 231 (1992).

[6] H. Lamb, *Hydrodynamics* (Cambridge University Press, Cambridge, UK, 1932).

[7] M. A. Alves, P. J. Oliveira, and F. T. Pinho, "Benchmark solution for the flow of oldroyd-b and ptt fluidds in planar contractions," Journal of Non-Newtonian Fluid Mechanics **110**, 45 (2003).

[8] R. F. Liang and M. R. Mackley, "Rheological characterization of the time and strain dependence for polyisobutylene solutions," Journal of Non-Newtonian Fluid Mechanics **52(3)**, 387 (1994).

[9] V. M. Entov and E. J. Hinch, "Effect of a spectrum of relaxation times on the capillary thinning of a filament of elastic liquid," Journal of Non-Newtonian Fluid Mechanics **72(1)**, 31 (1997).

Flow-induced oscillations:
A source mechanism for volcanic tremor?

Alison Rust

1 Introduction

Accurate predictions of volcanic activity are key to protecting the hundreds of millions of people who live near potentially active volcanoes. Over the past twenty years, the detection of long-period seismic signals (peak frequencies < 5Hz) has become an increasingly important tool in eruption forecasting, however, the physical mechanisms for their generation remain poorly understood. These long-period ground vibrations that precede and accompany eruptions, may be generated by complex interactions between fluids and rocks. Volcanic eruptions require flow of magma and/or aqueous fluids through rock and there is potential for long-period seismic signals to provide important information on changes in the location, velocity and types of fluids (e.g., gas, magma, bubbly magma) under volcanoes. However, such analysis requires understanding potential source mechanisms of the ground oscillations and the characteristics of the resulting signals. Here we examine the feasibility of inducing persistent long-period seismicity by fluid flow through a crack in an elastic rock, an idea first explored by Julian [1].

2 Characteristics of volcanic tremor

Long-period seismic signals near volcanoes can be of long duration and when a signal continues for several minutes or longer, it is called volcanic tremor. Shorter duration signals with similar waveforms and frequency spectra (and perhaps similar source mechanisms) are simply called long-period (LP) events. Tremor is a common precursor to volcanic eruptions and accompanies nearly all eruptions [2, 3] but the characteristics of tremor can vary considerably. The signal may a) originate from hundreds of meters below the ground surface down to as deep as 40 km, b) have a gradual or abrupt onset, c) be harmonic or anharmonic, and d) last minutes, days or months [2]. Typically, the signal comes from <10 km depth, emerges gradually in the time domain with a random distribution of sharp peaks concentrated between 0.1-7 Hz in the frequency domain. There can be systematic changes in tremor during eruptions including period-doubling, a phenomenon associated with a transition from periodic to chaotic behavior of a non-linear system [4, 1].
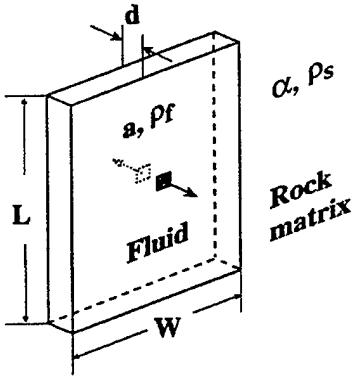
Figure 1: Sketch of the resonating fluid-filled crack model of Chouet [5, 6]. The two small boxes in the center of the crack faces mark where the pressure disturbance that triggers resonance is applied.

3 Models for generation of volcanic tremor

Given the range of tremor properties, depths of origin and association with all styles of eruptions (explosive, effusive; magmatic, phreatic; passive degassing), there are probably multiple origins of volcanic tremor. Several mechanisms for tremor generation have been proposed including bubble growth or collapse, jerky crack propagation, oscillations of magma chambers, resonance of fluid-filled cracks and flow-induced oscillations of conduits. For a review of tremor properties and potential source mechanisms, see [2]. Here we will briefly discuss only two models: 1) the resonance of fluid-filled cracks [5, 6, 7] which is probably the best-known and accepted model for long-period seismicity, and 2) the Julian [1, 4] model of vibrations induced by flow through a slot with elastic walls, which is the inspiration for our analysis.

Chouet [5, 6] proposed that the spectral peaks of tremor and LP events are the resonance modes of fluid-filled cracks. Chouet's model simulates motion along the walls of a rectangular fluid-filled crack in an infinite homogenous elastic solid that is excited into vibrations by a pressure-time source function at a specified position on the walls (Figure 1). The equations of elastic motion of the crack walls are solved simultaneously with the governing equations for fluid flow. The resulting far-field wavefield depends on the crack dimensions, the position and size of the pressure disturbance, the elastic constants of the solid (bulk modulus and rigidity), and the densities and sound speeds of both the solid and fluid. Thus comparing model results to long-period seismic signals recorded at volcanoes, Chouet and others [8, 9] infer parameters such as crack dimensions and sound speeds. There are numerous potential sources of the pressure disturbance required to trigger resonance including an earthquake, a new crack network connection, shock waves from "choked" flow [10], or bubble coalescence leading to a rising gas slug [8]. These are all plausible sources of LP-events, which decay after seconds or tens of seconds. However, tremor requires a disturbance that is sustained for minutes or even months and thus precludes transient resonance triggers such as earthquakes. Sustained resonance could be caused by continued formation of shock waves or gas slugs however these seem to require special circumstances and do not
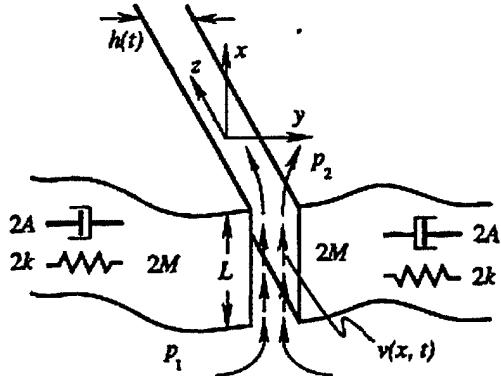
114

Figure 2: The lumped parameter model of Julian [1] for the generation of tremor by flow induced oscillations. Fluid flows from one reservoir to another (each with constant fluid pressure) via a slot of length L. The walls of the constriction each have a mass M, a stiffness k, and a damping constant A.

explain the near-ubiquity of tremor during volcanic eruptions of all styles and compositions.

If fluid flow through a crack induced oscillations in the conduit walls, this could be a source of sustained seismicity, lasting as long as flow continued at a sufficient speed. Julian [1] explored this tremor mechanism using an approach similar to [11] for blood flow through collapsible arteries. Julian set up a lumped-parameter model involving two-dimensional flow of an incompressible Newtonian fluid through a slot-like constriction with two movable walls (Figure 2). At each end of the constriction the conduit is wide enough that it can be considered to be a fluid reservoir with constant fluid pressure despite oscillations of the constriction. Each wall is modelled as a mass whose motion is controlled by a spring representing the elasticity of the country rock, and a dashpot for anelastic effects and radiation damping. The separation of the walls changes as a function of time only, and thus the walls of the constriction are always flat and parallel. This model leads to a third-order system of nonlinear ordinary differential equations. For different driving fluid pressures, numerical solutions show stable steady flow, simple oscillations, period-doubling cascades, or chaotic oscillations. Although the sample results presented by Julian involve very high fluid velocities (45-110 m/s) and frequencies on the high end of tremor (~5 Hz), his lumped parameter model demonstrates that flow-induced oscillations are a potential source of tremor and can explain observed non-linear phenomena observed at several volcanoes [4]. Like Julian [1, 4], we consider vibrations induced by fluid flow through an elastic solid. However, we take a mathematically more rigorous approach. Rather than using a lumped parameter model with walls that are blocks with masses connected to springs and dashpots, we assume the conduit is in a homogeneous elastic solid. We solve governing equations for deformation in both the fluid and the solid, and match stresses in the two materials at their interface (the walls). Unlike Julian, we allow the crack gap thickness to vary with both time and position (along the direction of dominant fluid flow). We also consider a tube-like conduit in addition to a slot-like geometry.
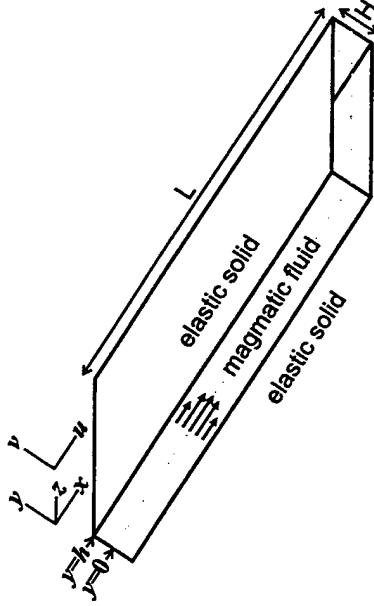
115

Figure 3: The geometry of our model. An incompressible, Newtonian fluid flows through a crack of length L and equilibrium gap thickness H in an elastic solid. Flow-induced oscillations cause the thickness of the gap $(2h)$ to vary in both x and time. Flow is two-dimensional with flow field $(u, v, 0)$ and $u \gg v$.

4 The fluid

We consider flow of an incompressible, Newtonian fluid through a crack of length L and gap thickness H in an isotropic elastic solid (Figure 3). The coordinate system (x, y, z) is set so that the crack is parallel to $y = 0$ and the two crack walls are at $y = \pm h(x, t)$ with $h = \frac{H}{2}$ at equilibrium. Flow is two-dimensional with velocity field $(u, v, 0)$. The governing equations for fluid flow are conservation of momentum,

$$u_t + uu_x + vu_y = -\frac{P_x}{\rho} + \nu(u_{xx} + u_{yy}), \tag{1}$$

and

$$u_t + uv_x + vv_y = -\frac{P_y}{\rho} + \nu(u_{xx} + u_{yy}), \tag{2}$$

and continuity (conservation of mass),

$$u_x + v_y = 0, \tag{3}$$

where ρ is the density, P is the pressure and ν is the kinematic viscosity of the fluid. To simplify this set of equations, we will take advantage of the small aspect ratio, $\epsilon = \frac{H}{L}$, of the fluid-filled crack. We begin by non-dimensionalizing the equations, using

$$x = L\tilde{x}, \quad y = H\tilde{y}, \quad u = U\tilde{u}, \quad v = \epsilon U\tilde{v}, \quad t = \frac{L}{U}\tilde{t} \text{ and } P = [P]\tilde{P}, \tag{4}$$
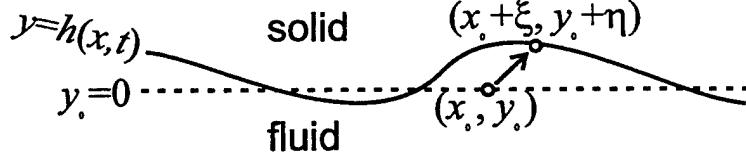
Figure 4: Sketch of the wall for which $h > 0$ at equilibrium. A point in the elastic solid with coordinates (x_0, y_0) at equilibrium has coordinates $(x_0 + \xi, y_0 + \eta)$ when disturbed by flow-induced oscillations. The dashed line is the equilibrium position of the fluid-rock interface; $y_0 = 0$ for all points on this line. When deformed this interface becomes the curve $h(x, t)$.

where $\tilde{\ }$ indicates a dimensionless variable, U is the average fluid speed and $[P] = \frac{U \nu \rho L}{H^2}$. The resulting dimensionless momentum equations to order ϵ^2 are

$$\epsilon\, Re\,(\tilde{u}_{\tilde{t}} + \tilde{u}\tilde{u}_{\tilde{x}} + \tilde{v}\tilde{u}_{\tilde{y}}) = -\tilde{P}_{\tilde{x}} + \tilde{u}_{\tilde{y}\tilde{y}}, \quad \tilde{P}_{\tilde{y}} = 0, \tag{5}$$

where $Re = \frac{UH}{\nu}$ is a Reynolds number using the crack gap thickness for the length-scale. Dropping the $\tilde{\ }$ notation, the dimensionless equations for momentum are

$$\epsilon\, Re\,(u_t + u u_x + v u_y) = -P_x + u_{yy}, \quad P_y = 0. \tag{6}$$

The base state is $P_x = u_{yy}$. Therefore at equilibrium (i.e., no flow-induced movement of the walls), the non-dimensional pressure gradient and pressure are $P_x = -3$ and $P = -3x$, respectively. The equilibrium fluid thickness, H, is the wall separation caused by the equilibrium fluid pressure. The pressure gradient driving flow will in fact cause the base state to be a wedge-shaped crack. However, we assume H is independent of x, which is a good assumption if the ambient (lithostatic) pressure is much greater than both the fluid pressure and changes in lithostatic pressure along the crack.

The fluid stress tensor is

$$\sigma_{fluid} = \begin{pmatrix} -P & 0 \\ 0 & -P \end{pmatrix} + \nu\rho \begin{pmatrix} 2u_x & u_y + v_x \\ u_y + v_x & 2v_y \end{pmatrix}. \tag{7}$$

Using the continuity equation (3) and the scalings in (4), the non-dimensional fluid stress is, to order ϵ^2,

$$\sigma_{fluid} = [P] \begin{pmatrix} -P & \epsilon u_y \\ \epsilon u_y & -P \end{pmatrix}. \tag{8}$$

5 The solid

We treat the country rock as an elastic solid. The coordinates of a point in the solid are $(x_0 + \xi, y_0 + \eta)$, where (x_0, y_0) is the undisturbed position and $y_0 = 0$ at the wall. To determine non-dimensional governing equations, we assume the wall moves a distance of order $\epsilon L = H$ and take H to be the unit of ξ and η, but L for x_0 and y_0:

$$x_0 = L\tilde{x}_0, \quad y_0 = L\tilde{y}_0, \quad \xi = H\tilde{\xi}, \quad \eta = H\tilde{\eta}. \tag{9}$$

Then, at the wall we have the non-dimensional relations

$$x = x_0 + \epsilon\, \xi_t(x_0, 0, t), \tag{10}$$

$$v(x, h, t) = \eta_t(x_0, 0, t), \tag{11}$$

$$u(x, h, t) = \epsilon\, \xi_t(x_0, t), \tag{12}$$

and taking the non-dimensional location of the wall, $h(x, t)$, to be $h_0 = 1$ when not disturbed,

$$\eta(x_0, 0, t) = h(x, t) - 1. \tag{13}$$

The constitutive equations for stress in the elastic solid are

$$\sigma_{xx} = \lambda(\xi_x + \eta_y) + 2\mu\, \xi_x, \tag{14}$$

$$\sigma_{yy} = \lambda(\xi_x + \eta_y) + 2\mu\, \eta_x, \text{ and} \tag{15}$$

$$\sigma_{xy} = \mu(\xi_y + \eta_x). \tag{16}$$

Again omitting the $\tilde{\ }$ notation, the non-dimensional stress tensor for the solid to order ϵ^2 is

$$\sigma_{solid} = \mu\epsilon \begin{pmatrix} 2\xi_{x_0} + \frac{\lambda}{\mu}(\xi_{x_0} + \eta_{y_0}) & \xi_{y_0} + \eta_{x_0} \\ \xi_{y_0} + \eta_{x_0} & 2\eta_{x_0} + \frac{\lambda}{\mu}(\xi_{x_0} + \eta_{y_0}) \end{pmatrix}. \tag{17}$$

We are interested in seismic waves created by oscillations of the crack. We express the elastic wave equations in terms of potentials, ϕ and ψ which are related to ξ and η by

$$\xi = \phi_{x_0} + \psi_{y_0} \text{ and } \eta = \phi_{y_0} + \psi_{x_0}. \tag{18}$$

The wave equations are

$$\phi_{tt} = \alpha^2 \nabla^2 \phi \text{ and } \psi_{tt} = \alpha^2 \nabla^2 \psi, \tag{19}$$

where α and β are compression and shear waves velocities, respectively. Using the average fluid speed to non-dimensionalize the elastic wave speeds,

$$\tilde{\alpha}^2 = \frac{\lambda + 2\mu}{\rho\, U^2} \text{ and } \tilde{\beta}^2 = \frac{\mu}{\rho\, U^2}, \tag{20}$$

where λ and μ are Lame elastic constants (μ is called the shear modulus).

Fourier transform solutions to the wave equations are

$$\phi = \int_{\omega=-\infty}^{\infty} \int_{k=-\infty}^{\infty} e^{ikx_0 + i\omega t}\, \Phi(k, \omega) \frac{dk\, d\omega}{2\pi}\, e^{-\kappa_\alpha y_0}, \tag{21}$$

and

$$\psi = \int_{\omega=-\infty}^{\infty} \int_{k=-\infty}^{\infty} e^{ikx_0 + i\omega t}\, \Psi(k, \omega) \frac{dk\, d\omega}{2\pi}\, e^{-\kappa_\beta y_0}, \tag{22}$$

where

$$\kappa_\alpha = \sqrt{k^2 - \frac{\omega^2}{\alpha^2}} \text{ and } \kappa_\beta = \sqrt{k^2 - \frac{\omega^2}{\beta^2}}. \tag{23}$$

To ensure that the waves are evanescent (decay as go to an infinite distance from the source), we require that κ_α and κ_β be positive.

118

6 Matching fluid and solid stresses at the wall

Stress must be continuous across the fluid-solid interface. Therefore from (7) and (17), at $x = x_0 + \mathcal{O}(\epsilon)$ and $y_0 = 0$ (i.e., at the wall),

$$G \begin{pmatrix} 2\xi_{x_0} + \frac{\lambda}{\mu}(\xi_{x_0} + \eta_{y_0}) & \xi_{y_0} + \eta_{x_0} \\ \xi_{y_0} + \eta_{x_0} & 2\eta_{x_0} + \frac{\lambda}{\mu}(\xi_{x_0} + \eta_{y_0}) \end{pmatrix} \begin{pmatrix} -\epsilon h_x \\ 1 \end{pmatrix} = \begin{pmatrix} -P & \epsilon u_y \\ \epsilon u_y & -P \end{pmatrix} \begin{pmatrix} -\epsilon h_x \\ 1 \end{pmatrix}, \tag{24}$$

where

$$G = \frac{\mu\epsilon}{[P]} = \frac{\epsilon^3 \beta^2 L}{U\nu}, \tag{25}$$

and $(-\epsilon h_x, 1)$ is a vector normal to the wall. This gives

$$\xi_{y_0} + \eta_{x_0} = \mathcal{O}(\epsilon) \quad \text{and} \quad G\left(2\,\xi_{y_0} + \frac{\lambda}{\mu}(\xi_x + \eta_y)\right) = -P + \mathcal{O}(\epsilon), \tag{26}$$

indicating that normal stresses dominate over shear stresses on the wall. Thus the full matching conditions at the wall are

$$x = x_0, \tag{27}$$

$$\xi = h - 1, \tag{28}$$

$$u = 0, \text{ and} \tag{29}$$

$$P = -G\left(2\,\xi_{y_0} + \frac{\lambda}{\mu}(\xi_x + \eta_y)\right). \tag{30}$$

From these conditions and equations (18, 19), for wave-like disturbances,

$$P = G[h(x,t) - 1]\beta^2 \left(\frac{\kappa_\beta^2 + k^2}{\omega^2 \kappa_\alpha}\right)\left(\frac{\omega^2}{\beta^2} - 2k^2 + \frac{4k^2 \kappa_\alpha \kappa_\beta}{\kappa_\beta^2 + k^2}\right). \tag{31}$$

For nonlinear stability analysis we calculate an equivalent Fourier Transform solution,

$$P = G\int_{\omega=-\infty}^{\infty}\int_{k=-\infty}^{\infty} e^{ikx + i\omega t}\beta^2 \left(\frac{\kappa_\beta^2 + k^2}{\omega^2 \kappa_\alpha}\right)\left(\frac{\omega^2}{\beta^2} - 2k^2 + \frac{4k^2 \kappa_\alpha \kappa_\beta}{\kappa_\beta^2 + k^2}\right) \cdots$$

$$\cdots \int_{x'=-\infty}^{\infty}\int_{t'=-\infty}^{\infty} e^{-(ikx' + i\omega t')}[h(x',t') - 1]\frac{dt'\,dx'\,dk\,d\omega}{2\pi\;2\pi}, \tag{32}$$

which for $\omega \ll \alpha$ and $\omega \ll \beta$ simplifies to

$$P = 2G\left(\frac{\alpha^2 - \beta^2}{\alpha^2}\right)\int_{x'=-\infty}^{\infty}[h(x',t) - 1]\int_{k=-\infty}^{\infty} |k|\,e^{ik(x-x')}\frac{dk\,dx'}{2\pi}. \tag{33}$$

7 Linear stability analysis

7.1 Lubrication theory

We begin by considering the case where the crack gap is so thin compared to its length, and flow is slow enough that $\epsilon Re \to 0$. Thus

$$P_x = u_{yy}, \tag{34}$$

119

which for a parabolic velocity profile and $u = 0$ at the walls gives

$$u = \frac{1}{2}P_x(y^2 - h^2). \tag{35}$$

We next integrate the continuity equation (3) in y and apply a kinematic boundary condition,

$$h_t = v, \tag{36}$$

to obtain

$$h_t - \frac{1}{3}\frac{\partial}{\partial x}h^3 P_x = 0. \tag{37}$$

Adding small perturbations in crack thickness and pressure

$$h = 1 + h'e^{ikx+i\omega t} \text{ and} \tag{38}$$

$$P = -3x + P'e^{ikx+i\omega t}, \tag{39}$$

we solve (37) using P' determined from (31). The resulting linearized dispersion relation is

$$i\omega + 3ik + \frac{1}{3}k^2\beta^2 G \left(\frac{k^2 + \kappa_\beta^2}{\kappa_\alpha\omega^2}\right)\left(\frac{\omega^2}{\beta^2} - 2k^2 + \frac{4k^2\kappa_\alpha\kappa_\beta}{k^2 + \kappa_\beta^2}\right) = 0. \tag{40}$$

The system will be unstable if there is a root for which the imaginary part of ω is negative ($\mathcal{I}(\omega) < 0$). This is because $i\omega = i\mathcal{R}(\omega) - \mathcal{I}(\omega)$ and so if $\mathcal{I}(\omega) < 0$ then $e^{ikx+i\omega t}$ will grow with time. For small k, roots are of the form $\omega = -3k + \mathcal{O}(k^3)$. If $\omega = -3k + \omega_{(3)}k^3$, then

$$i\omega_{(3)} \approx \frac{G\beta^2}{27\sqrt{1 - \frac{9}{\alpha^2}}}\left[\left(2 - \frac{9}{\beta^2}\right)^2 - 4\sqrt{\left(1 - \frac{9}{\alpha^2}\right)\left(1 - \frac{9}{\beta^2}\right)}\right]. \tag{41}$$

It is always true that $\beta \leq \alpha$ (20). It is reasonable to assume that $\beta > 3$, which means that the shear wave speed in the country rock (of order km/s) is more than triple the average fluid speed in the crack. With these constraints, we find $i\omega_{(3)} \geq \frac{3G}{\beta^2\sqrt{1 - \frac{9}{\alpha^2}}}$ and $i\omega_{(3)} > 0$.
Therefore, the imaginary part of ω is positive and instabilities will not grow with time.

For large k, roots of equation (40) satisfy

$$\left(1 - \frac{X}{2}\right)^2 - \sqrt{\left(1 - \frac{\beta^2}{\alpha^2}X\right)(1 - X)} = 0, \quad \text{where } X = \frac{\omega^2}{\beta^2 k^2}.$$

There are roots with $\mathcal{I}(\omega) < 0$ but none satisfy $\kappa_\alpha > 0$ and $\kappa_\beta > 0$ as required for evanescence. There are Rayleigh waves propagating along the surface, though, with small $\mathcal{I}(\omega) \geq 0$, that become damped due to fluid viscosity.

7.2 Averaged model

To allow Reynolds number (Re) dependence, while still taking advantage of the small crack gap to length ratio, we average the velocity across the gap (i.e., in the y-direction). We assume the fluid velocity in the crack is

$$u = \frac{3}{2}U\left(1 - \frac{y^2}{h^2}\right) \tag{42}$$

and thus has a parabolic profile with $u = 0$ at the wall ($y = h$), and an average velocity of U.

The momentum equation (6) averaged over y is

$$\epsilon\, Re \int_{y=0}^{h} u_t + uu_x + vu_y \, dy = -h\, P_x + [u_y]_{y=h}, \tag{43}$$

which, for u defined in (42), is

$$\epsilon Re \left[\frac{\partial}{\partial t}(Uh) + \frac{\partial}{\partial x}\left(\frac{6}{5}U^2 h\right)\right] = -h\, P_x - \frac{3U}{h}. \tag{44}$$

Similarly the kinematic boundary condition (36) averaged over y is

$$h_t + \frac{\partial}{\partial x}\int_{y=0}^{h} u\, dy = 0, \tag{45}$$

which gives

$$h_t + U_x h + U h_x = 0. \tag{46}$$

Combining (38, 39, 44, 46) and

$$U = 1 + U' e^{ikx + i\omega t}, \tag{47}$$

gives the dispersion relation

$$i\epsilon Re\left(\frac{\omega^2}{k} + \frac{12}{5}\omega + \frac{6}{5}k\right) + 9 + \frac{3\omega}{k} - ikG\beta^2\left(\frac{\kappa_\beta^2 + k^2}{\omega^2 \kappa_\alpha}\right)\left(\frac{\omega^2}{\beta^2} - 2k^2 + \frac{4k^2\kappa_\alpha\kappa_\beta}{\kappa_\beta^2 + k^2}\right) = 0, \tag{48}$$

which at $Re = 0$, reduces to the stable result from lubrication theory (40).

From asymptotic analysis for small k, roots of (48) at neutral stability are of the form

$$\omega = -3k + \omega_{(3)}k^3 \tag{49}$$

where

$$\omega_{(3)} = -i\frac{\epsilon Re}{k} + i\frac{G\beta^2}{27 f_\alpha}(1 + f_\beta^2)\left(\frac{9}{\beta^2} - 2 + \frac{4f_\alpha f_\beta}{1 + f_\beta^2}\right), \tag{50}$$

and

$$f_\alpha = \sqrt{1 - \frac{9}{\alpha^2}} \quad \text{and} \quad f_\beta = \sqrt{1 - \frac{9}{\beta^2}}. \tag{51}$$
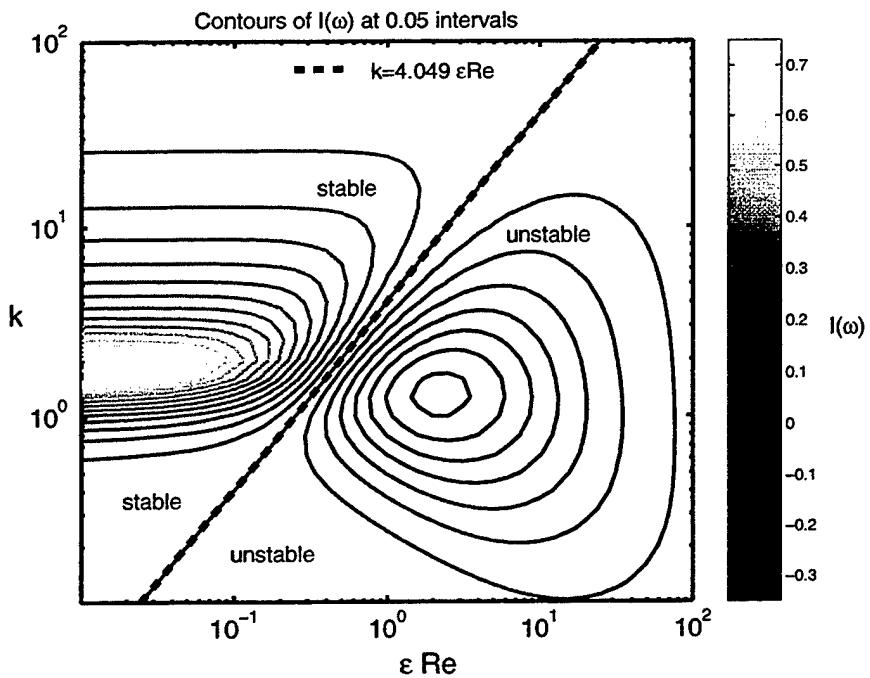
121

Figure 5: Contours of the imaginary part of the frequency at intervals of 0.05 in a non-dimensional wavenumber versus ϵRe plot. The non-dimensional α and β are set at 8 and 4, respectively. The thick dashed line is the calculated solution (equation 52) for neutral stability of the system. As expected, this line coincides with the $\mathcal{I}(\omega) = 0$ contour. For the parameters used to create this plot, the system is most unstable (fastest growth rate of waves) at both k and ϵRe $\mathcal{O}(1)$. Equivalent plots with α and β one or two orders of magnitude greater show similar patterns with the line of neutral stability matching equation (52).

122

Hence the waves are unstable if Re is large enough. At neutral stability, $\mathcal{I}(\omega) = 0$, which in this case means $\mathcal{I}(\omega_{(3)}) = 0$. Therefore the non-dimensional critical wave number, $\tilde{k}_{cr}$ (for clarity we return to the ~ notation to denote non-dimensional quantities), below which the system is unstable is

$$\tilde{k}_{cr} = \frac{27\epsilon Re f_{\tilde{\alpha}}}{G\tilde{\beta}^2 \left(1 + f_{\tilde{\beta}}^2\right)\left(\frac{9}{\tilde{\beta}^2} - 2 + \frac{4f_{\tilde{\alpha}}f_{\tilde{\beta}}}{1+f_{\tilde{\beta}}^2}\right)}, \tag{52}$$

which is equivalent to

$$\tilde{k}_{cr} = \left(\frac{27\,U^4}{\epsilon\,\beta^4}\right)\frac{f_{\tilde{\alpha}}}{\left(1 + f_{\tilde{\beta}}^2\right)\left(\frac{9}{\tilde{\beta}^2} - 2 + \frac{4f_{\tilde{\alpha}}f_{\tilde{\beta}}}{1+f_{\tilde{\beta}}^2}\right)}, \tag{53}$$

where β without the ~ is the true dimensional shear wave speed. Note that $\tilde{k}_{cr} = 1$ corresponds to a wave of wavelength equal to the length of the crack and the second fraction in (53) is of order 1. Interestingly, $\tilde{k}_{cr}$ is proportional to the reciprocal of a Mach number to the fourth power and does not directly depend on the fluid viscosity. Furthermore, from (53) the system could be unstable at arbitrarily low ϵRe.

7.3 Long wave expansion

Typically, results from an averaged model are qualitatively correct with some error from the averaging. To check the accuracy of the averaging results at small k we use asymptotic analysis. We begin by defining stream functions that satisfy continuity

$$u = \chi_y + U(y), \quad v = -\chi_x, \tag{54}$$

where $\chi \propto e^{ikx+i\omega t}$. In terms of these stream functions, the momentum equation in x is

$$\epsilon Re\left(i\omega\chi_y + \frac{3}{2}\left(1 - y^2\right)ik\chi_y + 3ik\chi_y\right) = -ik\hat{p} + \chi_{yyy}. \tag{55}$$

Solving for ω to order ϵ^2 using

$$\epsilon Re = \sum_{n=0}^{\infty} R_{(n)}k^n, \quad \omega = \sum_{n=1}^{\infty} \omega_{(n)}k^n, \quad \chi = \sum_{n=0}^{\infty} \chi_{(n)}k^n, \quad \hat{p} = \sum_{n=1}^{\infty} P_{(n)}k^n \tag{56}$$

($_{(n)}$ are indices of summation constants) and $\omega = -k\chi$ from the kinematic boundary condition, gives

$$\omega = -3k + i\left(\frac{1}{3}P_{(1)} - \frac{6}{5}R_{(1)}\right)k^3. \tag{57}$$

Therefore at neutral stability

$$R_{(1)} = \frac{5}{18}P_{(1)}, \tag{58}$$

and

$$\tilde{k}_{cr} = \frac{6}{5}\left(\frac{27\,U^4}{\epsilon\,\beta^4}\frac{f_{\tilde{\alpha}}}{\left(1 + f_{\tilde{\beta}}^2\right)\left(\frac{9}{\tilde{\beta}^2} - 2 + \frac{4f_{\tilde{\alpha}}f_{\tilde{\beta}}}{1+f_{\tilde{\beta}}^2}\right)}\right). \tag{59}$$
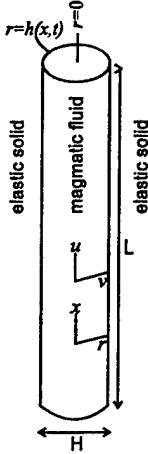
123

Figure 6: Geometry for our model with a cylindrical conduit. An incompressible, Newtonian fluid flows through a tube-like hole of length L and equilibrium diameter H in an elastic solid. Flow induced oscillations cause the tube radius (h) to vary in both x and time. Flow is two-dimensional with the along-tube velocity u much greater than the radial velocity v.

This result indicates that the across-gap-averaged model (53) is qualitatively correct but off by a factor of $\frac{6}{5}$.

7.4 Cylindrical conduit

Magma mostly rises through the Earth's brittle crust through fractures forming sheets of magma. Lava sometimes erupts from linear fissures, however, flow is usually localized by cooling, producing a cylindrical form at the top of the conduit. We assess the feasibility of flow through a cylindrical conduit generating tremor using long wave theory as done in section 7.3 for a crack.

We consider a fluid-filled tube of length L and diameter H in an elastic solid. The cylindrical coordinate system (x, r, θ) is set so that the x-axis is in the center of the tube and the solid-fluid interface is at $r = h(x, t)$. Flow is two-dimensional with velocity field $(u, v, 0)$ (Figure 6). We nondimensionalize as for the crack problem (4) with x and y replaced with z and r respectively. The non-dimensional governing equations for fluid flow are conservation of momentum,

$$\epsilon Re(u_t + uu_z + vu_r) = -P_z + \frac{1}{r}\frac{\partial}{\partial r}(ru_r), \quad P_r = 0, \tag{60}$$

and continuity,

$$u_z + \frac{1}{r}\frac{\partial}{\partial r}(rv) = 0. \tag{61}$$

We take the velocity of the fluid to be

$$U(r) = 2 - 2r^2, \tag{62}$$

so that the average velocity is one and the profile is parabolic. We define stream functions

$$u = \frac{1}{r}\frac{\partial}{\partial r}(r\chi) + U(r) \text{ and } v = -\chi_z, \tag{63}$$

124

where $\chi \propto e^{ikx+i\omega t}$. Using Bessel functions, matching of stresses in the Newtonian fluid and the elastic solid at their cylindrical interface gives

$$P = G[h(x,t) - 1] \left(\frac{2}{\epsilon} - \epsilon \ln(\epsilon\kappa_\alpha) \frac{\beta^2}{\alpha^2} \left(\frac{\alpha^2}{\beta^2} - 2 \right) (\kappa_\beta^2 + k^2) \right), \qquad (64)$$

and thus

$$P \approx \frac{2G}{\epsilon}[h(x,t) - 1]. \qquad (65)$$

Long wave expansion using the kinematic boundary condition (36), indicates that neutral stability for the cylindrical conduit occurs at

$$\frac{U^2}{\beta^2} \sim \frac{1}{\epsilon k}, \qquad (66)$$

for small k, in contrast to

$$\frac{U^4}{\beta^4} \sim \epsilon k, \qquad (67)$$

for the planar conduit. As discussed further below (section 9) for realistic parameter values, this result means that the cylindrical conduit is always much more stable to flow-induced oscillations than the planar conduit.

8 Non-linear stability analysis

Results from linear stability analysis are not necessarily a good indicator of the behaviour of non-linear systems. Our preliminary nonlinear analysis involves a periodic domain and the gap-averaged model (section 7.2) with the physically sensible simplifying assumption that $\omega << \alpha$ and $\omega << \beta$.

Given $h(x)$, we use a Fast Fourier Transform to compute fourier coefficients for the series

$$h - 1 = \sum_{n=-\infty}^{\infty} A_n e^{inx}. \qquad (68)$$

Using these coefficients, the Fourier Transform solution for pressure at the wall for $\omega << \alpha$ and $\omega << \beta$ (33), and a Hilbert Transform, we have an expression for determining P_x,

$$P_x = i\hat{G} \sum_{n=-\infty}^{\infty} A_n \, n \mid n \mid e^{inx}, \qquad (69)$$

where $\hat{G} = 2G\left(\frac{\alpha^2-\beta^2}{\alpha^2}\right)$. With this P_x, inverted with a Inverse Fast Fourier Transform, the differential equations for momentum (44) and the kinematic boundary condition (46) are then solved by a MATLAB PDE solver (finite-difference method with standard time integrator). The end result is the evolution of h as a function of time and position along the crack (e.g., Figure 7). We varied both $\hat{G}$ and ϵRe by several orders of magnitude and set initial random or sinusoidal ($k = 1$ to 6) perturbations in either h or in fluid flux. We found only simple, steady solutions; there was no complex behaviour such as multiplicity
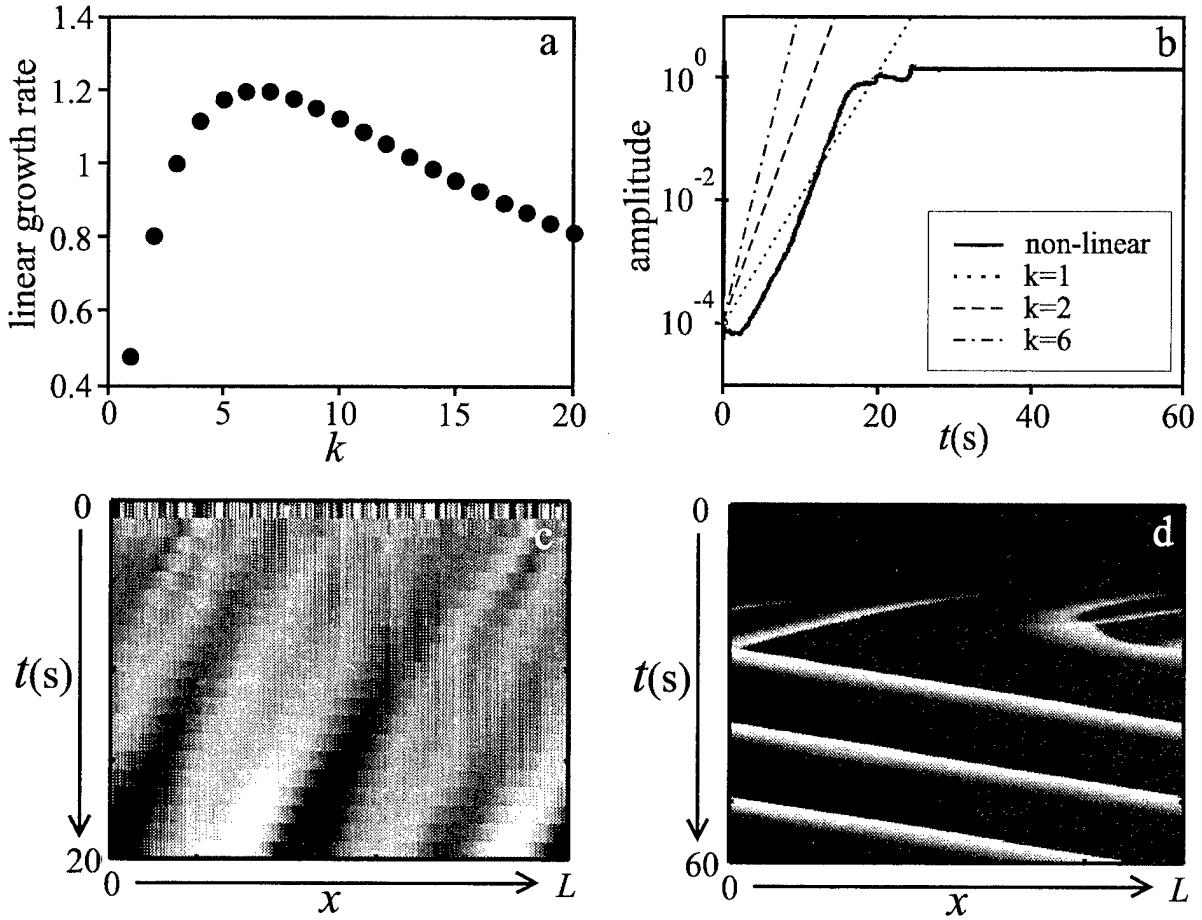
125

Figure 7: Results of a nonlinear simulation for $\epsilon Re = 2$ and $\hat{G} \equiv 2G\left(\frac{\alpha^2-\beta^2}{\alpha^2}\right) = 0.05$ beginning with random perturbations in h. For these parameters, the linear growth rate is greatest for $k \sim 6$ (a). (b) shows how the amplitude for the non-linear simulation changes with time (solid line). The broken lines illustrate growth rates for three k-values based on linear analysis. Subplots (c) and (d) show amplitude as a function of time and space (the horizontal axis is position along the crack of length L). The two subplots have different greyscales to maximize the range of tones but in both cases dark=high and light=low. A background speed of $2.5U$ was subtrated for more efficient computation and the apparent reversal in wave propagation in (d) is not real. (c) is the first 20 seconds of the simulation. Several waves form from the random perturbations. By 20 seconds it has coarsened to three waves. (d) is the first minute of the simulation. Note the sudden coarsening to two waves and then a single wave. The final wave has a very steep wave front (i.e., it is a roll wave).
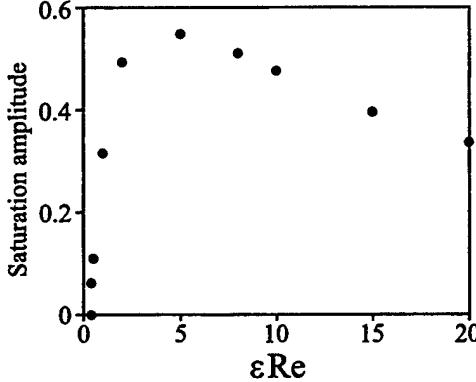
126

Figure 8: Plot of saturation amplitude versus ϵRe from non-linear analysis with a periodic domain and $\hat{G} \equiv 2G\left(\frac{\alpha^2-\beta^2}{\alpha^2}\right) = 1$. Amplitudes are normalized such that the equilibrium crack thickness is 2. The low saturation amplitude near the critical Re above which the system in unstable indicates a soft transition to instability (i.e., supercritical). This is unlike the familiar subcritical nature of turbulence where there is a sudden jump in behaviour above a critical Re.

or period-doubling. As shown in Figure 8, the transition from stable to unstable is "soft" with low-amplitude saturation near the critical Re.

No matter the initial conditions, when unstable, the waves coarsen to the longest possible wavelength ($k = 1$). Figure 8 shows an example where the linear growth rate, determined from the across-gap averaged model dispersion relation (48) for $\omega << \alpha$ and $\omega << \beta$,

$$\omega^2 + \left(\frac{12}{5}k + \frac{3}{i\epsilon Re}\right)\omega + \frac{6}{5}k^2 + \frac{9k}{i\epsilon Re} - 2G\left(\frac{\alpha^2 - \beta^2}{\alpha^2}\right) = 0, \tag{70}$$

is greatest for $k \sim 6$. After some adjustment at the start, the non-linear growth rate is comparable to that for $k = 6$ and then decreases as the waves coarsen until finally the $k = 1$ wave becomes saturated. Coarsening indicates that the most unstable linear wave is not necessarily that observed and the character of tremor may be given by the lengthscale of cracks or crack constrictions. The $\hat{G}$ of 0.05 used in the simulation for Figure 7 is much lower than expected for the volcanic system but was chosen to demonstrate coarsening. In the real volcanic system, the highest growth rate is probably $k \sim 1$ or $k \sim 2$ and the coarsening behaviour (transition to lower k until $k = 1$) is less evident.

9 Back to volcanoes

Our linear stability analysis suggests that for flow through a crack in an elastic solid, flow-induced oscillations are possible at arbitrarily low, non-zero Reynolds numbers. Furthermore, the stability of the system depends on the crack aspect ratio, fluid speed and elastic wave speeds. However, to this point we have not considered the physical parameters relevant to volcanic tremor. From (53), the range of wavenumbers and Reynolds numbers for which the system is unstable expands (to lower k and Re) if the crack thickness to length ratio or the shear wave speed in the rock are decreased. To assess the feasibility of our model
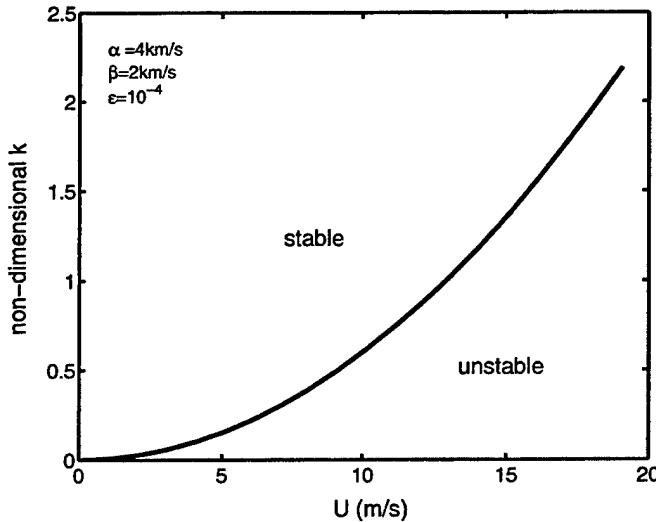
127

Figure 9: The curve on this plot of non-dimensional wavenumber versus average fluid velocity represents neutral stability for flow through a crack with aspect ratio $\epsilon = 10^{-4}$ in a solid with elastic wavespeeds $\alpha = 4$ km/s and $\beta = 2$ km/s. The plot is based on results of the averaged velocity model (53) with the slight correction from long wave theory $\left(\frac{6}{5}\right)$.

for generating volcanic tremor we consider $\epsilon = 10^{-4}$ and $\beta = 2$ km/s, which are at the low end of physically possible parameters. We require that the nondimensional wave number, $\tilde{k}$, be at least 1 which corresponds to a wavelength equal to the length of the crack (4). Figure 9 shows that even using these relatively low ϵ and β values, average fluid velocities of order 10 m/s or greater are needed to induce oscillations. Thus the feasibility of the model reduces to the feasibility of fluids flowing at speeds of order 10 m/s through cracks beneath volcanoes. Stability does not depend directly on viscosity but the more viscous the fluid, the greater the pressure gradient needed to drive flow at a given velocity through a crack with a given aperture. The required conditions of high flow speeds through thin cracks are most easily achieved for low viscosity fluids such as convecting groundwater or vapors and supercritical fluids exsolved from magma. There is potential for tremor triggered by such fluids to be common because aqueous fluids are present at all volcanoes and eruptions of magma are typically preceded by increased gas emissions.

To what depths are aqueous fluids present? There is growing evidence from volcanic gas emissions as well as the chemistry of crystals and pockets of melt trapped inside crystals, that magmas in storage regions kilometers below volcanoes are often saturated in volatiles (mixtures of H_2O, CO_2, etc.) [12]. For example, melt inclusions in quartz crystals indicate that the magma that became the Bishop Tuff (Long Valley, California) exsolved enough volatiles to comprise 30% by volume of the magma prior to rapid ascent and eruption [13]. Because of the low viscosity and density of the volatile phase, and the increased fluid pressure caused by its formation, a portion of this supercritical aqueous fluid likely rose through cracks in rock above the magma. Further evidence for aqueous fluid flow at several kilometers depth is preserved in porphyry deposits. The porphyry copper-gold mine in Butte Montana for instance, contains countless veins formed by aqueous fluids flowing

128

through rock fractures that were once about 7 km beneath a volcano [14].

Typically one does not expect there to be a free volatile phase below 10 km depth because the solubility of volatiles in silicate melts increases with increasing pressure. However, saturation at great depth is possible if there is sufficient CO_2 in the melt. To take an extreme (and exceedingly rare) example, kimberlite magmas, the most common source of diamonds, are thought to contain about 30% CO_2 by **weight** and saturate in volatiles at about 150 km depth. The deepest reported tremor originated about 40 km below Kilauea Volcano, Hawaii [15] in the 1970's. Recent data on gas emissions from the summit of Kilauea [16] show a surprisingly high CO_2 emission rate ($\approx 8.5 \times 10^6$ kg/day), which, in conjunction with information on the chemistry and supply rate of the magma, indicates that the basalt contained about 0.7 % CO_2 by weight and saturated in volatiles at about 0.95 GPa. For inferred crust and upper mantle densities [17], this means that volatile exsolution from the magma to form a low viscosity, low density fluid, could occur about 30 km under Kilauea [16]. Although not as deep as the deepest tremor reported by Aki and Koyanagi, the data of Gerlach et al. open the possibility that a volatile phase played a role in generating the deep sustained vibrations below Kilauea. It is possible for there to be a free volatile phase at greater depths than 30 km without invoking greater bulk CO_2 contents in the basalt. Crystallization of basalt concentrates CO_2 in the melt because the crystals contain negligible CO_2. Thus, substantial crystallization of basalt stalled at 40 km depth could leave a residual melt that is saturated in CO_2. Pressure increase from the exsolution of a low-density fluid could cause fractures in the overlying rock through which the CO_2-rich fluid escapes. In fact sudden onsets to the deep tremor at Kilauea reported by [15] are what allowed Aki and Koyanagi to locate the source depths. We conclude that flow of aqueous or CO_2-rich fluids is a plausible source mechanism for volcanic tremor in the upper several km of crust where most tremor is generated as well as deep tremor for magmas with high CO_2 contents.

It is also possible that magma transport could generate tremor in the upper crust during explosive eruptions and fire-fountaining as exit velocities for these eruption styles can reach hundreds of m/s and 50 m/s, respectfully [18, 19]. However, the viscosity of magma (10 to 10^{12} Pa s) makes sustained velocities of 10 m/s unreasonable for subsurface magma flow that is not coincident with, or immediately preceding, eruption of magma at the surface. Very thick dikes reduce the resistance to flow and thus may allow large magma velocities but our scaling of the problem (4), combined with the frequencies of volcanic tremor, limit the size of the crack. The characteristic time scale is $t = \frac{L}{U}$, and as the period of tremor is typically seconds, the length of the crack (in m) cannot be more than an order of magnitude greater than the average fluid velocity (in m/s). To keep the minimum fluid velocity required for flow-induced oscillations down to $\mathcal{O}(10 \text{ m/s})$, we used $\epsilon = 10^{-4}$. With our time-scale constraints, the crack could be as long as $\mathcal{O}(100 \text{ m})$ which gives a crack thickness of only $\mathcal{O}(1 \text{ cm})$. For laminar flow of basalt with $\mu = 100$ Pa s, this corresponds to a pressure gradient of $\mathcal{O}(10^8 \text{ Pa/m})$ and decompression rate of $\mathcal{O}(10^9 \text{ Pa/s})$, values which are probably only reached by rapid bubble expansion and fragmentation at shallow levels during explosive eruptions. Therefore, linear stability analysis suggests that magma transport is unlikely to generate flow induced oscillations except at shallow levels (perhaps top 2 km) during explosive or fountaining eruptions. If a low viscosity fluid is required for deep tremor, this could explain the general lack of long period seismicity in recharge zones

beneath intermediate and silicic volcanoes where there is magma movement but the magma is not saturated in volatiles.

Our analysis indicates that some fluids, conduit geometries and eruption styles are more likely to cause tremor by flow-induced oscillations than others. In particular, we found that planar rather than tube-like fluid conduits, small thickness to length ratios of conduits, and high fluid speeds are factors that tend to generate flow-induced tremor. Except for shallow seismicity during explosive or fountaining activity, for realistic pressure gradients, maintaining sufficient fluid speeds (>10 m/s) to induce oscillations requires sustained flow of low viscosity aqueous or carbonaceous fluid rather than magma. These conclusions from stability analysis are consistent with observations by McNutt [3] in a study of tremor from 50 eruptions at 31 volcanoes comparing tremor characteristics and corresponding eruption parameters. McNutt lists four trends in the data:

"1) large eruptions produce stronger tremor than small ones;

2) fissure eruptions produce stronger tremor than circular vents for the same fountain height;

3) eruptions with higher gas content produce stronger tremor than those with low gas content at the same volcano; and

4) phreatic eruptions [*eruptions that eject broken rock and vapor but no magma*] produce stronger tremor than magmatic eruptions [*eruptions that do eject magma*] for the same VEI [*Volcanic Explosivity Index, a measure of the magnitude and intensity of an eruption*]."

Therefore, flow-induced oscillations are a plausible source mechanism for volcanic tremor that is consistent with observations from volcanoes.

10   Future work

There are several possible avenues for future research. These include fluid compressibility, non-linear analysis with a non-periodic domain and application of results to other systems. Perhaps the simplest and most obvious is to add fluid compressibility. We concluded that flow-induced tremor is most readily generated by flow of vapors and other aqueous fluids through cracks. The compressibility of these fluids will be significant at pressures in the first few kilometers below volcanoes and thus we will incorporate compressibility in the across-gap averaged model.

Further non-linear analysis is required. Our preliminary model involving a crack with a periodic domain may not be adequate as it does not produce period doubling, a non-linear phenomenon observed at several volcanoes. The difficulty in treating the fluid conduit as a slot with a non-periodic domain is setting the boundary conditions.

In addition to volcanic tremor, the generation of oscillations by flow past a deformable material has applications in diverse fields such as physiology [11] and drag reduction in gel-lined tubes and other surfaces [20]. It would be interesting to examine our results for conditions relevant to these applications (e.g., much lower elastic velocities).

11   Acknowledgements

typical fellow. Thanks also to my fellow fellows and other inhabitants of The Palace for a tasty summer.

References

[1] B. R. Julian, "Volcanic tremor: Nonlinear excitation by fluid flow," J. Geophys. Res. **99**, 11859 (1994).

[2] K. I. Konstantinou and V. Schlindwein, "Nature, wavefield properties and source mechanism of volcanic tremor: a review," J. Volc. Geotherm. Res. **119**, 161 (2002).

[3] S. R. McNutt, "Volcanic tremor and its use in estimating eruption parameters," Eos Trans. Amer. Geophys. Un., Fall Meeting Suppl. **83**, F1500 (2002).

[4] B. R. Julian, "Period doubling and other nonlinear phenomena in volcanic earthquakes and tremor," J. Volc. Geotherm. Res. **101**, 19 (2000).

[5] B. A. Chouet, "Dynamics of a fluid-driven crack in three dimensions by the finite difference method," J. Geophys. Res. **91**, 967 (1986).

[6] B. A. Chouet, "Resonance of a fluid-driven crack: radiation properties and implications for the source of long-period events and harmonic tremor," J. Geophys. Res. **93**, 4375 (1988).

[7] B. A. Chouet, "A seismic model for the souce of long-period events and harmonic tremor", in: P. Gasparini, R. Scaarppa, and K. Aki (eds.), *Volcanic Seismology*, (IAV-CEI, 1992).

[8] F. G. Cruz and B. A. Chouet, "Long-period events, the most characteristic seismicity accompanying the emplacement and extrusion of a lava dome in Galeras Volcano, Colombia, in 1991," J. Volc. Geotherm. Res. **77**, 121 (1997).

[9] B. A. Chouet, R. A. Page, C. D. Stephens, J. C. Lahr, and J. A. Power, "Precursory swarms of long-period events at Redoubt Volcano (1989-1990), Alaska; their origin and use as a forecasting tool," J. Volc. Geotherm. Res. **62**, 95 (1994).

[10] M. M. Morrissey and B. A. Chouet, "Trends in long-period seismicity related to magmatic fluid compositions," J. Volc. Geotherm. Res. **108**, 265 (2001).

[11] T. J. Pedley, *Fluid Mechanics of Large Blood Vessels* (Cambridge University Press, Cambridge, 1980).

[12] P. J. Wallace and A. T. Anderson, *Volatiles in magma*, in: H. Sigurdsson, B. Houghton, S. R. McNutt, H. Rymer and J. Stix (eds.), *Encyclopedia of Volcanology*, (Elsevier Science & Technology Books, 1999).

[13] P. J. Wallace, A. T. Anderson, and A. M. Davis, "Gradients in H_2O, CO_2, and exsolved gas in a large-volume silicic magma system: Interpreting the record preserved in melt inclusions from the Bishop Tuff," J. Geophys. Res. **104**, 20097 (1999).

[14] B. Rusk, M. H. Reed, J. H. Dilles, L. Klemm, and C. A. Heinrich, "Fluid inclusion evidence for magmatic fluid evolution in the porphyry copper deposit; Butte, Montana," Geol. Soc. Am., Cord. Sect., 98th annual meeting, Abstracts with Programs **34**, 16 (2002).

[15] K. Aki and R. Koyanagi, "Deep volcanic tremor and magma ascent mechanism under Kilauea, Hawaii," J. Geophys. Res. **86**, 7095 (1981).

[16] T. M. Gerlach, K. A. McGee, T. Elias, A. J. Sutton, and M. P. Doukas, "Carbon dioxide emission rate of Kilauea Volcano: Implications for primary magma and the summit reservoir," J. Geophys. Res. **107**, ECV3 1 (2002).

[17] M. P. Ryan, "Neutral boyancy and the mechanical evolution of magmatic systems", in: B. O. Mysen (ed.) *Magmatic processes: Physiochemical principles*, Spec. Publ. Geochem. Soc. **1**, 259 (1987).

[18] F. Dobran, *Volcanic Processes: Mechanisms in Material Transport* (Kluwer Academic Publishers Group, 2001).

[19] M. T. Mangan and K. V. Cashman, "The structure of basaltic scoria and reticulite and inferences for vesiculation, foam formation, and fragmentation in lava fountains," J. Volc. Geotherm. Res. **73**, 1 (1996).

[20] V. Shankar and V. Kumaran, "Stability of wall modes in fluid flow past a flexible surface," Phys. Fluids **14**, 2324 (2002).

Wave–mean-flow interaction in Oldroyd-B fluid

Amit Apte

1 Introduction

The effects of waves on the mean-flow have been extensively studied, most notably in the studies of oceanic and atmospheric waves. But waves in non-Newtonian fluids have not received much attention. I will be focusing here on the wave–mean-flow interaction in Oldroyd-B fluid. This is done in a very simple flow profile to study clearly various phenomena arising because of elasticity.

I will start by studying the linear equations in section Sec. 2. The equations for mean-flow response are obtained after introducing zonal averaging in section Sec. 3. I discuss and apply the Generalized Lagrangian Mean theory in section Sec. 4. The spin-up and spin-down problem, discussed in section Sec. 5, illustrates some of the peculiar features of the mean-flow response. I conclude with a few remarks and indicate some directions for further studies.

2 Linear theory

The Oldroyd-B model for an incompressible fluid is given by:

$$\nabla \cdot \mathbf{u} = 0 \,, \tag{1}$$

$$\frac{\partial \mathbf{u}}{\partial t} + \mathbf{u} \cdot \nabla \mathbf{u} = -\nabla p + \nu \nabla^2 \mathbf{u} + G \nabla \cdot \mathbf{A} \,, \tag{2}$$

$$\frac{\partial \mathbf{A}}{\partial t} + \mathbf{u} \cdot \nabla \mathbf{A} - (\nabla \mathbf{u})^T \cdot \mathbf{A} - \mathbf{A} \cdot \nabla \mathbf{u} = -\frac{1}{\tau}(\mathbf{A} - \mathbf{I}) \,. \tag{3}$$

I have set the constant fluid density $\rho = 1$. The momentum equation contains the divergence of the polymeric stress $G\mathbf{A}$. This extra stress simply advects with the flow, as given by the "upper convected derivative" [left hand side of (3)], but it also relaxes to I with a time constant τ.

multiplying the momentum equation (2) by $\mathbf{u}\cdot$ we can get the equation for energy:

$$\left(\frac{\partial}{\partial t} + \mathbf{u} \cdot \nabla \right) \left(\frac{1}{2}\mathbf{u}^2 + \frac{G}{2} \operatorname{tr} A \right)$$
$$= \nabla \cdot \left(-\mathbf{u}p + \nu \nabla \mathbf{u} \cdot \mathbf{u} + G\mathbf{u} \cdot \mathbf{A} \right) - \nu \nabla \mathbf{u} : \nabla \mathbf{u} - \frac{G}{2\tau}\left(\operatorname{tr} A - 3 \right) \,. \tag{4}$$

Thus we see that in addition to viscosity, the relaxation of polymeric stress also dissipates energy. In most of the following, I will consider the "ideal" limit of this model: an inviscid, relaxation-less Oldroyd-B fluid with $\nu = 0$ and $1/\tau = 0$. In this limit, the energy is conserved.

I consider the flow in an semi-infinite two dimensional domain $D = \{(x, y)| - \infty < x < \infty, h(x) <= y < \infty\}$. We can satisfy two boundary conditions at the boundary $y = h(x)$: the free-slip condition $\mathbf{u} \cdot \hat{n} = 0$, and the condition of no tangential stress $\hat{n} \times (\mathbf{A} \cdot \hat{n}) = 0$. Here $\hat{n}$ is the normal to the lower boundary: $\hat{n} = (-h_x(x), 1)$.

I will study waves on following one dimensional constant flow profile, thus avoiding problems of critical layers:

$$\mathbf{u} = (U, 0), \qquad p = p_0, \qquad \mathbf{A} = \mathbf{I}, \qquad \text{and} \qquad h(x) = 0. \tag{5}$$

In the absence of relaxation, the stress $\mathbf{A}$ can be any constant matrix, not necessarily $\mathbf{I}$. But the above choice was made with the following in mind: The qualitative features of the wave–mean-flow interaction do not change by assuming it to be $\mathbf{I}$; Also, one of the extensions of this problem, to be studied later, is the flow in presence of relaxation when the stress $\mathbf{A}$ for the background flow must be $\mathbf{I}$.

Substituting

$$\mathbf{u} = (U, 0) + \mathbf{u}', \qquad p = p_0 + p', \qquad \text{and} \qquad \mathbf{A} = \mathbf{I} + \mathbf{A}', \tag{6}$$

in (1)-(3), denoting $D_t := \partial/\partial t + U \partial/\partial x$, and keeping terms linear in perturbed quantities, we get the following linear equations:

$$\nabla \cdot \mathbf{u}' = 0, \tag{7}$$

$$D_t \mathbf{u}' = -\nabla p' + G \nabla \cdot \mathbf{A}', \tag{8}$$

$$D_t \mathbf{A}' = \left(\nabla \mathbf{u}'\right)^T + \nabla \mathbf{u}'. \tag{9}$$

The boundary for the linear problem is chosen to be $h(x) = h_0 \cos(kx)$ with a small amplitude h_0, i.e., $a := h_0 k \ll 1$ is the small parameter. The energy conservation equation for the linear problem is the following:

$$D_t \left(\frac{1}{2} \mathbf{u}'^2 + \frac{G}{4} \text{tr } \mathbf{A}'^2 \right) = \nabla \cdot \left(-\mathbf{u}' p' + G \mathbf{u}' \mathbf{A}' \right). \tag{10}$$

I will introduce the particle displacement associated with the perturbation flow $\mathbf{u}'$ as $D_t \boldsymbol{\xi}' = \mathbf{u}'$. Then we can explicitly integrate (9) to get

$$\mathbf{A}' = (\nabla \boldsymbol{\xi}')^T + \nabla \boldsymbol{\xi}'. \tag{11}$$

Using the incompressibility equation $\nabla \cdot \boldsymbol{\xi}' = 0$, we get

$$\nabla \cdot \mathbf{A}' = \nabla^2 \boldsymbol{\xi}' + \nabla(\nabla \cdot \boldsymbol{\xi}') = \nabla^2 \boldsymbol{\xi}'. \tag{12}$$

This reduces the momentum equation (8) to

$$D_t \mathbf{u}' = -\nabla p' + G \nabla^2 \boldsymbol{\xi}'. \tag{13}$$

134

By taking the divergence of the above equation, and using incompressibility, we see an important consequence that pressure is an harmonic function:

$$\nabla^2 p' = 0 \tag{14}$$

The relation (11) is reminiscent of the stress-strain relation for a solid. In fact, we will see later that the vorticity waves for this linear model are the same as elastic waves in an incompressible linear elastic solid. The analogy fails when I consider the potential flow and satisfy the boundary condition on tangential stress: a solid can support tangential stresses at the boundary and these must be specified to solve the problem, while I impose the condition that the tangential stress is zero for this ideal Oldroyd-B fluid. Thus the only difference between a solid and this ideal limit of Oldroyd-B fluid is in the boundary conditions.

We can find two kinds of waves from the linear equations. I begin by considering the vorticity waves. With vorticity defined as $q' = v'_x - u'_y$, we get

$$\begin{aligned}
D_t^2 q' &= D_t \left(D_t v'_x - D_t u'_y \right), \\
&= D_t \left(\left(-p_{xy} + G\nabla^2 \eta'_x \right) - \left(-p_{xy} + G\nabla^2 \xi'_x \right) \right), \\
&= G\nabla^2 \left(D_t \left(\eta'_x - \xi'_x \right) \right),
\end{aligned}$$

which gives the vorticity wave equation:

$$(D_t^2 - G\nabla^2)q' = 0. \tag{15}$$

The dispersion relation for the vorticity waves [with $q' \sim \exp(i\boldsymbol{k} \cdot \boldsymbol{x} - i\omega t)$] is

$$\omega = Uk \pm \sqrt{G}|k| =: Uk + \hat{\omega}. \tag{16}$$

Here, $\hat{\omega}$ is the *intrinsic* frequency of the waves ,i.e., frequency in the frame moving with the background flow, whereas ω is the frequency with respect to the boundary. The magnitudes of intrinsic group and phase velocities are equal and are given by

$$v_p = v_g = \pm\sqrt{G}. \tag{17}$$

Stationary vorticity waves have $\omega = 0$. Choosing $U > 0$ and $k > 0$, we see that we must choose the lower sign in (16). Then solving for l, we get

$$l = \pm k\sqrt{\frac{U^2}{G} - 1}. \tag{18}$$

This shows that for $U^2 > G$ the waves are propagating while for $U^2 < G$ they are evanescent. This is also seen by writing (15) as

$$[(U^2/G - 1)\partial_x^2 - \partial_y^2]q' = 0. \tag{19}$$

I note that this equation is elliptic for $U^2 < G$ and parabolic for $U^2 = G$, but is hyperbolic otherwise.

135

I choose the lower sign in (18) so that these are outgoing waves (i.e., the y-component of $v_p \mathbf{k}/|\mathbf{k}|$ is positive). These are pressure-less waves $p' = 0$. All the other fields are given by

$$\xi' = -\frac{G\sqrt{U^2/G - 1}}{kU^2}\cos(kx + ly)\,, \qquad \eta' = -\frac{G}{kU^2}\cos(kx + ly)\,, \qquad (20)$$

$$u' = \frac{G\sqrt{U^2/G - 1}}{U}\sin(kx + ly)\,, \qquad v' = \frac{G}{U}\sin(kx + ly)\,, \qquad (21)$$

$$A'_{xx} = -A'_{yy} = \frac{2G\sqrt{U^2/G - 1}}{U^2}\sin(kx + ly)\,, \qquad A'_{xy} = \frac{2G - U^2}{U^2}\sin(kx + ly)\,. \quad (22)$$

The vorticity waves alone cannot satisfy both the free-slip and tangential stress-free boundary conditions. Thus I look for the other solution of the linear problem, i.e., potential flow. Assuming $\mathbf{u}' = \nabla\phi'$, i.e. $q' = 0$, we get from the continuity equation that ϕ' is a harmonic function $\nabla^2\phi' = 0$. Requiring that ϕ' oscillates in x, remains bounded as $y \to \infty$, and looking for stationary solutions ($\partial/\partial t = 0$), we get

$$\phi' = \Re\frac{U}{k}ie^{ikx - ky} = -\frac{U}{k}\sin(kx)e^{-ky}\,. \qquad (23)$$

Using $\mathbf{u}' = \nabla\phi'$, $D_t\xi' = (\partial/\partial t + U\partial/\partial x)\xi' = U\partial\xi'/\partial x = \mathbf{u}'$, and $\mathbf{A}' = (\nabla\xi')^T + \nabla\xi'$ gives all the quantities for the potential flow:

$$\xi' = -\frac{1}{k}\sin(kx)e^{-ky}\,, \qquad \eta' = -\frac{1}{k}\cos(kx)e^{-ky}\,, \qquad (24)$$

$$u' = -U\cos(kx)e^{-ky}\,, \qquad v' = U\sin(kx)e^{-ky}\,, \qquad (25)$$

$$A'_{xx} = -A'_{yy} = -2\cos(kx)e^{-ky}\,, \qquad A'_{xy} = 2\sin(kx)e^{-ky}\,. \qquad (26)$$

The pressure for the potential flow is not zero but decays exponentially: $p' = U^2\cos(kx)e^{-ky}$.

Both the above solutions are written so that the y-particle displacement is in phase with the boundary $h(x)$. I write the total solution as $\xi' = \alpha\xi'_{(1)} + \beta\xi'_{(2)}$, where $\xi'_{(1)}$ and $\xi'_{(1)}$ are respectively the vorticity wave and potential flow solutions. The constants α and β can be found from the two boundary conditions as follows:

$$\mathbf{u}\cdot\hat{\mathbf{n}} = 0\,, \Rightarrow \quad v'|_{y=0} = Uh_x(x)\,, \quad \Rightarrow \quad G \qquad \alpha + U^2\beta \quad = -aU^2\,.$$

$$\hat{\mathbf{n}}\times(\mathbf{A}\cdot\hat{\mathbf{n}}) = 0\,, \Rightarrow \quad A'_{xy}|_{y=0} = 0\,, \qquad \Rightarrow \quad (2G - U^2) \quad \alpha + 2U^2\beta \quad = 0\,.$$

Solving the last two equations, we get

$$\alpha = -2a\,, \qquad \text{and} \qquad \beta = a\left(\frac{2G}{U^2} - 1\right)\,. \qquad (27)$$

Thus, we see that $\beta = 0$ for $U^2 = 2G$, which can also be seen directly from (22), because $A'_{xy} = 0$ in that case and the boundary condition is satisfied with the vorticity waves alone. This specific velocity will be important again when we later consider drag.

Briefly going back to the full set of Oldroyd-B equations (1)-(3), I will get the dispersion relation for vorticity waves with relaxation and dissipation. The linear equations in that

case are

$$\nabla \cdot \mathbf{u}' = 0, \tag{28}$$

$$D_t \mathbf{u}' = -\nabla p' + \nu \nabla^2 \mathbf{u}' + G \nabla \cdot \mathbf{A}', \tag{29}$$

$$D_t \mathbf{A}' = (\nabla \mathbf{u}')^T + \nabla \mathbf{u}' - \frac{1}{\tau} \mathbf{A}'. \tag{30}$$

Then the equations for vorticity $q' = \nabla \times \mathbf{u}$ and $\Omega' := \nabla \times (\nabla \cdot \mathbf{A}')$ become

$$D_t q' = -\frac{1}{\tau} q' + \nabla^2 \Omega', \tag{31}$$

$$D_t \Omega' = \nu \nabla^2 \Omega' + G q'. \tag{32}$$

These equations give the following dispersion relation:

$$\omega = Uk - \frac{i}{2} \left(\frac{1}{\tau} + \nu |\mathbf{k}|^2 \right) \pm \sqrt{G} |\mathbf{k}| \sqrt{1 - \frac{(\nu \tau |\mathbf{k}|^2 - 1)^2}{4G\tau^2 |\mathbf{k}|^2}}. \tag{33}$$

As another aside, if the background $\mathbf{A}$ is not equal to $\mathbf{I}$ but some constant symmetric matrix $\mathbf{M}$, then the dispersion relation is given by

$$\hat{\omega} = \sqrt{G} \sqrt{\mathbf{k} \cdot \mathbf{M} \cdot \mathbf{k}}. \tag{34}$$

This is very much like the dispersion relation for Alfvén waves in magnetohydrodynamic flows. This kind of analogy between non-Newtonian fluid flow and magnetohydrodynamic has been studied in different context in [5] and exploring it in greater details will be interesting.

3   Zonal averaging and small amplitude expansion

We will be interested in the effect of the waves on the mean-flow. To study this, we introduce the concept of *zonal averaging*, which is defined by

$$\overline{f} := \frac{1}{L} \int_0^L f(x, y, t) dx, \tag{35}$$

for any function which is periodic in x with period L. I will take L to be the wavelength $2\pi/k$ of the boundary. The *disturbance part* is defined as $f' := f - \overline{f}$. This is an exact decomposition without any assumption about small amplitude expansion, i.e., f' is not necessarily a "small" quantity.

A few properties, obtained by integrating by parts, will be very useful for further calculations:

$$\overline{f_x} = (\overline{f})_x = \frac{1}{L} \int_0^L f_x dx = f(L) - f(0) = 0; \tag{36}$$

$$\overline{f_x g} = \frac{1}{L} \int_0^L f_x g \, dx = -\overline{f g_x}; \qquad \overline{f_y g} = \overline{(fg)}_y - \overline{f g_y}; \tag{37}$$

$$\overline{AB} = \overline{A}\,\overline{B} + \overline{A'B'}. \tag{38}$$

137

Now we will look for equations for the averaged quantities like $\bar{u}$ etc. by averaging the Oldroyd-B equations. The continuity equation gives

$$\overline{u_x} + \overline{v_y} = \overline{v_y} = 0, \Rightarrow \bar{v} = 0.$$

This is the first simplification obtained by introducing the concept of zonal averaging: the average y-velocity is zero and we need to consider only the equation for $\bar{u}$.

The averaged x-momentum equation is:

$$\overline{u_t} + \overline{uu_x} + \overline{vu_y} + \overline{p_x} = G(\overline{A_{xx,x}} + \overline{A_{xy,y}}). \tag{39}$$

The second, fourth, and fifth terms vanish while the third term reduces to average over product of disturbance parts:

$$\overline{uu_x} = \frac{1}{2}\left(\overline{u^2}\right)_x = 0,$$

$$\overline{p_x} = 0, \quad \text{and} \quad \overline{A_{xx,x}} = 0,$$

$$\overline{vu_y} = \bar{v}\,\bar{u}_y + \overline{v'u'_y} = 0 + (\overline{v'u'})_y - \overline{v'_y u'} = (\overline{v'u'})_y + \overline{u'_x u'} = (\overline{v'u'})_y + 0.$$

Thus we get the following x-momentum equation:

$$\bar{u}_t + (\overline{v'u'})_y = G\overline{A_{xy,y}}. \tag{40}$$

This equation shows another simplification of zonal averaging: the nonlinear terms contain only the disturbance parts and only one component of $\overline{\mathbf{A}}$ appears in the x-momentum equation.

The equations for $\overline{\mathbf{A}}$ can also be reduced to simpler form in similar fashion. Since only the component $\overline{A_{xy}}$ appears in the x-momentum equation, I will concentrate on the equation for $\overline{A_{xy}}$:

$$\overline{A_{xy,t}} + (\overline{v'A'_{xy}})_y = \bar{u}_y\overline{A_{yy}} + \overline{u'_y A'_{yy}} + \overline{v'_x A'_{xx}} \tag{41}$$

Again almost all the nonlinear terms, except the first one on right hand side, contain only the disturbance parts. In order to get a full set of equations, we will need equations for $\overline{A_{yy}}$ and $\overline{A_{xx}}$. But, at this stage I will introduce the small-amplitude expansion to study small-amplitude waves [which are $O(a)$] and their effect, accurate only up to $O(a^2)$, on the flow. We will see later that the above equations for $\bar{u}$ and $\overline{A_{xy}}$ form a closed set of equations after introducing the small-amplitude expansion.

For considering the small-amplitude waves, I will expand all the physical quantities in the following asymptotic expansion:

$$f = F + f_1 + f_2 + \cdots + f_n + O(a^{n+1}), \tag{42}$$

where F is the $O(1)$ background and $f_n = O(a^n)$. Each term of this expansion is decomposed into an average and a disturbance part:

$$f_n = \bar{f}_n + f'_n. \tag{43}$$

By definition, the background contains no disturbance part, i.e. $F' = 0$, while the first order quantities contain no mean part: $\bar{f}_1 = 0$. Thus, keeping only the terms up to $O(a^2)$ gives:

$$\bar{u} = U + \overline{u_2}; \quad u' = u'_1 + u'_2; \quad \overline{\mathbf{A}} = \mathbf{I} + \overline{A_2}; \quad \mathbf{A}' = \mathbf{A}'_1 + \mathbf{A}'_2.$$

Thus we see that (40) and (41) correct up to $O(a^2)$ are:

$$\overline{u}_{2t} + G\overline{A}_{2xy,y} = \overline{(v_1' u_1')}_y \,, \tag{44}$$

$$\overline{A}_{2xy,t} - \overline{u}_{2y} = -\overline{(v_1' A_{1xy}')}_y + \overline{u_{1y}' A_{1yy}'} + \overline{v_{1x}' A_{1xx}'} \,. \tag{45}$$

We note that only the first order part of the disturbance and second order part of the mean appear in the above equations. This allows us to drop $(\ )_1$ from disturbances and $(\ )_2$ from means.

The above are wave equations for the means $\overline{u}$ and $\overline{A}_{xy}$. Note that there are source terms which appear as products of first order disturbances. Thus the effect on the mean-flow of the propagating vorticity waves and evanescent potential flow travels as a wave. The wave speed of this wave is $\sqrt{G}$ which is greater than $(l/\sqrt{k^2 + l^2})\sqrt{G} = \sqrt{G}\sqrt{1 - G/U^2}$ that is the y-component of group velocity of $O(a)$ vorticity waves. Thus we will distinguish between the waves of the mean part as "fast" vs. the waves of the disturbance part as "slow" waves.

The sources in the above equations appear only in terms of the first order disturbance parts. If we take a particular solution of the linearized equations (as given towards the end of Sec. 2), then we know the right hand sides of the above equations and we can solve them explicitly for $\overline{u}$ and $\overline{A}_{xy}$. But at this stage, I will introduce the ideas of Lagrangian mean averaging in contrast with the Eulerian zonal averaging $\overline{(\ )}$ that we have been using so far. The motivation for this step is that, in many cases, the equations in terms of Lagrangian averaged quantities are much simpler than those in terms of Eulerian means. We will soon see that such is indeed the case here.

4 Lagrangian mean averaging

In this section, I give a very brief introduction to Generalized Lagrangian Mean theory,[1, 2, 3] before applying it to the present problem. The GML theory obtains equations in terms of quantities averaged along the particle trajectory instead of averaging at a given spatial point, which is the case for Eulerian averaging. Thus, one of the main quantities to be used through-out the GLM theory is the disturbance related particle displacement field $\boldsymbol{\xi}(\boldsymbol{x},t)$. For example, the $\boldsymbol{\xi}'$ in (20) is the particle displacement field for the $O(a)$ vorticity waves.

The crux of the GLM theory is in the following two requirements:

- The field $\boldsymbol{\xi}(\boldsymbol{x},t)$ is defined in such a way that $\boldsymbol{x} + \boldsymbol{\xi}(\boldsymbol{x},t)$ is the actual position of the fluid particle whose mean position at time t is $\boldsymbol{x}$. Thus if we define $\boldsymbol{\Xi} = \boldsymbol{x} + \boldsymbol{\xi}(\boldsymbol{x},t)$, then we require that $\overline{\boldsymbol{\Xi}} = \boldsymbol{x}$. This is equivalent to requiring that $\boldsymbol{\xi}$ is a disturbance quantity.

$$\overline{\boldsymbol{\xi}}(\boldsymbol{x},t) = 0 \,. \tag{46}$$

- The other requirement is that $\boldsymbol{x} + \boldsymbol{\xi}(\boldsymbol{x},t)$ gives the actual trajectory of the material element of the fluid, i.e., the velocity of that point is the actual fluid velocity $\mathbf{u}^{\xi}$ at $\boldsymbol{x} + \boldsymbol{\xi}$.

$$\overline{D}^L \boldsymbol{\Xi} = \mathbf{u}^{\xi} \,, \tag{47}$$

where I have defined $\overline{D}^L := (\partial/\partial t + \overline{\mathbf{u}}^L \cdot \nabla)$.

Any field $f(x,t)$ is "lifted" to the actual particle position by defining

$$f^{\xi}(x,t) := f[x + \xi(x,t)].$$ (48)

The *Lagrangian-mean* operator $\overline{(\ )}^L$ is then defined to be the average taken with respect the displaced position $x + \xi$, i.e.,

$$\overline{f(x,t)}^L := \overline{f^{\xi}(x,t)} = \overline{f[x + \xi(x,t)]}.$$ (49)

The main idea behind GLM theory is that the equations in terms of Lagrangian-averaged quantities should be of the same form as the original equations. As an example, consider a scalar quantity θ that is advected by the flow:

$$\frac{D\theta}{Dt} = \left(\frac{\partial}{\partial t} + u \cdot \nabla\right)\theta = 0.$$ (50)

With the above definitions and requirements, we can show that the Lagrangian-mean version of this equation is simply

$$\overline{D}^L \overline{\theta}^L = \left(\frac{\partial}{\partial t} + \overline{u}^L \cdot \nabla\right)\overline{\theta}^L = 0.$$ (51)

This is much simpler than the Eulerian mean equation which contains products of disturbance parts from the nonlinear terms:

$$\left(\frac{\partial}{\partial t} + \overline{u} \cdot \nabla\right)\overline{\theta} = -\overline{(u' \cdot \nabla\theta')}.$$ (52)

For a vector or tensor field that is advected by the flow, the corresponding *mean* field can be defined in appropriate way so that the equation for advection remains form invariant under Lagrangian averaging.[3] In the absence of relaxation, the symmetric tensor A satisfies the equation

$$\frac{\partial A}{\partial t} + u \cdot \nabla A - (\nabla u)^T \cdot A - A \cdot \nabla u = 0.$$ (53)

If we define the mean stress tensor by

$$\hat{A}_{ij} := \overline{\left(\frac{A^{\xi}_{mn} K_{mi} K_{nj}}{J}\right)},$$ (54)

where J is the Jacobian of the transformation $x \to \Xi = x + \xi(x,t)$:

$$J = \left|\frac{\partial(\Xi)}{\partial(x)}\right| = |\delta_{ij} + \xi_{i,j}|,$$ (55)

and K_{mn} are the cofactors of the above matrix, then it can be verified that this mean vector is advected by the Lagrangian-mean velocity field, i.e.,

$$\frac{\partial \hat{A}}{\partial t} + \overline{u}^L \cdot \nabla\hat{A} - \left(\nabla\overline{u}^L\right)^T \cdot \hat{A} - \hat{A} \cdot \nabla\overline{u}^L = 0.$$ (56)

Now we transform the wave equations for $\bar{u}$ and $\bar{A}_{xy}$ into equations for the Lagrangian-mean quantities $\bar{u}^L$ and $\hat{A}_{xy}$ defined as follows:

$$\bar{u}^L := \bar{u} + \overline{(\eta' u')}_y\,,$$
$$\hat{A}_{xy} := \bar{A}_{xy} + \overline{(\eta' A'_{xy})}_y + \overline{\xi'_x \xi'_y} + \overline{\eta'_x \eta'_y}\,.$$

These definitions agree with the above definitions (49) and (54) up to $O(a^2)$.

The averaged equations for these Lagrangian mean quantities take very simple form as seen by using the linear equations [(7)-(9) and $\nabla \cdot \boldsymbol{\xi} = 0$] for the $O(a)$ disturbance fields and the properties (36)-(38) of the Eulerian averaging:

$$\bar{u}^L_t - G\hat{A}_{xy,y} = \overline{(\eta'_x p')}_y =: S_y(y,t)\,, \tag{57}$$
$$\hat{A}_{xy,t} - \bar{u}^L_y = 0\,. \tag{58}$$

For example,

$$\begin{aligned}
\hat{A}_{xy,t} - \bar{u}^L_y &= -\overline{(v' A'_{xy})}_y + 2\overline{v'_x \xi'_x} + 2\overline{u'_y \eta'_y} \\
&\quad + \overline{(v' A'_{xy})}_y + \overline{(u'_y \eta')}_y + \overline{(v'_x \eta')}_y \\
&\quad + \overline{u'_x \xi'_y} + \overline{u'_y \xi'_x} + \overline{v'_x \eta'_y} \\
&\quad + \overline{v'_y \eta'_x} - \overline{(u'_y \eta')}_y - \overline{(u' \eta'_y)}_y \\
&= 0\,.
\end{aligned}$$

A very similar, though tedious, calculation verifies the other equation. Using the previous linear solution, we can get the source inside the fully-developed wave-front to be:

$$S_y(y,t) = \overline{(\eta'_x p')}_y = h_0 k^2 G e^{-ky}\left[\sin(ly) - \cos(ly)\sqrt{\frac{U^2}{G} - 1}\right]\,. \tag{59}$$

Thus we see that the source term drops off exponentially because it gets contribution only from to the evanescent potential flow. Far enough from the boundary, these are source-free wave equations. This is in contrast to the much more difficult situation of the wave equations (44)-(45). The source terms for those equations get contributions from both the potential flow and the vorticity waves and are present even far from the boundary.

5   Spin-up problem

I will present the solution of the wave equations for the fast waves with the perturbation turned on at $t = 0$. The boundary condition of no tangential stress ($A'_{xy} = 0$ at the boundary) gives the boundary condition for $\hat{A}_{xy}$. I define the *drag* D to be $G\hat{A}_{xy}$ at the boundary:

$$D := G\hat{A}_{xy}|_{y=0} = 2G\overline{\xi'_x \eta'_x}\,\big|_{y=0} = \frac{2h_0^2 k^2 G^2}{U^2}\sqrt{\frac{U^2}{G} - 1} > 0$$

First I solve equations (57)-(58) dropping the source term S_y but with the boundary condition

$$\hat{A}_{xy}(y = 0, t) = \frac{D}{G}H(t)\,, \tag{60}$$

where $H(t)$ is the Heaviside step function. This gives the following solution:

$$\hat{A}_{xy}(y,t) = \frac{D}{G}H(\sqrt{G}t - y),$$

(61)

$$\bar{u}^L(y,t) = -\frac{D}{\sqrt{G}}H(\sqrt{G}t - y).$$

(62)

Thus the total mean-flow (including the $O(1)$ and $O(a^2)$ parts) is

$$\bar{u}^L = \begin{cases} U - D/\sqrt{G} & \text{if } y < t\sqrt{G}, \\ U & \text{if } y > t\sqrt{G}. \end{cases}$$

(63)

Now solving these equations by keeping the source term $\partial S(y,t)/\partial y$ but with the boundary condition $\hat{A}_{xy}(y=0,t) = 0$, we get the following solution:

$$\hat{A}_{xy}(y,t) = \frac{1}{G}\left[S(y + \sqrt{G}t) + S(|y - \sqrt{G}t|)\right],$$

(64)

$$\bar{u}^L(y,t) = \frac{1}{\sqrt{G}}\left[S(y + \sqrt{G}t) + S(|y - \sqrt{G}t|)\right].$$

(65)

Since $S(y,t)$ decays exponentially in y, the effect of this term is seen only locally near the wave front. The main effect on the mean-flow is because of the drag at the boundary as given by (62).

Now, I plot the drag as a function of *Mach number* $M := U/\sqrt{G}$ in Fig. 1. We see that the drag reduces as a function of velocity for large background velocity U. Also for a fixed U, decreasing G leads to increasing Mach number and decreasing drag. This suggests that there might be an interesting connection of this problem to drag reduction.

Now we look at the energy conservation for the linear equations. Averaging (10) over x and integrating over y we get:

$$\frac{d}{dt}\int_0^{v_g t}\left(\frac{1}{2}\overline{u'^2} + \frac{G}{4}\overline{\text{tr}(\mathbf{A}'^2)}\right)dy + \int_0^\infty \left(\overline{v'p'} + G\overline{u'A'_{xy}} + G\overline{v'A'_{yy}}\right)_y dy$$

$$= v_g\left(\overline{u'^2} + \overline{v'^2}\right) + \left(\overline{v'p'} - G\overline{u'A'_{xy}} - G\overline{v'A'_{yy}}\right)|_{y=0}^{y=\infty}$$

$$= -(2h_0^2 k^2 G^2/U)\sqrt{U^2/G - 1} + UG\hat{A}_{xy}|_{y=0}$$

$$= -UD + UG\hat{A}_{xy}|_{y=0}$$

$$= 0.$$

This shows that the energy at $O(a^2)$ is carried by the $O(a)$ vorticity waves. This can be seen from, for example, the kinetic energy term $\mathbf{u}^2/2$. The contribution to this term from the $O(a^2)$ mean-flow $\bar{u}$ is only $O(a^4)$. Thus the $O(a^2)$ contribution comes only from the $O(a)$ disturbance solution.

The momentum balance is given by integrating the momentum equation:

$$\frac{d}{dt}\int_0^{\sqrt{G}t}\bar{u}^L dy - \int_0^\infty G\hat{A}_{xy,y}dy - \int_0^\infty S_y dy$$

$$= \sqrt{G}\bar{u}^L - G\hat{A}_{xy}|_{y=0}^{y=\infty} - S|_{y=0}^{y=\infty}$$

$$= \sqrt{G}\bar{u}^L + G\hat{A}_{xy}|_{y=0}$$
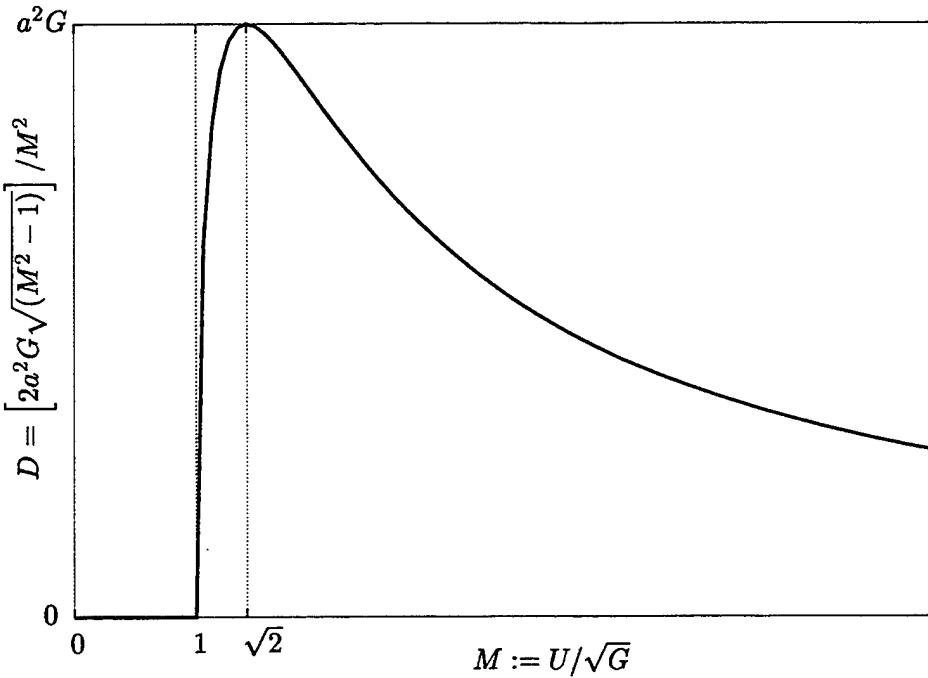
$$= 0.$$

142

Figure 1: Drag on the mean-flow as a function of Mach number

Thus we see that the momentum at $O(a^2)$ is carried by the fast moving mean-flow response. This is because momentum is linear in, for example, u and the $O(a)$ disturbance part does not make any contribution.

The curious difference between the speeds of propagation of the $O(a)$ disturbance waves and $O(a^2)$ mean-flow response gives rise to separation between energy and momentum of the flow at $O(a^2)$. Suppose that the perturbation is kept on from $t = 0$ to $t = T$. Also assume T to be large enough for the stationary waves to develop fully. Then, at some later time $t \gg T$, the wavefront of the slow $O(a)$ vorticity waves will be traveling at a speed $v_s := \sqrt{G}\sqrt{1 - G/U^2}$ and these are the waves that carry the energy from the boundary. But the fast $O(a^2)$ waves (the mean-flow response), which carry the momentum from the boundary, will be traveling at a speed $\sqrt{G}$. Also, the effect on the mean-flow is seen even before the $O(a)$ waves arrive! This is shown in Fig. 2.

6 Conclusion

We have studied the various phenomena associated with waves propagating in the inviscid relaxation-less Oldroyd-B fluid. One of the main results is that the waves do not directly affect the mean-flow in the sense that the region where the mean-flow is affected can be separate from the region where the waves actually exist. The results were obtained by using the Generalized Lagrangian Mean theory.

There are several directions in which these results can be extended. Studying the full Oldroyd-B equations (with viscosity and relaxation) will be interesting. This might change
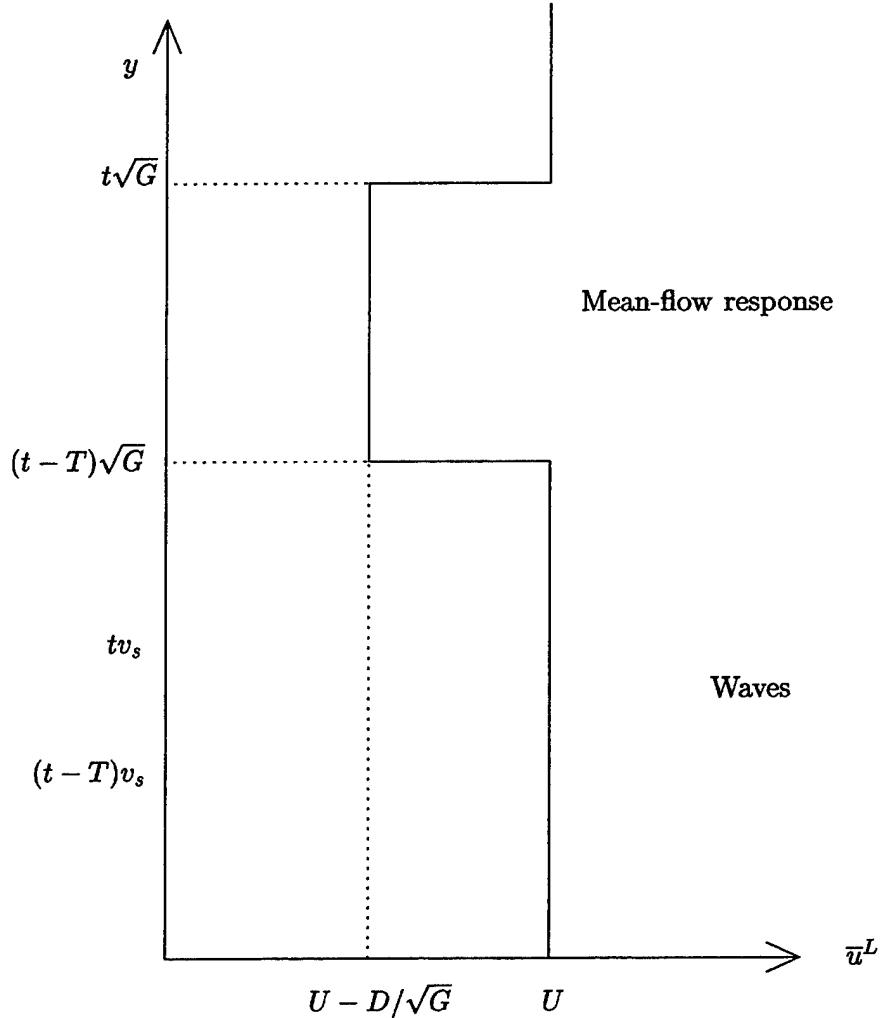
Figure 2: Mean-flow response due to the waves. Here v_s is the speed of the vorticity waves, shown by the shaded region.

the results significantly because we will need to use the no-slip boundary condition instead of free-slip condition. The inviscid relaxation-less model can be studied in the Hamiltonian formulation [using a non-canonical Poisson bracket and the Hamiltonian given by the left hand side of (4)]. Such an approach is developed in [4]. Studying the Lagrangian-mean theory in this Hamiltonian formulation can give insights into the (pseudo)energy and momentum equations. The interesting result about decrease in drag as a function of velocity can have some implications for turbulent drag reduction!

Acknowledgments

References

[1] D.G. Andrews and M.E. McIntyre. An exact theory of nonlinear waves on a lagrangian-mean flow. *J. Fluid Mech.*, 89:609–646, 1978.

[2] D.G. Andrews and M.E. McIntyre. On wave-action and its relatives. *J. Fluid Mech.*, 89:647–664, 1978.

[3] Oliver Bühler. On the vorticity transport due to dissipating or breaking waves in shallow-water flow. *J. Fluid Mech.*, 407:235–263, 2000.

[4] B.J. Edwards and A.N. Beris. Non-canonical poisson bracket for nonlinear elasticity with extensions to viscoelasticity. *J. Phys.*, A 24:2461–2480, 1991.

[5] Gordon I. Ogilvie and Michael R. E. Proctor. On the relation between viscoelastic and magnetohydrodynamic flows and their instabilities. *J. Fluid Mech.*, 476:389–409, 2003.

Diffusively-driven overturning of a stable density gradient

Andrew F. Thompson

1 Introduction

Oceanographic observations from CTD (conductivity, temperature and depth) casts have shown that rapid reversals in the gradient of temperature and salinity with depth is a common feature in many areas, especially in polar regions [14, 12]. These oscillations in temperature and salinity which are typically on the order of tens of meters are thought to be a signature of horizontal intrusions. These intrusions are often referred to as thermohaline intrusions because they are driven by processes related to the different diffusing properties of heat and salt, or what is commonly known as double diffusion.

Double diffusion can occur when two components contribute to the density of a fluid (such as heat and salt in the ocean), but they diffuse at different rates. Double diffusive convection refers to the case when one of the components is stably stratified, the second component is stratified in a destabilizing sense, but the fluid is overall stably stratified. Double diffusive convection is the process by which potential energy stored in the destabilizing component is released. There are two possible configurations for double diffusion at an interface between two fluids. If the slower diffusing component is destabilizing, this is known as a fingering interface and if the faster diffusing component is destabilizing this is known as a diffusive interface. A complete review of double diffusion can be found in the seminal work on buoyancy effects in fluids by Turner [13] and a discussion of double diffusive processes important in the ocean can be found in the review by Schmitt [9].

To understand how double diffusion can generate thermohaline intrusions first consider lateral, density-compensating gradients of temperature and salinity and a vertical stratification that supports salt fingering for example. If this basic state is then perturbed by alternating shear zones, the lateral gradients will create alternating regions where the salt fingers are strengthened (when greater concentrations of salt run over colder water) and weakened (when colder water is over salty water). Since fingering leads to a downward density flux, the regions above increased fingering (the warm salty water) become lighter. If there is some initial slope to the sheared perturbations the warm salty water will continue to rise and propagate, while the cold fresh regions will sink while propagating in the opposite direction. A schematic of this model, which was first explained by Stern [11] and reviewed recently by Ruddick and Kerr [6], appears in figure 1.

While the model described above assumes that the vertical density gradient is initially stratified in a fingering sense, there have been observations of intrusion formation in regions where the ocean is stably stratified in both temperature and salinity [12]. This raises the
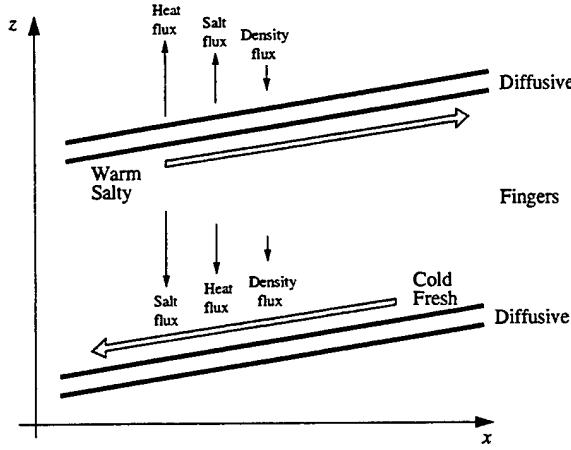
146

Figure 1: Schematic diagram of a thermohaline intrusion [6]. In the fingering region between the two diffusive interfaces, the downward density flux causes the warm, salty fluid to rise as it propagates to the right, while the cold, fresh fluid becomes denser and sinks.

question of how thermohaline intrusions can form in the lack of a vertical stratification that supports double diffusion.

The aim of this project is to present a model for intrusion formation driven by vertical diffusion in a layer of constant density, but lateral gradients of two diffusing components. The layer sits above a reservoir that has higher concentrations in both components so that the system is stably stratified in both components. In section 2 we briefly discuss previous laboratory experiments that have considered similar problems. In section 3 and 4 we describe the experiments carried out over the summer and our observations. In section 5 we present a simple model of how density and the intrusion lengths evolve. Section 6 contains results from our experiments and a discussion of how they compare to the theory, and we finish with some conclusions and suggestions for future work in section 7.

2 Previous Experiments

There has been a number of previous studies considering laboratory models of intrusion formation in double diffusive systems. All of the models discussed here use a sugar–salt system as opposed to a heat–salt system. This is a common practice in laboratory work because of the complications that arise due to heat losses through the walls of the experimental tank. For this same reason we also use a sugar–salt system in the experiments to be described below. It should be noted that while heat diffuses 100 times faster than salt, in the sugar–salt system, salt diffuses only three times as fast as sugar. Traditionally T (here, salt) refers to the faster diffusing component and S (here, sugar) refers to the slower diffusing component.

Ruddick and Turner [8] in a study familiarly known as the "Christmas tree experiment," first looked at horizontal intrusions from a stable density gradient. They filled the left and right hand sides of a divided tank with a stably stratified sugar and salt solution respectively. The stratifications were set up so that there were no horizontal density gradients anywhere.

147

At the start of the experiment the barrier was removed which created perturbations that allowed both fingering and diffusive interfaces to form. The study found that fingering dominated the vertical fluxes; sugary intrusions, which lost density through sugar fingers, rose as they propagated to the right, while salty intrusions fell as they propagated to the left. A series of intrusions formed in the tank, the height of which was determined by the initial density stratification. Ruddick, Phillips and Turner [1] returned to these experiments and completed a more thorough study that included theories for the propagation speed of the noses and overturning circulations that occur within each intrusion.

Noting similarities between thermohaline intrusions and gravity currents, Maxworthy [5] completed an experimental study on double diffusive gravity currents. He considered both the release of a fixed volume of fluid and a constant inflow for both diffusive and fingering interfaces. Maxworthy found that horizontal momentum could be transferred across the interface of the current and in many cases this transfer dominated the viscous forces more commonly associated with gravity currents. This process was modeled as a double diffusive retarding force that depended on both the horizontal velocity of the current and a vertical velocity defined by the ratio of the vertical flux to the vertical density gradient of the more rapidly transferred component (S for a fingering interface and T for a diffusive interface).

Yoshida, Nagashima and Ma [4] later used this double diffusive retarding force to help explain their observations of double diffusive lock exchange experiments. The experiments considered homogeneous solutions of sugar and salt separated by a barrier. A slight density difference between the two sides of the tank determined whether the sugar solution ran under the salt solution and generated a diffusive interface or alternatively the sugar solution ran over the salt solution and formed a fingering interface. Yoshida *et al.* found that the length of the intrusions grew linearly with time, and they developed a simple theory to explain this linear relationship.

3 Experimental Procedure

Before each experiment four solutions, corresponding to the four regions marked in figure 2, were prepared using distilled water, pure cane sugar (obtained from a grocery store) and kosher salt. Solutions 1 and 2 had a density of approximately 1.02 g/cm^3, but contained different concentrations of sugar and salt. In one configuration the contribution of sugar to the density of solution 1 was twice that of salt, while in solution 2, the contribution of salt to the density was twice that of sugar. In the second configuration, solution 1 contained only sugar and solution 2 contained only salt. In all experiments solution 1 was dyed blue. By diluting with distilled water, the densities of these two upper layers were set equal to $\pm 5 \times 10^{-6}$ g/cm^3 using an Anton Paar precision densitometer. Solution 3, composed of both salt and sugar, had a density of 1.05 g/cm^3 with the same concentration of salt as solution 2. Finally solution 4 had a density of 1.065 g/cm^3 with again the same salt concentration as solutions 2 and 3. The appropriate quantities of salt and sugar necessary to create these solutions were determined from Ruddick and Shirtcliffe [7]. The solutions were allowed to sit overnight to achieve room temperature. This minimized the effects of temperature fluctuations and heat diffusion in the experiments.

The experiments were conducted in a Perspex tank 60 cm long, 20 cm deep and 10 cm wide. The tank was fitted with a lock gate that could be raised to any height and fixed in
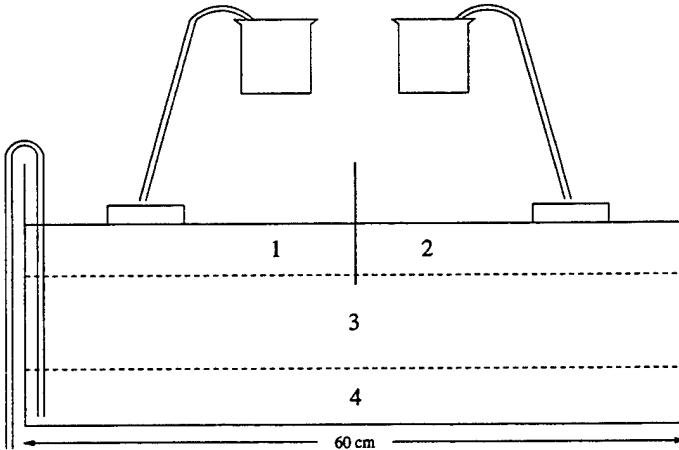
Figure 2: Diagram of laboratory equipment. Solutions 1 and 2 have the same density, but are composed of different concentrations of sugar and salt. The density due to sugar is larger in solution 1 than solution 2. Solution 3 is denser than 1 and 2, but contains the same amount of salt as solution 2. Solution 4 is denser than solution 3, but again contains the same amount of salt as 2 and 3. A barrier separates solutions 1 and 2 before the start of the experiment and fluid from region 4 is removed with a siphon to lower the surface and initiate the experiment.

place with a small clamp. This gate was used to separate solutions 1 and 2 until the start of the experiment. The different solutions were layed down in the tank as depicted in figure 2. The fluid was poured through siphons at a flow rate of approximately 3 mL/s onto sponges floating on the surface in order to minimize mixing. The thickness of the upper layer was varied in each experiment; layers 3 and 4 were generally 1.5 to 2 cm thicker than the upper layer.

The experiments were initiated using a new method for lock release. In similar experiments the barrier is removed by manually or mechanically pulling it out of the tank. Here we removed water from layer 4 by use of a siphon. This lowered the surface of the entire system at a slow rate until the surface was entirely below the barrier.

After initiation, measurements were made using a number of visualization techniques including shadowgraphs, still photography and time-lapse video. Measurements were made of the propagation of the intrusions as they formed. Flow visualization was also aided by dropping potassium permanganate crystals in the flow at different times during the experiment. Samples were removed at various locations and times using a syringe and density measurements were made using the precision densitometer.

Parameters varied in the system were the initial thickness of the upper layer, and the variation in properties across the barrier in the upper layer. These parameters are listed in table 1, where configuration 1 refers to mixed solutions in the upper layer and configuration 2 refers to pure sugar/pure salt solutions in the upper layer.

Experiment Number	Configuration	Initial upper layer depth h_0 (cm)
14	1	1.5
12	1	1.8
15	1	2.0
17	1	2.2
9	1	2.5
16	1	4.8
8	1	8.0
19	2	1.2
21	2	1.3
18	2	1.8
26	2	2.0
22	2	2.5
25	2	3.0
24	2	5.0
27	2	2.5

Table 1: Parameters varied in the experiments. Configuration 1 refers to mixed solutions where sugar contributes twice as much as salt to the density on the left hand side of the barrier, and salt contributes twice as much as sugar to the density on the right hand side. Configuration 2 refers to a pure sugar solution on the left hand side and pure salt solution on the right hand side. Experiment 27 was carried out to measure density as a function of time.

4 Observations

4.1 Initiation

As soon as the sugary upper layer solution was added to the top layer, salt began to diffuse upward from the reservoir below. Since the salty layer had the same salt concentration as the reservoir no salt diffused upward. Therefore, the bottom of the sugary layer became more denser than the salty layer. As fluid was siphoned out of the lowermost layer, the right and left sides of the upper layer came into contact at time $t = 0$. Observations showed that the densities could be calibrated such that in most experiments there was a period of five to ten seconds where neither fluid showed a net propagation into the opposite region. This was then followed by a slight intrusion of sugary fluid (dyed blue) toward the right. The shape of this intrusion was a very thin wedge with no turbulent motions apparent near the nose. This intrusion of sugary fluid in turn induced a return flow into the left hand side simply by mass conservation. Figure 3a shows a photograph of an experiment after these initial intrusions.

Since salty fluid pushed into a region with sugary fluid above, sugar fingers formed that vigorously mixed the region to the left of the barrier (figure 3b). This caused fluid depleted of sugar to become buoyant, rise and pool at the surface to the left of the rising barrier. Once reaching the surface the lighter fluid began to propagate to the left into the sugary region while remaining at the surface.

While vigorous convection characterized the initiation of this experiment, the turbulent nature of the flow quickly resolved itself into a sharp diagonal interface that linked the leftward moving upper intrusion and the rightward moving lower intrusion (figure 3c). Despite the vigorous convection, there still seemed to be minimal mixing of salty and sugary fluid as evidenced by the lack of mixing of the blue dye. Once this interface formed, strong convective plumes were observed both above and below the interface. In general, the greater the depth of the upper layer and the larger the salt and sugar contrast across the barrier the stronger the convective plumes appeared to be.

4.2 Intrusion shape

As the lower, sugary intrusion received salt from both the lower reservoir and the fluid above, it continued to become denser and propagated to the right along the interface between the upper layer and the reservoir (figure 4). The current intruded as a wedge and did not exhibit the turbulent head common to gravity currents in a homogeneous ambient. The flow of the current was on the order of 1 cm/min, but seemed to depend strongly on the depth of the upper layer. The interface between the dyed lower intrusion and the clear upper intrusion appeared to be a straight line connecting the fronts, with some small curvature at the noses.

The current propagating to the left at the surface seemed to move at a nearly constant velocity that was also dependent on the height of the upper layer. In all experiments the leftward moving intrusion hit the end wall first and generally did not seem to slow upon nearing the end wall. The rightward moving lower intrusion did slow upon nearing the end wall.

In all the experiments with a small aspect ratio, only two layers were observed to form in the upper region with the clear, salty layer running over the dyed, sugary layer. The interface
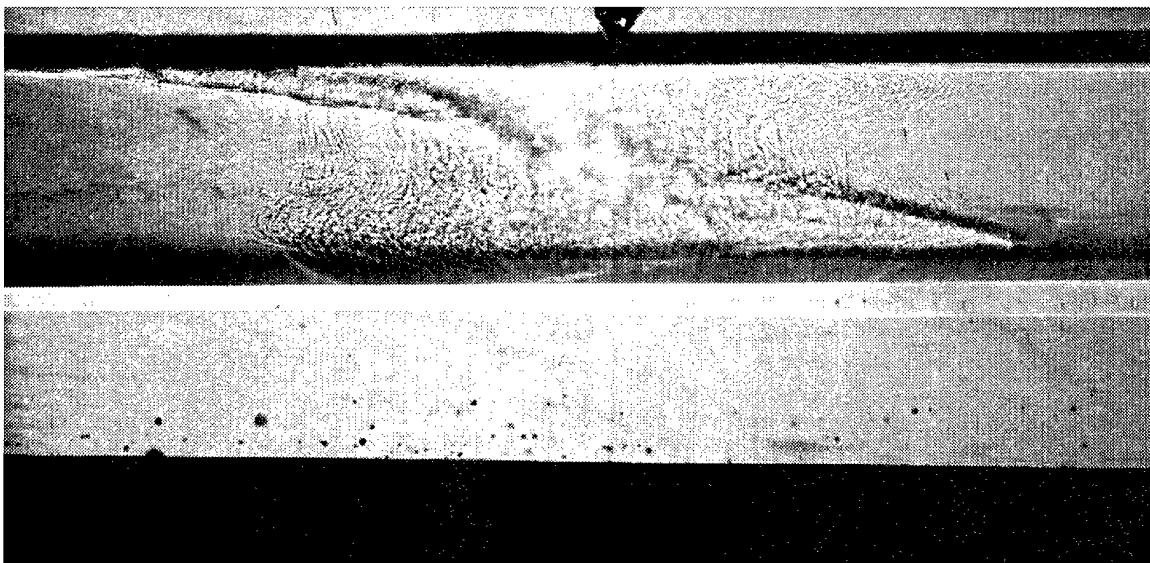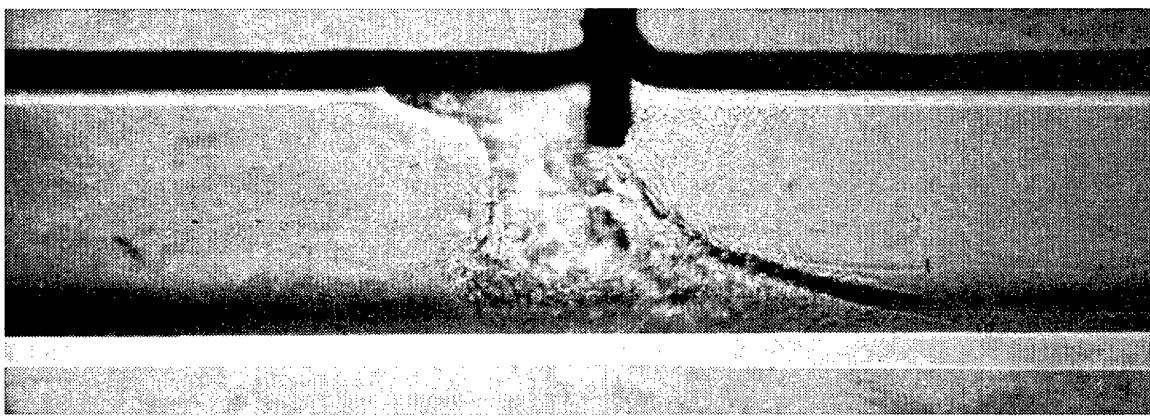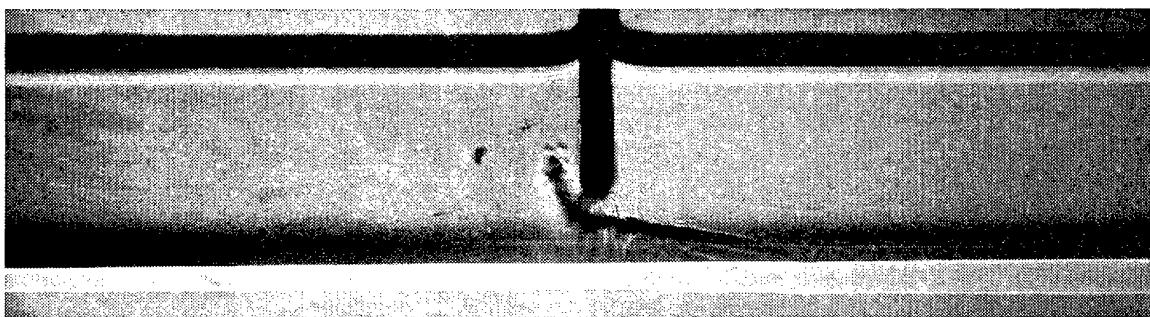
Figure 3: Photographs of initiation of experiment 25 at (a) $t = 58$ s, (b) $t = 122$ s, (c) $t = 184$ s.
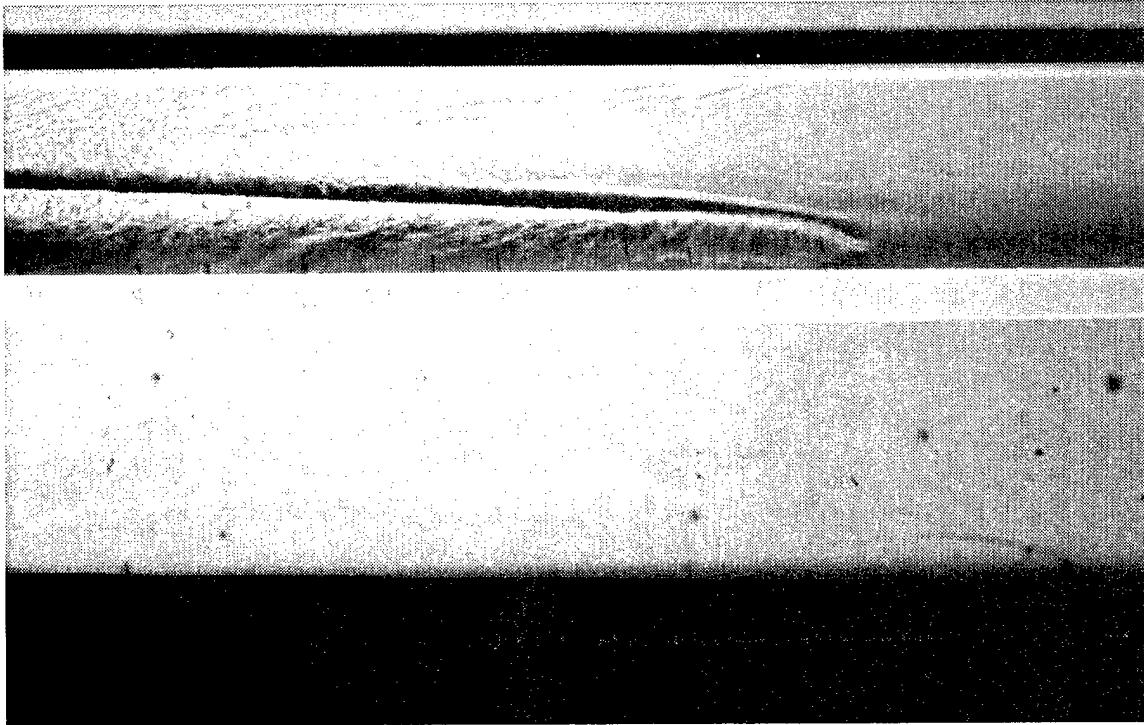
152

Figure 4: Photograph of right-moving lower intrusion from experiment 25 at $t = 10:50$.

between these two regions remained sharp throughout the experiment until convection ran down and diffusion started to thicken the interface slowly. Convection lasted for most of the experiment although it weakened steadily throughout. The convective motions appeared to have a vertical length-scale, which was most likely determined by the shear in the two layers discussed below. Convection was not observed in a region extending a centimeter or two behind the head of the current (figure 4). It is possible that this length-scale is related to the diffusivity of the salt and the velocity of the nose.

4.3 Velocity structure

Besides the leftward and rightward propagation of the upper and lower intrusions respectively, there was also an overturning circulation within each layer. The sense of this circulation was clockwise in both layers and in general the velocities were greater than those of the intrusions. This feature was observed and commented upon by Ruddick *et al.* [1]. Visualization with the use of dye crystals showed strong shear occurred along the interface between the two regions of fluid as the horizontal velocity is to the left (up slope) in the upper layer and to the right (down slope) in the lower layer. Return flows were to the right near the surface in the upper layer and to the left near the interface with the reservoir in the lower layer. Observations also seemed to indicate regions of high shear both near the surface and at the interface between the upper layer and reservoir. Dye crystals that fell through the upper layer showed that velocities in the lower reservoir were very small compared to the velocities in the upper layer. While we expect no net transport over the entire height

of the upper layer, there was a net transport of fluid to the left in the clear layer and a net transport to the right in the blue-dyed layer since the sloped interface continued to flatten until it appeared horizontal.

5 Some Simple Theory

5.1 Initiation

We begin this section by writing down the governing equations for our experiment. We assume a two-dimensional, incompressible, Boussinesq salt and sugar system (T and S respectively). The equations of motion are given by

$$\xi_t + J(\psi, \xi) = -g\left(\alpha T_x + \beta S_x\right) + \nu \nabla^2 \xi, \tag{1}$$

$$T_t + J(\psi, T) = \kappa_T \nabla^2 T, \tag{2}$$

$$S_t + J(\psi, S) = \kappa_S \nabla^2 S, \tag{3}$$

$$w = \psi_x, \quad u = -\psi_z, \quad \xi = \nabla^2 \psi, \tag{4}$$

$$\rho = \rho_0 \left(1 + \alpha T + \beta S\right) \tag{5}$$

where

$$\alpha = \frac{1}{\rho_0}\frac{\partial \rho}{\partial T}, \qquad \beta = \frac{1}{\rho_0}\frac{\partial \rho}{\partial S} \tag{6}$$

are the coefficients of expansion of salt and sugar respectively and J represents the Jacobian. These equations represent the curl of the horizontal and vertical momentum equations, conservation of salt, conservation of sugar and conservation of mass. It is quickly apparent from these equations that it would be difficult to solve these equations analytically, and even numerically it would be a non-trivial task. Therefore, in the scope of this project we have attempted to understand parts of the problem rather than a complete solution.

We first considered the initiation of the experiment by assuming that the barrier is removed instantaneously without any disturbances at time $t = 0$. Because of the differences in diffusion rates, we expect that at early times we can neglect the effects of sugar diffusion.

A simple problem is to consider the horizontal diffusion of salt across the vertical interface separating the two regions in the upper layer. At early times we assume the non-linear terms in the governing equations above are small and that across the front $\partial_x \gg \partial_z$. We simply solve the diffusion equation,

$$T_t = \kappa_T T_{xx} \tag{7}$$

with the boundary conditions $T \to 0$ as $x \to -\infty$ and $T \to \Delta T_0$ as $x \to +\infty$. Solving these equations gives us a solution in terms of the error function, but we will choose to solve the diffusion equation using Laplace transforms so we can use the solution in the momentum equation as well. After taking the Laplace transform of equation 7 and the boundary conditions we find the solution in Laplace space is given by

$$\tilde{T} = \frac{\Delta T_0}{2s}\left(2 - \exp\left[-\sqrt{\frac{s}{\kappa_T}}x\right]\right) \qquad x > 0 \tag{8}$$

$$\tilde{T} = \frac{\Delta T_0}{2s}\exp\left[\sqrt{\frac{s}{\kappa_T}}x\right] \qquad x < 0. \tag{9}$$
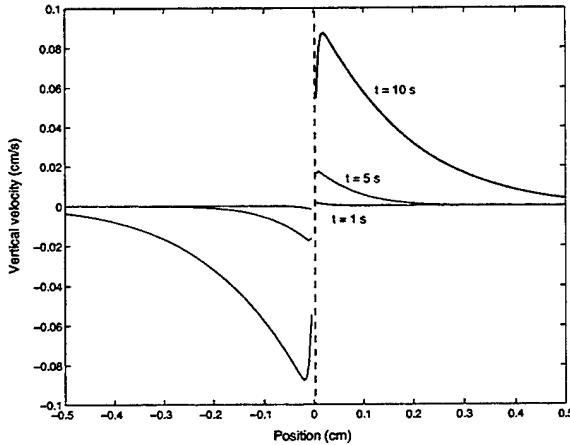
Figure 5: Plot of vertical velocity as a function of position from the vertical interface at various times caused by horizontal diffusion of salt.

Neglecting the nonlinear terms in the curl of the momentum equation and dropping derivatives with respect to z we seek to solve,

$$\psi_{xxt} = -g\alpha T_x + \nu\psi_{xxxx}. \tag{10}$$

Again we proceed by taking the Laplace transform of this equation, and apply the expressions for $\tilde{T}$ that we found above. We can solve this equation for $\tilde{\psi}_{xx}$ and integrate once with respect to x. We then transform back to the time domain using the convolution theorem to find ψ_x or

$$w = \frac{g\alpha\Delta T_0}{2\nu}\left(\frac{1}{\nu} - \frac{1}{\kappa_T}\right)^{-1}\left(\int_0^t [\text{erfc}(\eta_\kappa) - \text{erfc}(\eta_\nu)]\,du\right), \qquad x > 0, \tag{11}$$

where $\eta_\kappa = x/2\sqrt{\kappa_T u}$ and $\eta_\nu = x/2\sqrt{\nu u}$. Using the same procedure we can find the vertical velocity for $x < 0$, and find that it is just the opposite of the expression given above. A plot of the vertical velocity as a function of distance from the interface at various times using parameters typical from our experiments is shown in figure 5. As we expect, salt diffuses horizontally from positive to negative x generating a larger density that drives a downward flow for $x < 0$ and reducing the density and driving an upward flow for $x > 0$. This seems to indicate that an instability could occur even without the lower reservoir. We expect the reservoir has a much larger effect, though, and we are planning further experiments to test this more thoroughly.

We next consider diffusion of salt across the horizontal interface between the dense lower reservoir and the sugar solution in the upper layer. Once again we will neglect the effects of sugar diffusion and only consider vertical derivatives since they are much larger than the horizontal derivatives at early times. We consider the diffusion equation

$$T_t = \kappa_T T_{zz}, \tag{12}$$

which we can solve in terms of an error function and then use to express the density in the

155

upper layer as a function of vertical position and time. Using equation 5,

$$\rho = \rho_0 \left(1 + \alpha \Delta T_0 + \frac{\alpha \Delta T_0}{2} \text{erfc}(\eta_z) \right), \tag{13}$$

where $\eta_z = z/2\sqrt{\kappa_T t}$, and ΔT_0 is the initial salinity difference across the interface.

As a simple analysis at this point, we can argue that the region that gained density due to diffusion will intrude into the salty fluid as a gravity current. We can estimate the increase in density due to diffusion by taking the mean density increase across the diffusive boundary layer $\sqrt{\kappa_T t}$. Rather than integrating (13), we can take the density gradient as linear to leading order to find that the mean density change is given by

$$\Delta \rho = \frac{\rho_0 \alpha \Delta T}{4}. \tag{14}$$

A gravity current is characterized by the Froude number, $\text{Fr} = u/\sqrt{g'h}$. Here $g' = g\Delta \rho / \rho_0$ is the reduced gravity and we take the length scale h to be the diffusive length scale $\sqrt{\kappa_T t}$. Typically $Fr = 1$ at the nose of a gravity current. Considering times less than one minute, $t \sim O(10)$, we find that $u \approx 0.5$ cm/s. Although this represents an extremely thin layer of fluid, the velocity determined by this simple method is much larger than the velocities observed in the experiments.

One likely reason for the disagreement is that the horizontal interface is not actually sharply defined. In the process of filling the tank, some mixing occurs that leads to a thin region of stratification on both sides of the barrier. This then makes it much more difficult to quantify the rate at which salt diffuses from the reservoir into the upper layer. Ruddick et al. [1] found that the velocity of intrusions propagating into a stratified ambient scaled like Nh, where N is the buoyancy frequency. The quantity u/Nh is equivalent to a Froude number, and they also found the velocity was much smaller than expected for gravity current dynamics. Their results showed,

$$u \sim 0.005 Nh. \tag{15}$$

Ruddick et al. did not provide an explanation for the small size of the Froude number, and it is a problem that begs further study.

An important quantity in double diffusive convection is the flux ratio γ defined as

$$\gamma = \frac{\beta F_S}{\alpha F_T} \tag{16}$$

for a diffusive interface, and the reciprocal of (16) for a fingering interface (so that γ is always less than 1). Measurements of γ have shown that its value depends on the density ratio, which is given by

$$R_\rho = \frac{\beta \Delta S}{\alpha \Delta T} \tag{17}$$

for a diffusive interface. For $R_\rho > 2$, Turner [13] has found that

$$\gamma = \sqrt{\frac{\kappa_S}{\kappa_T}}. \tag{18}$$

156

As R_ρ approaches 1, though, the value of γ also approaches 1. Turner interpreted this result by arguing that as R_ρ approaches 1, convection becomes more turbulent and therefore the same processes are transporting both diffusing components and the ratio of the fluxes are approximately equal. At the initiation of our experiments, the value of R_ρ has carefully been set to 1 so that density is compensated across the front. This may indicate that although we observe strong turbulent motions, there may be very little change in density associated with these motions.

5.2 Intrusion propagation

A second approach we have taken to modeling the rightward and leftward moving intrusions is based on the work on Yoshida *et al.* [4]. We assume that after some period of time the vertical interface between the salt solution and sugar solution has tilted so that salty water is riding over fresh. As an initial condition we assume that the density jump across the interface is still zero which may be accurate for early times if the flux ratio γ is close to 1 as discussed above.

We can write that the change in density in the salty solution is due to a flux of salt out of this layer and a flux of sugar into this layer. This can be written as

$$\frac{d\rho_T}{dt} = -\alpha F_T \frac{1-\gamma}{h_0/2}, \tag{19}$$

where ρ_T is the density in the salty layer and h_0 is the initial depth of the upper layer. This model assumes that the layers are well mixed and that the density is a function of time only. The factor of 2 is a geometrical factor included because the current is approximately triangular. We note that this is a simplified model as our measurements have indicated that there are spatial gradients in the density field.

The flux of salt across the interface can be related to the change in the salinity difference across the interface,

$$\alpha F_T = \frac{\rho_0 h_0}{2} \frac{d}{dt} \left(\alpha \Delta T \right). \tag{20}$$

Finally a third equation is needed as a parameterization of the salt flux as a function of the salt gradient. A review of flux laws for double diffusive convection across a diffusive interface is given in Kelley *et al.* [3]. For simplicity we use the flux relationship determined by Turner [13] where he argued that for turbulent convection

$$\alpha F_T = C(\alpha \Delta T)^{4/3}, \tag{21}$$

where C is a dimensional constant that depends on the solution properties and the density ratio R_ρ [10]. It is more difficult to judge the validity of assuming that C is a constant because in the scope of this project we were unable to measure concentrations of salt and sugar separately, and therefore it is difficult to estimate how R_ρ changes over the course of the experiment.

At this point we can use equations (20) and (21) to find an expression for the salt jump across the interface as a function of time,

$$\alpha \Delta T = (\alpha \Delta T_0)(1 + t/\tau)^{-3}, \tag{22}$$

157

where τ is a time scale given by

$$\tau = \frac{3\rho_0 h_0}{2C(\alpha\Delta T_0)^{1/3}}.$$ (23)

Assuming $R_\rho \approx 2$ in determining C, and using parameters from our experiments we find that $\tau = O(10^3\text{s})$. We note here that we expect R_ρ to be small based on the propagation speed of our current (density differences must be small), but there are also large fluctuations in the value of C for $1 < R_\rho < 2$.

Finally we can use equations (21) and (22) to integrate equation (19) with time. From this we obtain

$$\rho_T = \rho_0 \left[1 + \alpha\Delta T_0(1-\gamma)(1+t/\tau)^{-3} + \alpha\Delta T_0\gamma\right].$$ (24)

The density in the lower, sugary layer can be determined in a similar manner and using the fact that $\alpha\Delta T_0 = \beta\Delta S_0$ we find,

$$\rho_S = \rho_0 \left[1 - \alpha\Delta T_0(1-\gamma)(1+t/\tau)^{-3} + \alpha\Delta T_0(2-\gamma)\right].$$ (25)

Combining these two equations then gives us an expression for the density difference across the interface as a function of time,

$$\Delta\rho = 2\rho_0(\alpha\Delta T_0)(1-\gamma)\left(1 - (1+t/\tau)^{-3}\right).$$ (26)

We have also analyzed this model for a flux condition that is controlled purely by diffusion. This modification only affects our parameterization of the flux law given in (21), where now the flux of salt across the interface depends on the salinity gradient across the interface. To model this we assumed that there is some length scale h_m associated with the thickness of the interface and that this was maintained at a constant value. We believe that this assumption may be valid while the shear at the interface is high. Then we can write

$$\alpha F_T = \rho_0 \kappa_T \frac{\alpha\Delta T}{h_m}.$$ (27)

Following the same steps as before we can integrate up equations 20 and 27 to obtain

$$\Delta\rho = 2\rho_0(\alpha\Delta T_0)(1-\gamma)\left(1 - \exp\left[-\kappa t/h_0 h_m\right]\right).$$ (28)

Following the work of both Maxworthy [5] and Yoshida et $al.$ [4], we now argue that for most of the experiment, the buoyancy force generated by density differences across the interface is balanced by a double diffusive retarding force. This double diffusive force is given in Maxworthy [5] as

$$F_{DD} = \rho UVL,$$ (29)

where U and V are defined as

$$U = \frac{L}{t}, \quad \text{and} \quad V = \frac{\alpha F_T}{\rho\alpha\Delta T}.$$ (30)

The buoyancy force is given by $F_B = \Delta\rho g h_0^2$, so we can write

$$F_B = 2\rho_0(\alpha\Delta T_0)(1-\gamma)g h_0^2 \left[1 - (1+t/\tau)^{-3}\right],$$ (31)

$$F_{DD} = C(\alpha\Delta T_0)^{1/3}(1+t/\tau)^{-1}L^2 t^{-1},$$ (32)

158

where we have used the four-thirds flux parameterization as opposed to the diffusive flux parameterization. Equating these two forces we obtain a scaling for L,

$$L \propto (\rho_0 g)^{1/2} (\alpha \Delta T_0)^{1/3} h_0 \sqrt{(1 + t/\tau) \left(1 - (1 + t/\tau)^{-3}\right)} \, t. \tag{33}$$

We can show that for both $t \ll \tau$ and $t \gg \tau$, $L \propto t$ from the expression above, and even when $t \sim \tau$ the t dependence is well approximated by a linear curve [4].

6 Results

Figures 6 and 7 show measurements of density as a function of position in the tank after the experiment has neared run-down. All measurements were taken between one hour and one and a half hours after the start of the experiment. On the x-axis, 0 cm corresponds to the lefthand wall of the tank and 60 cm corresponds to the right-hand wall. The clear symbols represent measurements taken in the upper layer above the interface between the two fluids and the closed symbols represent measurements taken below this interface. Note that density decreases upward on the y-axis in figures 6, 7, and 8 for easier interpretation of the graph.

Figure 6 shows the density measurements from the experiments that had mixed initial conditions. In these experiments, the density in the upper layer was 1.02 g/cm^3. Sugar contriubted twice as much to the density in the left side and salt twice as much in the right side leading to a property contrast across the barrier, $\alpha \Delta T_0 = \beta \Delta S_0 = 0.0067$. The data show that there is still a small positive horizontal density gradient. This most likely means that the experiment has not fully run down to completion. The jump in density across the interface is roughly 0.002 g/cm^3. Fewer measurements of density were made in the experiments with pure sugar and pure salt initial conditions, figure 7. It is clear, though, that the density jump is considerably larger than in the other experiments. The density difference here is roughly 0.006 g/cm^3 which is three times as large as $\Delta \rho$ in figure 6. This agrees well with our theory that the run-down density jump across the interface should scale linearly with $\alpha \Delta T_0$, since $\alpha \Delta T_0$ is 0.02 in the pure salt/pure sugar configuration, or roughly three times as large as the mixed configuration experiments.

In experiment 27 we took density measurements at various heights and times in the center of the tank. These values appear in figure 8 with the different symbols representing the location at which the sample was taken as described in the key. As expected, density decreased steadily in the upper layer and increased steadily in the lower layer. Measurements made just above and below the interface (regions 2 and 3) seem to reach a quasi-equilibrium state after approximately 20–30 minutes, while measurements taken near the surface and near the reservoir interface reach nearly steady values after an hour or more. These measurements seem to show that despite the convection observed in the experiments, there may be either a staircase or a stratified density profile. The vertical density structure could depend strongly on the overturning circulation that is observed. We further note that the density change at region 4 is the largest because of the continuous diffusion of salt into this region from the lower reservoir.

From equations (26) and (28) we can see that the run-down time for the density jump across the interface is τ or $h_0 h_m / \kappa_T$ for the four-thirds flux law or the diffusive flux law
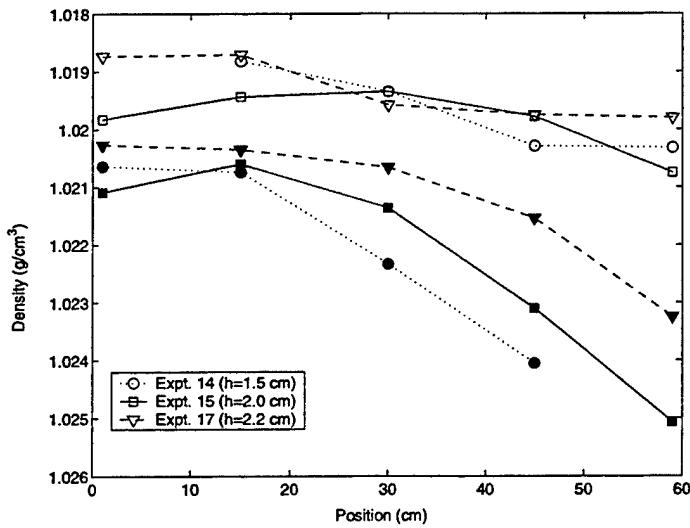
159

Figure 6: Density in the upper layer as a function of position in the tank after run-down (between 60 and 80 minutes after initiation) for mixed solution initial conditions. The open symbols correspond to measurements taken above the interface and closed symbols to measurements taken below the interface. Density decreases along the y-axis.
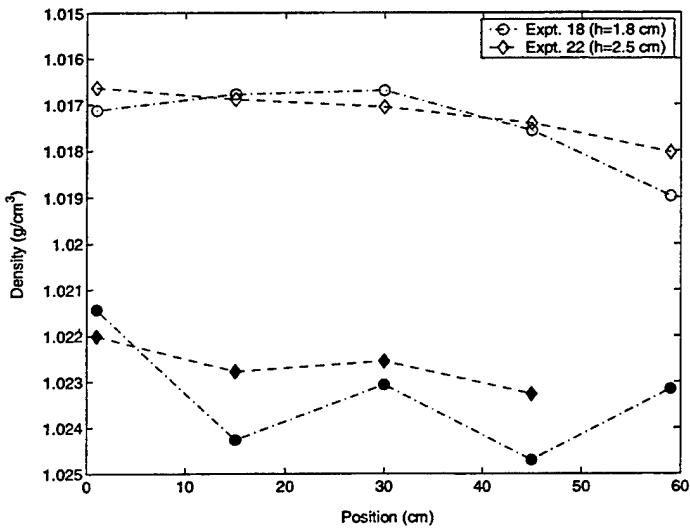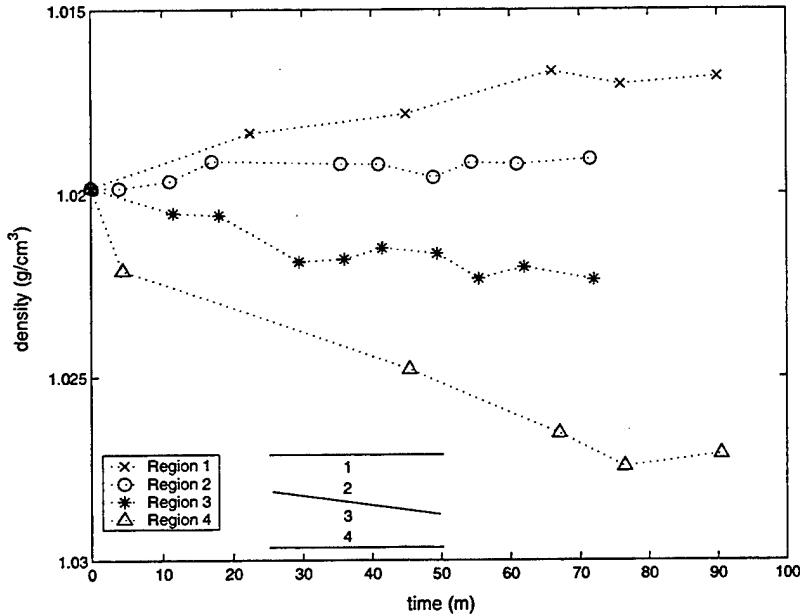

Figure 7: Density in the upper layer as a function of position in the tank after run-down (between 60 and 80 minutes after initiation) for pure salt/pure sugar initial conditions. The open symbols correspond to measurements taken above the interface and closed symbols to measurements taken below the interface. Density decreases along the y-axis.

Figure 8: Density measurements as a function of time from experiment 27. The symbols refer to different heights where samples were removed as indicated in the key above. All samples were removed from the center of the tank.

respectively. As given earlier, $\tau \sim 10^3$ s and

$$\frac{h_0 h_m}{\kappa_T} \sim \frac{1\text{cm}(.05\text{cm})}{1 \times 10^{-5}\text{cm/s}^2} \sim 5 \times 10^3\text{s}. \tag{34}$$

Figure 8 may then indicate that the four-thirds law is a decent approximation close to the interface, but the assumption that both layers are well-mixed is certainly not valid. Also, after run-down, we expect $\Delta\rho \approx 2\rho_0(\alpha\Delta T)(1 - \gamma)$. For a diffusive interface and $R_\rho > 2$, Turner [13] gives $\gamma = 0.577$ for a one-dimensional salt–sugar system. Therefore we expect $\Delta\rho \approx 0.87\rho_0(\alpha\Delta T)$ or 0.0174 g/cm^3 for the pure salt/pure sugar intitial conditions. Our measurements show that the density difference is smaller than this estimate by a factor of 2 or 3. This may be explained by the fact that at least at the initiation of our experiment, $R_\rho = 1$ and as R_ρ approaches 1, γ also approaches 1. Furthermore, our system is two-dimensional, while Turner's value for γ was derived from a one-dimensional system.

Figures 9 and 10 show measurements of the front position of the upper and lower intrusions respectively as a function of time from the experiments with pure salt/pure sugar initial conditions. The various symbols represent different initial thicknesses h_0. From both figures it is clear that the intrusion velocity depends strongly on the layer depth. Both figures have log-log axes and various power law relations are shown with dashed lines for reference. The length of the upper intrusion seems to depend linearly on time, so that the velocity is constant. There are no pronounced end wall effects, although there may be some late-time behaviour and a change in regime for the slowest experiment where $h_0 = 1.2$ cm. Most of the measurements of the lower intrusions seem to indicate that the velocity is approximately constant, although there does seem to be a monotonic increase in slope
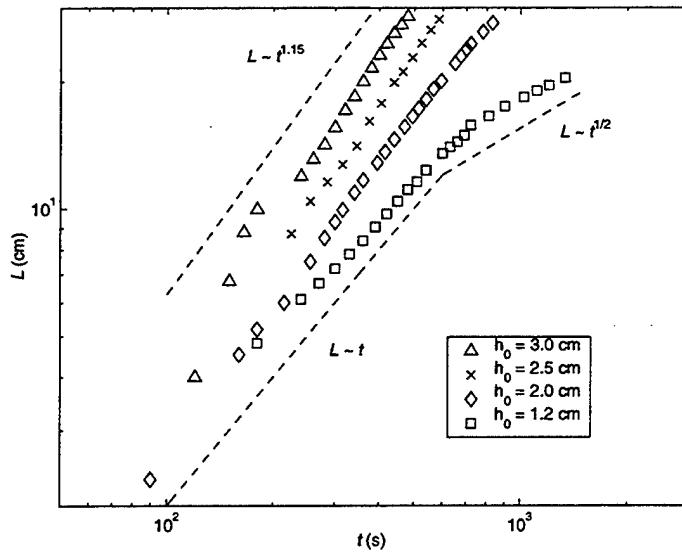
161

Figure 9: Position of upper intrusion fronts as a function of time for pure salt/pure sugar initial conditions. Power law relations are shown with dashed lines for reference.
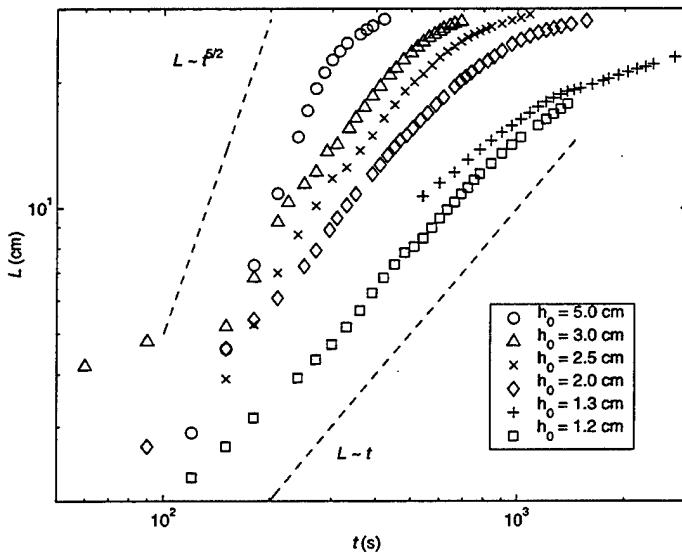

Figure 10: Position of lower intrusion fronts as a function of time for pure salt/pure sugar initial conditions. Power law relations are shown with dashed lines for reference.
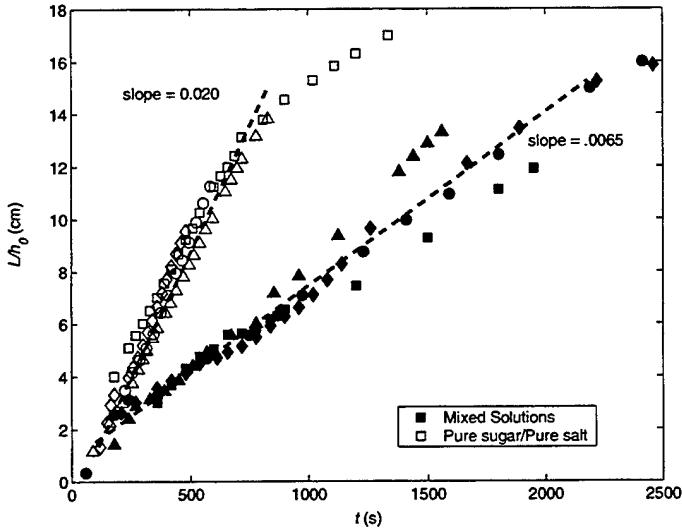
162

Figure 11: Position of upper intrusion fronts non-dimensionalized with respect to upper layer thickness. Open symbols refer to pure salt/pure sugar initial conditions, closed symbols refer to mixed solutions initial conditions.
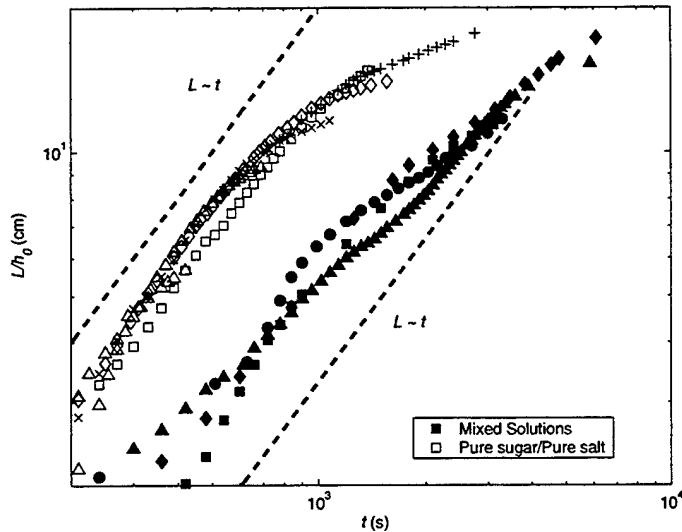
Figure 12: Position of lower intrusion fronts non-dimensionalized with respect to upper layer thickness. Open symbols refer to pure salt/pure sugar initial conditions, closed symbols refer to mixed solutions initial conditions.

163

in figure 10 with increasing layer depth. For a very deep upper layer, $h_0 = 5.0$ cm, the velocity increases with time with $L \sim t^{5/2}$ or $U \sim t^{3/2}$. There is a much more pronounced end wall effect in the lower layer intrusion due to stratification that arises at the upper layer–reservoir interface when filling the tank. This leads to a blocking flow, which feels the presence of the end wall much earlier than the upper intrusion [2].

Finally, in figures 11 and 12 we have non-dimensionalized the length of the intrusions with the initial height h_0, and included both the mixed solution initial condition (closed symbols) and the pure salt/pure sugar initial conditions (open symbols). Figure 11 shows the upper intrusion data, which seem to collapse so that L scales linearly with h_0. This agrees with the force balance argument given in (33). We have also included the average slope, or penetration velocity, of the experiments for both initial conditions. The velocity of the pure solutions is approximately three times larger than the mixed solutions. It is true that $\alpha \Delta T_0$ is three times larger for the pure solutions than for the mixed solutions, but from (33) we expect the velocity to vary like $(\alpha \Delta T_0)^{1/3}$. The data also collapses fairly well when we non-dimensionalize the length of the lower intrusion. The difference in velocities is more difficult to determine in this case due to the strong end wall effects.

7   Conclusions

We have attempted to show how horizontal thermohaline intrusions may develop because of vertical diffusion in a system stably stratified in both S and T. The problem was studied experimentally using sugar and salt solutions. We found that horizontal intrusions that lead to overturning in a layer initially of uniform density, but with horizontally varying concentrations of sugar and salt, can be driven purely by diffusion of the faster diffusing component from below. We also believe that the composition of this lower reservoir plays a large role in determining whether a diffusive or a fingering interface forms. This then in turn governs how sugar and salt are exchanged between the two upper layers. Further experiments will be carried out varying the reservoir concentrations to verify the importance of diffusion at this interface. Hopefully in future experiments we will be able to measure salt and sugar concentrations, which will provide information about the diffusive transfers across the interface and the evolution of the flux ratio. These experiments should offer helpful insights into the formation and mixing properties of thermohaline intrusions in regions such as the Southern Ocean.

References

[1] O. M. Phillips B. R. Ruddick and J. S. Turner. A laboratory and quantitative model of finite-amplitude thermohaline intrusions. *Dyn. Atmos. Oceans*, 30:71–99, 1999.

[2] F. K. Browand and C. D. Winant. Blocking ahead of a cylinder moving in a stratified environment: An experiment. *Geophys. Fluid Dynamics*, 4:29–53, 1972.

[3] A. E. Gargett J. Tanny D. E. Kelley, H. J. S. Fernando and E. Ozsoy. The diffusive regime of double-diffusive convection. *Prog. in Oceanog.*, 56:461–481, 2003.

[4] H. Nagashima J. Yoshida and W. Ma. A double diffusive lock-exchange flow with small density difference. *Fluid Dynamics Res.*, 2:205–215, 1987.

[5] T. Maxworthy. The dynamics of double-diffusive gravity currents. *J. Fluid Mech.*, 128:259–282, 1983.

[6] B. Ruddick and O. Kerr. Oceanic thermohaline intrusions: theory. *Prog. in Oceanog.*, 56:483–497, 2003.

[7] B. R. Ruddick and T. G. L. Shirtcliffe. Data for double diffusers: Physical properties of aqueous salt–sugar solutions. *Deep-Sea Res.*, 26A:775–787, 1979.

[8] B. R. Ruddick and J. S. Turner. The vertical length scale of double-diffusive intrusions. *Deep-Sea Res.*, 26A:903–913, 1979.

[9] R. W. Schmitt. Double diffusion in oceanography. *Ann. Rev. Fluid Mech.*, 26:255–285, 1994.

[10] T. G. L. Shirtcliffe. Transport and profile measurements of the diffusive interface in double diffusive convection with similar diffusivities. *J. Fluid Mech.*, 57:27–43, 1973.

[11] M. E. Stern. Lateral mixing of water masses. *Deep-Sea Res.*, 14:747–753, 1967.

[12] W. Zenk T. M. Joyce and J. M. Toole. The anatomy of the antarctic polar front in the drake passage. *J. Geophys. Res.*, 83:6093–6113, 1978.

[13] J. S. Turner. *Buoyancy Effects in Fluids*. Cambridge University Press, Cambridge, 1973.

[14] D. Walsh and E. Carmack. A note on evanescent behavior of arctic thermohaline intrusions. *J. Mar. Res.*, 60:281–310, 2002.

165

Viscoelastic Catenary

Anshuman Roy

1 Introduction

This paper seeks to determine the shape of a thin viscoelastic fluid filament as it sags under its own weight. The problem is an extension of the viscous catenary [1] and we refer to this problem as "viscoelastic catenary". Viscoelastic filaments appear in applications such as fiber processing from melts and solutions, extensional rheometry etc. An understanding of the dynamics of the viscoelastic catenary will therefore aid in better design of such applications.

2 Experimental Observations

We investigated a Boger fluid composed of 0.025% w/w Polystyrene of molecular weight 1.877×10^6 dissolved in styrene oil. The relaxation time for this fluid is around 4 seconds and its zero-shear viscosity, η_0, is 50 Pa.s. There is no shear thinning in the fluid over several decades of strain rate, and expecially in the regime of our experiments. We took some fluid between two plates and stretched out in the horizontal direction to shape it into a thin filament, $h \ll L$, where h is the thickness of the filament and L is the length to which it is stretched. Figure (1) shows a snapshot of one such experiment with $h = 0.002$ m, $L = 0.025$ m.

Two problems emerged out of this experiment that need to be understood. First is the problem of the viscoelastic catenary, wherein the fluid filament sags under its own weight and its shape evolves with time. Second, is what we refer to as the *chewing-gum* problem. In this problem, fluid between two plates is stretched out into a thin filament and then instantaneously, the two plates are brought closer together. This makes the filament buckle in the direction of gravity, thereby making a viscoelastic catenary to begin with. What happens then is, to our knowledge, a phenomenon unique to viscoelastic fluids only - the catenary starts moving upwards against gravity, like a recoil. However, if the plates are brought together at a rate equivalent to the inverse of the relaxation time of the fluid, we do not see this recoil effect. We refer to this effect as the *chewing-gum* problem because we observed the effect for the first time in a chewing-gum.
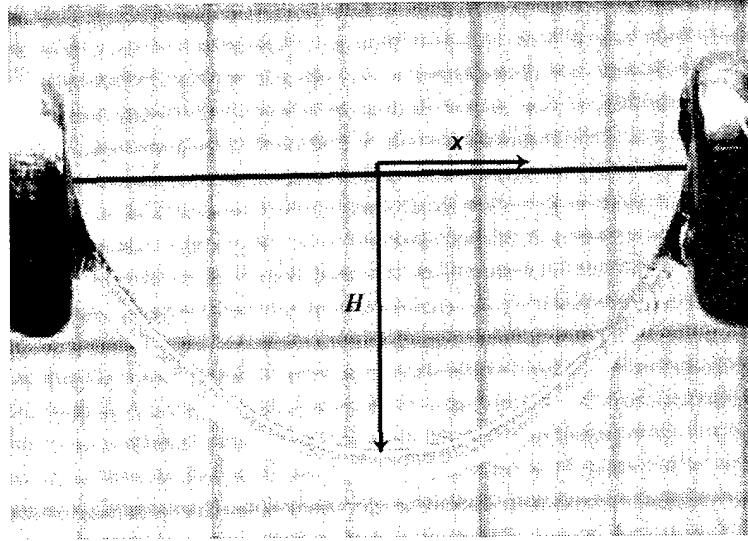
166

Figure 1: Snapshot of a viscelastic catenary.In this case, the fluid used is a mixture of Polystyrene (MW 1.877 x 10^6) in styrene oil - a Boger fluid. The zero shear viscosity is approximately 50 Pa.s and there is no shear thinning for the shear rates under consideration.Squares in the background are 1 mm in dimension.

3   Governing Equations

All the dynamics of a viscoelastic filament can be understood by considering the simpler problem of a 2D sheet. The analysis that we will present is applicable to many viscoelastic systems that do not shear-thin. However, for now consider a solution of polymer molecules in a viscous solvent. The governing equations for the fluid are conservation of mass, conservation of momentum and the closure model to describe the polymer stress within the fluid:

$$\nabla . u = 0 \tag{1}$$

$$\rho \left(u_t + u.\nabla u \right) = -\nabla p + \mu \nabla^2 u + \nabla . \tau - \rho g \tag{2}$$

$$\tau_t + u.\nabla \tau - \left(\nabla u \right)^T . \tau - \tau . \left(\nabla u \right) = -\frac{1}{\lambda} \left(\tau - G \right) \tag{3}$$

where, the subscripts represent differentiation with respect to the subscripted variables. τ is the polymer stress tensor, G is the equilibrium polymer stress and λ is the relaxation time of the polymer molecules. Note that eqs. (1) and (2) not closed without eq. (3) which describes the evolution of polymer stress in the flow, referred to as the Oldroyd-B constitutive model.

In order to make the above equations dimensionless, we choose a velocity scale U and a length scale L. Then, the scaling for time is L/U, where L is the length of the sheet between the clamps. We scale the pressure and polymer stress with $\mu \frac{U}{L}$. We perform the

following expansion:

$$u = u_0 + \epsilon^2 u_2 + O(\epsilon^4)$$
$$\epsilon v = v_0 + \epsilon^2 v_2 + O(\epsilon^4)$$
$$H = \epsilon H_0 + \epsilon^3 H_2 + O(\epsilon^4)$$
$$h = \epsilon h_0 + \epsilon^3 h_2 + O(\epsilon^4)$$
$$p = p_0 + \epsilon^2 p_2 + O(\epsilon^4)$$
$$\tau = \tau_0 + \epsilon^2 \tau_2 + O(\epsilon^4)$$

$$(4)$$

Then the governing equations for a 2D sheet become,

$$\epsilon^2 u_x + v_y = 0 \tag{5}$$

$$\epsilon^4 Re \left(u_t + \epsilon^2 u u_x + v u_y \right) = -\epsilon^2 p_x + \epsilon^2 u_{xx} + u_{yy} + \epsilon^2 \tau_x \tag{6}$$

$$\epsilon^4 Re \left(v_t + \epsilon^2 u v_x + v v_y \right) = -\epsilon^2 p_y + \epsilon^2 v_{xx} + v_{yy} - \epsilon^4 \varpi \tag{7}$$

where, $Re = \rho U L / \mu$ is the Reynolds number and $\varpi = \frac{\rho g}{\mu U / L}$ is the dimensionless weight variable. In the limit of $Ca = \mu U / \gamma \gg 1$, the effects due to surface tension can be ignored. So, we consider traction-free boundaries. At $y = H \pm h/2$, the kinematic boundary condition is:

$$v = \left(H \pm \frac{h}{2} \right)_t + \epsilon^2 u \left(H \pm \frac{h}{2} \right)_x \tag{8}$$

The stress boundary condition results in the following two equations:

$$-\epsilon^2 \left(-p + 2u_x + \tau \right) \left(H_x \pm \frac{h_x}{2} \right) + (u_y + v_x) = 0 \tag{9}$$

$$-\epsilon^2 \left(u_y + v_x \right) \left(H_x \pm \frac{h_x}{2} \right) - \epsilon^2 p + 2v_y = 0 \tag{10}$$

At leading order, $O(1)$, the incompressibility equation reduces to:

$$v_{0y} = 0 \tag{11}$$

The x-momentum and y-momentum balances are respectively:

$$u_{0yy} = 0 \tag{12}$$

$$v_{0yy} = 0 \tag{13}$$

We assume that the polymer stress tensor has only one non-zero component, τ^{xx}, where the superscript refers to the component of the stress tensor. Here onwards, we drop the superscript and refer to τ^{xx} as τ. The Oldroyd-B equation for τ at this order is:

$$\tau_{0t} + v_0 \tau_{0y} = -\frac{1}{Wi} (\tau_0 - G) \tag{14}$$

168

We assume that $\tau_{0y} = 0$. Stretching the filament embeds a stress within the fluid, $\tau_0(0, t) = \tau_0(0)$. Boundary conditions at $y = H \pm h/2$ are:

$$v_0 = \left(H_0 \pm \frac{h_0}{2} \right)_t \tag{15}$$

$$u_{0y} + v_{0x} = 0 \tag{16}$$

$$v_{0y} = 0 \tag{17}$$

Then we conclude that $h_{0t} = 0$. Also

$$v_0 = H_{0t} \tag{18}$$

$$u_0 = H_{0xt}(H - y) + \overline{u_0}(x) \tag{19}$$

where, $\overline{u_0}(x)$ is the velocity of the centerline of the filament, i.e. $y = H_0$. Integrating Eq. (14) gives the equation for the leading order polymer stress that decays with time.

$$\tau_0 = G + (\tau_0(0) - G) e^{-t/Wi} \tag{20}$$

At second order, $O(\epsilon^2)$, the incompressibility equation and momentum balances yield,

$$v_{2y} = -u_{0x} \tag{21}$$

$$p_{0x} - u_{2yy} = u_{0xx} + \tau_{0x} \tag{22}$$

$$p_{0y} = v_{0xx} - u_{0xy} \tag{23}$$

The Oldroyd-B equation becomes

$$\tau_{2t} + v_0 \tau_{2y} + \frac{\tau_2}{Wi} = 2\tau_0 u_{0x} - u_0 \tau_{0x} \tag{24}$$

The kinematic and stress boundary conditions at this order are:

$$v_2 = \left(H_2 \pm \frac{h_2}{2} \right)_t + u_0 \left(H_{0x} \pm \frac{h_{0x}}{2} \right) \tag{25}$$

$$u_{2y} + v_{2x} + p_0 \left(H_{0x} \pm \frac{h_{0x}}{2} \right) = (2u_{0x} + \tau_0) \left(H_{0x} \pm \frac{h_{0x}}{2} \right) \tag{26}$$

$$p_0 = 2v_{2y} \tag{27}$$

Integrating the y-momemtum balance, Eq. (23) and applying the appropriate boundary condition, Eq. (27), we can evaluate the leading order pressure.

$$p_0 = -2u_{0x} \tag{28}$$

To calculate v_2, we integrate the second order incompressibility equation, Eq. (21),

$$v_2 = \frac{H_{0xxt}}{2}(y - H)^2 - T(y - H) + \tilde{v}_2 \tag{29}$$

169

where, $\tilde{v}_2 = H_{2t} + \overline{u_0}H_{0x}$ and $T = \bar{u}_{0x} + H_{0x}H_{0xt}$. Note that T is the viscous contribution to the dimensionless tension in the viscoelastic sheet. The second order horizontal velocity then is

$$u_2 = \frac{H_{0xxxt}}{2}(y-H)^3 - \frac{3}{2}\left(H_{0x}H_{0xxt} + T_x\right)(y-H)^2 - \frac{T_{0x}}{2}(y-H)^2 + k(x)(y-H) + \tilde{u}_2(x) \quad (30)$$

where $k(x) = -H_{0xxxt}h_0^2/2 + (3T + \tau_0)H_{0x} - \tilde{v}_{2x}$ and $\tilde{u}_2(x)$ is the constant of integration.

At this order, the boundary conditions and the equations impose the following solvability conditions:

$$h_{2t} = -\left(\bar{u}_0 h_0\right)_x \quad (31)$$

$$\left[(4T + \tau_0)\,h_0\right]_x = 0 \quad (32)$$

Eq. (32) is a statement of tension balance. Inertia is too small to appear at this order. So the catenary is in a quasi-static balance. At the next order, $O(\epsilon^4)$ the incompressibility, momentum balances and the Oldroyd-B equation are as follows.

$$v_{4y} = -u_{2x} \quad (33)$$

$$-p_{2x} + u_{4yy} = Re\left(u_{0t} + v_0 u_{0y}\right) - u_{2xx} - \tau_{2x} \quad (34)$$

$$p_{2y} = -Re\left(v_{0t}\right) + v_{2xx} + v_{4yy} - \varpi_0 \quad (35)$$

The boundary conditions are,

$$v_4 + v_{2y}\left(H_2 \pm \frac{h_2}{2}\right) = \left(H_4 \pm \frac{h_4}{2}\right)_t + u_2\left(H_{0x} \pm \frac{h_{0x}}{2}\right) + u_0\left(H_{2x} \pm \frac{h_{2x}}{2}\right) \quad (36)$$

$$-\left(-p_0 + 2u_{0x} + \tau_0\right)\left(H_{2x} \pm \frac{h_{2x}}{2}\right) - \left(-p_2 + 2u_{2x} + \tau_2\right)\left(H_{0x} \pm \frac{h_{0x}}{2}\right) + u_{4y} + v_{4x} = 0 \quad (37)$$

$$-\left(u_{2y} + v_{2x}\right)\left(H_{0x} \pm \frac{h_{0x}}{2}\right) - \left[p_2 + p_{0y}\left(H_2 \pm \frac{h_2}{2}\right)\right] + 2\left[v_{4y} + v_{2yy}\left(H_2 \pm \frac{h_2}{2}\right)\right] = 0 \quad (38)$$

Integrating the y-momentum balance, we get another solvability condition. For the sake of simplicity, we assume that $h_{0x} = 0$ and that $\tau_{0x} = 0$. Then,

$$h_0 Re H_{0tt} + \frac{h_0^3}{3}H_{0xxxxt} = (4T + \tau_0)h_0 H_{0xx} - \varpi h_0 \quad (39)$$

We can now rescale Eq. (39) to gain more insight into the problem. All lengths are scaled with L and time with $6\mu/\rho g h$. The centerline velocity at $x = 0$ and the ends of the catenary, $x = \pm 1/2$ is zero. So integrating the first solvability condition, we have that

$$4T + \tau_0 = \frac{8}{L}\left(\int_0^{L/2}(H_x)_t^2\,dx + \tau_0\right) \quad (40)$$

170

which is a statement of tension balance. The second solvability condition becomes,

$$Re_g H_{tt} + \frac{\epsilon^3}{32} H_{xxxxt} = \left(\int_0^{1/2} (H_x)_t^2 \, dx + \Lambda \tau_0 \right) \epsilon H_{xx} - 1 \qquad (41)$$

where we have dropped the subscript "0" from the equation. $Re_g = \left(\frac{\rho g h}{6\mu} \right)^2 \frac{L}{g}$ is the appropriate Reynolds number, often referred to as the Galileo number in engineering circles. $\Lambda = \frac{G}{\rho g h}$, where G is the equilibrium polymer stress. Eq. (41), along with the boundary conditions $H(\pm 1/2, t) = 0$ and $H_x(\pm 1/2, t) = 0$, describes the shape of the viscoelastic catenary as it sags under its own weight. The second term on the left hand side, H_{xxxxt} is the contribution from torque balance and is referred to as the beding term.

4   Results and discussion

The final equation to be solved, Eq (41) is not, apparently amenable to analytical solutions.However, some simplifcations are in order. For the fluid filaments that we constructed, $Re_g \sim 10^{-5}$. So we can entirely neglect the inertial term. Also, at early times, the straight filament must first bend to begin the formation of a catenary. Neglecting the non-linear viscous stretching term, we have

$$\frac{\epsilon^3}{32} H_{xxxxt} = (\Lambda \tau_0) \epsilon H_{xx} - 1 \qquad (42)$$

where, the parameter $\Lambda \sim 5$ and τ_0 can be evaluated from Eq.(20). As the catenary evolves, stretching will result in tension due to viscous stresses and the non-linear stretching term can no longer be ignored. At present, we present only these hypotheses. We hope to examine them in the process of solving Eq.(41) numerically.

We intend to attack *chewing-gum* problem using the framework that we have developed for the viscoelastic catenary. It appears to be a special case of the catenary - one in which the initial state of the filament is a catenary to begin with.

5   Acknowledgements

References

[1] J. Teichman and L. Mahadevan. Viscous catenary. *J. Fluid Mech.*, 478:71–80, 2003.

Eddy Generation by Flow Over Variable Topography: Some Experiments

Christopher L. Wolfe

1   Introduction

The Labrador Sea is a marginal sea of the North Atlantic Ocean bounded by Canada on the west and Greenland on the east. The prevailing winds are from the west and, in the winter, very cold and dry. The surface waters of the Labrador Sea are typically warmer and salter than the water at depth. In severe weather, the sensible and latent heat fluxes can be sufficient to render the surface water denser than the water below. Convective overturning ensues that can mix the water column to depths of over 2 kilometers, creating an intermediate mode water known as Labrador Sea Water[1].

The Labrador Sea Water that forms in these deep convective events spreads out at depth and forms part of the driving force for the global thermohaline circulation whereby dense water formed at high latitudes spreads throughout the world oceans, upwells and warms, and returns to the polar oceans. This circulation transports a large amount of heat from the topics to the poles and is important for maintaining a temperate climate at high latitudes. The deep convection driving this circulation occurs only in a few isolated locations in the arctic and antarctic and an understanding the dynamics of these areas is essential to an understanding of the world climate.

After winters of intense convection, the newly formed Labrador Sea Water is rapidly capped by a thick layer of stratified water. There are too few observations of the restratification process to provide a clear picture of its mechanism, but it is too rapid to be driven simply by surface warming at the beginning of spring. This suggests that horizontal fluxes driven by eddies may be responsible. A possible source of warm, fresh water is eddies shed by the Irminger Current—a fresh, buoyancy driven boundary current rimming the Labrador Sea. West of Greenland the continental shelf is narrower and the continental slope steeper than along the rest of the coast, and the most intense region of eddy formation is at the downstream end of this constriction[1]. A modeling study by Katsman et al.[2] indicate that Irminger Current eddies are triggered by rapid variations in shelf topography. In particular, they showed that narrow alongshelf gaps were less effective at generating eddies than large gaps, and that topography with abrupt transitions generates eddies more efficiently than gently varying topography.

The stability of a buoyant boundary current flowing along topography which does not vary in the downstream direction is a hard enough problem, for which there are few general

theoretical results. A necessary condition for baroclinic instability of a two layer flow is known, namely that the gradient of the potential vorticity (PV),

$$\Pi = \frac{\zeta + f}{h} \quad \text{where} \quad \zeta = (\nabla \times \boldsymbol{u}) \cdot \hat{\mathbf{k}}, \tag{1}$$

must change signs somewhere in the flow (see, for example, [3]). If the PV gradient is of a single sign in each layer, this condition implies that the PV gradient in the upper layer must be of opposite sign as the PV gradient in the lower layer for instability to occur. Simple application of this condition shows that bottom topography that slopes in the same direction as a front can render the front completely baroclinically stable[4]. Topography that slopes in the opposite direction can be destabilizing, but there are many instances of currents flowing over topography with a 'destabilizing' (i.e. opposing) slope that are nevertheless stable[5, 6, 7].

Several authors have studied the stability of fronts over sloping topography in specific situations. Flagg and Beardsley[8] and Gawarkiewicz[9] investigated the linear stability of surface to bottom shelfbreak fronts over topography that slopes away from the front. They find that the front is unstable for any slope, but is most unstable over gentle slopes, becoming rapidly more stable for very steep slopes. The stability of a surface trapped front over sloping topography was studied by Reszka and Swaters[10] using a nonlinear numerical model based on an asymptotic expansion of the primitive equations that assumes that the ratio of the upper layer depth to the lower layer depth is small. They also find that an opposing slope is destabilizing, but that the front becomes less stable as the slope is increased. The very different mean frontal structures (surface to bottom verses surface trapped) may be a source of the discrepancy between these two sets of studies.

The effect of rapidly varying topography on the stability of buoyant currents is less well studied. Bracco and Pedlosky[11], building on a study by Samelson and Pedlosky[12], investigated the stability of a two-layer, quasi-geostrophic channel model with topographic variations in the along-channel direction. The flow in the bulk of the channel was stabilized by a bottom that sloped in the same direction as the interface between the two layers. The slope was smoothly reduced to zero in a narrow gap, thus inducing instability in the gap. They found that the gap strongly influenced the flow downstream of the gap; in their nonlinear model this influence was in the form of coherent vortices that formed in the gap and propagated downstream. These vortices formed and propagated for arbitrarily narrow gaps, contrary to the naive expectation that a gap narrower than one Rossby radius of deformation should have no effect on the flow. The authors suggest that their model could be a possible model for the formation of eddies in the Irminger Current. However, the restriction to small interface deflections (required by quasi-geostrophy) and a bottom that slopes in the same direction as the front (opposite to that of a shelfbreak front) makes the application of this model to the Irminger Current problematic.

We performed a series of laboratory experiments in order to better understand the effect of variable topography on buoyant coastal currents. In order to determine the stability characteristics of a buoyant current on a single slope, we performed a set of preliminary experiments in which the input parameters were varied over a large range. We then allowed the current to flow from a slope which was known to be stable to an unstable slope, or from a slope which was unstable to a slope which was stable. Finally, we attempted to simulate
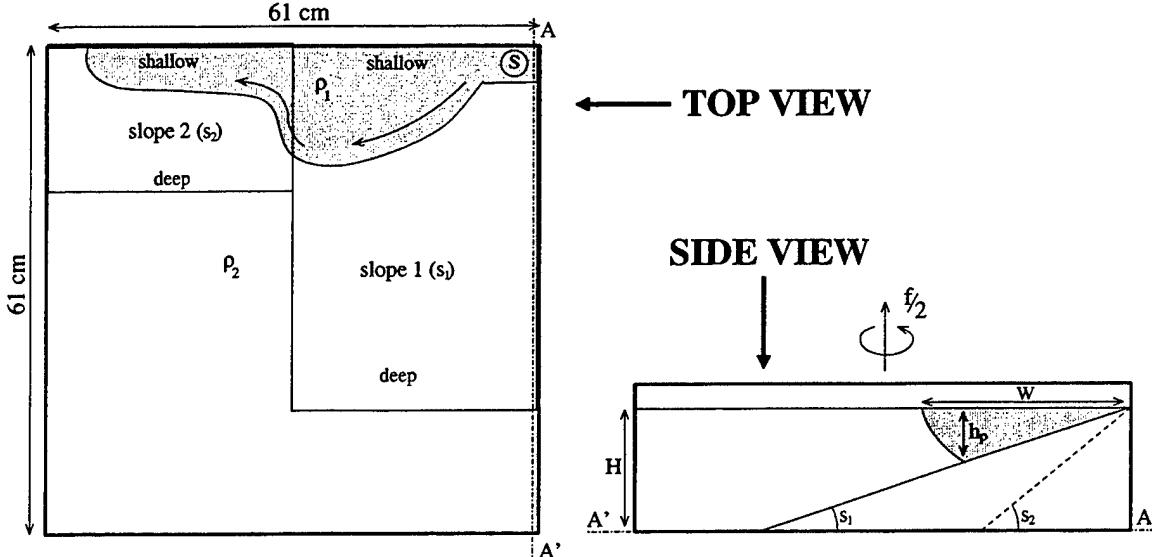
Figure 1: Experimental apparatus used in the preliminary experiments. Left: top view, Right: side view. The arrows indicate the flow direction.

the Irminger Current west of Greenland by allowing the current to flow over two identical, stable slopes separated by a variable width gap containing an unstable slope.

The format of the paper is as follows: In section 2, we will describe the experimental methods. Section 3 will introduce some theoretical results pertaining to buoyant coastal currents. In sections 4 and 5 we discuss the qualitative and quantitative results, respectively, of the experiments. Finally, we conclude in section 6.

2   Experimental Methods

The experiments were performed in three phases, using three different experimental apparatuses. The three phases will be referred to as the preliminary, two-slope, and gap experiments, respectively.

A sketch of the apparatus used in the preliminary experiments is shown in figure 1. These experiments were conducted in a transparent plastic tank of depth 60 cm with a square base measuring 61 cm on a side. The tank was mounted on a 1 meter diameter, belt-driven, rotating table with a vertical axis of rotation. The tank was filled with salt water of density ρ_2 to a depth of about 15 cm. The right 30 cm (in the frame of figure 1) of the tank had a bottom with slope s_1, with the fluid shallowest toward the top of the figure. The left 30 cm had a sloping bottom with slope $s_2 \neq s_1$, again with fluid shallowest toward the top of the figure. The level of water in the tank was adjusted so that the two slopes intersected at the free surface. Dyed buoyant water of density $\rho_1 < \rho_2$ flowed from the 1.1 cm diameter nozzle (marked 'S' in the figure) placed about 0.5 cm below the free surface. The nozzle was covered with a piece of sponge to reduce mixing between the buoyant and ambient fluids. The buoyant water flowed onto the right-hand slope where it developed into a buoyancy forced boundary current which flowed with the coast on its right
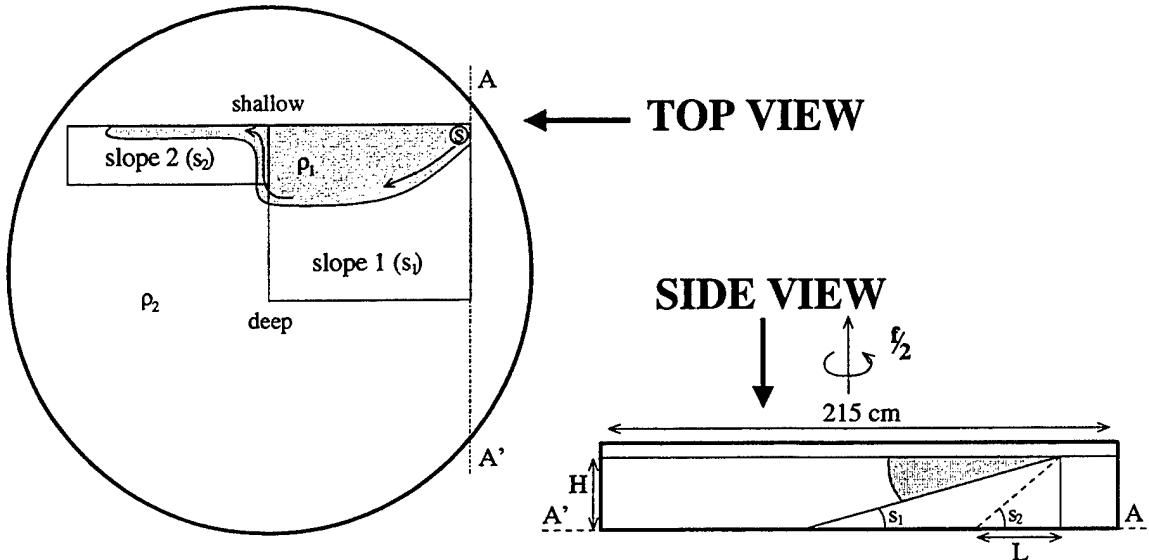
174

Figure 2: Experimental apparatus used in the two-slope experiments. Left: top view, Right: side view. The arrows indicate the flow direction.

(looking downstream) before flowing onto the left-hand slope. In this arrangement, buoyant fluid could flow all the way around the tank and rejoin the current near the source. The experiment was ended before this happened.

In all that follows, the first slope that the buoyant fluid encounters will be referred to as slope 1 and the other slope is slope 2. The buoyancy force on the current is described by the reduced gravity $g' = g(\rho_2 - \rho_1)/\bar{\rho}$, where g is the gravitational acceleration and $\bar{\rho} = (\rho_2 + \rho_1)/2$. The reduced gravity was calculated using the densities of the fluids before the beginning of the experiment; the actual value was reduced somewhat by mixing. Sampling of buoyant water from developed current revealed that g' was reduced in the experiments by between 20% and 50%. In the first set of experiments $s_1 = 0.25$ or 0.30 and $s_2 = 0.79$ or ∞ (a vertical wall). For the preliminary experiments, the other parameters were varied greatly to explore a large region of parameter space. The Coriolis parameter f varied from 0.20 s^{-1} to 3.0 s^{-1} and the reduced gravity g' took on values from 0.40 cm/s^2 to 12 cm/s^2. The flow rate Q was varied from 0.75 cm^3/s to 18 cm^3/s.

The two-slope experiments (shown in figure 2) were performed in a 215 cm diameter, 45 cm deep, opaque plastic tank mounted on a 2 meter diameter, direct-drive rotating table with a vertical axis of rotation. The tank was filled to a depth of either $H = 15$ cm or $H = 22.5$ cm with salt water of density ρ_2. The two slopes where mounted in the tank away from the side walls. The lengths of the first and second slopes were 72 cm and 82 cm, respectively, and both slopes were painted with a 10 cm by 10 cm grid. The first slope was fixed with $s_1 = 0.29$ while the second slope was adjustable from $s_2 = 1.0$ to $s_2 = \infty$. The source of buoyant fluid as well as the progress of the experiments is the same as that described above. However, since the slopes were mounted away from the side walls of the tank, the buoyant fluid could not make a circuit of the tank and rejoin the current near the source. This allowed us to run the experiment until our reserves (about 20 liters) of
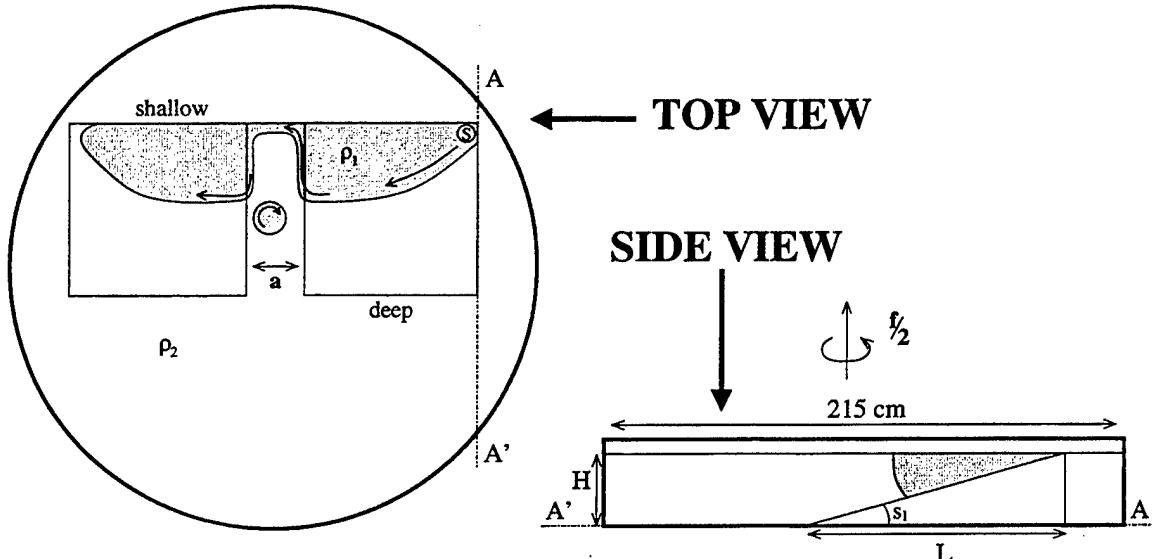
Figure 3: Experimental apparatus used in the gap experiments. Left: top view, Right: side view. The arrows indicate the flow direction. The isolated circle of buoyant fluid represents an eddy which often forms in the gap.

buoyant fluid were depleted. For several experiments, we wanted the current to start on a steep slope and flow onto the gentle slope. Rather than physically reverse the position of the slopes, we simply moved the source to the left end of the left-hand slope and spun the table anti-clockwise. The current then flowed from left to right, with the coast on the left (looking downstream). In all the two-slope experiments, the reduced gravity was kept fixed at $g' \approx 1$ cm/s^2, except for four experiments where $g' \approx 13$ cm/s^2. The magnitude of the Coriolis parameter $|f|$ varied from 0.5 s^{-1} to 2.0 s^{-1}, but was usually fixed at $|f| = 2.0$ s^{-1}. The flow rate was fixed at $Q = 12$ cm^3/s, except for one experiment where $Q = 6.0$ cm^3/s.

The gap experiments (shown in figure 3), where performed in the same tank as the two-slope experiments using two identical slopes with slope $s = 0.29$ separated by a gap of width a. The shoreward side of the gap was a vertical wall. In all other respects, these experiments were identical to the two-slope experiments. The gap width a took on values of 1 cm, 5 cm, 10 cm, 20 cm, and 40 cm. All other parameters were kept fixed with $g' = 1$ cm/s^2, $f = 2.0$ s^{-1}, and $Q = 12$ cm^3/s.

For all of the above experiments, data was captured using a video camera which was co-rotating with the table. The current was made visible by the addition of food coloring and, in several experiments, surface velocities were visualized by floating paper pellets on the surface. The gap experiments were additionally visualized using potassium permanganate dye crystals. The width of the current was determined as the average of three measurements separated by 20 cm, starting at 20 cm downstream from the source on slope 1 or 20 cm downstream from the joint between the two slopes on slope 2.
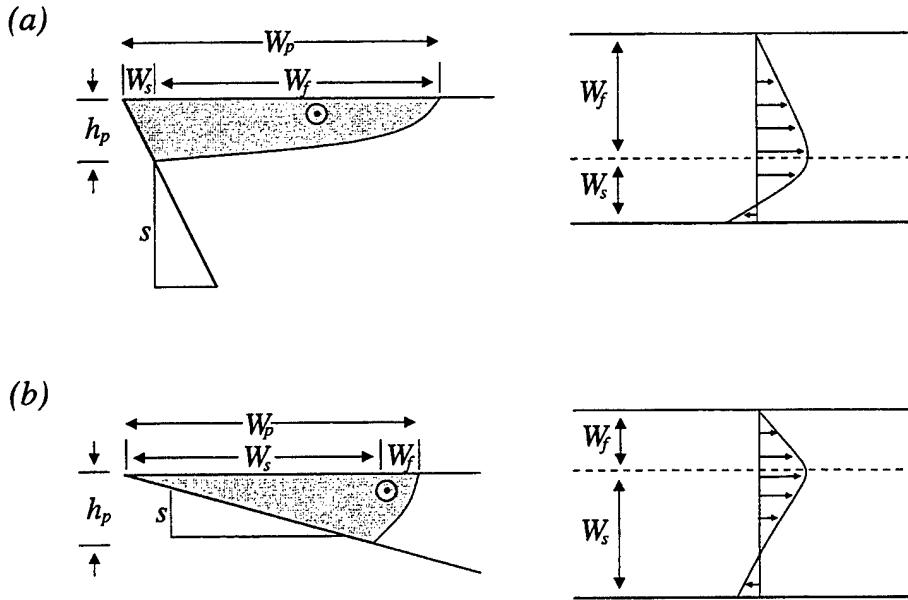
176

Figure 4: Basic structure of a buoyant current over a sloping bottom, cross-section on the left and plan view on the right. (a) Surface trapped front. (b) Bottom trapped front.

3 Scaling for Buoyant Boundary Currents

Lentz and Helfrich[13] introduced and tested a scaling theory for buoyant currents flowing over a sloping bottom in a rotating fluid. The basic structure of a buoyant current over a sloping bottom is shown in figure 4. The buoyant fluid occupies the entire water column in a wedge of width W_s and depth h_p. Offshore of this point, the front detaches from the bottom and curves upward to meet the surface at a distance W_p offshore. The point where the front intersects the bottom is called the foot of the front and the distance from the foot to the seaward edge of the front will be referred to as W_f.

We assume throughout that the front is quasi-steady and in geostrophic and hydrostatic balance. If we also assume that the free surface deformation and the viscous forces are small then the wedge shoreward of the foot is quiescent, while the dynamics seaward of the foot are governed by

$$-fv = -g'h_x \qquad (2)$$

where v is the along-shelf velocity, h is the depth of the interface between the buoyant and dense water, and subscripts stand for partial differentiation. The position of the foot is fixed by requiring that the current transport a known flux Q, since

$$Q = \int_0^{W_p} vh\,dx = \frac{f}{2g'} \int_{W_s}^{W_p} (h^2)_x\,dx = \frac{fh_p^2}{2g'}, \qquad (3)$$

so

$$h_p = \sqrt{\frac{2Qf}{g'}}. \qquad (4)$$

177

The offshore position of the foot, then, is $W_s = h_p/s$. In fact, the foot is 'trapped' at this position[14] since this is exactly the position at which the vertically sheared, geostrophic velocity is zero at the bottom. If the front were to move toward shore, a negative geostrophic velocity would develop at the bottom. The resulting offshore Ekman flux in the bottom boundary layer would force the foot back offshore. Conversely, if the front moves offshore, a positive geostrophic velocity at the bottom would drive an Ekman flux onshore, forcing the foot back to its trapping depth. In practice, there is always some downstream transport shoreward of the foot driven, perhaps, by alongshore pressure gradients. This will lead to a somewhat reduced value of h_p and, hence, W_s.

The offshore portion of the front is assumed to initially adjust to a width of one Rossby radius based on the depth of the foot:

$$W_f(0) \sim L_R = \frac{\sqrt{g'h_p}}{f}, \tag{5}$$

giving an initial mean frontal slope and velocity of

$$s'_0 = \frac{h_p}{W_f(0)} = \frac{h_p}{L_R} \qquad\qquad v_0 = \frac{s'g'}{f} \sim \sqrt{g'h_p}. \tag{6}$$

The total width of the current is then

$$W_p = W_s + W_f(0). \tag{7}$$

The ambient fluid is assumed to be quiescent and the shear between the buoyant and ambient fluids is assumed to be concentrated at the interface between the layers. This shear produces drag on the moving layer which creates an interfacial Ekman layer that transports buoyant water offshore, causing the front to spread slowly. Assuming that the spreading rate is equal to the average offshore velocity in the interfacial Ekman layer,

$$\frac{\partial W_f(t)}{\partial t} \sim u_E = \frac{v}{4} = \frac{fL_R^2}{4W_f}, \tag{8}$$

we find that

$$W_f(t) \sim L_R \left(\frac{tf}{2}\right)^{1/2}. \tag{9}$$

This equation holds for times long compared to the initial adjustment of the front to its trapping depth. In terms of the total current width $W = W_s + W_f$, normalized by the width W_p given by equation (7),

$$\frac{W}{W_p} = \left(\frac{t}{2t_p}\right)^{1/2} + \frac{s'/s}{1 + s'/s}, \tag{10}$$

where $t_p = (1 + s'/s)/f$. The current will continue to spread until a diffusive boundary layer of thickness greater than an Ekman thickness develops between the layers. This will halt the interfacial Ekman transport and shut down the spreading of the current.

The parameter s'/s which appears above is an important parameter for predicting the behavior of a current over sloping topography. If $s'/s \gg 1$ the current is 'bottom trapped'
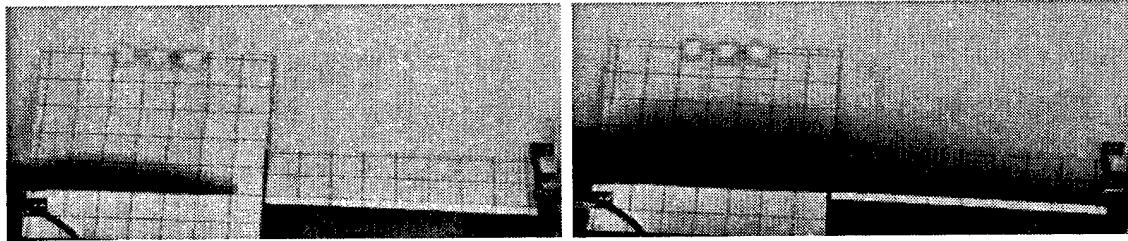
178

Figure 5: Evolution of a surface trapped front ($Q = 12.0$ cm^3/s, $f = 2.0$ s^{-1}, $g' = 13.2$ cm/s^2, $s_1 = 0.29$, $s_2 = 1.0$, $s' = 0.14$) after 12 s (left) and 144 s (right).

(figure 4b) and if $s'/s \ll 1$ the current is 'surface trapped' (figure 4a), using the terminology of Yankovsky and Chapman[15]. Bottom trapped currents are strongly controlled by bottom topography whereas surface trapped currents are only mildly so.

Lentz and Helfrich[13] performed a number of laboratory experiments to test this scaling theory. They found the width and spreading rates of the current to be well predicted if they take the trapping depth $h \approx (0.7 \pm 0.1)h_p$.

4 Qualitative Results

In all the experiments performed, buoyant water spread from the source and flowed along the coast with the coast on the right looking downstream (for positive f). The current broadened rapidly as it flowed away from the source and equilibrated to a width similar to that predicted by Lentz and Helfrich[13] about 20 cm downstream of the source. The foot of the current was visible as a maximum in dye intensity, but it was not feasible to measure its position accurately. After the initial equilibration, the current continued to widen slowly, possibly due to interfacial drag, occasionally forming filamentous streamers on the seaward edge due to offshore transport in the surface Ekman layer. When these occurred the width of the current was measured with the streamers excluded.

During the preliminary experiments, we varied all the input parameters over a wide range to characterize the stability of the current along a slope or a wall. Over the range of parameters used, the current was always stable on the gentle slope. It was found that a fairly large value of $s' > 3$ was needed to generate instabilities along a vertical wall within the time scale of the experiment and that flows over sloping topography were always more stable that flows along a vertical wall.

4.1 Two-Slope Experiments

4.1.1 Surface Trapped, Gentle to Steep

We performed five experiments with relatively high reduced gravities and low rotation rates in order to make a close comparison with the results of Lentz and Helfrich[13]. These flows are predominately surface trapped, with $s'/s \approx 0.3$–1.0. All of these experiments had the source located over gentle topography with steeper topography placed downstream. As expected for surface trapped flows, the topography did not greatly influence the evolution
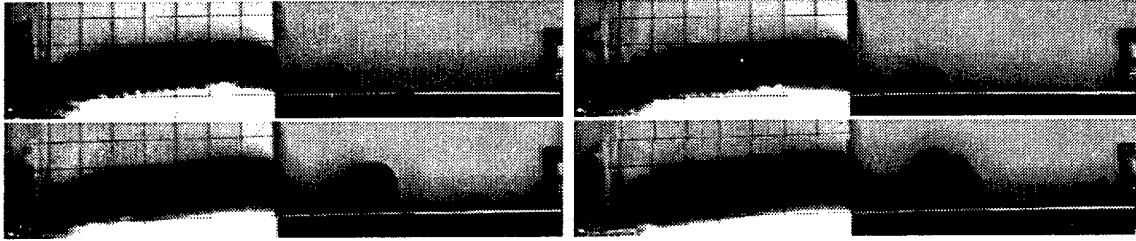
Figure 6: A bottom trapped front ($Q = 12.0$ cm^3/s, $f = 2.0$ s^{-1}, $g' = 0.78$ cm/s^2, $s_1 = 0.29$, $s_2 = \infty$, $s' = 6.1$) flowing from a gentle slope to a vertical wall after 240 s (upper left), 288 s (upper right), 408 s (lower left), and 504 s (lower right). Note the immediate formation of a large eddy on the vertical wall.

of the current. The evolution of a surface trapped front is shown in figure 5. The current propagated quickly across both slopes and was stable throughout the entire experiment. The width of the current decreased slightly on slope 2, but the current was otherwise unaffected by the change in topography. Aside from presence of two slopes, this figure is virtually indistinguishable from figure 5 in Lentz and Helfrich[13].

4.1.2 Bottom Trapped, Gentle to Steep

The bottom trapped currents evolved much more slowly than the surface trapped currents and their cross-shelf extent was smaller, with an equilibrated width on slope 1 rarely greater than 25 cm. Do to their slow spreading, these currents often trapped some dense ambient water between the current and the coast. This density contrast drove a flow along the shoreward edge of the current that was *upstream* relative to the mean flow of the current. The shoreward front was extremely susceptible to instabilities which tended to smooth out the edge of the front. These instabilities are visible in the first two panels of figure 6. However, no eddies were observed to form on the seaward edge of the front when the current flowed over a gentle slope.

When the nose of the current passed from the gentle to the steep slope, it often formed a wisp of fluid (visible in the first panel of figure 6) extending into the ambient fluid. This wisp may be caused by entrainment of buoyant fluid in a cyclonic eddy of ambient fluid formed when the current flows from the gentle to the steeply sloping topography. This initial perturbation propagated more slowly than the nose of the current and decayed downstream over all topography with less than a vertical slope. When the current flowed along a vertical wall, this perturbation grew rapidly into a large eddy. This eddy consumed much of the flux along the wall and delayed the formation of further instabilities downstream of the eddy. Other instabilities eventually grew and formed eddies, the beginnings of which are seen in the last two panels of figure 6. Immediate formation of a large eddy seemed to be a particular feature of flow onto a vertical wall and was not observed for large but finite slopes.

When the current flowed from a gentle slope to a steep—but not vertical—slope the initial perturbation died out before it could grow to a large amplitude eddy. The flow along the steep slope was initially steady and laminar. As the experiment progressed the current
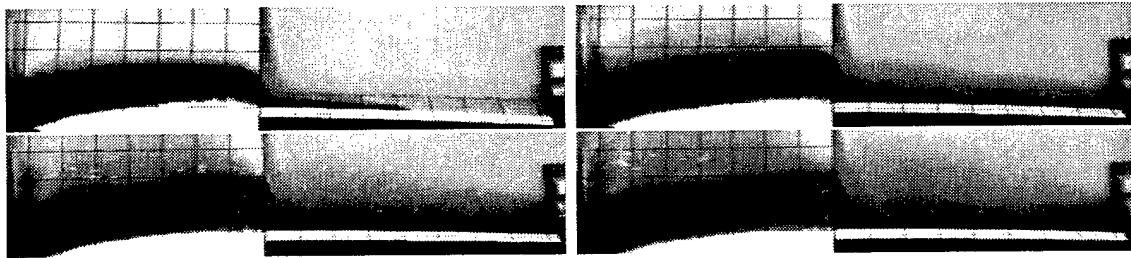
180

Figure 7: A bottom trapped front ($Q = 12.0$ cm^3/s, $f = 2.0$ s^{-1}, $g' = 1.0$ cm/s^2, $s_1 = 0.29$, $s_2 = 3.7$, $s' = 5.3$) flowing from a gentle slope to a steep slope after 124 s (upper left), 279 s (upper right), 465 s (lower left), and 589 s (lower right).

widened and occasionally developed meanders, but the development of large scale eddies was delayed until the current was wider than the sloping shelf and the seaward edge of the current lay over the flat bottom. An example of this behavior can be seen in figure 7. This behavior was observed on all slopes with $s > 1$. This lead us to believe that fully developed eddies cannot form over strongly sloping topography and that the current must be sufficiently wide so as to extend beyond edge of the sloping topography before eddies can form.

In order to test this idea, we performed a series of experiments where the depth of the ambient fluid was increased to 22.5 cm from 15.0 cm, but the slopes were unchanged. This increased the width of the sloping shelf without changing its steepness. In these experiments, the formation of eddies was again delayed until the current extended beyond the shelf and the seaward edge of the current lay over the flat bottom.

The detailed evolution of all currents that formed eddies over steep topography is shown in figure 8, showing that eddies only form once the current is wider than the shelf. In fact, in all cases the current was wider than the shelf by almost a factor of two before eddies formed. Another way to see this is to plot the width of the current when eddies start forming verses with width of the shelf. This is shown in figure 9 where, in addition, the width of the current at the end of the experiment has been plotted versus the width of the shelf for all experiments. Again, all of the eddying currents fall above the line $W = L$. Five currents that were steady at the end of the experiment also lie above the line $W = L$. These experiments were the surface trapped experiments discussed in section 4.1.1. These currents were stable under any condition tested.

4.1.3 Bottom Trapped, Steep to Gentle

We can also inquire as to what will happen if a flow which is initially unsteady and eddying is allowed to flow onto a gentle slope. We have observed that currents starting on gentle slope never form eddies, but it was not clear whether this was a result of a special initial condition or a general statement about the stability of currents over slopes. Figure 10 shows the evolution of a current flowing from a steep slope onto a gentle slope. The current was initially laminar on both slopes, but formed eddies once the current width on slope 1 exceeded the width of the shelf. Regardless of how unstable the current was on slope 1 it was immediately stabilized once it flowed onto slope 2. Eddies formed on slope 1 evidently
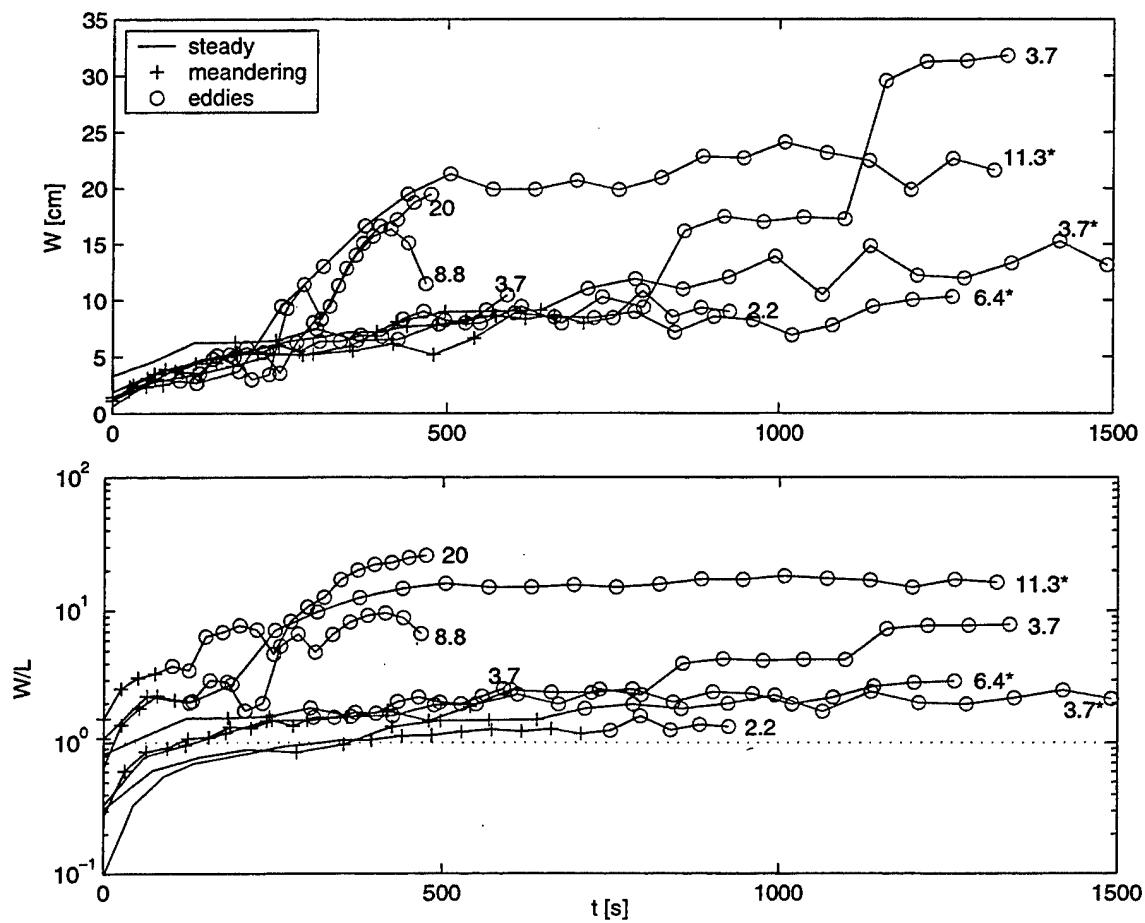
181

Figure 8: The total width verses time for currents on a slope that eventually formed eddies. '+'s and 'o's indicate that the current is meandering or forming eddies, respectively. Numbers at the end of each curve give the slope over which each current formed. Those with asterisks have total depth $H = 22.5$ cm, those without have $H = 15.0$ cm. Top: Total width W. Bottom: Total width normalized by the width of the shelf $L = H/s$.
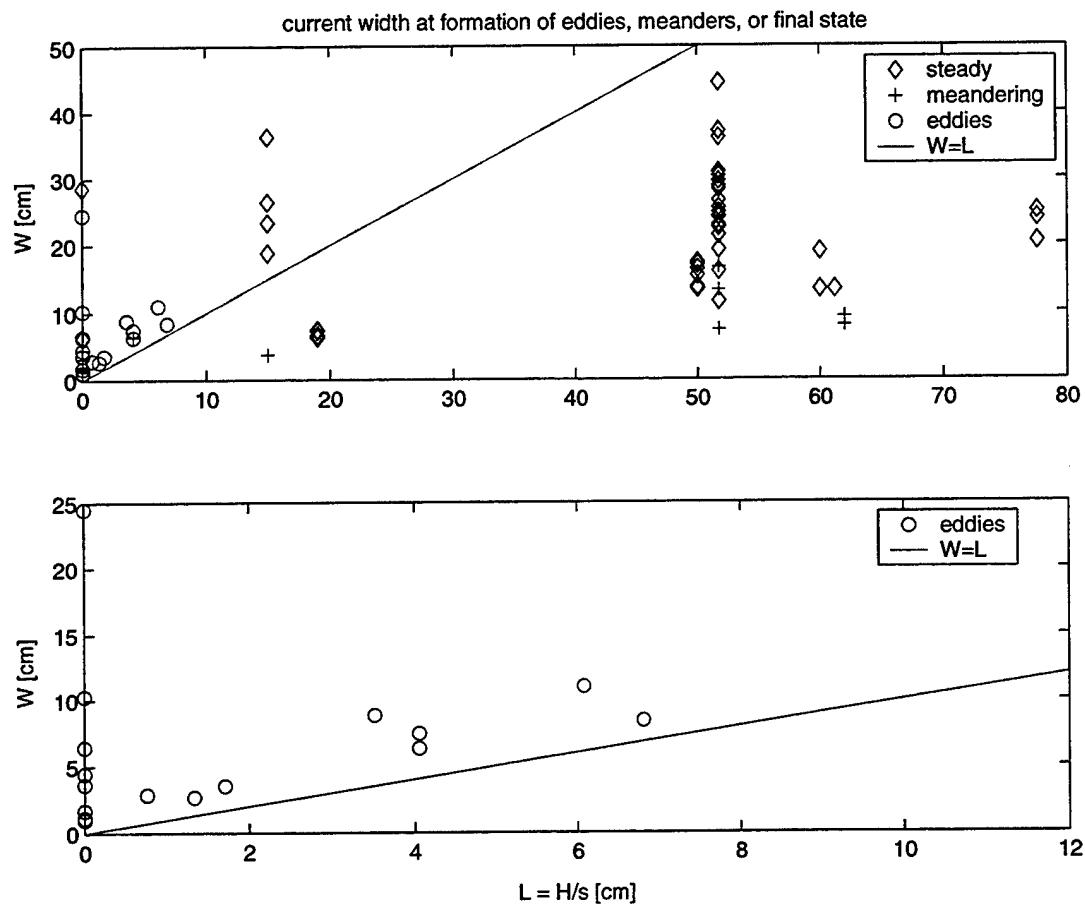
Figure 9: Final width of current verses shelf width $L = H/s$ for all experiments (upper panel) and only currents that form eddies (lower panel). For currents that form eddies, the final width was measured just before eddies began to form.
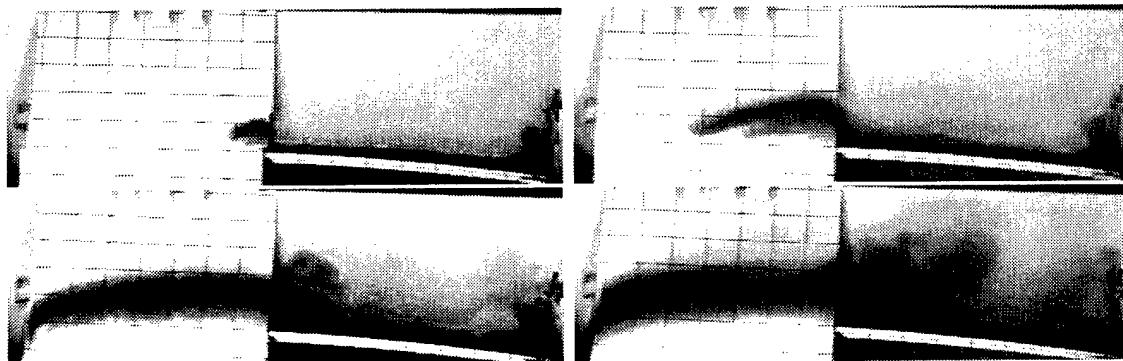
Figure 10: A bottom trapped front ($Q = 12.0$ cm^3/s, $f = -2.0$ s^{-1}, $g' = 1.0$ cm/s^2, $s_1 = 3.7$, $s_2 = 0.29$, $s' = 5.3$) flowing from a steep slope to a gentle slope after 122 s (upper left), 305 s (upper right), 610 s (lower left), and 1037 s (lower right). Note that the current flows from right to left since f is negative.

183
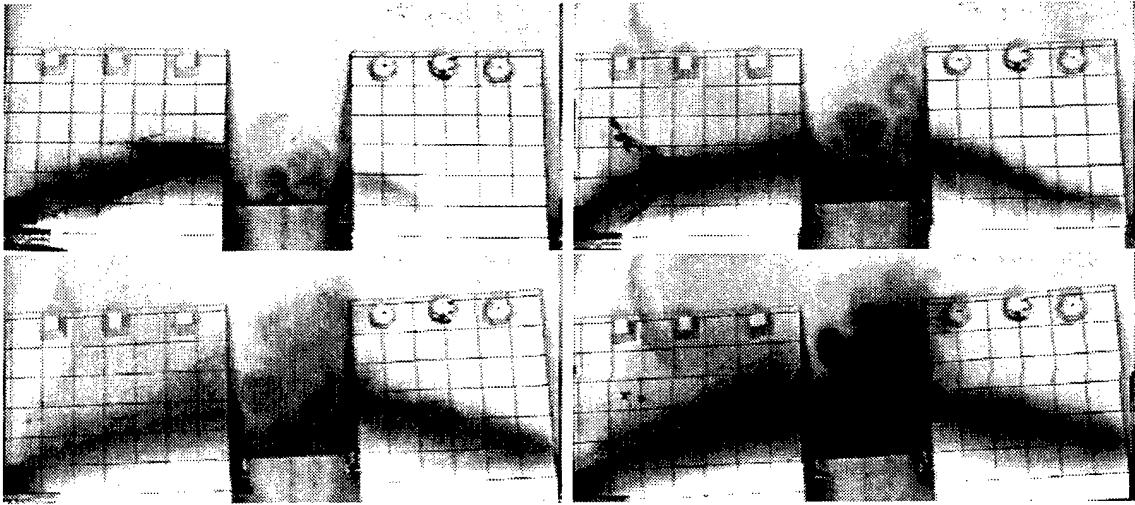
Figure 11: A bottom trapped front ($Q = 12.0$ cm^3/s, $f = 2.0$ s^{-1}, $g' = 1.0$ cm/s^2, $s_1 = 0.29$, $s_2 = 0.29$, $s' = 5.3$, $a = 40$ cm) flowing across a gap after 372 s (upper left), 837 s (upper right), 1302 s (lower left), and 1767 s (lower right). Darker dye was occasionally injected to help visualized the flow field. Note that the eddies pile up at the downstream edge of the gap.

could not propagate onto slope 2 and piled up at the upstream edge of the slope. This behavior is similar to the behavior of Irminger Current eddies formed in the constriction west of Greenland (see Katsman *et al.*[2] figure 1).

4.2 Gap Experiments

The gap experiments were performed with gap sizes ranging from $a = 1$ cm to $a = 40$ cm, corresponding to $a = 0.8L_R$ to $a = 32L_R$, where L_R is the Rossby radius of deformation given by equation (5). For experiments with $a \leq 4L_R$ the flow exhibited small perturbations that decayed downstream of the gap, but no eddies were observed to form.

Once the gap size was increased to $a = 8L_R$, eddies began to form in the gap. It should be noted that the smallest fully developed eddies observed in the previous experiments had diameter $D \approx 8L_R$. Thus, eddies were unable to form in the gap until the gap was wide enough to contain a least one fully developed eddy. Two coherent eddies formed in the gap when $a = 8L_R$: a cyclonic eddy of ambient fluid near the wall and an anticyclonic eddy of buoyant fluid seaward of the first eddy. When the gap was increased to $a = 16L_R$ three eddies formed, with a cyclonic/anticyclonic pair occupying the same positions as before and an additional cyclonic eddy seaward of the anticyclonic eddy. The first two eddies were stationary throughout the experiment, while the third eddy migrated back and forth across the gap, sometimes closer to slope 1, at other times closer to slope 2. The experiment with the largest gap ($a = 32L_R$, shown in figure 11) developed at random eddy field where the number of eddies increased as the experiment proceeded. By the end of the experiment, at least seven individual eddies and dipoles had formed. A summary of the gap experiments is shown in figure 12.
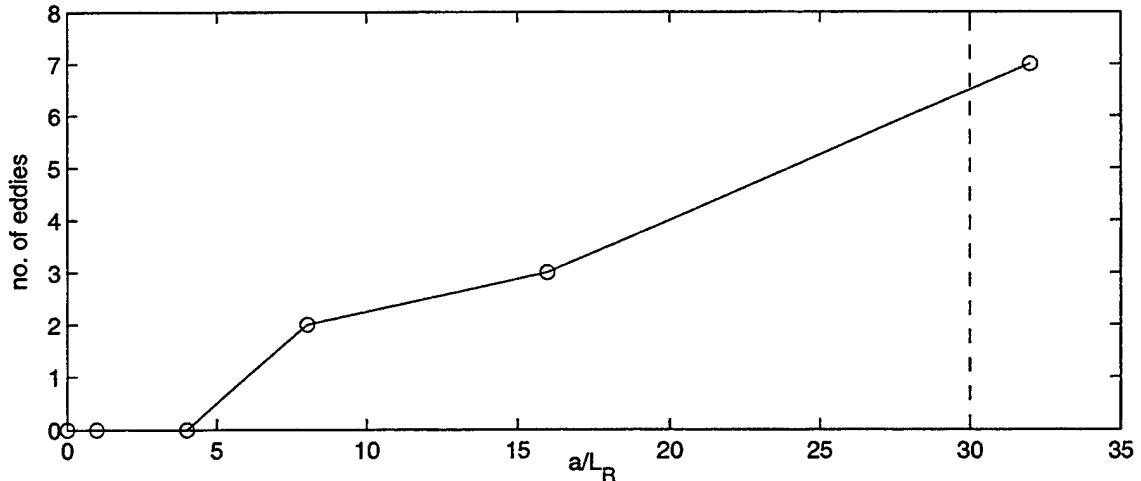
184

Figure 12: Number of eddies observed in gap experiments verses gap width in Rossby radii. The dashed line represents a lower bound on the width of the constriction associated with Irminger Current eddies.

In none of the gap experiments were eddies that formed in the gap able to propagate onto the gentle slopes, either upstream or downstream of the gap. Eddies advected downstream in the gap accumulated on the downstream edge of the gap rather than propagating onto the slope, as in figure 11.

5   Quantitative Results

If time and the width of the current are scaled as discussed in section 3, the data should collapse onto a set of curves with time dependence like $t^{1/2}$. Equation (10) places a bound on the expected variation of the data if bounds on s'/s are known. If the data is scaled using the value of h_p given by equation (4), it does not collapse onto a single curve well and does not fit within the required bounds. As noted in section 3, the observed value of the trapping depth h often falls short of the predicted value h_p. Using $h = h_p/2$ (shown in figure 13) produces a scaling which collapses the data and causes it fall within the required bounds reasonably well for the first slope. However, the width of the current on the second slope consistently falls short of the predicted width. This shortfall may be caused by a reduction in Q caused by upstream flow on the shoreward edge of the front (discussed in section 4.1.2).

An estimate of the growth rate of disturbances on the current can be found by measuring the growth of the current once it begins to meander. If we assume the growth rate of the disturbance is much larger than the spreading rate due to interfacial drag, then the mean growth rate of the disturbances is simply the growth of the current divided by the time it takes the current to grow:

$$\sigma = \frac{W_f - W_i}{W_i \Delta t}, \tag{11}$$

where W_i and W_f are the initial and final widths of the current, respectively. Figure 14
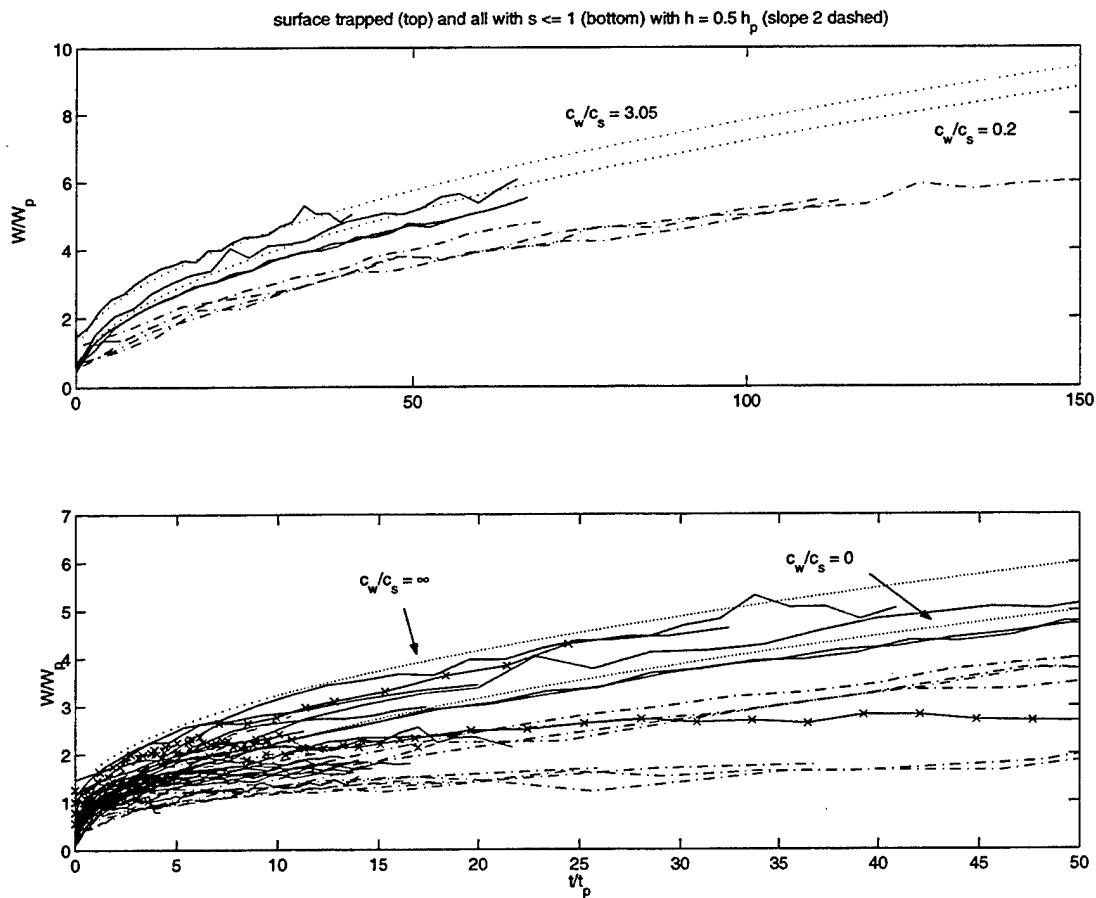
185

Figure 13: The total width W on slope 1 (solid) and slope 2 (dash-dot) verses time, normalized by the predicted width and time, respectively, assuming $h = h_p/2$. Upper panel: Surface trapped experiments only. Lower panel: All experiments with slope $s < 2$. (Currents with $s > 2$ evolved so quickly that they would not fit on this graph). The experimental measurements should lie between the dotted lines. 'x's indicate that the current is meandering.
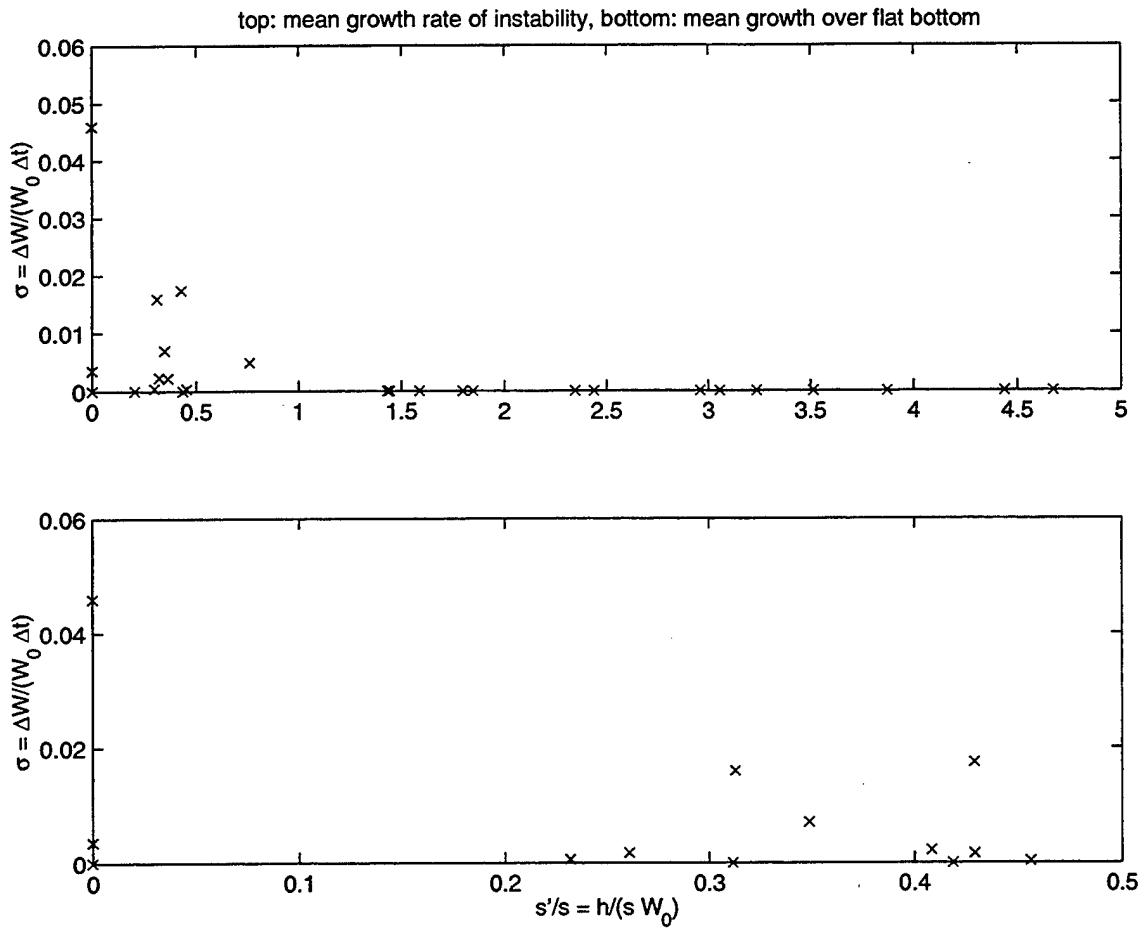
186

Figure 14: Mean disturbance growth rate as a function of $s'/s < 1$, the ratio of the interface slope to the topographic slope. Upper panel: All experiments. Lower panel: Experiments with $s'/s < 1/2$.

shows how the mean growth rate of disturbances on all currents observed in the experiments depends on the ratio of the interface slope to the topographic slope s'/s. Here we define s' to be the interface slope just before the growth of disturbances. Currents that remained laminar throughout the experiment were defined to have zero disturbance growth. Only those experiments with $s'/s < 1$ showed any disturbance growth, although several experiments with $s'/s < 1$ did *not* show disturbance growth. So $s'/s < 1$ seems to be a necessary, but not sufficient, condition for disturbance growth. The condition $s'/s < 1$ implies that disturbances grow on currents that are predominantly surface trapped and relatively uncoupled to the topography.

6 Conclusion and Discussion

We performed a series of laboratory experiments to investigate the effect of rapid changes in topography on the stability of buoyant coastal currents. It was found that buoyant coastal currents do not form eddies on gentle slopes and do not form eddies on steep slopes until the current width exceeds the shelf width. Eddies formed immediately when the current flowed from a gentle slope to vertical wall. Not only did eddies not form on sloping topography, but eddies generated off the topography were unable to propagate onto the slope. Unstable, eddy-forming currents were immediately stabilized when they flowed onto a gentle slope. Disturbances were able to grow only when the topographic slope exceeded the slope of the frontal interface (i.e. $s'/s < 1$), implying that—for fixed s'—steep slopes are less stable than gentle slopes. This observation is in agreement with some of the conclusions of Reszka and Swaters[10], who state that a steep bottom slope is essential for frontal instability. Our results do not agree, however, with those of Flagg and Beardsley[8] and Gawarkiewicz[9]. Their model fixes the shelf width while the topographic slope is varied, so that increasing the slope also increases the depth of the layer below the front. Given that a two-layer baroclinic instability is most active when the upper and lower layers are of comparable thickness it is not surprising that they should find reduced growth rates at large values of the topographic slope.

The gap experiments demonstrate that gaps which are small compared to the Rossby radius of deformation perturb the flow only weakly and locally. The eddies in our experiments seemed to have a preferred diameter of $\sim 8L_R$ and would not form in the gap until the gap was at least this large. The length of the topographic constriction associated with the formation of Irminger Current eddies is 30–60 L_R[2], which is in the range of the largest gap used in our experiments. We have demonstrated that a topographic gap can generate a large, incoherent eddy field where the eddies tend to accumulate on the downstream edge of the gap. In the Labrador Sea, the background mean flow or β-induced drift would eventually remove the eddies from the gap and inject them into the interior of the Sea. The experiments lacked a background flow and the β effect, so the eddies simply accumulated in the gap.

Viscous effects typically play a much larger role in the laboratory than they do in the ocean, but it difficult to make a quantitative assessment the importance of friction in these experiments. One measure of the impact of viscosity is the barotropic spindown time

$$\tau_{\text{sp}} = \frac{h_p}{\sqrt{\nu f}} = \sqrt{\frac{2Q}{\nu g'}}. \tag{12}$$

For most of the experiments $\tau_{\text{sp}} \approx 50$ s, which is short compared to the length of the experiment and roughly equal to the eddy formation time scale. While easy to calculate and interpret, this time scale is not appropriate for these experiments as the dynamics is clearly baroclinic. A baroclinic spindown time is harder to estimate and depends on the details of the stratification and flow. The baroclinic time scale is longer due to the reduced tendency of a stratified fluid to move as barotropic columns. Until a relevant baroclinic spindown time can be estimated an accurate assessment of the importance of viscosity in these experiments remains elusive.

The topographic slopes used in our experiments are quite large by oceanic standards, as are are the interface slopes. Reasonable oceanic values can be determined by conserving

$$\frac{s'}{s} = \frac{h}{Ls},$$

(13)

the ratio of the relative vorticity in the current to its topographically induced vorticity. For $h = 100$ m and $L = 10$ km we have $s_{oc} \approx 0.05 s_{lab}$. A topographic slope of 0.05 is still quite large, but this is about the order of magnitude of the continental slope off the Mid-Atlantic Bight[9].

7 Acknowledgments

References

[1] J. Lilly, P. Rhines, F. Schott, K. Lavender, J. Lazier, U. Send, and E. D'Asaro, "Observations of the Labrador Sea eddy field," Progress in Oceanography (2003), (Submitted).

[2] C. Katsman, M. Spall, and R. Pickart, "Boundary current eddies and their role in the restratification of the Labrador Sea," J. Phys. Ocean. (2003), (Submitted).

[3] J. Pedlosky, Geophysical Fluid Dynamics, 2nd ed. (Springer, ADDRESS, 1987).

[4] J. A. Barth, "Stability of a coastal upwelling front. 1. Model development and stability theorem," J. Geophys. Res. 94, 10844 (1989).

[5] C. Cenedese and P. Linden, "Stability of a buoyancy-driven coastal current at the shelf break," J. Fluid Mech. 452, 97 (2002).

[6] S. Condie, "Formation and stability of shelf break fronts," J. Geophys. Res. 98, 12405 (1993).

[7] J. Whitehead and D. Chapman, "Laboratory observations of a gravity current on a sloping bottom: the generation of shelf waves," J. Fluid Mech. 172, 373 (1986).

[8] C. Flagg and R. Beardsley, "On the stability of the shelf water/slope water front south of New England," J. Geophys. Res. 83, 4623 (1978).

[9] G. Gawarkiewicz, "Linear stability models of shelfbreak fronts," J. Phys. Ocean. 21, 471 (1991).

[10] M. K. Reszka and G. E. Swaters, "Eddy formation and interaction in a baroclinic frontal geostrophic model," J. Phys. Ocean. 29, 3025 (1999).

[11] A. Bracco and J. Pedlosky, "Vortex generation by topography in locally unstable baroclinic flows," J. Phys. Ocean. **33**, 207 (2003).

[12] R. Samelson and J. Pedlosky, "Local baroclinic instability of flow over variable topography," J. Fluid Mech. 411 (1990).

[13] S. Lentz and K. Helfrich, "Buoyant gravity currents along a sloping bottom in a rotating fluid," J. Fluid Mech. **464**, 251 (2002).

[14] D. Chapman and S. Lentz, "Trapping of a coastal density front by the bottom boundary layer," J. Phys. Ocean. 1464 (1994).

[15] A. Yankovsky and D. Chapman, "A simple theory for the fate of buoyant coastal discharges," J. Phys. Ocean. **27**, 1386 (1997).

Elastic Critical Layers

Joel C. Miller

Abstract

We consider the weakly nonlinear growth of instabilities of a submerged elastic jet. We look at the large Weissenberg and Reynolds number cases with small and moderate elasticity. As in inviscid Newtonian shear flows, critical layers develop, but they are affected by the elastic properties of the fluid. At small elasticity, the early development of the critical layer is not significantly changed. At moderate elasticity, the critical layer splits into two different layers, whose location depends on the elasticity. The resulting amplitude equation is significantly altered from the Newtonian case.

1 Introduction

Rallison and Hinch [1] studied the inertial instability of a submerged elastic jet having a parabolic velocity profile. They used a large Weissenberg and Reynolds number limit and concentrated on the effects of elasticity on the instability. At the end of their paper, they found hints of a critical layer for certain parameter values. This critical layer disappears when elasticity is removed from the equations and so depends on elastic effects.

As in [1], we consider a jet of an elastic fluid entering into a motionless fluid. We can think of the motionless fluid as being the same material as the jet, or we can consider it to be Newtonian without any change in the governing equations. Because it is motionless, its elastic properties will not affect the dynamics.

The jet itself is 2 dimensional, rectilinear (i.e., the fluid particles all travel parallel), symmetric about $y = 0$ and bounded between $y = -L$ and $y = L$. We are primarily interested in the large Weissenberg and Reynolds number limit of this jet. Hence the relaxation time of the elastic fluid will be large in comparison to the shear rate and inertia will dominate viscosity.

The velocity profile of the jet which we use is similar to the Rallison and Hinch profile. It is $U(y) = V(L^2 - y^2)^2/L^4$. The choice of this profile will be explained in more detail later (and our results are not strongly dependent on the particular profile), but it is chosen so that U' is continuous between the jet and the ambient fluid. We find that critical layers will exist, and we concentrate on the influence these critical layers have on the weakly nonlinear evolution of the instability.

In section 2 we give a brief description of related results in Newtonian fluids and magneto-hydrodynamics. In Section 3 introduces the equations that govern the motion of our elastic fluid. Section 4 describes the linear problem to be solved assuming large Weissenberg number, derives some results about neutrally stable modes and discusses the

influence of those results on the weakly nonlinear analysis. Sections 5 and 6 look at the influence of an elasticity parameter $E \ll 1$ and $E \sim 1$ respectively, performing both the linear and weakly nonlinear analysis. Section 7 concludes this work and suggests future lines of attack.

2 Rayleigh's Equation

An inviscid Newtonian fluid can have a 2-dimensional flow profile $U = (U(y), 0)$ where $U(y)$ is any function. If we restrict U to twice continuously differentiable functions, and look for linear disturbances $u \exp[ik(x - ct)]$ then the linear stability is governed by Rayleigh's equation

$$\left[(U - c)^2 \left(\frac{\psi}{U - c} \right)' \right]' = k^2 (U - c)\psi$$

where ψ is the stream function for u.

If c has positive imaginary part, then the disturbance will grow — the system is unstable. It was shown by Rayleigh that a necessary condition for instability is that $U'' = 0$ for some y.

In order to go a step beyond the linear analysis into a weakly nonlinear theory, we generally start from a mode which is neutrally stable, that is, c has zero real part. We then try to understand what happens as the growth rate is increased from zero to $\mathcal{O}(\epsilon)$. In the case of Rayleigh's equation, it can be shown that if c is real, then $U(y_c) = c$ for some y_c satisfying $U''(y_c) = 0$. In this case, a critical layer develops about where $U = c$, which is where the background flow is equal to the movement of the instability. It can be shown that although there is an apparent singularity in the differential equation, the solution for ψ is continuously differentiable.

A large amount of research has been done into the this problem, as well as the effect that weak viscosity has (see [2] and references therein). In the presence of viscosity, we can no longer use an arbitrary flow U. Generally, people will use a flow profile which does not satisfy the equations of motion, but justify it either by arguing that the time scale that the viscosity acts on is slower than the time scale of the instability or by explicitly adding a body force.

A paper by Hughes and Tobias [3] studies the linear stability of magneto-hydrodynamic shear flows. The linear stability has been studied by others as well (see references in [4]). Some papers by Shukhman [4, 5] have analyzed the weakly nonlinear problem in the presence of a magnetic field parallel to the flow. They used a modified Rayleigh equation

$$\left[[(U - c)^2 - c_A^2] \left(\frac{\psi}{U - c} \right)' \right]' = [(U - c)^2 - c_A^2] \frac{\psi}{U - c}.$$

Rather than the critical layer occurring where the background flow is as fast as the instability, the critical layer will occur here where the speed of the instability relative to the background flow is equal to the Alfven wave speed.

The magneto-hydrodynamic version of the Rayleigh equation is similar to that which

192

we will derive for an elastic fluid (previously derived by [6, 1])

$$\left[[(U-c)^2 - 2EU'^2]\left(\frac{\psi}{U-c}\right)'\right]' = [(U-c)^2 - 2EU'^2]\frac{\psi}{U-c}.$$

Here the critical layer occurs where the speed of the instability relative to the background flow equals the elastic wave speed.

3 Basic equations

Because we are interested in an elastic fluid, we cannot use the Navier-Stokes equations. There are a wide variety of equations developed to describe elastic fluids. Many of them are applicable in different regimes, and none seem to be universally valid. The principal lectures for this year discuss them more completely.

We use the Oldroyd-B equations

$$\rho\frac{DU}{Dt} = -\nabla P + \mu\nabla^2 U + G\nabla \cdot \mathsf{A}$$

$$\overset{\triangledown}{\mathsf{A}} = \frac{1}{\tau}(\mathsf{I} - \mathsf{A})$$

$$\nabla \cdot U = 0.$$

where U is the fluid velocity, P the pressure, ρ the density μ the viscosity, τ the relaxation time of the fluid and t time. Often G is considered to be C/τ where C is proportional to the concentration of a polymer in the fluid. It measures the strength of the fluid's response to stretching, while A measures the amount the fluid is stretched. The upper convected derivative is defined by $\overset{\triangledown}{\mathsf{A}} = \frac{D\mathsf{A}}{Dt} - \mathsf{A} \cdot (\nabla U) - (\nabla U)^T \cdot \mathsf{A}$.

We non-dimensionalize with a typical length scale L equal to the half-width of the jet and velocity scale V equal to the center-line velocity. Then using asterisks to denote the new non-dimensionalized variables, $\nabla^* = \frac{1}{L}\nabla$, $U^* = VU$, $\mu^* = \mu/\rho VL$, $P^* = P/\rho V^2$ and $t^* = \frac{V}{L}t$. In the base flow, A_{11} will be $1 + 2\tau^2 U_y^2$, and a characteristic value for U_y is V/L. Defining $\lambda = \text{Wi}^{-1} = L/V\tau$ we will normalize A by $\mathsf{A}^* = \lambda^2\mathsf{A}$. Setting $E = G\tau^2/\rho L^2$ and dropping the asterisks, we arrive at

$$\frac{DU}{Dt} = -\nabla P + \mu\nabla^2 U + E\nabla \cdot \mathsf{A} \tag{1}$$

$$\overset{\triangledown}{\mathsf{A}} = \lambda^3\mathsf{I} - \lambda\mathsf{A} \tag{2}$$

$$\nabla \cdot U = 0. \tag{3}$$

Because of the length rescaling, the jet is now bounded between $y = -1$ and $y = 1$. The elasticity parameter E is independent of the speed of the base flow. It depends entirely on geometrical and material properties. We will take the Newtonian viscosity μ to be small. We are interested in the influence of the elasticity and the inverse Weissenberg number, λ on the growth of instabilities.

In the presence of nonzero viscosity or elasticity, the momentum equation (1) will not allow $U = (U(y), 0)$ to be a solution. A body force $b(y)$ may be added to to the right

hand side to maintain this base flow. Alternatively, we can assume that the instability investigated develops over a short enough time scale that the base flow is effectively steady.

For a steady rectilinear flow, the elastic stress will reach a steady state, so $\frac{DA}{Dt} = 0$. Expanding the upper convected derivative in equation (2) yields $-A \cdot (\nabla U) - (\nabla U)^T \cdot A = \lambda^3 I - \lambda A$. Solving this we get

$$A = \begin{pmatrix} 2U'^2 + \lambda^2 & \lambda U' \\ \lambda U' & \lambda^2 \end{pmatrix}.$$

We allow perturbations to the base flow so that the velocity is $\hat{U} = U + u$ and the elastic stress is $\hat{A} = A + a$. We substitute $\hat{U}$ and $\hat{A}$ into equations (1) and (2). Since the flow is two dimensional and incompressible, we introduce a streamfunction ψ such that $u = (\psi_y, -\psi_x)$. We eliminate pressure by taking the curl of the momentum equation (1) yielding an equation for the vorticity ω and we expand the constitutive equation (2) giving

$$\nabla^2 \psi = -\omega \tag{4}$$

$$\omega_t + U\omega_x + U''\psi_x - J(\psi, \omega) = \mu \nabla^2 \omega + E[-\partial_{xy}a_{11} + (\partial_{xx} + \partial_{yy})a_{12} + \partial_{xy}a_{22}] \tag{5}$$

$$a_t + Ua_x - J(\psi, a) - \psi_x A' - U' \begin{pmatrix} 2a_{12} & a_{22} \\ a_{22} & 0 \end{pmatrix} - F - f = -\lambda a. \tag{6}$$

The Jacobian J satisfies $J(q, r) = q_x r_y - q_y r_x$. The tensors $F = A \cdot (\nabla u) + (\nabla u)^T \cdot A$ and $f = a \cdot (\nabla u) + (\nabla u)^T \cdot a$ are given by

$$F = \begin{pmatrix} 2A_{11}\psi_{xy} + 2A_{12}\psi_{yy} & A_{22}\psi_{yy} - A_{11}\psi_{xx} \\ A_{22}\psi_{yy} - A_{11}\psi_{xx} & -2A_{12}\psi_{xx} - 2A_{22}\psi_{xy} \end{pmatrix}$$

$$f = \begin{pmatrix} 2a_{11}\psi_{xy} + 2a_{12}\psi_{yy} & a_{22}\psi_{yy} - a_{11}\psi_{xx} \\ a_{22}\psi_{yy} - a_{11}\psi_{xx} & -2a_{12}\psi_{xx} - 2a_{22}\psi_{xy} \end{pmatrix}.$$

4 Linear Problem

We shall make the assumption that λ and μ are negligibly small, and so we reach a simpler expression for F

$$F = 2U'^2 \begin{bmatrix} 2\psi_{xy} & -\psi_{xx} \\ -\psi_{xx} & 0 \end{bmatrix}.$$

We now linearize the perturbation equations (4)–(6), holding on to the leading order linear terms. We seek solutions proportional to $\exp[ik(x - ct)]$. If c has positive imaginary part, then this mode will grow in time at a rate of $\Re[c]k$. It is referred to as *unstable*. If c has negative imaginary part, then the mode will decay in time and is called *stable*. The resulting relation between $\Re[c]k$ and k is a *dispersion relation*. It gives the growth rate as a function of the wavenumber k.

Equation (6) shows us that a_{22} and a_{12} are both much less than a_{11} and that

$$a_{11} = [4U'^2\psi_{xy} + 2U'^2\psi_x]/[ik(U - c)].$$

Substituting this into the vorticity equation (5) and dropping nonlinear terms provides

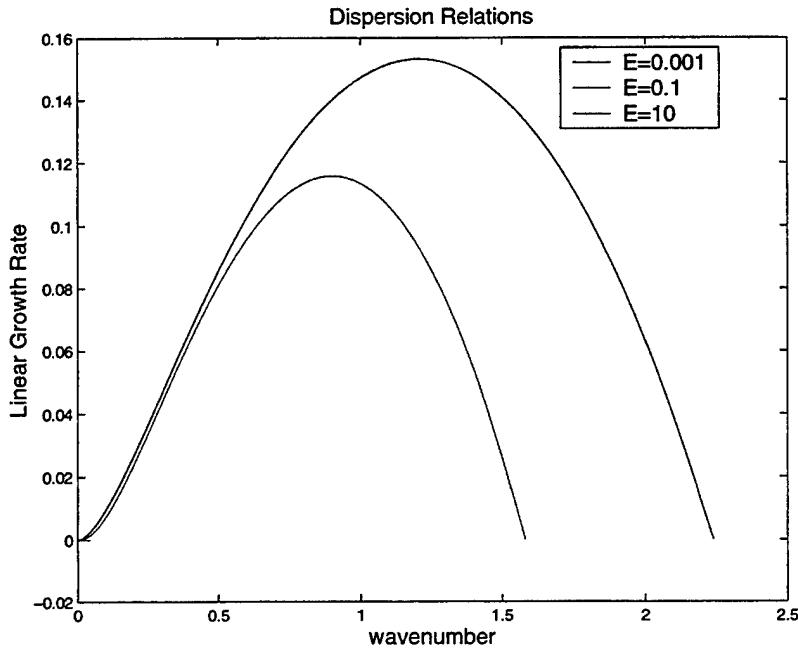$$\frac{\partial}{\partial y}\left(\Gamma\frac{\partial}{\partial y}\eta\right) = k^2\Gamma\eta \tag{7}$$

194

Figure 1: The dispersion relation for varicose modes with different values of E. The elasticity tends to stabilize the mode. For all cases, the growth rate is positive for sufficiently small k, and the mode disappears at some finite value of k.

where $\Gamma = (U - c)^2 - 2EU'^2$ and $\eta = \psi/(U - c)$. Note that Γ is continuous.

We will be looking for varicose and sinuous modes. Because of the symmetries of these modes, we can restrict our computations to just looking at half of the jet. For a varicose mode, the perturbation has no flow across the center line of the jet. Consequently, $\psi_x = 0$ at $y = 0$. This means that ψ is constant on the center line. Since ψ can have an arbitrary constant added to it, we choose that constant to make $\psi(0) = 0$ for a varicose mode.

Conversely, for a sinuous mode, the perturbation has no flow along the center line of the jet. Consequently for a sinuous mode $\psi_y(0) = 0$.

To find the boundary conditions at $y = \pm 1$, we observe that for $|y| > 1$, the value of Γ is c^2. Thus η solves

$$c^2\eta'' = k^2 c^2 \eta$$

and so $\eta = C_1^+ \exp(ky) + C_2^+ \exp(-ky)$ for $y \geq 1$ and $\eta = C_1^- \exp(ky) + C_2^- \exp(-ky)$ for $y \leq 1$. We assume that η decays as $|y| \to \infty$ so $C_1^+ = C_2^- = 0$. We use this to choose boundary conditions at $y = \pm 1$. The boundary condition we apply at 1 is that $\Gamma\eta' = -kc^2\eta$ and at $y = -1$, $\Gamma\eta' = kc\eta$. Either of these conditions along with the conditions previously discussed at $y = 0$ will suffice to determine the solutions. However, for what immediately follows, it is easier to use the conditions at ± 1.

We are interested in conditions under which we can have a marginally stable mode, that is, a solution where c is real. Clearly if c is such that $\Gamma = 0$ for some value of y, then c is real and the differential equation will be singular. The values of c which allow this will form

195

a continuous set, the continuous spectrum of the problem. We will now show that if c is not in the continuous spectrum, then c has nonzero imaginary part. For generality, we do not make many assumptions on U here. We take only that U is continuously differentiable and that $U(-1) = U(1) = 0$.

Assume that c is real but outside of the continuous spectrum. This means Γ is nowhere 0. We multiply equation (7) by η^*, the complex conjugate of η, and integrate from -1 to 1. One integration by parts gives

$$[\Gamma\eta'\overline{\eta}]_{-1}^1 - \int_{-1}^1 \Gamma|\eta'|^2 \, dy = k^2 \int_{-1}^1 \Gamma|\eta|^2 \, dy.$$

The boundary term evaluates to $-kc^2(|\eta(-1)|^2 + |\eta(1)|^2) \le 0$. Since $U(-1) = U(1)$, the mean value theorem can be used to prove that $U' = 0$ at some point in the interior. At this point $\Gamma = (U - c)^2 - 2EU'^2 \ge 0$. By assumption, $\Gamma \ne 0$, hence Γ is positive at some $y \in (-1, 1)$. Since Γ is continuous in this interval, and is nowhere 0, it is positive throughout. Both integrals are positive, and thus the left hand side is negative while the right hand side is positive, a contradiction.

We have shown that all real eigenvalues c lie within the continuous spectrum. Thus if an unstable mode stabilizes, the eigenvalue is actually entering the continuous spectrum. This will substantially complicate the nonlinear analysis. Generally when we attempt a weakly nonlinear analysis, we separate the dynamics into a small number of slowly growing or neutrally stable modes on which we focus along with some quickly decaying modes which are ignored. We then get coupled ODEs relating the amplitudes of these modes. Here there is a continuum of slow modes, so we cannot reduce the problem to even a finite set of modes, much less a small number. Consequently we will arrive at a PDE rather than the ODEs.

It has been shown [7, 8] that a jump in first normal stress (A_{11}) can lead to an instability at zero Reynolds number. If there were a discontinuity in U', then there would be such a jump, and we might expect it to play a significant role in the dynamics. To simplify our analysis, we will not investigate that effect. To prevent this from occurring, we need U' continuous everywhere, including $y = \pm 1$. This is why we have chosen $U(y) = (1 - y^2)^2$. The theoretical results we obtain here do not depend strongly on this form. Our numerical work has shown qualitatively similar behavior for other flow profiles.

We expect to find a neutrally stable mode proportional to $\exp[ik(x - ct)]$ which goes unstable. We will attempt a weakly nonlinear analysis of this mode, looking for modulations over a long time scale $T = \epsilon^{-1}t$ where $\epsilon \ll 1$.

We change to a frame moving with the disturbance, and so ∂_t is replaced by $-c\partial_x + \epsilon\partial_T$. The equations (4)–(6) become
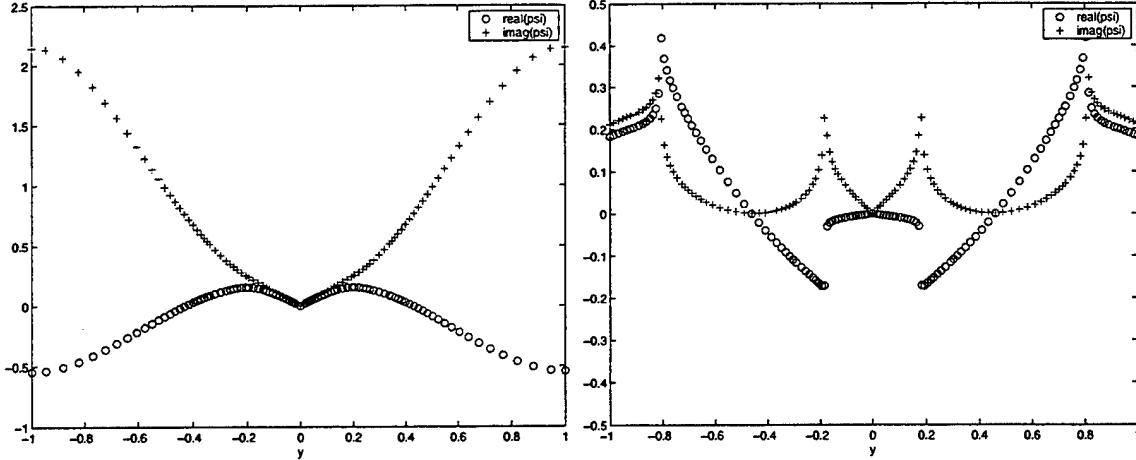
$$\nabla^2\psi = -\omega \tag{8}$$

$$\epsilon\omega_T + (U - c)\omega_x + U''\psi_x - J(\psi, \omega) = \mu\nabla^2\omega + E[-\partial_{xy}a_{11} + (\partial_{xx} + \partial_{yy})a_{12} + \partial_{xy}a_{22}] \tag{9}$$

$$\epsilon\mathsf{a}_T + (U - c)\mathsf{a}_x - J(\psi, \mathsf{a}) - \psi_x\mathsf{A}' - U'\begin{pmatrix} 2a_{12} & a_{22} \\ a_{22} & 0 \end{pmatrix} - \mathsf{F} - \mathsf{f} = -\lambda\mathsf{a}. \tag{10}$$

These are the equations we must use for the weakly nonlinear analysis.

We consider two cases

196

(a) Eigenfunction for a varicose mode with $E = 0.001$ with a value of k very close to where the mode disappears. Note that the solution is smooth.

(b) Eigenfunction for a varicose mode with $E = 0.1$ with a value of k very close to where the mode disappears. Note the two singularities for positive and negative y.

Figure 2: Plots of the varicose eigenfunctions for small and mdoerate elasticities.

- $E \ll 1, \quad \lambda \ll 1$

- $E \sim 1, \quad \lambda \ll 1$.

5 Small E, small λ

There are two limits which are of interest here. In the limit where $E \sim \epsilon^2$, $\lambda \sim \epsilon$ the elastic stresses appear in the leading order balance inside the critical layer. Almost all of the terms are of the same order, so this limit turns out to be quite hard. It corresponds to the scaling at which the critical layer splits into two layers whose width is comparable to the distance between them. The interaction between the two layers is important. We do not discuss this limit here.

The limit where $E \sim \epsilon^4$, $\lambda \sim \epsilon$ is more tractable. We set $E = \epsilon^4 E_4$ and $\lambda = \epsilon \lambda_1$. The elastic stresses do not appear at leading order inside the critical layer.

When the instability begins to appear, we expect ψ to be very small. As the instability develops, ψ should grow and saturate at some size ξ. We seek an appropriate relation between ξ and ϵ. The dominant terms in equation (9) are $\epsilon \omega_T$, $(U - c)\omega_x$, $U''\psi_x$ and $J(\psi, \omega)$. Inside the critical layer, U is about 0, and can be approximated by $(y - y_c)U_c'$. For small T, the balance between $\epsilon \omega_T$ and $(y - y_c)U_c'\omega_x$ tells us that $y - y_c = \mathcal{O}\epsilon$ and so the proper length scale inside the critical layer is $Y = \epsilon^{-1}(y - y_c)$. As T grows, we expect $J(\psi, \omega)$ to become order $\epsilon^{-1}\xi\omega$, which should be comparable in size to $\epsilon \omega$. This gives $\xi = \epsilon^2$.

We typically have a long wave instability which stabilizes at higher wave number k_0. We make the assumption that our domain is such that the longest wave possible corresponds

to the wavelength at which the modes restabilize. A small perturbation to the domain size allows an unstable mode to develop with wavenumber $k = k_0 + \epsilon k_1$. Using our scaling for ψ, we have (for the outer solution)

$$\psi = \psi_2 \epsilon^2 + \psi_3 \epsilon^3 + cc + hot$$
$$\omega = \omega_2 \epsilon^2 + \omega_3 \epsilon^3 + cc + hot$$

where cc denotes complex conjugate and hot denotes higher order terms. We expect ψ_2 and ω_2 to be proportional to $\exp(ikx)$ and separable in y and T. Let $\psi_2 = B(T)\hat{\psi}_2(y)e^{ikx}$ and $\omega_2 = B(T)\hat{\omega}_2(y)e^{ikx}$. At $\mathcal{O}(\epsilon^2)$ equation (8) becomes $\hat{\psi}_2'' - k_0^2\hat{\psi}_2 = -\hat{\omega}_2$ and equation (9) is $(U - c)\hat{\omega}_2 + U''\hat{\psi}_2 = 0$ which combine to give

$$(U - c)[\hat{\psi}_2'' - k_0^2\hat{\psi}_2] - U''\hat{\psi}_2 = 0 \tag{11}$$

which is identical to the Newtonian case. As in the Newtonian case, the mode of interest satisfies $U = c$ when $U'' = 0$. For future reference we define a linear operator $\mathcal{L}$ such that $\mathcal{L}[\hat{\psi}_2] = 0$

$$\mathcal{L}[\psi] := (U - c)(\psi_{yy} - k_0^2\psi) - U''\psi.$$

Solving this linear problem gives us information about the shape of $\hat{\psi}_2$, but tells us nothing about the evolution of B. That will come from the next order.

At $\mathcal{O}(\epsilon^3)$ equations (8) and (9) become

$$\nabla^2\psi_3 - 2k_0k_1\psi_2 = -\omega_3$$
$$-\omega_{2T} = (U - c)\omega_{3x} + U''\psi_{3x}.$$

The k_0k_1 term comes from the fact that $\partial_x^2\psi_2 = (-k_0^2 - \epsilon 2k_0k_1 - \epsilon^2 k_1^2)\psi_2$. We are only interested in the part of ψ_3 proportional to $\exp(ikx)$, which we express $\hat{\psi}_3$. The x derivatives again become multiplication by ik. Combining these equations gives

$$\mathcal{L}[\hat{\psi}_3] = -iB_T\hat{\omega}_2/k_0 + 2B(T)(U - c)k_0k_1\hat{\psi}_2. \tag{12}$$

We multiply this by $\hat{\psi}_2^*/(U - c)$ and integrate from $y = -1$ to 0 (the 0 to 1 contribution follows similarly). This will give us a differential equation to solve for B. A complication arises at y_c, so instead we integrate over $(-1, y_c - \delta)$ and $(y_c + \delta, 0)$ for a δ determined later, but assumed to be small. On the right hand side we approximate this integral in the limit $\delta \to 0$ with a principle value integral so that the right hand side evaluates to $iI_0B_T + k_1I_1B$ where $I_0 = \int_{-1}^0 |\psi_2|^2 U''/k_0(U - c)^2\, dy$ and $I_1 = \int_{-1}^0 2k_0|\psi_2|^2\, dy$.

When we integrate the left hand side by parts, we get

$$\int_{-1}^{y_c-\delta} \frac{\hat{\psi}_2^*\mathcal{L}[\hat{\psi}_3]}{U-c} + \int_{y_c+\delta}^0 \frac{\hat{\psi}_2^*\mathcal{L}[\hat{\psi}_3]}{U-c} = \int_{-1}^{y_c-\delta} \frac{\hat{\psi}_3\mathcal{L}[\hat{\psi}_2^*]}{U-c} + \int_{y_c+\delta}^0 \frac{\hat{\psi}_3\mathcal{L}[\hat{\psi}_2^*]}{U-c}$$
$$+ [\hat{\psi}_2^*\hat{\psi}_{3y}]_{-1}^{y_c-\delta} + [\hat{\psi}_2^*\hat{\psi}_{3y}]_{y_c+\delta}^0 - [\hat{\psi}_{2y}^*\hat{\psi}_3]_{-1}^{y_c-\delta} - [\hat{\psi}_{2y}^*\hat{\psi}_3]_{y_c+\delta}^0$$
$$\to \hat{\psi}_2^* \left[\!\left[\hat{\psi}_{3y}\right]\!\right]_c - \hat{\psi}_{2y}^* \left[\!\left[\hat{\psi}_3\right]\!\right]_c \qquad \text{as } \delta \to 0$$

198

where we use the fact that $\hat{\psi}_2^*$ satisfies $\mathcal{L}[\psi] = 0$, that the boundary conditions at -1 and 0 cause boundary terms to disappear and that continuity in $\hat{\psi}_2^*$ across y_c means the jump in $\hat{\psi}_2^*$ is 0. To evaluate the remaining jumps we need to know more about $\hat{\psi}_3$ close to y_c.

Close to y_c, we will use a Taylor Series approximation for $U - c$. At y_c, $U = c$ and $U'' = 0$, so $U - c = (y - y_c)U_c' + (y - y_c)^3 U_c'''/6 + \cdots$. As $y \to y_c$, $\hat{\psi}_3$ diverges and so to leading order in $y - y_c$ equation (12) becomes

$$\hat{\psi}_3{}'' = -\frac{iB_T\hat{\omega}_2}{k_0(y - y_c)U_c'}$$

which gives a solution of the form

$$\hat{\psi}_3 = -(y - y_c)B_T Q \ln|y - y_c| + |y - y_c|\gamma + R$$

where Q and R are regular functions of y and γ is a constant measuring the jump in $\hat{\psi}_{3y}$ across the critical layer. Note that $\hat{\psi}_3$ is continuous across the critical layer, so we arrive at

$$iI_0 B_T + k_1 I_1 B = 2\hat{\psi}_{2c}^*\gamma. \tag{13}$$

Our solution for $\hat{\psi}_3$ gives us no information about γ. However, it does show that $\epsilon\psi_3$ becomes larger than ψ_2 as $y \to y_c$. This continues at even higher orders, and the asymptotic expansion which we have assumed for ψ will fail close to y_c. Even before determining this solution, we could see that it would fail because in obtaining an equation for $\psi_3{}''$, we neglected terms which we expect to be small. However, we also divided by $U - c$, and so as $y \to y_c$ some discarded terms will inevitably become unbounded.

We will have to resolve the critical layer more carefully in order to retain an asymptotic solution. In the process, we will be able to determine the value of γ, which allows us to find B. We will introduce a new space variable Y satisfying $y - y_c = \epsilon Y$. Thus $\partial_y \mapsto \frac{1}{\epsilon}\partial_Y$. Inside the critical layer $U - c$ will be given by $U - c = \epsilon Y U_c' + \frac{\epsilon^3 Y^3}{6}U_c'''$ using the observation that $U_c - c = U_c'' = 0$. We will match the outer solution with the inner solution at $y = \delta$ corresponding to $Y = \Delta$. Δ satisfies $1 \ll \Delta \ll \epsilon^{-1}$ so that $\delta = \epsilon\Delta \ll 1$.

The outer solution evaluated at $y_c + \delta$ is

$$
\begin{aligned}
\psi &= \epsilon^2\psi_{2c} + \epsilon^2\delta\psi_{2c}' + \epsilon^3\psi_3 + \cdots \\
&= \epsilon^2\psi_{2c} + \epsilon^3\Delta\psi_{2c}' - \epsilon^4\Delta\ln|\epsilon|B_T Q - \epsilon^4\Delta B_T Q\ln|\Delta| + \epsilon^4|\Delta|\gamma + \epsilon^3 R_c + \cdots \\
\omega &= \epsilon^2\omega_{2c} + \cdots .
\end{aligned}
$$

5.1 Inner solution

To match we take an inner solution of the form

$$\psi(x, Y, T) = \epsilon^2\Psi_2(x, T) + \epsilon^3[\Psi_3(x, T) + Y\Phi_3(x, T)] + (\epsilon^4\ln\epsilon)Y\Psi_{31/2}(x, T) + \epsilon^4\Psi_4(x, Y, T) + \cdots$$

$$\omega = \epsilon^2 Z_2 + \cdots .$$

Note that the only dependence of ψ on Y is in $Y\Phi_3$ and Ψ_4. Ψ_4 will be allowed to grow large as $Y \to \Delta$. It is immediately obvious that

$$\Psi_2(x,T) = \psi_{2c}(x,T)$$
$$\Phi_3(x,T) = \psi_{2c}'(x,T)$$
$$\Psi_{31/2}(x,T) = -B_T Q$$
$$\Psi_3(x,T) = R_c(x,T).$$

The remaining terms from the outer solution will match with Ψ_4. In particular $2\Delta\psi_{2c}'' + [[\psi_3']] = [\Psi_{4Y}]_{-\Delta}^{\Delta}$. We know ψ_{2c}'', so we just need to find $[\Psi_4]_{-\Delta}^{\Delta}$ in order to get $\gamma = [[\psi_3']]/2$. From the $\mathcal{O}(\epsilon^2)$ component of equation (8), we get $\Psi_{2xx} + \Psi_{4YY} = -Z_2$ and so

$$[\Psi_{4Y}]_{-\Delta}^{\Delta} = -\left(\int_{-\Delta}^{\Delta} Z_2 \, dY + 2\Delta\Psi_{2xx}\right).$$

Substituting for $[\Psi_{4Y}]_{-\Delta}^{\Delta} = 2\Delta\psi_{2c}'' + 2\gamma$ we get

$$2\gamma = -\left(\int_{-\Delta}^{\Delta} Z_2 \, dY + 2\Delta(\Psi_{2xx} + \psi_{2c}'')\right).$$

Since $\Psi_2 = \psi_{2c}$, we can rewrite the final term as $2\Delta(\psi_{2xx} + \psi_{2c}'')$. L'Hôpital's rule and equation (11) tell us that this is $2\Delta U_c'''\psi_{2c}/U_c'$. Finally substituting for ψ_{2c} with Ψ_2, we reach

$$2\gamma = -\int_{-\Delta}^{\Delta}\left(Z_2 + \frac{U_c'''}{U_c'}\Psi_2\right) dY.$$

One further change of variables $\zeta = -Z_2 - U_c'''\Psi_2/U_c'$ reduces our problem to finding ζ.

Taking equation (9) will give a PDE for ζ. The $\mathcal{O}(\epsilon^2)$ terms will be zero since $U_c - c = U_c'' = 0$. We are left

$$\zeta_T + \frac{U_c'''}{U_c'}\Psi_{2T} + YU_c'\zeta - \Psi_{2x}\zeta_Y = \epsilon E_4[-\epsilon^{-1}\partial_{xY}a_{11} + (\partial_{xx} - \epsilon^{-2}\partial_{YY})a_{12} + \epsilon^{-1}\partial_{xY}a_{22}].$$

We need to determine how the stresses a_{11}, a_{12} and a_{22} scale.

Using equation (10) and the leading order approximation for $U - c$ we arrive at

$$\epsilon YU_c'a_{22,x} + \epsilon a_{22,T} - \epsilon^{-1}J_Y(\psi, a_{22}) - F_{22} - f_{22} = -\epsilon\lambda_1 a_{22}$$
$$\epsilon YU_c'a_{12,x} + \epsilon a_{12,T} - \epsilon^{-1}J_Y(\psi, a_{12}) - U_c'a_{22} - F_{12} - f_{12} = -\epsilon\lambda_1 a_{12}$$
$$\epsilon YU_c'a_{11,x} + \epsilon a_{11,T} - \epsilon^{-1}J_Y(\psi, a_{11}) - 2U_c'a_{12} - F_{11} - f_{11} = -\epsilon\lambda_1 a_{11}$$

where $J_Y(q,r) = q_x r_Y - q_Y r_x$. Looking at the order of the driving terms in each component suggests that $a_{11} = \alpha_{11}$, $a_{12} = \epsilon\alpha_{12}$ and $a_{22} = \epsilon^2\alpha_{22}$ is a good scaling. This yields

$$YU_c'\alpha_{22,x} + \alpha_{22,T} - \Psi_{2x}\alpha_{22,Y} - 2\lambda_1 U_c'\Psi_{2xx} - 2\alpha_{12}\Psi_{2xx} = -\lambda_1\alpha_{22} \tag{14}$$

$$YU_c'\alpha_{12,x} + \alpha_{12,T} - \Psi_{2x}\alpha_{12,Y} - U_c'\alpha_{22} + 2U_c'^2\Psi_{2xx} + \alpha_{11}\Psi_{2xx} = -\lambda_1\alpha_{12} \tag{15}$$

$$YU_c'\alpha_{11,x} + \alpha_{11,T} - \Psi_{2x}\alpha_{11,Y} - 2U_c'\alpha_{12} = -\lambda_1 a_{11} \tag{16}$$

200

coupled together with the PDE

$$\zeta_T + \frac{U_c'''}{U_c'}\Psi_{2T} + YU_c'\zeta - \Psi_{2x}\zeta_Y = E_4[\partial_{xY}\alpha_{11} - \partial_{YY}\alpha_{12}]. \tag{17}$$

Solving this system and taking the limit $\Delta \to \infty$, we can find $\gamma = \int_{-\infty}^{\infty} \hat{\zeta}/2\,dY$. Then finally we have

$$iI_0 B_T + k_1 I_1 B = \hat{\psi}_{2c}^* \int_{-\infty}^{\infty} \hat{\zeta}\,dY \tag{18}$$

5.1.1 Linearization

The coupled system of partial differential equations is nonlinear and generally difficult. To solve it completely would demand a numerical attack. We can still manage some progress through theoretical approaches. We follow [2] and references therein.

We can linearize these equations to get some idea of the early growth of the mode prior to its saturation. The linear equations are

$$(\partial_T + \lambda_1 + ikU_c'Y)\alpha_{22} = -2\lambda_1 U_c'k^2 B \tag{19}$$

$$(\partial_T + \lambda_1 + ikU_c'Y)\alpha_{12} = U_c'\alpha_{22} + 2k^2 U_c'^2 B \tag{20}$$

$$(\partial_T + \lambda_1 + ikU_c'Y)\alpha_{11} = 2U_c'\alpha_{12} \tag{21}$$

$$(\partial_T + ikU_c'Y)\zeta = -\frac{U_c'''}{U_c'}B_T - E(\alpha_{11,x} + \alpha_{12,Y})Y \tag{22}$$

5.1.2 Normal Modes

Taking the linear equations (19)–(22), we look for modes proportional to $\exp(\sigma T)$. So $\alpha_{22} = \hat{\alpha}_{22}\exp(\sigma T)$ and similarly for the other terms.

Then

$$\hat{\alpha}_{22} = -\frac{2\lambda_1 U_c'k^2\hat{B}}{\sigma + \lambda_1 + ikU_c'Y}$$

$$\hat{\alpha}_{12} = -\frac{2\lambda_1 U_c'^2 k^2\hat{B}}{(\sigma + \lambda_1 + ikU_c'Y)^2} + \frac{2k^2 U_c'^2\hat{B}}{\sigma + \lambda_1 + ikU_c'Y}$$

$$\hat{\alpha}_{11} = \frac{2U_c'\hat{\alpha}_{12}}{\sigma + \lambda_1 + ikU_c'Y}$$

$$\hat{\zeta} = -\frac{U_c'''\hat{B}_T}{U_c'(\sigma + ikU_c'Y)} - \frac{4k^4 U_c'^4 E\hat{B}}{(\sigma + ikU_c'Y)(\sigma + \lambda_1 + ikU_c'Y)^3}$$

We want to back out the integral $\int_{-\infty}^{\infty} \hat{\zeta}\,dY$. $\hat{\zeta}$ is the sum of two terms, each of which will have to be attacked separately.

The first term is not difficult

$$\int_{-\infty}^{\infty} -\frac{U_c'''\hat{B}_T}{U_c'(\sigma + ikU_c'Y)} = -\frac{U_c'''\hat{B}_T}{ikU_c'^2}\int_{-\infty}^{\infty} \frac{1}{Y - \frac{i\sigma}{kU_c'}}\,dY$$

$$= \frac{iU_c'''\hat{B}_T}{kU_c'^2}i\pi\,\text{sign}(\Re[\sigma]/U_c').$$

201

Since we are looking at $-1 < y < 0$, and $U(y) = (1-y^2)^2$, we know that $U'_c > 0$. The second term is the term that depends on the elasticity. Therefore it gives the elastic contribution.

$$\int_{-\infty}^{\infty} \frac{4k^4 U'^4_c E\hat{B}}{(\sigma + ikU'_c Y)(\sigma + \lambda_1 + ikU'_c Y)^3}\, dY = -4E\hat{B} \int_{-\infty}^{\infty} \frac{1}{(Y - \frac{i\sigma}{kU'_c})(Y - \frac{i(\sigma+\lambda_1)}{kU'_c})^3}\, dY$$

We use contour integration. For the following we assume $U'_c > 0$, though equivalent arguments can be made if it is negative. The contour we choose is from $-R$ to R and then closing it with a semicircle. The contribution from the arc goes to 0 as R gets large [since the denominator is $\mathcal{O}(Y^4)$]. The poles are at $Y = i\sigma/kU'_c$ and $Y = i(\sigma+\lambda_1)/kU'_c$. We know $\lambda_1 > 0$. If $\Re[\sigma] > 0$, both of these poles are in the upper half plane and so we close the contour in the lower half plane. This shows that the integral is 0. In contrast, if $\sigma_R < -\lambda_1$, then both poles are in the lower half plane, and we can close the integral in the upper half plane. We get a nonzero integral only when $-\lambda_1 < \sigma_R < 0$. In this case the integral is

$$-\frac{4E2\pi}{(\lambda_1/kU'_c)^3}$$

Thus elasticity only has an effect on the normal modes if the mode is decaying. From equation (18)

$$i\sigma I_0 + k_1 I_1 = \left[-\frac{U'''_c \sigma}{kU'^2_c}\pi\,\mathrm{sign}(\Re[\sigma]) - \frac{4E2\pi}{(\lambda_1/kU'_c)^3}\chi \right] \hat{\psi}^*_{2c}$$

where $\chi = 1$ if $-\lambda_1 < \Re[\sigma] < 0$. This can be used to solve for σ, but it is of limited value since we expect the solution to saturate at large enough values that the linearized inner equations are invalid. This can give useful information for small T.

5.1.3 Initial Value Problem

Rather than looking for a normal mode, we can alternately try to solve equations (19)–(22) as an initial value problem using Laplace transforms.

We get a very similar set of equations to the normal mode equations. Here we define $\hat{\alpha}_22$ such that $\hat{\alpha}_{22} = \int_0^\infty e^{-sT} \alpha_{22}(s)\, ds$. We similarly define the other hatted variables. As before we arrive at

$$\hat{\alpha}_{22} = -\frac{2\lambda_1 U'_c k^2 \hat{B}}{s + \lambda_1 + ikU'_c Y}$$

$$\hat{\alpha}_{12} = -\frac{2\lambda_1 U'^2_c k^2 \hat{B}}{(s + \lambda_1 + ikU'_c Y)^2} + \frac{2k^2 U'^2_c \hat{B}}{s + \lambda_1 + ikU'_c Y}$$

$$\hat{\alpha}_{11} = \frac{2U'_c \hat{\alpha}_{12}}{s + \lambda_1 + ikU'_c Y}$$

$$\hat{\zeta} = -\frac{U'''_c \hat{B}_T}{U'_c(s + ikU'_c Y)} - \frac{4k^4 U'^4_c E\hat{B}}{(s + ikU'_c Y)(s + \lambda_1 + ikU'_c Y)^3}$$

and we want $\int_{-\infty}^{\infty} \zeta\, dY$.

When we inverse transform $\hat{\zeta}$ using a Bromwich contour integral, we will take $\Re[s] > 0$. Using the arguments from the previous section, the contribution from the second term will

be identically 0 because s and $s + \lambda_1$ both have positive real part. So once again, the contribution from the elasticity disappears.

The first term gives a contribution. We end up with

$$i I_0 B_T + k_1 I_1 B = -\frac{\pi U_c''' B_T}{k U_c'^2} \hat{\psi}_{2c}^*$$

This is a linear, first order constant coefficient ODE for B. B will have exponential growth or decay. Until B becomes large, this equation should give useful information about its growth.

6 $E \sim 1, \ \lambda \ll 1$

We now consider larger values of E. To simplify the analysis in this case, we will completely ignore λ.

As before, we assume that ψ saturates at some size ξ. Balancing the leading terms, the width of the critical layer is ϵ again. The difference is that now E is order 1, so that the elastic stresses will have to appear in the leading order balance.

We still solve (8)–(10), but now when $\lambda = 0$, the value of F becomes

$$\mathsf{F} = \begin{pmatrix} 2A_{11}\psi_{xy} & -A_{11}\psi_{xx} \\ -A_{11}\psi_{xx} & 0 \end{pmatrix}.$$

It is convenient to use the following expression for a_{11} and a_{22}:

$$a_{11} = \frac{4U'U''\psi}{U-c} + \frac{\partial_x^{-1} 2U'a_{12}}{U-c} + \frac{4U'^2\psi_y}{U-c} + \frac{\partial_x^{-1}S}{U-c}$$

$$a_{12} = -\frac{2U'^2\psi_x}{U-c} + \frac{\partial_x^{-1}R}{U-c}$$

where ∂_x^{-1} denotes an integral and

$$R = -\epsilon a_{12,T} + J(\psi, a_{12}) - a_{11}\psi_{xx}$$
$$S = -\epsilon a_{11,T} + J(\psi, a_{11}) + 2a_{11}\psi_{xy} + 2a_{12}\psi_{yy}.$$

This results in the equation

$$\mathcal{L}[\psi]_x = -\epsilon\omega_T + J(\psi, \omega) + E\left(\left[\frac{\partial_x^{-1}2U'R}{(U-c)^2}\right]_y + \left[\frac{S}{U-c}\right]_y - \left[\frac{\partial_x^{-1}R}{U-c}\right]_{yy} + \left[\frac{R}{U-c}\right]_x\right) \quad (23)$$

where

$$\mathcal{L}[\psi] := \frac{\partial}{\partial y}\left(\Gamma\frac{\partial}{\partial y}\frac{\psi}{U-c}\right) + \frac{\partial^2}{\partial x^2}\left(\Gamma\frac{\psi}{U-c}\right)$$

with $\Gamma = (U-c)^2 - 2EU'^2$. At leading order, this is the linear problem (7). We expect that if there is a zero of Γ, then there is likely to be another zero. Usually we anticipate that there will be two critical layers. We can generally look at the critical layers independently of each other, and we will use a subscript j to distinguish between different critical layers.

203

The places where $\Gamma = 0$ correspond to where the elastic wave speed equals the speed of the disturbance relative to the base flow.

We now use a different ordering for ψ following [9]. In the outer solution

$$\psi = \epsilon^{5/2}\psi_{5/2} + \epsilon^3\psi_3 + \epsilon^{7/2}\psi_{7/2}$$
$$\omega = \epsilon^{5/2}\omega_{5/2}.$$

At leading order, the outer solution satisfies

$$\mathcal{L}[\psi_{5/2}] = 0.$$

If c is real, the solution to this is singular. We can use a Frobenius expansion to approximate the outer solution close to the j-th singularity as

$$\psi_{5/2} = B(T)(a_j^\pm \phi_1 + b_j^\pm \phi_2)\exp(ikx) + cc$$

where $a_j^\pm$ and $b_j^\pm$ are constants that depend on the sign of $y - y_j$ and

$$\phi_1 = 1 + \frac{k^2(y - y_j)^2}{4} - \frac{\Gamma_j'' k^2(y - y_j)^3}{18} + hot$$

$$\phi_2 = -\Gamma_j''(y - y_j) - \left(\Gamma_j''' + \frac{k^2}{2} - \Gamma_j''^2\right)\frac{(y - y_j)^2}{2} + \left(\frac{2\Gamma_j'''\Gamma_j''}{3} - \frac{5\Gamma_j'' k^2}{108} - \frac{\Gamma_j''^3}{3}\right)(y - y_j)^3$$

$$+ \phi_1 \ln|y - y_j| + hot$$

We need to determine what the jumps are and how B evolves. This will require careful analysis inside the critical layer.

At order ϵ^3, the outer solution satisfies the same problem

$$\mathcal{L}[\psi_3] = 0.$$

At the next order, $\mathcal{O}(\epsilon^{7/2})$, we get a new equation

$$\mathcal{L}[\psi_{7/2}]_x = 2ik_0^2 k_1 \Gamma \frac{\psi_{5/2}}{U - c} + \psi_{5/2yyT} - k_0^2 \psi_{5/2T}$$

$$+ E\left(\left[\frac{4U'^3\psi_{5/2T}}{(U - c)^3}\right]_y - \left[\frac{4U'U''\psi_{5/2T}}{(U - c)^2} - \frac{4U'^3\psi_{5/2T}}{(U - c)^3} + \frac{4U'^2\psi_{5/2yT}}{(U - c)^2}\right]_y\right.$$

$$\left. - \left[\frac{2U'^2\psi_{5/2T}}{(U - c)^2}\right]_{yy} + \left[\frac{2U'^2\psi_{5/2xT}}{(U - c)^2}\right]_y\right)$$

As before, we multiply by $\psi_{5/2}^*/(U - c)$. We would like to integrate from -1 to 1, but this integral will have singularities at the critical layers causing it to diverge. To accomodate this, we will have to leave out regions of width 2δ about each critical layer. On the left hand side, we will use integration by parts. After using the fact that $\mathcal{L}[\psi_{5/2}] = 0$ all that will be left is boundary terms involving $\psi_{7/2}$ and $\psi_{5/2}$. The values of those boundary terms will

have to be evaluated by solving the inner problem. On the right hand side, all the integrals will involve $\psi_{5/2}$. We can evaluate them. As δ gets small, a careful matching in orders of δ will match the portions of the integrals on each side that go to infinity. We will be left with an expression of the form

$$\text{boundary terms} = iI_0 B_T + k_1 I_1 B \tag{24}$$

We need to solve the inner problem to advance further.

Figure 3: We see that across the critical layers there is a change in phase of the solution.

6.1   Inner Solution

The inner solution will have

$$\psi = \epsilon^{5/2}\Psi_{5/2} + \epsilon^3 \Psi_3 + \epsilon^{7/2}\Psi_{7/2}$$
$$\omega = \epsilon^{1/2} Z_{1/2}$$

Notice that in the previous section the leading order term of ψ in the inner solution is independent of Y. Here however it depends on Y. We know $\omega = -\nabla^2\psi$ which has two derivatives in Y. Each derivative in Y introduces a factor of ϵ^{-1}, consequently ω is two orders larger than ψ. It is straightforward to see that

$$R = R_{7/2}\epsilon^{7/2} + R_4\epsilon^4 + R_{9/2}\epsilon^{9/2} + \cdots$$
$$S = S_{5/2}\epsilon^{5/2} + S_3\epsilon^3 + S_{7/2}\epsilon^{7/2} + \cdots .$$

Again we use the variable $Y = \epsilon^{-1}(y - y_j)$. The left hand side of equation (23) becomes

$$\left[\frac{1}{\epsilon}\frac{\Gamma'_j}{U_j - c}Y\psi_Y + \frac{\Gamma'_j U'_j}{(U_j - c)^2}Y^2\psi_Y + \frac{\Gamma''_j}{U_j}Y^2\psi_Y - \frac{\Gamma'_j U'_j}{(U_j - c)^2}Y\psi\right]_{xY} + \mathcal{O}(\epsilon^{7/2})$$

while the right hand side becomes

$$- \epsilon\omega_T + J(\psi, \omega)$$
$$+ E\left[\left(\frac{2U''}{(U-c)^2} - \frac{4U'^2}{(U-c)^3}\right)\partial_x^{-1}R + \frac{2U'}{(U-c)^2}\partial_x^{-1}R_y\right]$$
$$+ E\left[\frac{1}{U-c}S_Y + \frac{U'}{(U-c)^2}S\right]$$
$$- E\left[\left(\frac{U''}{(U-c)^2} - \frac{2U'^2}{(U-c)^3}\right)\partial_x^{-1}R - \frac{2U'}{(U-c)^2}\partial_x^{-1}R_y + \frac{1}{U-c}\partial_x^{-1}R_{yy}\right]$$
$$+ E\frac{R_x}{U-c}$$
$$= \frac{1}{\epsilon}\psi_{YYT} - \frac{1}{\epsilon^3}J_Y(\psi, \psi_{YY}) + E\left[\frac{1}{\epsilon}\frac{2U'_j}{(U_j-c)^2}\partial_x^{-1}R_Y\right] + E\left[\frac{1}{\epsilon}\frac{1}{U_j-c}S_Y - \frac{U'_j}{(U_j-c)^2}YS_Y + \frac{U'_j}{(U_j-c)^2}S\right]$$
$$- E\left[-\frac{1}{\epsilon}\frac{2U'_j}{(U_j-c)^2}\partial_x^{-1}R_Y + \frac{1}{\epsilon^2}\frac{1}{U_j-c}\partial_x^{-1}R_{YY} + \frac{1}{\epsilon}\frac{U'_j}{(U_j-c)^2}Y\partial_x^{-1}R_{YY}\right] + \mathcal{O}(\epsilon^{7/2})$$

We want to match these equations order by order.

At $\mathcal{O}(\epsilon^{3/2})$, equation (23) becomes

$$\left[\frac{\Gamma'_j}{U_j - c}Y\Psi_{5/2Y}\right]_{xY} = \Psi_{5/2YYT} + \frac{ES_{5/2Y}}{U_j - c} - \frac{E\partial_x^{-1}R_{7/2YY}}{U_j - c}. \tag{25}$$

Order ϵ^2 gives

$$\left[\frac{\Gamma'_j}{U_j - c}Y\Psi_{3Y}\right]_{xY} = \Psi_{3YYT} - J_Y(\Psi_{5/2}, \Psi_{5/2YY}) + \frac{ES_{3Y}}{U_j - c} - \frac{E\partial_x^{-1}R_{4YY}}{U_j - c} \tag{26}$$

and order $\epsilon^{5/2}$ gives

$$\left[\frac{\Gamma'_j}{U_j - c}Y\Psi_{7/2Y} + \frac{\Gamma'_j U'_j}{(U_j - c)^2}Y^2\Psi_{5/2Y} + \frac{\Gamma''_j}{U_j}Y^2\Psi_{5/2Y} - \frac{\Gamma'_j U'_j}{(U_j - c)^2}Y\Psi_{5/2}\right]_{xY}$$

$$= \Psi_{7/2YYT} - J_Y(\Psi_{5/2}, \Psi_{3YY}) - J_Y(\Psi_3, \Psi_{5/2YY}) + \frac{2EU'_j\partial_x^{-1}R_{7/2Y}}{(U_j - c)^2} + \frac{ES_{7/2Y}}{U_j - c} \tag{27}$$

$$- \frac{EU'_j Y S_{5/2Y}}{(U_j - c)^2} + \frac{EU'_j S_{5/2}}{(U_j - c)^2} + \frac{2EU'_j\partial_x^{-1}R_{7/2Y}}{(U_j - c)^2} - \frac{E\partial_x^{-1}R_{9/2YY}}{U_j - c} - \frac{EU'_j Y \partial_x^{-1}R_{7/2YY}}{(U_j - c)^2}.$$

We need to go into detail on the expansions for ψ, R and S. Before we do this, we make the observation that if $(U_j - c)^2 - 2EU'^2_j = 0$, then $2EU'^2_j/(U_j - c)^2 = 1$.

Some messy algebra shows that

$$R_{7/2} = \frac{U_j - c}{E}\Psi_{5/2xT}$$

$$R_4 = \frac{U_j - c}{E}\left[\Psi_{3T} - (\Psi_{5/2Y}\Psi_{5/2x})\right]_x$$

$$R_{9/2} = \frac{U_j - c}{E}\left[Y\Psi_{5/2T} - \Psi_{5/2TT} + \Psi_{7/2T} - (\Psi_{3Y}\Psi_{5/2x}) - (\Psi_{3x}\Psi_{5/2Y})\right]_x$$

$$S_{5/2} = -\frac{2(U_j - c)}{E}\Psi_{5/2YT}$$

$$S_3 = -\frac{2(U_j - c)}{E}\left[\Psi_{3YT} - \Psi_{5/2Y}\Psi_{5/2xY}\right]$$

$$S_{7/2} = -\frac{2(U_j - c)}{E}\left[\left(\frac{U'_j}{U_j - c} + \frac{2U''_j}{(U_j - c)U'_j}\right)Y\Psi_{5/2YT} + \frac{U''_j}{U'_j}\Psi_{5/2T} + \Psi_{7/2YT}\right.$$

$$\left. - \frac{U'_j}{U_j - c}\Psi_{5/2T} - \frac{1}{U_j - c}\partial_x^{-1}\Psi_{5/2YTT} - (\Psi_{5/2Y}\Psi_{3Y})_x\right].$$

We are finally in a position to write down equations for the evolution of ψ inside the critical layers.

We can immediately make a perhaps remarkable observation. When these values for R and S are inserted in equations (25)–(27) E is cancelled in every term where it appears. So the only role E appears to play is in determining where the critical layers are. Other than that it does not directly affect the dynamics within the critical layers.

After substituting for R and S and integrating once in Y, equation (25) becomes

$$\Psi_{5/2YT} + \frac{\Gamma'_j}{2(U_j - c)} Y\Psi_{5/2xY} = V_1(x,T). \tag{28}$$

Substituting for R and S in equation (26) gives

$$\left[\frac{\Gamma'_j}{U_j - c} Y\Psi_{3xY} \right]_Y = -2\Psi_{3YYT} - J_Y(\Psi_{5/2}, \Psi_{5/2YY}).$$

However,

$$\begin{aligned}
J_Y(\Psi_{5/2}, \Psi_{5/2YY}) &= \Psi_{5/2x}\Psi_{5/2YYY} + \Psi_{5/2xY}\Psi_{5/2YY} - \Psi_{5/2xY}\Psi_{5/2YY} - \Psi_{5/2Y}\Psi_{5/2xYY} \\
&= (\Psi_{5/2x}\Psi_{5/2YY} - \Psi_{5/2xY}\Psi_{5/2Y})_Y \\
&= [J_Y(\Psi_{5/2}, \Psi_{5/2Y})]_Y
\end{aligned}$$

and so integrating in Y gives

$$\Psi_{3YT} + \frac{\Gamma'_j}{2(U_j - c)} Y\Psi_{3xY} = -J_Y(\Psi_{5/2}, \Psi_{5/2Y})/2 + V_2(x,T). \tag{29}$$

After some effort, equation (27) becomes

$$\begin{aligned}
\Psi_{7/2YT} &+ \frac{\Gamma'_j}{2(U_j - c)} Y\Psi_{7/2xY} \\
&= -\frac{1}{2}\left(\frac{\Gamma'_j U'_j}{(U_j - c)^2} + \frac{\Gamma''_j}{U_j} \right) Y^2\Psi_{5/2xY} + \frac{\Gamma'_j U'_j}{2(U_j - c)^2} Y\Psi_{5/2x} \\
&\quad - \left[\left(\frac{U'_j}{U_j - c} + \frac{2U''_j}{(U_j - c)U'_j} \right) - \frac{U'_j}{U_j - c} + \frac{1}{2} + \frac{U'_j}{2(U_j - c)} \right] Y\Psi_{5/2YT} \\
&\quad + \left[\frac{U'_j}{U_j - c} - \frac{U''_j}{U'_j} + \frac{U'_j}{U_j - c} \right] \Psi_{5/2T} + \left[\frac{1}{2} + \frac{1}{U_j - c}\partial_x^{-1} \right] \Psi_{5/2YTT} \\
&\quad - 2(\Psi_{5/2x}\Psi_{3YY} + \Psi_{3x}\Psi_{5/2YY}) + V_3(x,T).
\end{aligned} \tag{30}$$

We can now get the jumps in a_j and b_j in the outer solution ($\psi_{5/2}$) from our inner solution for $\Psi_{5/2}$.

The large Y limit of (28) forces

$$\Psi_{5/2xY} \sim 2(U_j - c)V_1/Y\Gamma'_j$$

and so $\Psi_{5/2x} \sim 2(U_j - c)V_1(\ln|Y|)/\Gamma'_j$ However, we must be able to match this to the outer solution for ψ. At $Y = \Delta$, this term has become $\mathcal{O}(\epsilon^{5/2}\ln\Delta)$, and so this must match to $ikB(T)b_j^+ \ln|\Delta|\exp(ikx)$. Hence we can choose $b_j^+ = 2(U_j - c)/\Gamma'_j$, and $V_1 = ikB(T)\exp(ikx)$. A similar look at $Y = -\Delta$ will show that $b_j^- = b_j^+$.

Since $V_1 \propto \exp(ikx)$, equation (28) implies that $\Psi_{5/2} \propto \exp(ikx)$. Defining $\hat{\Psi}_{5/2}$ such that $\Psi_{5/2} = \hat{\Psi}_{5/2}\exp(ikx)$ yields the equation

$$\hat{\Psi}_{5/2YT} + \frac{ik}{b_j} Y\hat{\Psi}_{5/2Y} = ikB(T).$$

207

We integrate this in T using an integrating factor

$$\hat{\Psi}_{5/2Y} = ik \int_0^T e^{\frac{ikY(S-T)}{b_j}} B(S)\, dS$$

The jump in a_j can now be calculated by integrating $\Psi_{5/2Y}$ from $-\Delta$ to Δ and dividing by $B(T)$. To simplify the calculation, we take $\Delta \to \infty$.

$$a_j^+ - a_j^- = \frac{ik}{B(T)} \int_0^T B(S) \int_{-\infty}^{\infty} e^{\frac{ikY(S-T)}{b_j}}\, dY\, dS$$

$$= \frac{2b_j\pi}{B(T)} \int_0^T B(S)\tilde{\delta}(S-T)\, dS$$

$$= b_j\pi$$

where $\tilde{\delta}$ is the Kronecker delta function. Because the outer integral only goes to $S = T$, the delta function picks out only half of the value of $B(T)$.

We now turn to equation (29). Rather than going into detail on it, we note that it can be solved with the integrating factor $\exp[\Gamma_j' Y/2(U_j - c)] = \exp(Y/b_j)$. However, we will end up with an integral from 0 to T of the nonlinear terms in the Jacobian. Ψ_3 will have a dependance on an integral of a quadratic in B.

Approaching equation (30), a similar problem occurs with the nonlinear terms that involve Ψ_3 and $\Psi_{5/2}$. $\Psi_{7/2}$ has a tangled dependence on B. It will have a double integral of a cubic term in B involving a delay. When we return to the outer solution and update the boundary terms in equation 24, we will have a delay differential equation, which we expect to diverge in finite time.

It is likely that introducing a sufficiently large λ should prevent this divergence.

7 Conclusions

We have made a significant step towards understanding critical layers in elastic fluids at high Weissenberg and high Reynolds number limits.

We have found that the presence of small elasticity does not significantly affect the early growth of the instability, though it may affect the later development. To understand the later development would require solving a nonlinear system of coupled PDEs.

In the case of moderate elasticity, the elasticity substantially affects the critical layers, changing the position and number of critical layers. The equation governing the growth of the amplitude is nonlinear, and depends on earlier times. Consequently, we expect that the solutions will grow to infinity in finite time. Decreasing the Weissenberg number from infinity (increasing λ from 0) may help to stabilize this unbounded growth.

7.1 Future Work

There is a lot of work left to do on this problem. Quite likely a PhD thesis or two's worth.

We have done part of the $E = \mathcal{O}(\epsilon^4)$, $\lambda = \mathcal{O}(\epsilon)$ case. To do more would likely require considerable computations. We have also done part of the $E = \mathcal{O}(1)$, $\lambda = 0$ case. It should not be difficult to add small λ in to this analysis.

It would be difficult to attack the $E = \mathcal{O}(\epsilon^2)$, $\lambda = \mathcal{O}(\epsilon)$ case because there are two critical layers which will interact strongly. A successful attack on this should also be straightforward to translate into the MHD community, where the corresponding case has also been neglected for being too difficult.

It would be interesting to approach the $E \gg 1$ case because in that limit we can neglect inertia. We would then be looking at the zero Reynolds number limit.

In all cases we discussed in this we used the high Weissenberg number limit ($\lambda \ll 1$). Dropping this assumption would complicate matters because we would not arrive at the same elastic Rayleigh equation. A new continuous spectrum is created at where $ik(U - c) + \lambda = 0$ (note that this has $\Re[c] < 0$). For small λ, this overlapped with the continuous spectrum of the standard Rayleigh's equation. We did the case where $E = \mathcal{O}(\epsilon^3)$, $\lambda = \mathcal{O}(1)$ though we did not report it here. This case is not difficult since the small value of E keeps λ from affecting the leading order and hence the Rayleigh equation remains unchanged. In this case, the effect of elasticity is identical to the effect of weak viscocity. It is not clear what happens as E gets larger.

Acknowledgments

References

[1] J. M. Rallison and E. J. Hinch, "Instability of a high-speed submerged elastic jet," Journal of Fluid Mechanics **288**, 311 (1995).

[2] N. J. Balmforth, P. J. Morrison, and J.-L. Thiffeault, "Pattern formation in systems with continuous spectra or the single-wave model," preprint .

[3] D. W. Hughes and S. M. Tobias, "On the instability of magnetohydrodynamic shear flows," Proceedings of the Royal society of London A **457**, 1365 (2001).

[4] I. G. Shukhman, "Nonlinear evolution of a weakly unstable wave in a free shear flow with a weak parallel magnetic field," Journal of Fluid Mechanics **369**, 217 (1998).

[5] I. G. Shukhman, "A weakly nonlinear theory of the spatial evolution of disturbances in a shear flow with a parallel magnetic field," Physics of Fluids **10**, 1972 (1998).

[6] J. Azaiez and G. M. Homsy, "Linear stability of free shear flow of viscoelastic liquids," Journal of Fluid Mechanics **268**, 37 (1994).

[7] E. J. Hinch, O. J. Harris, and J. M. Rallison, "The instability mechanism for two elastic liquids being co-extruded," Journal of Non-Newtonian Fluid Mechanics **43**, 311 (1992).

[8] K. P. Chen, "Interfacial instability due to elastic stratification in concentric coextrusion of two viscoelastic fluids," Journal of Non-Newtonian Fluid Mechanics **40**, 155 (1991).

[9] F. J. Hickernell, "Time-dependent critical layers in shear flows on the beta-plane," Journal of Fluid Mechanics **142**, 431 (1984).

Laboratory experiments on nonlinear Rossby adjustment in a channel

Julia Mullarney
Research School of Earth Sciences, Australian National University

1   Introduction and review

Gravity currents in geophysical scenarios such as river outflows or atmospheric boundary layers often occur over sufficiently large scales that they are influenced by the Earth's rotation and therefore behave differently to their non-rotating equivalents. Effects of rotation include lateral mixing, baroclinic instability and the current is deflected to the right (left) in the northern (southern) hemisphere (see Griffiths, 1986, for a review). As the current flows along a boundary (such as a coastline or mountain range) mixing occurs and reduces the density difference between the current and ambient fluid, thus changing its velocity and run out distance.

We focus here on the propagation of rotating *dam-break* gravity currents along a vertical wall. These currents are formed by a finite and instantaneous release of a large volume of fluid into a second fluid of different density and are typically realised in the laboratory by the removal of a barrier between two volumes of fluid. Early laboratory experiments by Stern, Whitehead & Hua (1982) revealed an unsteady bore-like current with a blunt nose from which large eddies were detrained and a thin and approximately laminar 'neck' region behind the nose. The nose velocity decreased with time, and in some experiments the current stagnated and formed a large gyre. Two self-similar solutions of the long-wave equations were found to describe the shape of the current: a thinning 'wedge' solution and a 'bore-like' solution with the front steepening in time. Stern (1980) and Stern *et al.* (1982) also predicted the existence of a *limiting bore*. This bore has the property that its dimensionless upstream width is maximal among all intrusions ($L < 1/\sqrt{2}L_R$, where L is the width and L_R is the Rossby radius of deformation based on the local depth of the nose). Intrusions initiated in wider channels adjust so that a thinner current propagates downstream. It should be noted that the theory developed by Stern *et al.* (1982) is not a complete solution to the dam-break initial value problem and thus the connection of this solution to the dam break problem is unresolved.

An extensive set of experiments by Griffiths & Hopfinger (1983) also showed that the width of the current appeared to asymptote (in this case to $0.6L_R$) directly behind the nose, however further upstream the current is widened by mixing and the width exceeds the

theoretical maximum ($L \approx L_R$ at ten deformation radii upstream of the nose). The currents observed were qualitatively similar to those in Stern et $al.$ (1982) and it was shown further that the nose velocity decays exponentially with time. Griffiths & Hopfinger (1983) found that the growth rate of the current billows was much greater than the rotation rate and hence the billows were attributed to a Kelvin-Helmholtz instability and not to a hydrostatic instability as suggested by Stern (1980). Diffusion of momentum by horizontal eddy motions caused broadening of the current upstream of the nose.

We note here that both Stern et $al.$ (1982) and Griffiths & Hopfinger (1983) scaled the nose velocity using the local depth of the current which is in contrast to our analysis in which the nose velocity is scaled by the initial layer heights.

Numerical simulations and theoretical analyses of dam-break problems have also revealed interesting features which may have important consequences for the modelling of coastal currents. A weakly nonlinear analysis was developed by Fedorov & Melville (1996) to describe three-dimensional hydraulic jumps propagating along a vertical boundary. A discontinuous solution of the full shallow-water equations was obtained and showed that a shock may exist and it can be felt up to three times further offshore than a regular Kelvin wave. Furthermore, the shock evolves into and maintains a permanent shape which travels at a constant velocity. Far behind the shock the alongshore flow is geostrophic however directly in the lee of the shock there is a region of moderate offshore flow.

Helfrich et $al.$ (1999) compared a semi-geostrophic theory (in which geostrophic balance holds in the cross stream but not in the along stream direction) with numerical solution of the two-dimensional shallow water equations. They found a rarefying intrusion (banked along the right hand wall) controlled by the non-dimensional ratio, $\hat{w}$, of the channel width to the Rossby radius of deformation. There is generally good agreement between the two solutions except for in the limit of a wide channel $\hat{w} \gtrsim 2$. In this case the cross channel motions increased and the semigeostrophic assumption becomes invalid. The speeds of the intrusion nose were significantly less in the numerical solution, however this discrepancy was attributed to the finite resolution of the grid being unable to capture the ever thinning nose.
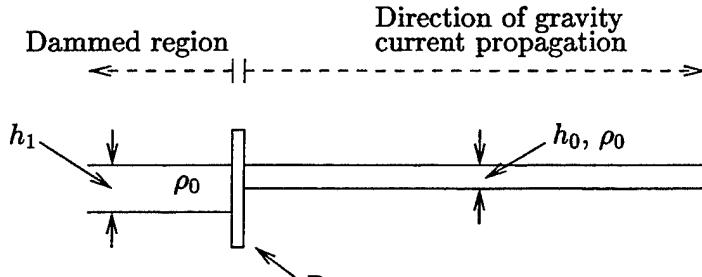

Figure 1: Sketch of two-layer dam break conditions.

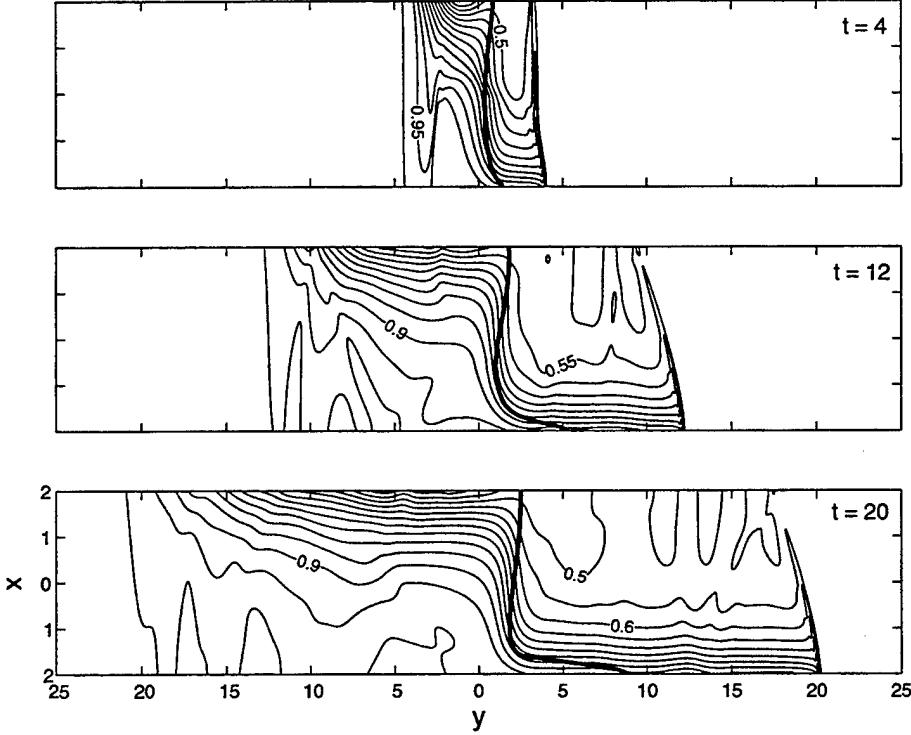If the height of the fluid layer outside of the dammed region is non-zero then the flow gains

Figure 2: Numerical solution for the non-dimensional depth of the intrusion caused by lifting a dam at $y = 0$. The contour integral is 0.025 and the thicker line is the $c = 0.5$ concentration contour which identifies the interface between the water masses originally upstream and downstream of the dam. In this case $h_0/h_1 = 0.5$ and the ratio of channel width to Rossby deformation radius, $\hat{w} = 4$. For $t = 20$ the potential vorticity front reaches $y \approx 8$, while the leading edge of the shock is located at $y \approx 20$. From Helfrich *et al.* (1999).

much complexity (figure 1). Hermann *et al.* (1989) examined a flow in which the depth difference across the dam was small ($h_1/h_0 \approx 1 + \epsilon$, for $\epsilon \ll 1$). The potential vorticity intrusion propagated down both sides of the channel and for thin channels a small parcel of fluid was ejected from the main boundary current and propagated ahead of the intrusion along the right hand wall. In the case when the depth difference across the dam is not small ($0 < h_1/h_0 < 1$) Helfrich *et al.* (1999) found that the leading rarefying intrusion was replaced by a Kelvin shock. The shock propagated ahead of the potential vorticity front, which appeared again as a rarefying intrusion (figures 2 and 3a). The shock curved across the channel with the angle to the x-axis decreasing with bore amplitude. For small $\hat{w}$ or for small depth difference across the dam the shock attached to both walls; however, as the above quantities increased, it detached from the left hand wall. Behind the shock was a boundary layer of approximately one deformation radius in width, in which the flow was strongly ageostrophic with a large off-shore velocity, figure 3(c) (in agreement with Fedorov & Melville 1996). Potential vorticity was not conserved over the shock and the shock also generated oscillations which Helfrich *et al.* (1999) interpret as Poincaré waves.
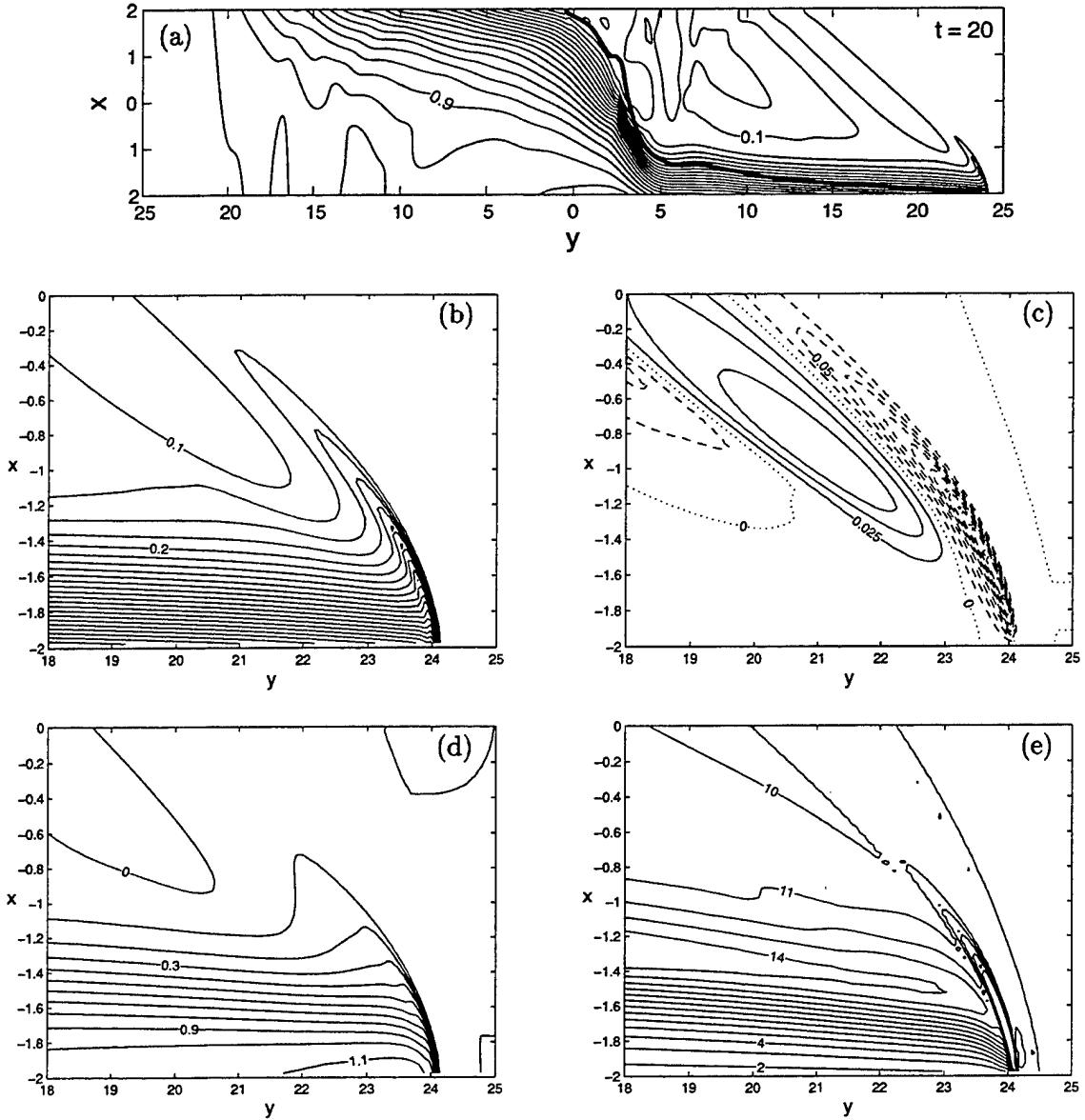
213

Figure 3: (a) Non-dimensional solution at $t = 20$ as for figure 2, except with $\hat{w} = 4$ and $h_0/h_1 = 0.1$. (b)–(e) show close-up profiles of the bore in (a). Contours plots are of: depth (b), cross-channel velocity u (c), along-channel velocity v (d) and potential vorticity q (e). In (c) solid, dashed and dotted lines correspond to positive, negative and zero velocities, respectively. From Helfrich *et al.* (1999).

A similar representation of the above problem would be the case in which a dam break current flows into a stratified two-layer fluid in which the upper layer is of the same density as the dammed fluid. This situation could arise in a geophysical context with the relaxation of an ocean front (of finite length) after the cessation of wind forcing (Stern & Helfrich, 2002) or when considering the penetration of coastally trapped disturbances into the marine

214
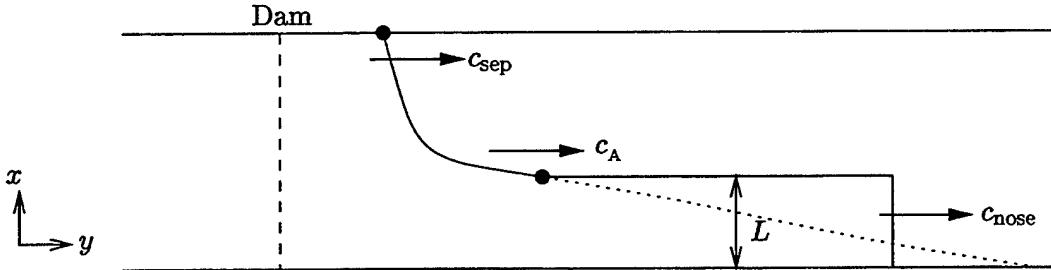
Figure 4: Schematic of the new model. The rarefying gravity current (illustrated by the dotted line) is matched to a bore solution. The attachment point connects the rarefaction and the bore and moves with velocity C_A.

atmospheric boundary layer (Rogerson, 1999). Stern & Helfrich (2002) extended the study of Helfrich *et al.* (1999) to examine this scenario. The theoretical analysis once again gave an 'expansion' wave (thinning wedge) or a bore solution for the shape of the potential vorticity intrusion. By assuming that the Kelvin shock speed is greater than the speed of the leading potential vorticity intrusion the expansion wave solution was selected. The laboratory experiments of Stern & Helfrich (2002) appear to validate this assumption. The dyed fluid of lower potential vorticity rarefied as it advanced and there were clearly visible instabilities and backward breaking lateral waves at the edge of the current. The Kelvin wave was not directly observable, however its existence was inferred from its effect as it reached the trailing edge of the potential vorticity intrusion. Once the wave had propagated around the full length of the circular tank it displaced the dyed stationary fluid out into the interior and this displaced fluid formed a vortex pair.

2 Aims of this project

New theory developed by Helfrich extends the work of Helfrich *et al.* (1999) and Stern & Helfrich (2002) and aims to describe the evolution of a rarefying gravity current. Both Stern *et al.* (1982) and Griffiths & Hopfinger (1983) used a localised analysis to describe the dynamics at the nose, however their analyses give no information about the current further upstream and in the dammed region. The novel aspect of the new theory is the connection of a rarefaction to a uniform gravity current and uses an explicit bore speed relation of the form $c_b = f(h_b; ...)$, where h_b is the height of the gravity current head. (In particular the choice of $c_b = 1.2\sqrt{g'h_b}$ is supported by Stern *et al.* 1982 and Griffiths & Hopfinger 1983). The present solutions give depth contours of the current for all x and y and the speed of the nose, separation point velocity, attachment point velocity and width of the current as functions of the initial depth of the dammed fluid h_1 and $\hat{w}$ (figure 4). The analytical results agree well with results obtained using a two-layer numerical model.

The present work involves an experimental study for comparison with the above model. The first set of experiments is similar to those conducted by Stern *et al.* (1982) and Griffiths & Hopfinger (1983) and we contrast the three sets of results.

215

The second set of experiments explores the propagation of a gravity current breaking into a two-layer stratified ambient. Although the experiments are conducted in an annulus they share some similarities with those conducted by Stern & Helfrich (2002). The focus of the study is on the Kelvin bore which propagates ahead of the intrusion of the lower potential vorticity fluid. We aim to obtain a clear direct visualisation of this feature, to measure its velocity and amplitude and to make a comparison with results from Helfrich et al. (1999).

3 Experimental set-up

3.1 Apparatus and procedure

The experiments were carried out on in a tank on the 1 m diameter rotating table in the geophysical fluid dynamics laboratory at the Woods Hole Oceanographic Institution. The cylindrical Acrylic tank had an internal diameter and depth of 0.965 m and 0.418 m, respectively. The sides and base of the tank were 10 mm thick. A concentric inner barrier was attached within the tank (by four equally-spaced supports) to form an annulus of width 0.15 m. The inner barrier consisted of a thin clear polycarbonate sheet 0.3 m in depth and was fixed in place 10 mm above the base. This gap at the base of the tank connected the fluid in the inside cylindrical region and the outer annulus to ensure that pressures on either side of the barrier were equal. The water mass in the inner cylinder played no active role in the experiments and its only purpose was to hold the barrier in shape.

A quarter of the annulus was isolated between a fixed vertical end wall and a removable vertical dam to form the dammed region of lower potential vorticity fluid. The end wall and dam also did not reach the base of the tank ensuring the interfaces of the two different fluid regions within the annulus were at identical heights.

The dam was initially left out and the tank was filled with saltwater of density $\rho_2(> \rho_1)$ to a depth of 27.5 to 30 cm. Densities were measured using an Anton Paar densimeter with an accuracy of 10^{-5}g cm^{-3}. The tank was spun-up counterclockwise at a rate $\Omega = f/2$ until close to solid body rotation. Relatively fresh water of density ρ_1 was then added at the surface until a layer of depth h_0 overlayed the lower denser layer. The fluid was pumped slowly (from source fluid reservoirs attached to the table) through a foam float to minimise mixing.

The tank was allowed to spin-up for a further period of 10–20 minutes before the dam barrier was inserted. Additional source fluid (density ρ_1) was then added to the surface layer in the dammed region until it had reached a depth of h_1. The total depth throughout the tank was H (figure 5). The entire system was brought to near solid body rotation (30 minutes) at which time the experiment was initiated with the removal of the dam. Although the dam was lifted as quickly and smoothly as possible, some unwanted disturbances were created, however their effects dissipated quickly. A summary of all experimental runs is given in table 1.
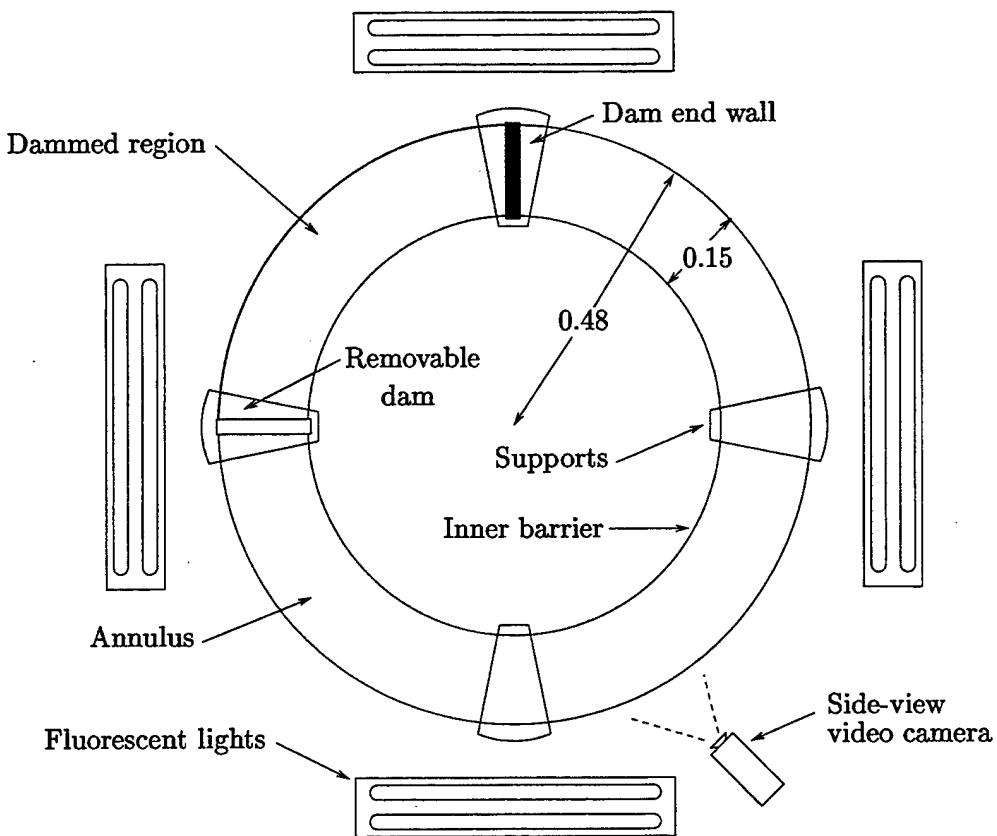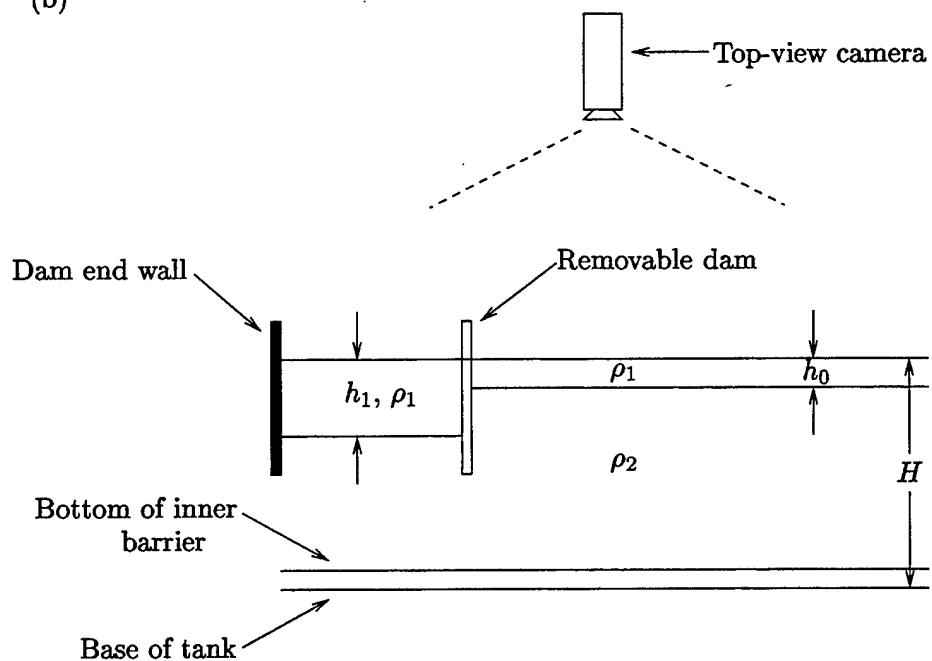
Figure 5: Schematic of experimental apparatus. All lengths are in m. (a) plan view. (b) side view (unwrapped).

Run	h_0	h_1	H	g'	f	h_0/h_1	L_R	$\hat{w}$
1	0	4.5	28.5	5.16	1	0	4.81	3.11
2	0	4.4	28.9	4.95	1.25	0	3.73	4.02
3	0	4.7	28.6	12.56	1	0	7.68	1.95
4	0	4.6	28.5	12.52	0.5	0	15.18	0.99
5	0	5.9	28.8	18.35	0.35	0	29.72	0.50
6	0	6.1	28.8	13.53	0.15	0	60.55	0.25
7	1	4.5	27.5	5.47	1	0.22	4.96	3.02
8	2.8	6	28.7	4.89	1	0.47	5.41	2.77
9	2.2	4.5	28.4	12.47	0.5	0.49	14.98	1.00
10	1.3	4.6	28.9	12.52	0.5	0.28	15.18	0.99
11	3.1	4.1	28.7	12.54	0.5	0.76	14.34	1.05
12	1	3.9	29	5.02	1.25	0.26	3.54	4.24
13	2.2	4.7	28.8	5.01	1.25	0.47	3.88	3.86
14	4.1	5.1	29	5.06	1.25	0.80	4.06	3.69
15	2	6.3	28.4	13.49	0.15	0.32	61.45	0.24
16	2.8	5.4	28.6	13.53	0.15	0.52	56.97	0.26
17	4.5	6	28	13.52	0.15	0.75	60.06	0.25
18	1.7	5.9	29.3	18.39	0.35	0.29	29.76	0.50
19	3.1	6.4	28.5	18.47	0.35	0.48	31.06	0.48
20	4.7	6	29	18.38	0.35	0.78	30.00	0.50
21	1.2	4.4	29	12.53	1	0.27	7.42	2.02
22	2.3	4.8	29.2	12.56	1	0.48	7.77	1.93
23	3	4.4	29.6	12.52	1	0.68	7.42	2.02
24	1.5	5	29.3	5.59	1	0.3	5.29	2.84
25	1.9	4	28.8	5.56	1	0.48	4.71	3.18
26	3.5	4.7	29.9	5.57	1	0.74	5.12	2.93

Table 1: Summary of experimental runs. All parameters are in cgs units. The width of the annulus was 0.15 m in all runs.

3.2 Visualisation

Four sets of (0.585 m long) two-bar fluorescent lights were attached to the table structure. The lights were placed 0.15–0.25 m from the side wall at a height of approximately 0.4 m and were angled slightly down toward the fluid surface. The upper layer of light fluid in front of the dam was usually dyed red and the fluid in the dammed region was dyed blue. After the dam break, the blue fluid therefore marked the position and extent of the potential vorticity intrusion while the propagation of the internal Kelvin wave could be observed by viewing the tank from the side. The wave formed from the lighter red fluid and travelled along the interface between the surface light layer and the denser underlying fluid. The inside edge of the inner boundary was covered with mylar to sharpen the side-view images and to obscure visual effects from the opposite far side of the annulus.

The evolution of the flow after the dam break was monitored by two co-rotating video cameras mounted on the table structure. The plan view was captured by a centred colour camera placed 1.5 m above the surface. The development of the flow at a fixed position with time was captured by a black and white camera mounted on the side of the tank to view a region 0.9–1 m from the dam gate. Over this small region effects of curvature were negligible. Images from both video cameras were digitised and saved directly into a computer at known time intervals (from 1/6 to 2 s). The plan view images were also recorded onto video tape as a back up.

Qualitative images showing the flow at varying positions and time were obtained with a still camera positioned on the floor 2 m from the tank.

4   Results for the experiments with an unstratified fluid ambient $(h_0 = 0)$

4.1   Qualitative description of the flow

The flow behaviour both qualitatively and quantitatively matches that described by Stern *et al.* (1982) and Griffiths & Hopfinger (1983). Figure 6 shows the progress of the current (indicated by the dyed fluid) with time. Immediately after the removal of the dam the released relatively light fluid collapsed forwards and upwards (figure 6a). The fluid collapsed uniformly across the channel until the nose had reached a distance of approximately one Rossby radius of deformation from the dam, at which point the effects of rotation began to be felt by the current and the fluid banked up against the right hand wall (figure 6b). The current propagated as a bore with a blunt bulbous nose which joined to a thin laminar 'neck' region. As described by Stern *et al.* (1982) this neck region was usually the thinnest part of the current. There was some unsteadiness at the edge of the current due to Kelvin-Helmholtz instability and billows were detrained predominantly from the nose but also from further upstream. The unsteadiness and billows were three-dimensional features with much mixing also occurring at the lower edge of the current (figure 7 shows a side view of the current nose).
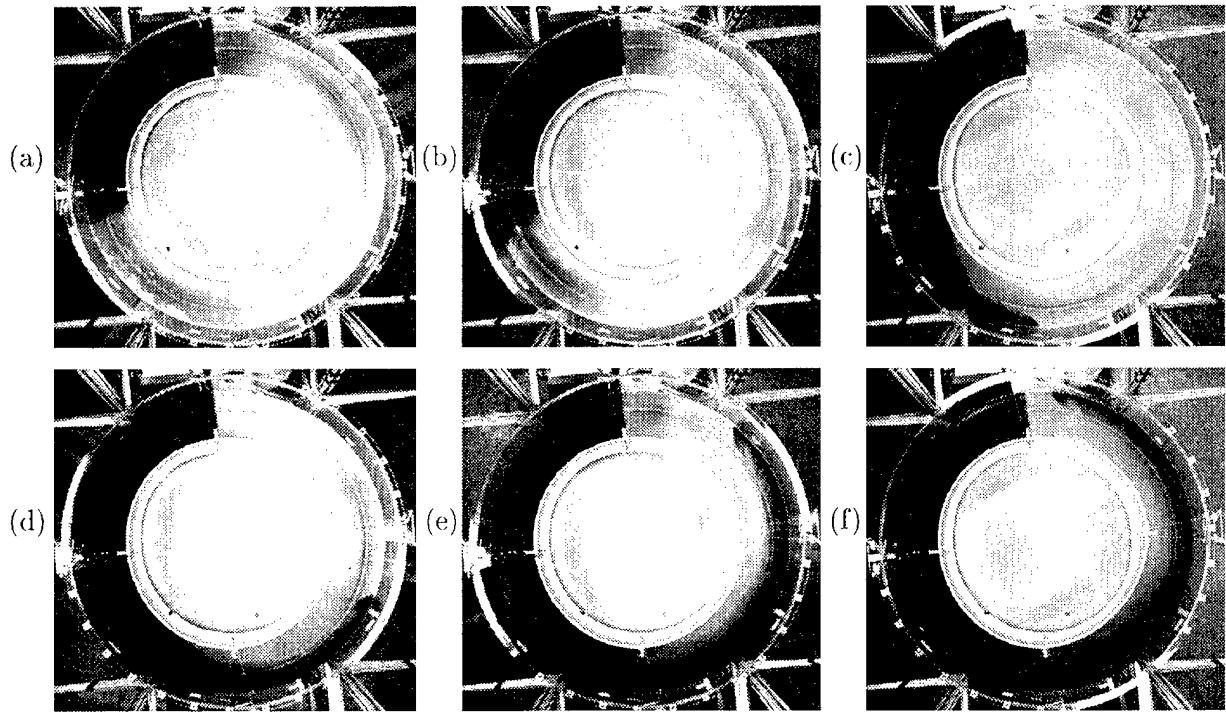
Figure 6: A sequence of photographs from the experiment with $\hat{w} = 0.99$ showing the propagation of the gravity current. The time in seconds after the dam was removed was (a) 2, (b) 3.5, (c) 10, (d) 18, (e) 28, (f) 35.

Although not visible in the photographs, a Kelvin wave formed at the beginning of the experiment. The wave could be seen by looking directly along the dammed region toward the inside back wall of the dam. Immediately after the removal of the dam, the wave of elevation propagated upstream along the interior barrier until it reached the dam end wall, at which point it was reflected around to the outside wall and it continued to propagate downstream behind the nose and in some cases probably caught up with the nose of the current.

In all experiments the digitised images were processed using *Matlab*. Measurements were taken of the position of the nose of the current along the right hand wall and also of the position of the separation point along the left hand wall. The position of the current was plotted as a function of time (with the removal of the dam occurring at $t = 0$) and the results are shown in figure 8. Allowing for an initial adjustment period after the removal of the dam, the velocity remains roughly constant for a period of time and we use a linear fit to this region to give the velocities for comparison with the theoretical predictions. As the current nears the end of the annulus however there is a noticeable decrease in velocity and this departure from the linear fit is more pronounced for larger $\hat{w}$. We hypothesize that lateral friction plays an important role in this decay. In some cases the Kelvin wave which initially propagated upstream catches up with the nose of the current after its reflection off the inside dam wall and this interference may also have an effect on the nose velocity.
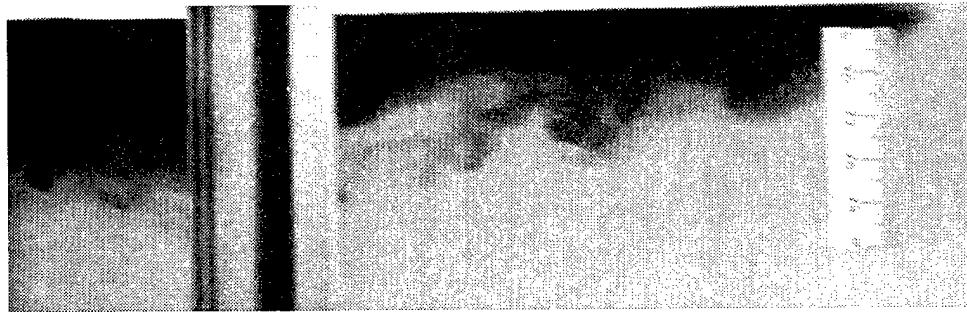
220

Figure 7: Photograph showing a side view of the current in the experiment with $\hat{w} = 0.99$. Note the unsteadiness and the billows trailing behind the nose. The nose has reached a circumferential distance from the dam of approximately 1 m.
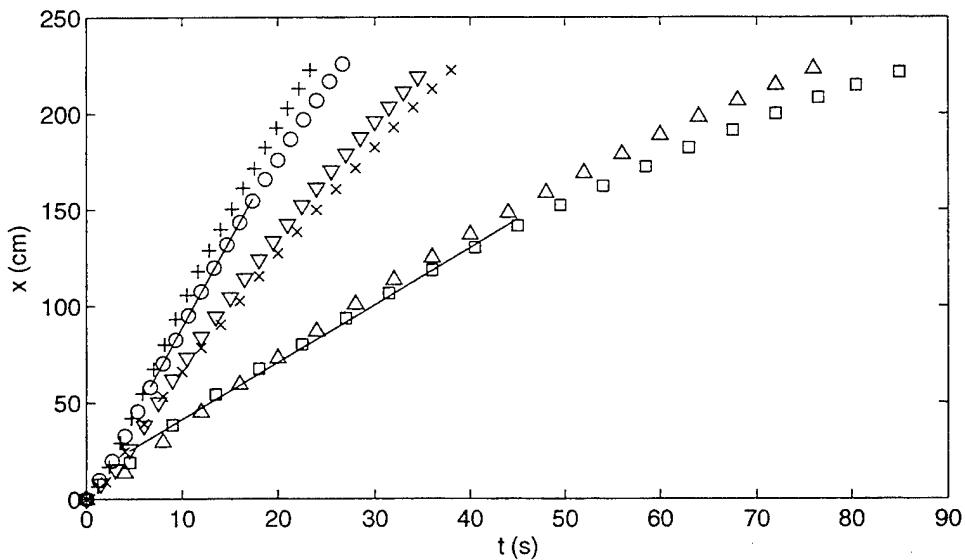

Figure 8: Position of the nose of the current on the outside wall against time. x is the circumferential distance from the dam, which was removed at time $t = 0$. The different symbols are results from experimental runs with parameter $\hat{w} = 0.25$ (+), 0.5 (○), 0.99 (∇), 1.95 (×), 3.11 (△), 4.02 (□). The two solid lines are examples of the linear fit used to determine the velocity of the current.

The width was also measured at each time step. Two definitions of the width were recorded; firstly, the 'vortex sheet' width used by Stern et al. (1982) that is, the width from the side wall to the maximum shear line which separates the coherent laminar part of the current from the region of eddies and billows (the darker dyed region in figure 6. Our second definition includes the billows and eddies as part of the current and the width was then the radial distance from their outer edge to the wall. In order to eliminate some of the subjectivity in the measurement process (in both cases), the width was measured at

221
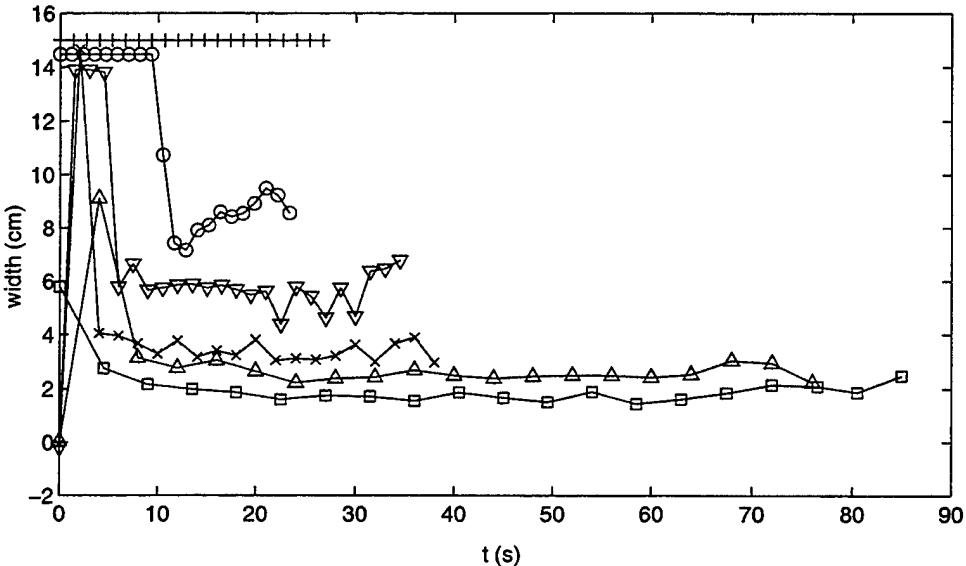
Figure 9: Width of the current against time t for runs with $\hat{w} = 0.25$ (+), 0.5 ($\bigcirc$), 0.99 (∇), 1.95 ($\times$), 3.11 ($\triangle$), 4.02 ($\square$). The dam was removed at time $t = 0$. Here the definition of width includes the billows on the edge of the current.

approximately one Rossby radius of deformation behind the leading edge of the intrusion and, at each time step, five estimates of the edge of the current were made. The mean of these estimates was used as the value for the width at that time step. The width against time graph (figure 9) revealed some initial transience as the fluid slumped followed by a period in which the width of the current remained approximately constant. Here, we use the mean value for each run (neglecting the initial adjustment time) to compare with the numerical and theoretical results found by Helfrich.

The sudden jump in the record for $\hat{w} = 0.5$ indicates that at $t \approx 12\,$s the current separated from the interior wall within the region one deformation radius behind the nose. In the run with $\hat{w} = 0.25$ the current width is exactly equal to the width of the channel throughout the experiment, that is the nose and separation point were less that a Rossby radius of deformation apart throughout and in this case the current behaves very similarly to its equivalent (one driven by the same density difference) in a non-rotating frame of reference.

4.2 Comparison with theoretical and numerical predictions

Figure 10 shows theoretical, numerical and experimental results for current width, velocity and height plotted against the governing non-dimensional parameter $\hat{w}$. We also include the results obtained by Stern *et al.* (1982), however these are not in their original form, but have been non-dimensionalised using the initial height of the dammed fluid so as to allow comparison with the present results. Generally there is reasonable agreement between the new results and the theoretical and numerical predictions. The most noticeable discrepancy
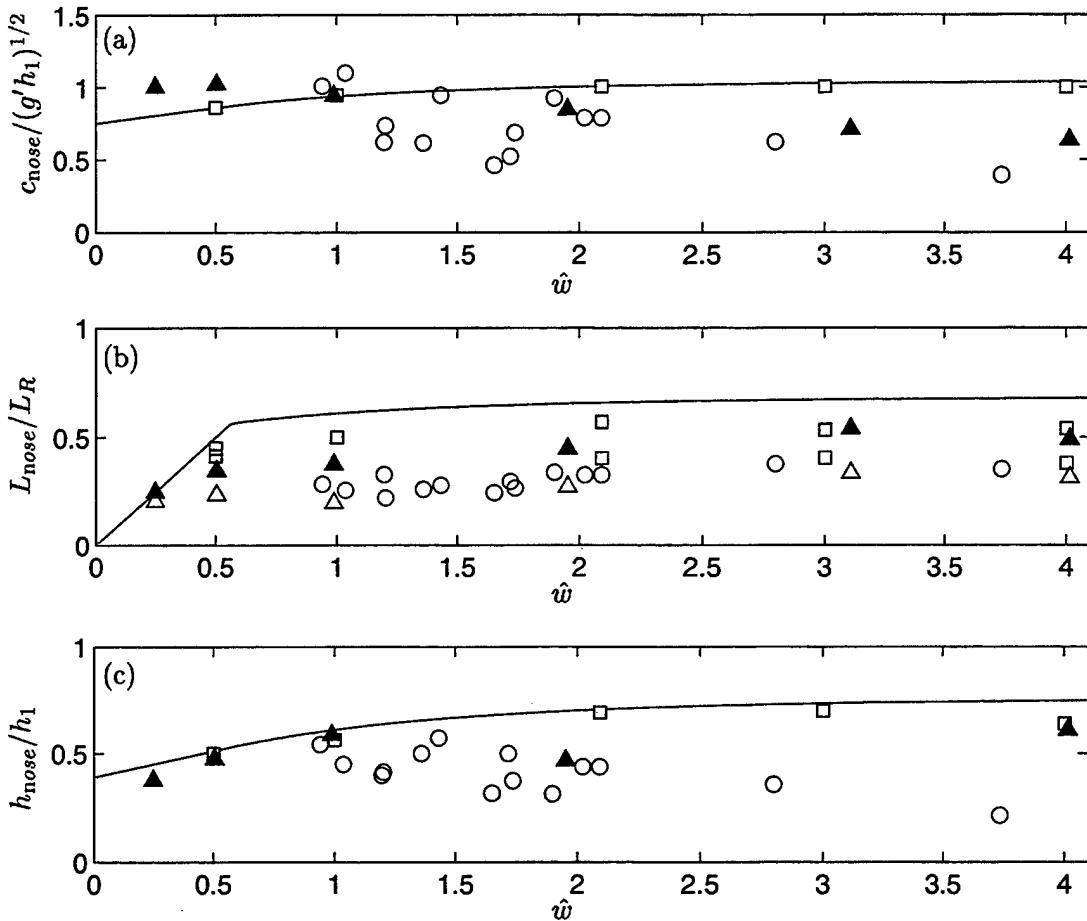
Figure 10: Comparison of the present results for experiments 1–6 (table 1) with previous experimental data (from Stern *et al.*, 1982) and new numerical and theoretical results (from Helfrich). The plots show the current velocity (a), width (b), and height at the nose (c). All results are non-dimensional and plotted against the governing parameter $\hat{w}$. The straight lines are the theoretical results using the bore speed relation $c_{nose} = 1.2\sqrt{g'h_b}$. The squares are the numerical results, the circles are the results from Stern *et al.* (1982) and the triangles are the results from the present study. In (b) the solid and outline symbols correspond to the two different definitions of width (§4.1): the solid symbols include the billows and outline symbols show the width of just the laminar part of the current.

is in the velocity data: the experimental data show a clear decrease for larger $\hat{w}$, whereas the numerical and theoretical data show a very slight increase in nose velocities between $\hat{w} = 1$ and $\hat{w} = 4$.

The theoretical and numerical models do not include all of the physical effects that exist in the experiment and so it is unclear exactly what the discrepancy between the sets of results is due to. Some part can be attributed to the numerical scheme used. The numerical solution points in figure 10 are from the Rutgers ROMS model which is a continuously
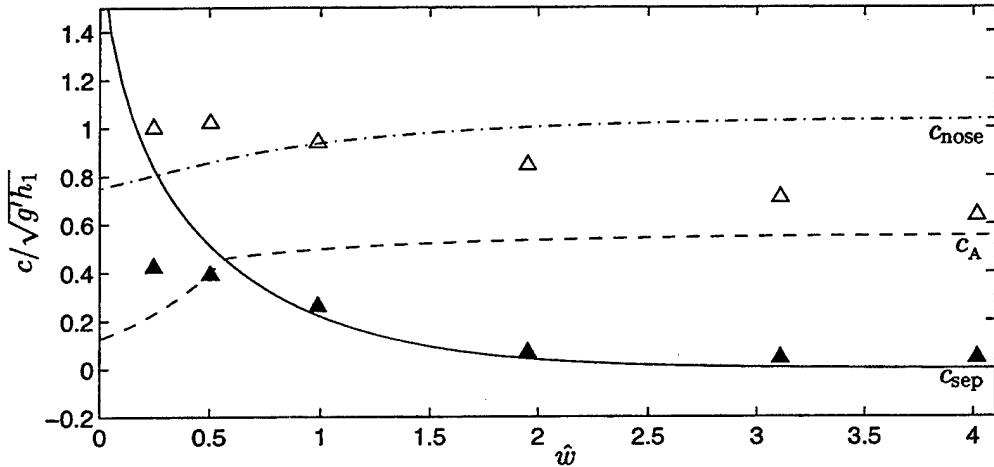
223

Figure 11: Theoretical and experimental velocities. The lines correspond to theoretical predictions for velocities of the current nose ----, separation point -- and attachment point -- (see figure 4). Triangles show experimental results for nose velocity ($\triangle$) and separation point velocity ($\blacktriangle$).

stratified hydrostatic ocean model set up to replicate laboratory scales. It does not include any vertical turbulent mixing sub-model and also uses slip boundaries, so the effects of frictional dissipation are neglected. If this effect were included we would expect the predicted velocities to be lowered, particularly in the cases with larger c_{nose}. The effects of mixing are also neglected in the theoretical and numerical predictions. Mixing would change the value of g' locally at the nose and hence lead to a lower velocity. The finite lower layer may also play a role however these effects are neglected in the theoretical model. Griffiths & Hopfinger (1983) conjecture that cyclonic vortices are generated in the lower layer by turbulence in the current and their experiments show wave and eddy motions exist in the deep lower layer.

The separation point and nose velocities from the present set of experiments are shown in figure 11. The separation point velocities match very well to the theoretical predictions. The agreement is much closer than with the nose velocities. This is probably because the separation point velocities are much slower and hence frictional dissipation plays a much smaller role. There is also less mixing far upstream of the nose in the vicinity of the separation point. We note that in the theoretical results $c_{sep} < c_A$ for $\hat{w} \lesssim 0.5$, and hence the current is attached across the width of channel to both walls. In this case the separation point velocity should equal the nose velocity ($c_{sep} \approx c_{nose}$) however the experimental results do not show a jump between the two curves. However it proved too difficult to measure the attachment point velocity precisely, so this effect could not be studied.
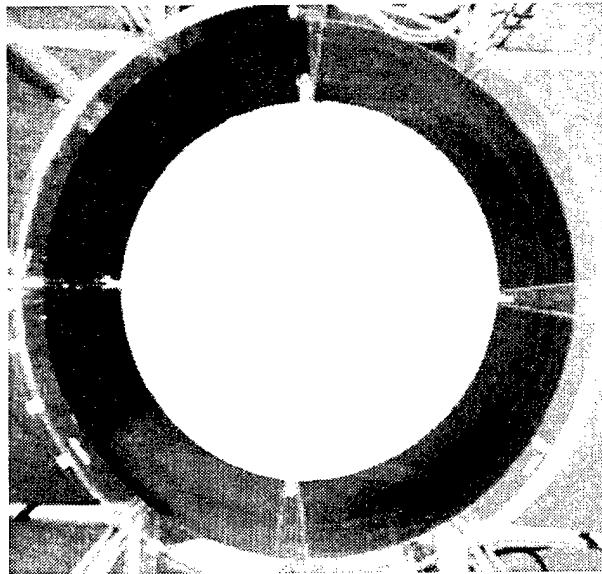
224

Figure 12: Photograph from the co-rotating camera mounted above the tank in the experiment with $\hat{w} = 1.93$ and $h_0/h_1 = 0.48$. The darker dyed fluid marks the intrusion of lower potential vorticity fluid (which has propagated around $< 1/4$ of the annulus). The Kelvin wave is not seen in this image. The photo was taken approximately 15 s after the removal of the dam.

5 Results for the experiments with a two-layer fluid ambient $(h_0 \neq 0)$

5.1 Qualitative description of the flow

The intrusion of the lower potential vorticity fluid (marked experimentally by the blue dye) propagated as a very thin laminar rarefying front (figure 12) in agreement with the numerical solutions of Helfrich *et al.* (1999). As the experiment progressed the exact position of this intrusion became difficult to see. Thus, in order to estimate the velocity of the nose of the current, its position was plotted against time for the early section of the run when the nose was clearly visible and a linear fit was again used. In the experiments when the depth difference across the dam was small ($h_0/h_1 \approx 0.75$) the current travelled only a short distance (≈ 0.75 m) around the tank before stagnating and forming a large eddy.

There was a disturbance which propagated ahead of, and at a faster velocity than, the potential vorticity intrusion, similar to the shock in the numerical solutions of Helfrich *et al.* (1999). In the experiments this took the form of an undular or a shock-like bore. The series of internal Kelvin waves were clearly visible and propagated along the interface between the lighter red fluid and the clear lower layer. The amplitude of the leading disturbance was the largest with subsequent waves decreasing in size (figure 13). Each time the waves reached an end wall they were reflected off and propagated around the opposite wall of the
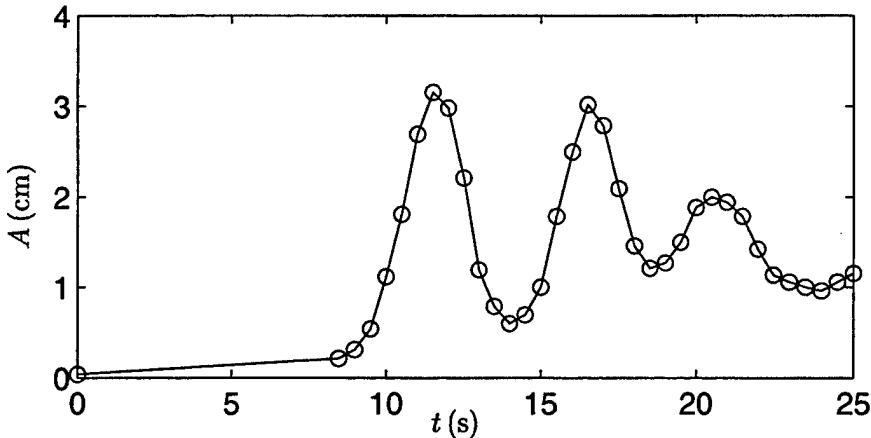
Figure 13: Distortions in the interface measured at a fixed point (~1 m from the dam) against time from the experiment with $\hat{w} = 0.48$ and $h_0/h_1 = 0.48$. The measurements were taken from images captured by the co-rotating camera mounted on the side of the tank. The data shows the leading internal Kelvin wave and the subsequent chain of smaller waves. The upstream propagation of these waves after reflection off the end wall is not shown here.

annulus in the other direction. Each time a reflection occurred the waves decayed in size however they propagated around the annulus several times before becoming too small to observe. The amplitude of the leading disturbance is plotted in figure 14 and it is found to be proportional to the depth difference across the dam between the two layers of the same density. The reflected bore also affected the advance of the lower potential vorticity fluid (causing the stagnation mentioned above in the cases with $h_0/h_1 \approx 0.75$). As the bore travelled past the potential vorticity front, the front either recoiled or advanced suddenly depending on whether the bore was travelling upstream or downstream, respectively. In many cases a large eddy split off from the current as the bore passed.

For experiments with a large depth difference across the dam $h_0/h_1 \approx 0.25$ the difference between the bore speed and the advancement velocity of the potential vorticity intrusion was small and the two features were almost co-located. In these cases (and those with $h_0/h_1 \approx 0.5$ and $\hat{w} \gtrsim 3$) the bore was turbulent with eddies detraining from the nose (figure 15). For larger values of h_0/h_1 the intrusion of the potential vorticity front was located far behind the leading disturbance which was a much smoother series of waves (figure 16).

5.2 Comparison with theoretical and numerical results

Figure 17 shows the amplitude of the leading bore plotted against the ratio of the initial depths of the layers on either side of the dam. The amplitudes are up to a factor of two larger than in results obtained numerically by Helfrich et al. (1999) however the qualitative agreement is good. The amplitude of the leading wave increases as the difference in depths across the dam becomes larger, except when close to the limiting case of $h_0 = 0$ (no layer
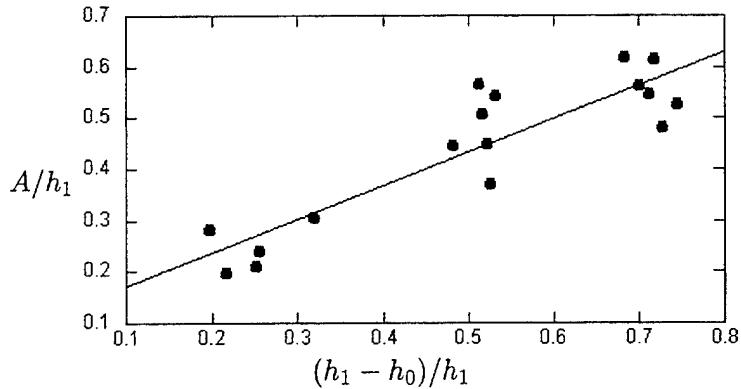
226

Figure 14: The non-dimensional amplitude A/h_1 of the leading disturbance (measured downward from the interface) against the non-dimensional depth difference across the dam $(h_1 - h_0)/h_1$. The straight line is a linear fit to the data.

Figure 15: Photographs showing the turbulent structure of the bore from experiments with (a) $\hat{w} = 0.99, h_0/h_1 = 0.28$ and (b) $\hat{w} = 0.5, h_0/h_1 = 0.29$. In both cases the darker fluid marks the fluid of lower potential vorticity. (a) shows the nose of the intrusion (approximately 1/5 from the right hand end of the photo) inside the Kelvin wave. (b) shows the eddying structures just behind the nose of the intrusion.

227

Figure 16: Photographs from the experiment with $\hat{w} = 0.48$ and $h_0/h_1 = 0.48$. (a) shows the leading internal wave and the potential vorticity can just be seen on the left hand side of the photo. (b) shows the smooth shape of the initial and second wave. The white marks are scales on the side of the tank and should be ignored.

of lighter fluid ahead of the dam) and there is a wider range of amplitudes for lower h_0/h_1 across the same range of $\hat{w}$. There is however no clear systematic variation with $\hat{w}$, which is in contrast to the numerical results.

The position of the leading bore was plotted from the sequence of images recorded as it passed into the view of the video camera mounted on the side of the tank. The velocity was then estimated using a linear fit to the data. We note that it is difficult to obtain an accurate estimate over such a short range (particularly for the experiments with $h_0/h_1 \approx 0.75$ in which the wave had a small amplitude) and a better measurement technique is required to allow a careful comparison of results, however the current data are included here for completeness (figure 18). As in the results from § 4.2 the trend indicated in figure 18 is that the velocities are again lower in the experimental case. This is probably attributable to the lack of side wall friction in the numerical model. There is also a large spread in the data and no clear variation with $\hat{w}$.

The velocity of the potential vorticity front was also measured and despite a large scatter matches the numerical data reasonably (figure 19). The agreement is probably better than in the case with $h_0 = 0$ because the current velocities are slower when it propagates into the two-layer ambient and hence there is less frictional dissipation. Also the intrusion rarefies as it advances so mixing is negligible.
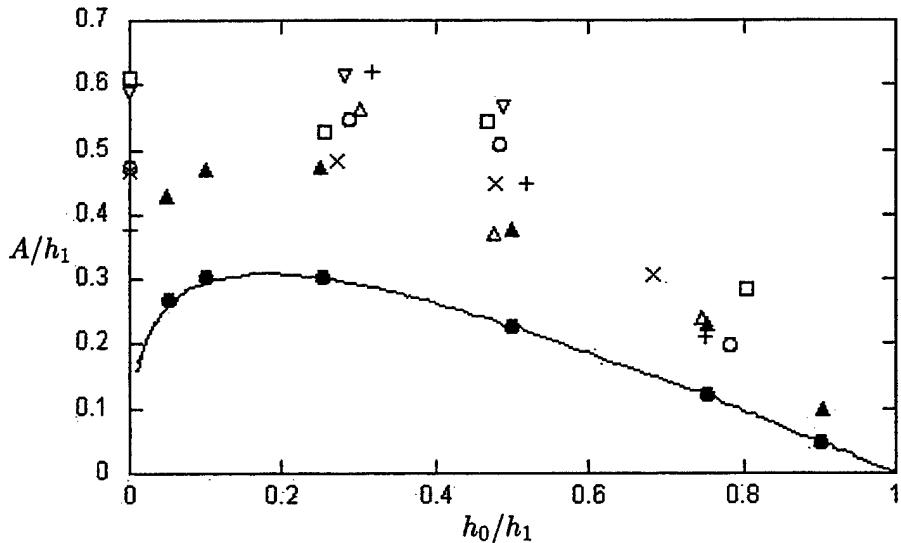
228

Figure 17: The non-dimensional amplitude of the disturbance against the ratio of depths across the dam. The straight line is the non-rotating theory $\hat{w} = 0$. The solid symbols are the results from Helfrich *et al.* (1999) for $\hat{w} = 0$ (•) and 4 (▲). The outline symbols correspond to the results from the present set of experiments with $\hat{w} = 0.25$ (+), 0.5 (○), 0.99 (▽), 1.95 (×), 3.11 (△), 4.02 (□).
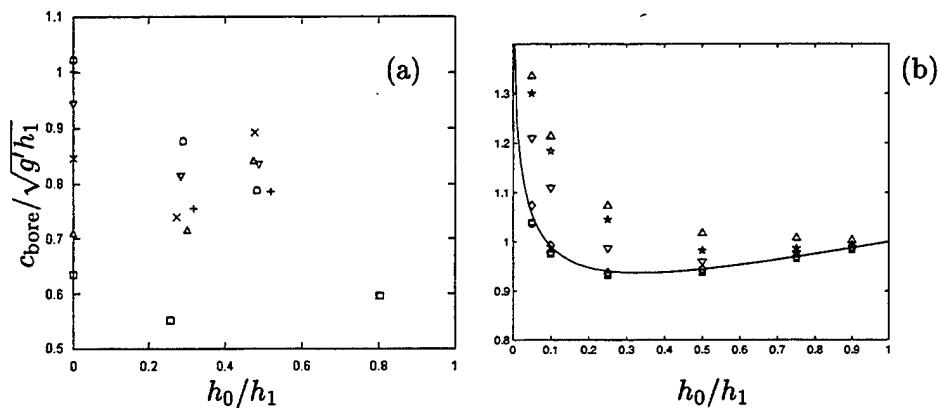
Figure 18: Results showing the bore velocities from (a) the present set of experiments and (b) from Helfrich *et al.* (1999). (a) shows the experiments with $\hat{w} = 0.25$ (+), 0.5 (○), 0.99 (▽), 1.95 (×), 3.11 (△), 4.02 (□). In (b) the velocity increases with $\hat{w}$ from 0 (○) to 4 (△).

229
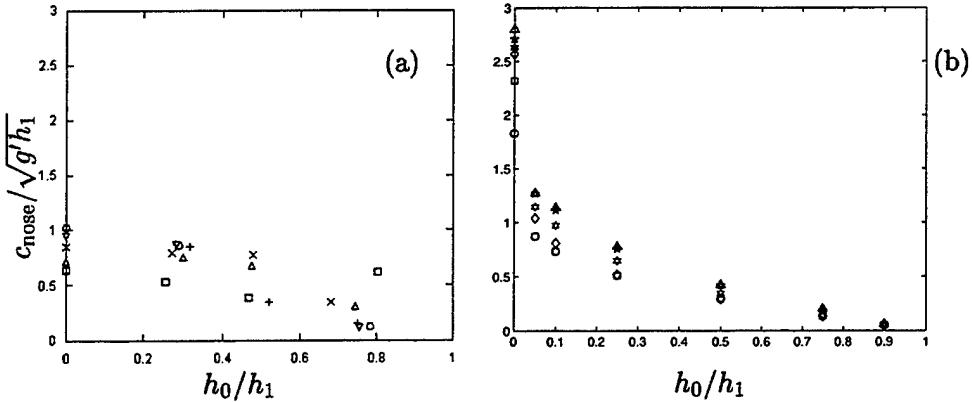
Figure 19: Results showing the velocities of the potential vorticity intrusion from (a) the present set of experiments and (b) from Helfrich *et al.* (1999). (a) shows the experiments with $\hat{w} = 0.25\,(+)$, $0.5\,(\bigcirc)$, $0.99\,(\nabla)$, $1.95\,(\times)$, $3.11\,(\triangle)$, $4.02\,(\square)$. In (b) the velocity increases with $\hat{w}$ from 0 (o) to 4 ($\triangle$).

6 Conclusions and further work

We have considered the problem of a dam break gravity current in a rotating frame in two different scenarios. In the first situation we return to the well-studied problem of the current flowing into a uniform ambient. The purpose of the experimental study was a comparison with new theoretical results by Helfrich. The new model connects a bore solution at the nose of the current to a rarefaction solution and relates the height, depth and width of the current to the initial dam conditions. There is good agreement between the theoretical solutions and numerical solutions from a three-dimensional continuously stratified hydrostatic ocean circulation model (set up to imitate laboratory conditions). The laboratory results agree reasonably well with the two sets of results and the differences between them were attributed to viscous effects at the boundaries and mixing, neither of which are present in the models. We note also that small scale turbulence and vertical shear are more significant in the laboratory, so the numerical solutions may be of more use when extrapolating to the oceans.

The second set of experiments considered the case when the ambient fluid outside of the dam region consisted of a two-layer stratification, in which the upper layer of relatively light fluid was of the same density as that released from the dammed region. It was found that a undular bore propagated ahead of the intrusion of fluid of lower potential vorticity. For larger separations between the bore and the potential vorticity front, the bore was a smooth series of waves, whereas when the separation between the potential vorticity front and the bore was small, the bore was turbulent with eddying structures on its lower edge. The amplitude of the leading disturbance was proportional to the initial height difference between the dammed region and the upper layer of the ambient fluid. The preliminary results also show qualitative agreement with numerical results obtained by Helfrich *et al.* (1999) (using a single layer shallow water model).

There are several possible extensions to the work presented here. Both sets of experiments could be repeated in a rectangular tank, which would allow visualisation of the side of the current for a longer time and propagation distance. The set of experiments with the current propagating into the two-layer ambient should be extended over a wider parameter range so a better comparison with the numerical data could be made. The numerical solutions also predict existence of a strong offshore boundary layer directly behind the shock. This feature was not observed in these experiments, possibly it was obscured by the dye in the current. The use of particle tracking in the experiments would give confirmation of whether this flow occurs in the laboratory and enable us to characterise it.

7   Acknowledgements

References

FEDOROV, A. & MELVILLE, W. 1996 Hydraulic jumps at boundaries in rotating fluids. *Journal of Fluid Mechanics* **324**, 55–82.

GRIFFITHS, R. 1986 Gravity currents in rotating systems. *Annual Review of Fluid Mechanics* **18**, 59–86.

GRIFFITHS, R. & HOPFINGER, E. 1983 Gravity currents moving along a lateral boundary in a rotating fluid. *Journal of Fluid Mechanics* **134**, 357–399.

HELFRICH, K., HUO, A. & PRATT, L. 1999 Nonlinear Rossby adjustment in a channel. *Journal of Fluid Mechanics* **390**, 187–222.

HERMANN, A., RHINES, P. & JOHNSON, E. 1989 Nonlinear Rossby adjustment in a channel: beyond Kelvin waves. *Journal of Fluid Mechanics* **205**, 469–502.

ROGERSON, A. 1999 Transcritical flows in the coastal marine atmospheric boundary layer. *Journal of Atmospheric Sciences* **56**, 2761–2779.

STERN, M. 1980 Geostrophic fronts, bores, breaking and blocking waves. *Journal of Fluid Mechanics* **99**, 687–703.

STERN, M. & HELFRICH, K. 2002 Propagation of a finite-amplitude potential vorticity front along the wall of a stratified fluid. *Journal of Fluid Mechanics* **468**, 179–204.

STERN, M., WHITEHEAD, J. & HUA, B. 1982 The intrusion of a density current along the coast of a rotating fluid. *Journal of Fluid Mechanics* **123**, 237–265.

Stability of viscoplastic flow

Junjun Liu

1 Introduction

Air and water, the most common fluids on the Earth, are Newtonian fluids. It means that the viscous behaviors of these fluids can be described by Stokes' law of viscosity. In other words, the viscosity, which is defined as the ratio of shear stress versus shear rate, is constant. However, there are many liquids that do not obey Stokes' law of viscosity. For example, many geological and industry materials, such as mud, ice, lava, painting oil, toothpaste, drilling mud, chocolate and so forth, are not Newtonian fluids. Any fluid that does not follow the constant-viscosity law is called non-Newtonian fluid. Non-Newtonian fluids often exhibit some very interesting behaviors.

There are many types of non-Newtonian fluids: shearing thinning fluid, viscoplastic fluid and viscoelastic fluid... In this report, we will focus on the viscoplastic fluid. Viscoplastic fluid is also called "yield stress" fluid. Such fluid has a property in which the fluid behaves like a solid below some critical stress value (the yield stress), but flows like a viscous liquid when the yield stress is exceeded. It is often associated with highly aggregated suspensions. Flow of the muddy rivers is a typical example. Among many viscoplastic fluids, there is a special class called Bingham plastics. For Bingham plastic fluid, the shear stress beyond the yield stress is linearly proportional to the shear rate. If the yield stress approaches zero, the Bingham plastic fluid can be approximately treated as Newtonian fluid. Mathematically, this model can be represented as ([11]):

$$\tau_{ij} = \left(\nu + \frac{\tau_Y}{\dot{\gamma}}\right)\dot{\gamma}_{ij} \quad for \quad \tau > \tau_Y, \tag{1}$$

and

$$\dot{\gamma}_{ij} = 0 \quad for \quad \tau < \tau_Y. \tag{2}$$

where τ_{ij} is the deviatoric stress tensor, ν is the viscosity, the rate-of-strain tensor is:

$$\dot{\gamma}_{ij} = \frac{\partial v_i}{\partial x_j} + \frac{\partial v_j}{\partial x_i}. \tag{3}$$

where v_j represents the velocity field, and

$$\tau = \sqrt{\frac{1}{2}\tau_{ij}\tau_{ij}} \quad and \quad \dot{\gamma} = \sqrt{\frac{1}{2}\dot{\gamma}_{ij}\dot{\gamma}_{ij}}. \tag{4}$$
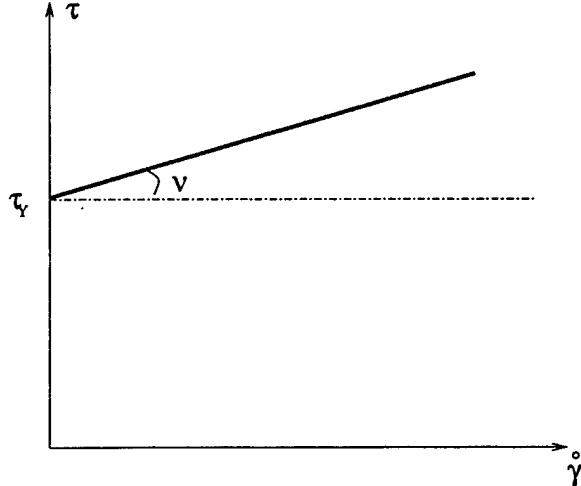
232

Figure 1: The Rheology of the Bingham model.

are the second invariants of τ_{ij} and $\dot{\gamma}_{ij}$. The rheology of the Bingham fluid is shown in Figure 1.

For the flow of the Bingham fluid, the stress varies in space and time. There can be regions in the fluid where the yield stress is exceeded, and other regions in which it is not. The boundaries between the two regions are the yield surfaces. Tracking the yield surfaces as the flow evolves is one of the most complicated problems associated with the Bingham model. The stability of the viscoplastic flows depends on what happens to these non-material surfaces when a sudden perturbation is introduced? Do the yield surface remain intact and merely displaced, or do they disappear and the plug is "broken" by the perturbation? In the study of the channel flow of the Bingham fluid, Friggard ([4]) address that an infinitesimal perturbation to the flow should displace the yield surfaces but otherwise leave them intact, since the unyielded region is "an elastic solid that would not break up". However, the identification of the yield surface leads to some confusion in the free surface flow of the Bingham fluid down an inclined plane and through narrow conduit ([2]). In this kind of problems, asymptotic expansion can be used to reduce the governing equations due to the small aspect ratio of the fluid. The leading order asymptotic solution contains apparent yield surface, however, the theory subsequently predicts that fluid flow is extensional even in the supposedly non-yielding regions. The resolution of this paradox is to re-interpret the apparent yield surfaces as "fake" ones and apparent "plug flow" as a weakly yielding flow, or a "pseudo-plug" ([1]; [2]).

Then, when the "plug flow" can be treated as "pseudo-plug flow"? How the stability criterion changes as we interpret the "plug flow" differently? What is the meaning of the yield surface and yield stress for the Bingham plastic flow? In this paper, we will try to answer these questions by studying various kinds of Bingham flow phenomena: free surface flow, channel flow and thermal convection. Based on the understanding of the yield surface and yield stress in the Bingham fluid, we then get an improved vertical average mode for the free surface flow of the Bingham thin film.
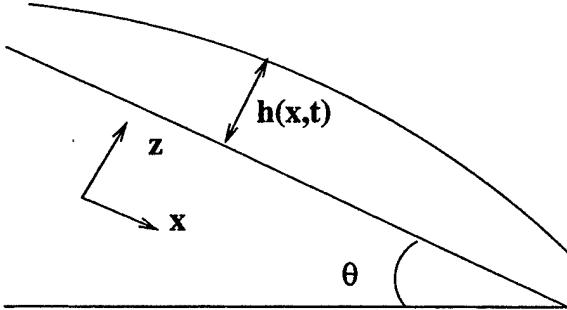
233

Figure 2: Fluid flowing down the inclined plane.

2 Free surface flow

Mud, the common geological fluid, has Bingham rheology. Every year, accompanying the heavy and persistent rainfalls in mountainous areas, mudflow can be induced by mixture of the water and mud flowing down the hill. It can move stones, boulders and even trees. It threatens the lives of the people who inhabit in the mountain area and is a main source of the natural hazards. Mudflows caused by Hurricane Mitch in 1998 have incurred devastating floods in Central America. In Honduras alone more than 6000 people perished. Half of the nations infrastructures were damaged([9]).

River with a large amount of clay suspension can also be characterized as Bingham fluid. The mud concentration at low water in the Yellow river of China is known to reach 50% by volume ([10]). In Jiang-xia Ravine China, the mudflow surges down during the wet season in groups of successive bores. The maximum wave height reaches $4m$ and the maximum wave velocity $13ms^{-1}$. The wavelength varied between 20 and 100m, while the period of each wave ranges from 5 to 60s. The bore fronts splattered with so much force that even large stones were thrown into the air. The flow in the rear of the waves was much shallower, slower and essentially laminar, and frequently stagnant before next surge. ([10])

Better understanding of the free surface flow of the Bingham fluid and accurate derivation for the stability criterion can help us to monitor the mudflows down the hill and mud surges in the rivers. In this section, we first give the governing equations for two-dimensional free surface flow, and then we introduce the pseudo-plug theory for the Bingham flow under the lubrication approximation. After that, we briefly describe the vertical average mode and its limitations. We also compare the pseudo-plug theory for the Bingham model with the bi-viscous model. Finally, we derive an improved vertical average model.

2.1 Governing equations

Consider a two-dimensional laminar flow of a thin layer of mud flowing down a plane with inclination θ. We define an (x, z) coordinate system with the x-axis along and the z-axis normal to the plane. We denote the longitudinal and transverse velocity components by $u(x, z, t)$ and $w(x, z, t)$ respectively, the pressure by $p(x, z, t)$ and the depth normal to the bed by $h(x, t)$ (Shown in figure 2).

The momentum equations along x and z directions are:

$$\rho(u_t + uu_x + wu_z) = -p_x + \partial_x\tau_{xx} + \partial_z\tau_{zx} + \rho g \sin(\theta), \qquad (5)$$

$$\rho(w_t + uw_x + ww_z) = -p_z + \partial_z\tau_{xz} + \partial_z\tau_{zz} - \rho g \cos(\theta), \qquad (6)$$

with the continuity equation:

$$u_x + w_z = 0. \qquad (7)$$

At the bottom $z = 0$, the velocity vanishes (non-slip boundary condition):

$$u = w = 0. \qquad (8)$$

On the free surface $z = h$, the kinematic boundary condition requires:

$$h_t + u(x, h, t)h_x = w(x, h, t); \qquad (9)$$

and the stress free boundary condition states:

$$\begin{pmatrix} \tau_{xx} - p & \tau_{xz} \\ \tau_{xz} & \tau_{zz} - p \end{pmatrix} \begin{pmatrix} h_x \\ 1 \end{pmatrix} = \begin{pmatrix} 0 \\ 0 \end{pmatrix}. \qquad (10)$$

The constitutive law of the Bingham fluid is:

$$\begin{cases} \tau_{ij} &= (\nu + \frac{\tau_Y}{\dot{\gamma}})\dot{\gamma}_{ij} & if & \tau > \tau_Y, \\ \dot{\gamma}_{ij} &= 0 & if & \tau < \tau_Y, \end{cases} \qquad (11)$$

where τ_{ij} is the stress tensor, $\dot{\gamma}_{ij}$ is the rate-of-strain tensor and $\dot{\gamma}$ is the second-invariant of the rate-of-strain tensor.

For the slow flow of the thin mud layer, the height of the fluid layer H is much less than the length L and the vertical velocity V is much less than the horizontal velocity U. We can define the aspect ratio: $\epsilon = \frac{H}{L}$ ($\epsilon \ll 1$) and non-dimensionalize the equations in the following way: $p = \rho g H cos(\theta)p'$, $z = Hz'$, $x = Lx'$, $u = Uu'$, $w = \frac{H}{L}Uw'$, and $t = \frac{L}{U}t'$. Drop the primes and the scaled momentum equations are:

$$\epsilon R_e(u_t + uu_x + wu_z) = -p_x + \epsilon^2\partial_x\tau_{xx} + \partial_z\tau_{zx} + S, \qquad (12)$$

$$\epsilon^3 R_e(w_t + uw_x + ww_z) = -p_z + \epsilon^2\partial_z\tau_{xz} + \epsilon^2\partial_z\tau_{zz} - 1. \qquad (13)$$

where S is the dimensionless slope defined as: $S = \frac{L}{H}\tan\theta$. R_e is the Reynolds number defined as: $\epsilon R_e = \frac{UH}{\nu}$.

Under this scaling, the stress tensor can be expressed as:

$$\tau = \nu\frac{U}{H}\begin{pmatrix} 2\epsilon u_x & u_z + \epsilon^2 w_x \\ u_z + \epsilon^2 w_x & 2\epsilon w_z \end{pmatrix}. \qquad (14)$$

We can scale the stress as $\nu\frac{U}{H}$ and define the Bingham number as $B = \frac{\tau_Y H}{\nu U}$, which is the dimensionless yield stress. Then the largest element in the stress tensor will be:

$$\tau_{zx} = \tau_{xz} = \left(1 + \frac{B}{|u_z|}\right) u_z. \qquad (15)$$

235

2.2 Lubrication Approximation

There are several ways to analyze the stability of the flow. Lubrication approximation is the simplest way. Under the standard lubrication approximation, we let ϵ be zero. The momentum equation can be simplified as:

$$0 = -p_x + \partial_z \tau_{xz} + S,$$
$$0 = -p_z - 1. \tag{16}$$

The stress free boundary condition at the top surface requires: $p = 0$ and $\tau_{xz} = 0$ (at $z = h$). Solution of the momentum equations shows that the vertical distribution of shear stress is:

$$\tau_{xz} = (h_x - S)(z - h). \tag{17}$$

The yield surface Y is defined at the place where the shear stress τ_{xz} is equal to the Bingham number:

$$B = \tau_{xz} = (h_x - S)(Y - h). \tag{18}$$

Thus,

$$Y = h + \frac{B}{|h_x - S|}. \tag{19}$$

Below the yield surface ($0 \leq z \leq Y$), the material is yielded. Above the yield surface ($h \geq z > Y$), the material remains to be unyielded. We usually call the region above the yield surface as the plug region.

Integrating the momentum equation (16) along the x-direction gives the vertical distribution of the horizontal velocity u:

$$\begin{cases} u = (S - h_x)\frac{z}{2}(2Y - z) & for \quad z < Y, \\ u = (S - h_x)\frac{Y^2}{2} & for \quad z > Y. \end{cases} \tag{20}$$

Below yield surface ($0 \leq z \leq Y$), the velocity u has parabolic dependence on height z. Above the yield surface ($h \geq z > Y$), the velocity u is independent of height z and called plug velocity.

Integrating the kinematic boundary condition (9)across the layer, we arrive:

$$h_t + \frac{\partial}{\partial x} \int_0^h u \, dz = 0. \tag{21}$$

Substituting the horizontal velocity $u(z)$ (Equation 20)into this equation, we find that the height of the free surface satisfies:

$$h_t + \frac{1}{6}\frac{\partial}{\partial x}\left[Y^2(3h - Y)(S - h_x)\right] = 0. \tag{22}$$

Linear stability analysis with an infinitesimal perturbation shows that the profile is linearly unconditionally stable. However, instabilities has been observed for the free surface flow of Bingham fluid down the inclined plane both in nature ([8]) and in the laboratory . Then, the lubrication approximation cannot be used to describe the stability of the Bingham fluid flowing down the inclined plane. Since the Reynolds number for the free surface flow

236

of Bingham fluid can be very large, then $\epsilon Re \sim O(1)$, the inertia term must be included for correctly describing the stability of the free surface flow for the Bingham fluid.

However, the lubrication approximation reveals some interesting features about the Bingham fluid. During the initiation period, the viscoplastic flow usually contains perturbation, which can be the noise in the laboratory or natural environment. Then the velocity at the plug region can treated as a sum of the plug velocity $u_0(x,t)$ and the $O(\epsilon)$ perturbation velocity $u_1(x,z,t)$:

$$u = u_0(x,t) + \epsilon u_1(x,z,t). \tag{23}$$

Notice that the velocity in the plug region will not be independent of height any more. We can treat the plug as a "fake" one, and call this region as " pseudo-plug" region. The stress tensor in the pseudo-plug region can be written as:

$$\{\tau_{ij}\} = \epsilon \left(1 + \frac{B}{\dot\gamma}\right) \begin{pmatrix} 2u_{0x} & u_{1z} \\ u_{1z} & -2u_{0x} \end{pmatrix}. \tag{24}$$

Substituting the strain rate: $\dot\gamma = \epsilon\sqrt{4u_{0x}^2 + u_{1z}^2}$ into the above expression, we then have:

$$\tau_{ij} = \frac{B}{\sqrt{4u_{0x}^2 + u_{1z}^2}} \begin{pmatrix} 2u_{0x} & u_{1z} \\ u_{1z} & -2u_{0x} \end{pmatrix}. \tag{25}$$

Therefore, as the flow reaches the steady state, the variation of the zero order plug velocity along the x direction goes to zero: $u_{0x} \to 0$, the stress tensor through the pseudo-plug region can be written as:

$$\tau_{ij} = B \begin{pmatrix} 0 & 1 \\ 1 & 0 \end{pmatrix} sgn(u_{1z}) + O(\epsilon). \tag{26}$$

As the flow settles down to a steady state, the stress in the pseudo-plug region will be $O(\epsilon)$ above the yield stress B. It implies that the flow in the pseudo-plug region will relax to a slightly yielded state if we consider the noise in the initialization period.

In figure 3, we compared the vertical stress distribution obtained in the uniform true equilibrium state (17) with that obtained in the pseudo-plug state. From this figure we can see that the uniform true equilibrium state will produce a true plug, but the limiting lubrication solution will always produce a slightly yielded pseudo-plug.

For the experiment carried out in the laboratory and geological Bingham fluid flowing down the inclined plane, the uniform true equilibrium state is very hard to achieve. In most cases, the flow in the plug region will always relax to a slightly yielded pseudo-plug state after the flow is initiated.

2.3 Vertical averaged model

For describing stability of the Bingham fluid flowing down the inclined plane, the more accurate boundary layer approximation including the inertia term can be used. In boundary layer approximation, the momentum equations are:

$$\begin{aligned} R(u_t + uu_x + wu_z) &= 1 - p_x + \frac{\partial}{\partial z}\tau_{xz}, \\ 0 &= -1 - p_z. \end{aligned} \tag{27}$$
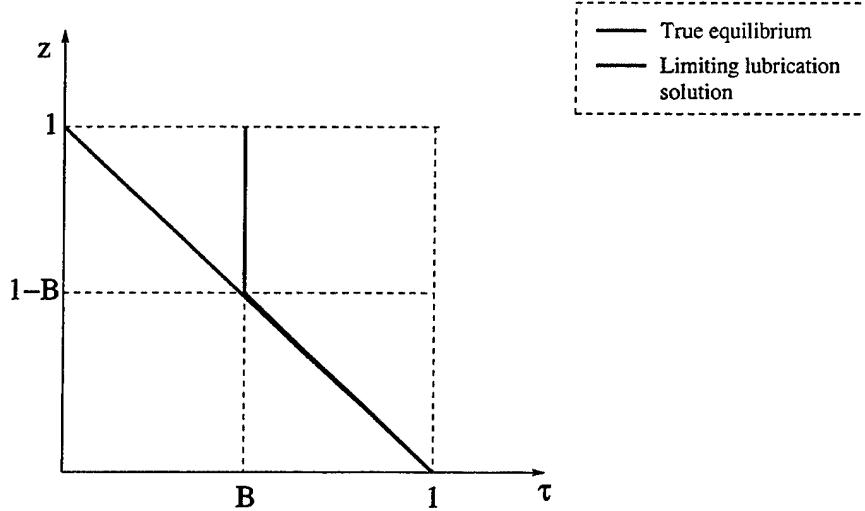
237

Figure 3: Compare the vertical stress distribution between the true equilibrium state and the pseudo plug state.

where $R = \epsilon R_e$. Following the study of the Newtonian fluid flowing down the inclined plane ([15]), further simplification of this mode can be obtained for Bingham fluid by vertically integrating the momentum equation assuming the following velocity profile ([8]):

$$\begin{cases} u = U_P(x,t)\frac{z}{Y}(2 - \frac{z}{Y}) & for \quad z < Y, \\ u = U_P(x,t) & for \quad z > Y. \end{cases} \tag{28}$$

where $U_P(x,t)$ is the plug velocity. This velocity profile is obtained from the lubrication approximation. Integrating the momentum equation along the x-direction for the plug region $Y < z < h$ gives:

$$R(U_{Pt} + U_P U_{Px}) = 1 - h_x - \frac{B}{h - Y}. \tag{29}$$

And integrating the x-direction momentum equation for the yielded region $0 < z < Y$ gives:

$$R\left(\frac{2}{3}YU_{Pt} - \frac{1}{3}U_P Y_t + \frac{2}{5}YU_P U_{Px} - \frac{2}{15}U_P^2 Y_x\right) = (1 - h_x)Y - \frac{2U_P}{Y}sgn(U_P). \tag{30}$$

Finally, integration of the kinematic boundary condition across the whole layer yields:

$$h_t + \frac{\partial}{\partial x}\left[\frac{U_P(x,t)}{3}(3h - Y)\right] = 0. \tag{31}$$

The vertical average model (VAM) is composed of the above three equations (29, 30, 31). Linear stability analysis of this model has been conducted by Liu and Mei ([8]). However, even for the Newtonian fluid flowing down the inclined plane, VAM does not give the correct Reynolds number ([3]; [15]).

For Newtonian fluid, VAM is usually used to study the turbulent flow. Since the flow of the

238

Bingham fluid down to the inclined plane is usually laminar, it is not necessary to apply the vertical average model.

Furthermore, VAM is built on the assumption that the vertical profile of the velocity u is the same with or without considering the inertia term in the momentum equation. Due to the existence of the yield stress and yield surface in the Bingham fluid, there is no justification for assuming this velocity profile. A better understanding of the Bingham fluid is necessary for obtaining the stability criteria.

2.4 Long wave expansion

For Newtonian fluid flowing down the inclined plane, it is well known that the long wave expansion for the boundary layer model (27) yields the correct Reynolds number ([3],[15]). To see how good the vertical averaged model for Bingham fluid is, let us check the critical Reynolds number for the Bingham fluid using a long wave expansion for the boundary layer model (27). First, we will carry out the stability analysis under the pseudo-plug assumption. After that, we will do the stability analysis under the true plug assumption.

Under the boundary layer approximation (See equation 27), we can integrate the momentum equation along the z-direction and considering $p = 0$ on the free surface $z = h$. Then, we get the vertical distribution of the pressure: $p = h - z$. Substituting it to the momentum equation along the x-direction, we get:

$$R(u_t + uu_x + wu_z) = 1 - h_x + \frac{\partial}{\partial z}\tau_{xz}. \tag{32}$$

For simplification, we set the slope to be unity: $S = 1$. In equilibrium, the horizontal velocity U is:

$$\begin{cases} U = \frac{1}{2}z(2Y - z) & for \quad z < Y, \\ U = \frac{1}{2}Y^2 & for \quad z > Y. \end{cases}$$

And the vertical velocity W is zero. We can also normalize the height of the free surface at the equilibrium to be unity $h = 1$.

Applying the following infinitesimally small perturbations to the equilibrium state:

$$u = U(z) + \hat{u}(x, z, t), \quad w = \hat{w}(x, z, t), \quad h = 1 + \hat{h}(x, z, t). \tag{33}$$

Dropping the hats, the momentum equation can be rewritten as:

$$R(u_t + Uu_x + wU_z) = 1 - h_x + \frac{\partial}{\partial z}\tau_{xz}. \tag{34}$$

Since the velocity perturbation satisfies the following continuity equation: $u_x + w_z = 0$, we can define a stream function Ψ and the perturbations can be rewritten as:

$$u = \Psi_z, \quad w = -\Psi_x. \tag{35}$$

First, we assume the periodic perturbations: $\Psi, h \propto exp(\lambda t + ikx)$ carry out the stability analysis for the pseudo-plug assumption. We divide the layer into two parts: the upper part is the pseudo-plug region and the low part is the yielded region. If we use the superscript

239

t and b to express the function of the top and bottom part respectively, the momentum equations in these two regions can be written as:

$$\Psi^t_{zz} = 0, \qquad for \quad z > Y, \tag{36}$$

and,

$$\Psi^b_{zzz} = ik + R(\lambda\Psi_z + ikU\Psi_z - ik\Psi U_z) \quad for \quad z < Y. \tag{37}$$

From the expression of the stream function in the region above the yield surface, we can see that the motion is allowed in this region under the pseudo-plug assumption. The linearized kinematic boundary condition at the free surface $h_t + Uh_x = w$ is:

$$\lambda = -\frac{ik}{2}Y^2 - ik\Psi^t, \quad at \quad z = 1. \tag{38}$$

Non-slip boundary condition at the bottom $z = 0$ requires:

$$\Psi^b_z(z=0) = \Psi^b(z=0) = 0. \tag{39}$$

Under the pseudo-plug assumption, the zero order stress in the pseudo-plug region is equal to the yield stress B. And the stress free boundary condition at the top surface is satisfied by the first order correction (See the discussion in the section of the lubrication approximation).

At the interface of the two parts (the perturbed yield surface), the continuation of the stress implies:

$$U^t_z + \Psi^t_{zz} = U^b_z + \Psi^b_{zz}, \tag{40}$$

Since $U^t_z = 0$ and $\Psi^t_{zz} = 0$ at the interface, we then have:

$$YU^b_{zz}(z=Y) + \Psi^b_{zz}(z=Y) = 0. \tag{41}$$

Recall the perturbation of the yield surface is: $Y' = 1 - ikB - R(\lambda + iU^t)\Psi_z B$, the interface condition (41) can be written as:

$$(1 - ikB - R(\lambda + ikU^t)\Psi_z B)U^b_{zz}(z=Y) + \Psi^b_{zz}(z=Y) = 0. \tag{42}$$

Similarly, the continuation of the perturbed velocity u across the interface implies:

$$\Psi^b_z(z=Y) = \Psi^t_z(z=Y), \tag{43}$$

and the continuation of the stream function across the interface needs,

$$\Psi^b(z=Y) = \Psi^t(z=Y). \tag{44}$$

We can then do long wave expansion by taking $k \ll 1$:

$$\lambda = k\lambda_1 + k^2\lambda_2 + ... \tag{45}$$

$$\Psi = k\Psi_1 + k^2\Psi_2 + ... \tag{46}$$

where λ_1, λ_2, Ψ_1, and Ψ_2 denote the expansion coefficients. To the leading order, the momentum equations can be written as:

$$\Psi^t_{0zz} = 0, \tag{47}$$

$$\Psi^b_{0zzz} = 0, \tag{48}$$

with the interface conditions:

$$U_{zz}^b(z = Y) + \Psi_{0zz}^b(z = Y) = 0, \tag{49}$$

$$\Psi_{0z}^b(z = Y) = \Psi_{0z}^t(z = Y), \tag{50}$$

$$\Psi_0^b(z = Y) = \Psi_0^t(z = Y), \tag{51}$$

From the leading order calculation, we obtain: $\lambda_1 = -iY$. To the second order, the momentum equations are:

$$\Psi_{1zz}^t = 0, \tag{52}$$

$$\Psi_{1zzz}^b = i + R(\lambda_1 \Psi_{0z}^b + iU^b \Psi_{0z}^b i \Psi_0^b U_z^b). \tag{53}$$

and the interface conditions are:

$$(-iB - R(\lambda_1 + iU^b)\Psi_{0z}^b B)U_{zz}^b(z = Y) + \Psi_{0zz}^b(z = Y) = 0, \tag{54}$$

$$\Psi_{1z}^b(z = Y) = \Psi_{1z}^t(z = Y), \tag{55}$$

$$\Psi_1^b(z = Y) = \Psi_1^t(z = Y). \tag{56}$$

Putting the second order solution into the kinematic boundary condition (38), we then have:

$$\lambda_2 = -\frac{RB^6}{5} + \frac{RB^5}{5} + \frac{RB^4}{3} - \frac{RB^3}{3} + \frac{B^3}{3} - \frac{2RB}{15} + \frac{2R}{15} - \frac{1}{3}. \tag{57}$$

And the critical Reynolds number is then:

$$R = \frac{5(B^2 + B + 1)}{3B^5 - 5B^3 + 2}. \tag{58}$$

We can compare the critical Reynolds number obtained by the long wave expansion with that gotten from VAM in the long wave length limit (See Figure 4). From this figure, we find that the Reynolds number obtained in VAM is always larger than that in the long wave expansion. When the yield stress equals zero, the Reynolds number gotten from the long wave expansion is $\frac{5}{6}$ of that from VAM, which is consistent with the calculation for the Newtonian fluid. As the yield stress increases (yield surface decreases), the difference increases. If the dimensionless yield stress approaches one, the difference approaches infinity.

Now, let us carry out the stability analysis under the true plug assumption. Since the true plug behaves as the elastic solid, it will not be destroyed by the infinitesimal perturbation. Then the perturbation velocity is zero in the plug region. Under the linear perturbation: $u, w, h, \Psi \propto exp(\lambda t + ikx)$, the stream function in the plug region satisfies:

$$\Psi^t = \Psi_z^t = \Psi_{zz}^t = 0 \quad for \quad z \geq Y, \tag{59}$$

which means that no motion can be transferred from the yield region to the plug region.

The stream function in the yielded region, the boundary condition, and the interface condition will remain to be the same with that under the pseudo-plug assumption. Taking the long wave expansion, to the leading order we have:
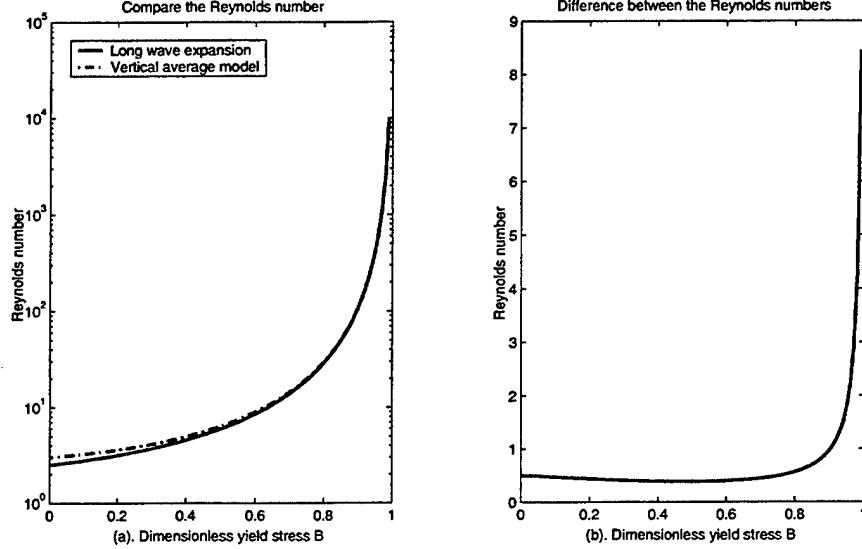
$$\Psi_0^t = \Psi_0^b = 0. \tag{60}$$

241

Figure 4: (a) Compare the critical Reynolds number obtained from the long wave expansion with that from the vertical average mode. (b) The difference between the Reynolds number obtained by different methods.

and $\lambda_1 = 0$. To the second order, we have:

$$\Psi_1^t = \Psi_{1z}^t = \Psi_{1zz}^t = 0 \quad \text{for} \quad z \geq Y, \tag{61}$$

$$\Psi_{1zzz}^b = i \quad \text{for} \quad z < Y. \tag{62}$$

There is no solution satisfying these two equations, the boundary conditions, as well as the interface conditions. It means the solution does not exist under the true plug assumption.

2.5 Compare pseudo-plug theory for the Bingham fluid with bi-viscous model

Under the pseudo-plug assumption, the motion can exist in the plug region for the Bingham fluid. Then the relationship between the rate of strain tensor and the stress is like the modified constitutive model:

$$\tau_{ij} = \left(\nu + \frac{\tau_Y}{\sqrt{\Delta^2 + \dot{\gamma}^2}} \right) \dot{\gamma}_{ij} \tag{63}$$

When the parameter Δ becomes small, the model becomes more and more Bingham-like, with flow regions that resemble the fully plastic regions of the Bingham fluid, and other regions in which the flow is just slightly yielding and reminiscent of the pseudo-plug. Here, we will consider the simplest regularized model: the bi-viscous model.

The constitutive relationship for the bi-viscous fluid is illustrated in figure 5, with a lower viscosity ν for the high shear rate and much higher viscosity ν for the lower shear rate. We can use α to express the viscosity ratio: $\alpha = \frac{\nu}{\bar{\nu}}$. If α goes to zero, the bi-viscous
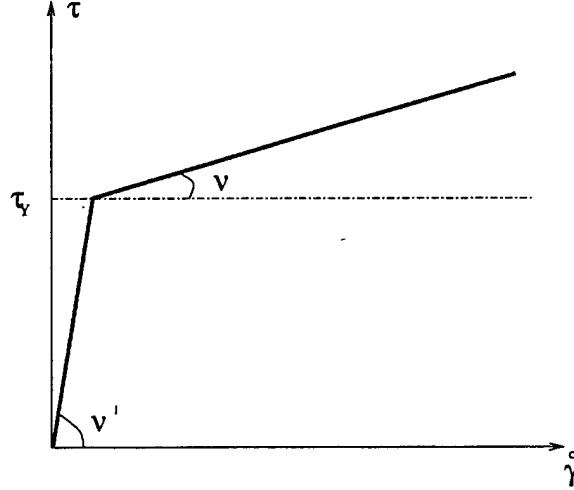
242

Figure 5: The Rheology of the bi-viscous fluid.

fluid will approaches the Bingham fluid. If α goes to one, the bi-viscous fluid is reduced to the Newtonian fluid.

$$\tau_{ij} = \nu \dot{\gamma}_{ij} \quad for \quad \tau \le \tau_Y, \tag{64}$$

$$\tau_{ij} = \nu \dot{\gamma}_{ij} + (1 - \alpha)\frac{\tau_Y}{\dot{\gamma}}\dot{\gamma}_{ij} \quad for \quad \tau > \tau_Y. \tag{65}$$

We use the same scaling as free surface flow of the Bingham fluid. The boundary layer approximation requires:

$$R(u_t + uu_x + wu_z) = 1 - p_x + \frac{\partial}{\partial z}\tau_{xz}, \tag{66}$$

$$0 = -1 - p_z. \tag{67}$$

For the bottom layer, the shear stress is $\tau_{xz} = u_z + B(1 - \alpha)$. For the top layer, the shear stress is $\tau_{xz} = \frac{1}{\alpha}u_z$ Substitute the expression for the shear stress into the momentum equation, we can then get the equilibrium velocity profile:

$$U^t = -\frac{\alpha z^2}{2} + \alpha z + \frac{Y^2}{2} - \frac{\alpha Y^2}{2} \quad for \quad z > Y, \tag{68}$$

$$U^b = -\frac{z^2}{2} + (-\alpha Y + Y + \alpha)z \quad for \quad z < Y. \tag{69}$$

with $Y = 1 + \frac{B}{|h_x - S|}$. Here the superscript t and b denotes the function for the top and bottom layer respectively.

As before, we perturb the equilibrium by infinitesimal amount: $u = U(z) + u'(x, z, t)$ and $w = w'(x, z, t)$. We also use a stream function Ψ to express the perturbation velocity: $u'(x, z, t) = \Psi_z$, and $w'(x, z, t) = -\Psi_x$. We can then carry out the linear stability analysis by assuming: $\Psi \propto exp(ikx + \lambda t)$. Then the stream function satisfies:

$$\Psi^t_{zzz} = ik\alpha + R\alpha(\lambda\Psi_z + ikU\Psi_z ik\Psi U_z) \quad for \quad z > Y, \tag{70}$$

$$\Psi^b_{zzz} = ik + R(\lambda\Psi_z + ikU\Psi_z ik\Psi U_z) \quad for \quad z \le Y. \tag{71}$$

At the free surface ($z=1$), the linearized kinematic condition gives:

$$\lambda + U(z=1)ik = -ik\Psi^t, \qquad (72)$$

and the stress free condition gives:

$$\Psi^t(z=1) + U_{zz}(z=1) = 0. \qquad (73)$$

The non-slip boundary condition at the bottom implies:

$$\Psi_z^b(z=0) = \Psi^b(z=0) = 0. \qquad (74)$$

At the interface between the two layers, the continuation of the shear stress requires:

$$\Psi_{zz}^b(z=Y) = \frac{1}{\alpha}\Psi_{zz}^t(z=Y). \qquad (75)$$

The continuation of the velocity and the stream function needs:

$$\Psi_z^b(z=Y) = \Psi_z^t(z=Y) \quad and \quad \Psi^b(z=Y) = \Psi^t(z=Y). \qquad (76)$$

Do long wave expansion, the Reynolds number is given in figure 6. From this figure we find that the Reynolds number of the bi-viscous fluid approaches the Reynolds number for the Bingham fluid as the viscosity ratio approaches zero. This result is quite different from the result obtained by Hjorth ([5]), which states that the free surface flow of the bi-viscous fluid is linearly unconditionally stable as the viscosity ratio α goes to zero. The reason for this difference is probably due to the different interfacial conditions between two different viscosity region.

2.6 Improved vertical averaged model

Researches on the Newtonian fluid flowing down the inclined plane have shown that the vertical averaged model can not give the correct stability criterion. The limitations of this model exist in the rustic character of the averaging method and the lack of freedom in the description of the hydrodynamic fields. The improved model has been derived by combining a gradient expansion to weighted residual techniques with polynomials as test functions ([12]; [13]). Based on the understanding of the free surface Bingham flow and the pseudo-plug assumption, we can use this technique to improve the vertical average model for the free surface Bingham flow.

We separate the fluid into two regions: the pseudo-plug region and the yield region. In the pseudo-plug region ($Y \leq z < h$), the velocity is the same as the plug velocity $u = U(x,t)$, which is guaranteed by the pseudo-plug theory. In the yielded region($0 \leq z < Y$), the boundary layer equations are:

$$R(\partial_x u + u\partial_x u + w\partial_z u) - u_{zz} = 1 - \partial_x h, \qquad (77)$$

$$u_x + w_z = 0, \qquad (78)$$

$$u_z|_{z=Y} = 0, \qquad (79)$$
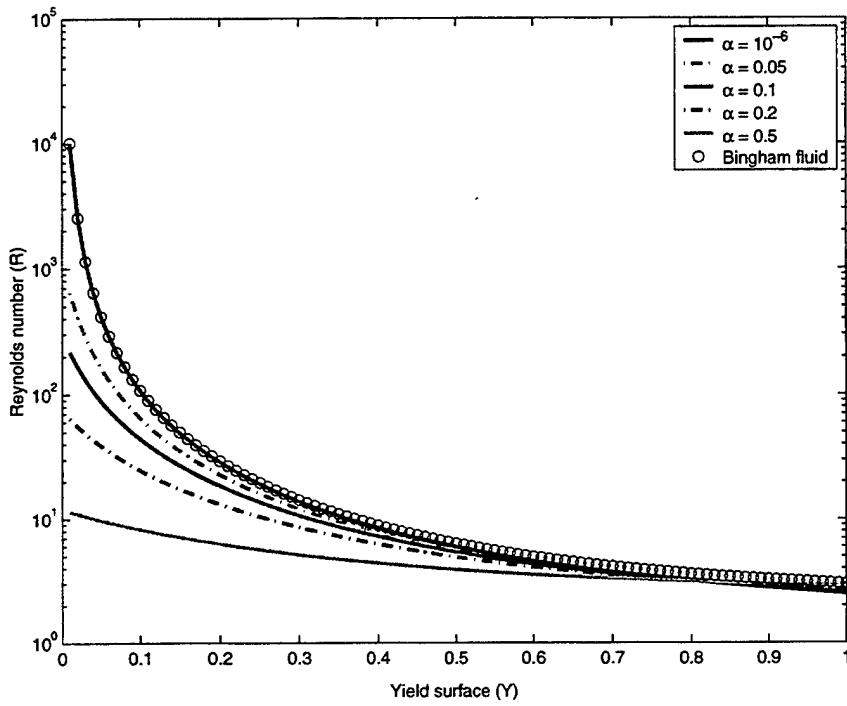
$$u|_0 = w|_0 = 0. \qquad (80)$$

Figure 6: Compare the critical Reynolds number for the long wave expansion and the bi-viscous mode.

From the continuity equation: $u_x + w_z = 0$ and the non-slip boundary condition $u|_0 = w|_0 = 0$, we can replace w by $w = -\int_0^z u_x dz$ so that the only remaining dynamical variable is $u(x, z, t)$. Expanding $u(x, z, t)$ in the following form:

$$u(x, z, t) = a_j(x, t) f_j(\bar{z}), \tag{81}$$

where $\bar{z}$ is defined as: $\bar{z} = \frac{z}{Y}$. Both Y and expansion coefficients a_j are supposed to be slowly varying function of time t and the stream-wise coordinate x. The base function $f_j(\bar{z})$ can be chosen to be:

$$f_j(\bar{z}) = \bar{z}^{j+1} - \frac{j+1}{j+2} \bar{z}^{j+2}. \tag{82}$$

which fulfills the boundary condition: $f_j(0) = f_j'(1) = 0$. It is easily observed that the vertical velocity profile used in VAM is merely proportional to $f_0(\bar{z})$. It can be shown that the consistent first order model can be obtained by considering a reduced set of test functions comprising monomials up to degree 6 included.

Inserting the truncated expansion $u(x, z, t) = \sum_{j=0}^4 a_j(x, t) f_j(\bar{z})$ into the momentum equation along the x-direction, and neglecting all terms in $a_j (j > 0)$ involving derivatives

245

with respect to x and t, we will have:

$$0 = \frac{1}{RY^2}(a_0 - 2a_1) - \frac{1}{R} + \frac{\partial_x h}{R}, \tag{83}$$

$$0 = \frac{1}{RY^2}(4a_1 - 6a_2) + \partial_t a_0 - \frac{a_0}{Y}\partial_t Y, \tag{84}$$

$$0 = \frac{1}{RY^2}(9a_2 - 12a_3) - \frac{1}{2}\partial_t a_0 + \frac{a_0}{Y}\partial_t Y + \frac{1}{2}a_0\partial_x a_0 - \frac{a_0^2}{2Y}\partial_x Y, \tag{85}$$

$$0 = \frac{1}{RY^2}(16a_3 - 20a_4) - \frac{1}{3}a_0\partial_x a_0 + \frac{2a_0^2}{3Y}\partial_x Y, \tag{86}$$

$$0 = \frac{1}{RY^2}25a_4 + \frac{1}{6}(\frac{1}{2}a_0\partial_x a_0 - \frac{a_0^2}{Y}\partial Y). \tag{87}$$

Eliminating a_1, a_2, a_3 and a_4 by inserting their expression into the first equation, we arrive:

$$a_0 = Y^2 - \frac{R}{3}Y^2\partial_t a_0 + \frac{RY}{6}a_0\partial_t Y - \frac{RY^2}{10}a_0\partial_x a_0 + \frac{RY}{30}a_0^2\partial_x Y - Y^2\partial_x h. \tag{88}$$

Now we need to obtain the plug velocity: $u(z = Y) = U(x,t)$. The plug velocity can be expressed as:

$$U(x,t) = \sum_j a_j(x,t)f_j(\bar{z} = 1). \tag{89}$$

Substituting the expansion coefficient $a_j(x,t)$ into this equation, thus we have:

$$U(x,t) = \frac{1}{2}a_0 - \frac{1}{45}RY^2 a_0\partial_x a_0 + \frac{1}{360}RYa_0^2\partial_x Y - \frac{1}{24}RY^2\partial_t a_0. \tag{90}$$

Also, we use p to denote the local instantaneous flow rate: $p = \int_0^Y u\,dz = Y\int_0^1 u\,d\bar{z}$. The value for p can be calculated out and expressed as:

$$P(x,t) = \frac{1}{3}a_0 - \frac{3}{280}a_0 Y^2 R\partial_x a_0 + \frac{1}{504}a_0^2 Y R\partial_x Y - \frac{1}{45}\partial_t a_0 RY^2 + \frac{1}{360}a_0 RY\partial_t Y. \tag{91}$$

Integrating the kinematic boundary condition across the pseudo-plug region gives:

$$h_t + \frac{\partial}{\partial x}(U(x,t)(h-Y)) + \frac{\partial}{\partial x}P = 0. \tag{92}$$

Also we can integrate the momentum equation in x-direction across the pseudo-plug region, we then have:

$$R(U_t + UU_x) = 1 - h_x - \frac{sgn(B)}{h-Y}. \tag{93}$$

Plus the equations for a_0, p and U, we then have a set of five equations. These five equations close the system. To test this set of equations, we can do linear stability analysis and comparing the critical Reynolds number with that obtained from the long wave expansion for the boundary layer model. The equilibrium is:

$$h = 1, Y = 1 - B, U = \frac{1}{2}(1-B)^2, a_0 = (1-B)^2, P = \frac{a_0}{3}Y. \tag{94}$$

246

Apply small perturbations: $h = h + h', Y = Y + Y', U = U + U', p = p + p'$, and $a_0 = a_0 + a_0'$. Do normal mode expansion for these perturbations: $h', U', Y', P', a_0' \propto exp(\lambda t + ikx)$. Then the perturbed equations will be:

$$\lambda h + ikBU(x,t) + \frac{1}{2}(1-B)^2 ik(h-Y) + ikp = 0, \tag{95}$$

$$R(\lambda U + \frac{1}{2}(1-B)^2 ikU) = -ikh - \frac{h-Y}{B}, \tag{96}$$

$$U = \frac{a_0}{2} - \frac{1}{45}R(1-B)^4 ika_0 + \frac{R}{360}(1-B)^5 ikY - \frac{R}{24}(1-B)^2 \lambda a_0, \tag{97}$$

$$
\begin{aligned}
a_0 = {} & 2(1-B)Y - \frac{R(1-B)^2}{3}\lambda a_0 + \frac{R(1-B)^3}{6}\lambda Y \\
& - \frac{R(1-B)^4}{10} ika_0 + \frac{R(1-B)^5}{30} ikY - (1-B)^2 ikh,
\end{aligned} \tag{98}
$$

$$P = \frac{1}{3}a_0 Y - \frac{3RY}{280}(1-B)^4 ika_0 + \frac{RY}{504}(1-B)^5 ik - \frac{R}{45}(1-B)^2 \lambda a_0 + \frac{\lambda RY}{360}(1-B)^3. \tag{99}$$

For the improved vertical average model, the Reynolds number R in the long wave length limit is very close to that obtained from the long wavelength expansion for the boundary layer model (See figure 7).

3   Channel flow of Bingham fluid

In this section, we will study the channel flow of Bingham fluid.

3.1   Govening equations

For the Bingham fluid flowing through a channel with width L, the momentum equation can be written as[1]:

$$\rho(u_t + uu_x + wu_z) = -p_x + \partial_x \tau_{xx} + \partial_z \tau_{zx}, \tag{100}$$
$$\rho(w_t + uw_x + ww_z) = -p_z + \partial_z \tau_{xz} + \partial_z \tau_{zz}, \tag{101}$$

with the continuity equation: $u_x + w_z = 0$, with the boundary condition: $w = u = 0$ on $z = L, -L$. We scale the problem in the following way:

$$u \sim Uu; \quad w \sim Uw; \quad x \sim Lx; \quad z \sim Lz; p \sim \rho U^2 p. \tag{102}$$

Define the Bingham number as: $B = \frac{\tau_Y L}{\nu U}$, and the dimensionless viscosity coefficient ν as: $\nu = \frac{\mu}{\rho UL}$. Also we separate the background pressure gradient from the evolving pressure gradient:
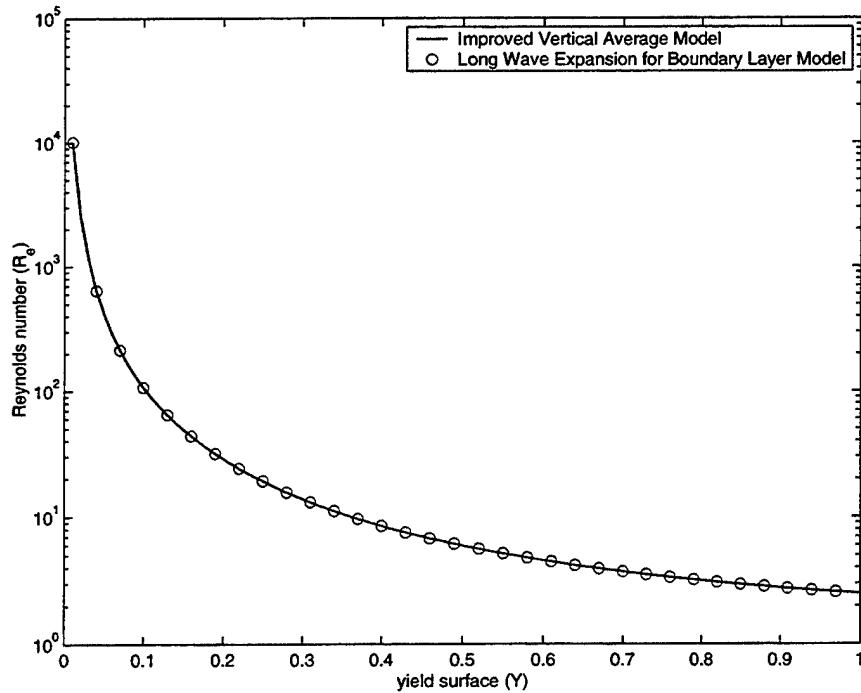
$$p = \nu x + p'(x, z, t). \tag{103}$$

247

Figure 7: Compare the critical Reynolds number for the improved vertical averaged model.

Droping the primes, the momentum equation can be written as:

$$\rho(u_t + uu_x + wu_z) = \nu - p_x + \nu(\partial_x \tau_{xx} + \partial_z \tau_{zx}),$$ (104)

$$\rho(w_t + uw_x + ww_z) = -p_z + \nu(\partial_z \tau_{xz} + \partial_z \tau_{zz}),$$ (105)

with,

$$\begin{cases} \tau_{xz} = (1 + \frac{B}{|U_z|})U_z & if \quad \tau > B, \\ \tau_{xz} = 0 & if \quad \tau < B. \end{cases}$$ (106)

The equilibrium state will be $w = p = 0$ and $u = U(z)$:

$$U(z) = -\frac{1}{2}(1 - z^2) - B(1 - |z|) \quad \text{for} \quad |z| > B,$$ (107)

$$U(z) = (1 - B)^2/2 \quad \text{for} \quad |z| < B$$ (108)

Do linear stability analysis:

$$(u, w, p) = (U, 0, 0) + (\Psi_y, ik\Psi, p)exp(ikx + \lambda t).$$ (109)

Then we will get the Orr-Sommerfeld equation;

$$(\frac{ikU}{\nu} + \frac{\lambda}{\nu})(\Psi_{yy} - k^2\Psi) - U''\Psi = (\partial_y^2 - k^2)^2\Psi - 4Bk^2\partial_y(\frac{\Psi_y}{|U'|}).$$ (110)

The boundary conditions are $\Psi = \Psi_y = 0$ at $y = -1, 1$.

248

3.2 $k \ll 1$ mode

For $k \ll 1$ mode, we can do long wave expansion and the leading order term for outside of the plug region is:

$$\psi_{yy} - \frac{\lambda}{\nu}\Psi = 0, \tag{111}$$

with the boundary condition: $\psi_y = 0$ on $y = 1$. For the region inside the pseudo-plug region, we have:

$$\psi_{yy} = 0. \tag{112}$$

We can solve these equations analytically, and get the eigen-value and eigen-functions for odd mode and even mode respectively. The odd mode in stream function Ψ is corresponding to the 'sausage' mode of the flow, the even mode in stream function Ψ is corresponding to the 'kink' mode of the flow. For the odd mode in stream function, we have: $\Psi = 0$ on $y = 0$. The eigen-value satisfies:

$$\lambda = -\frac{n^2\pi^2}{(1-B)^2}\nu. \tag{113}$$

For the even mode, we have: $\psi_y = 0$ on $y = 0$. And the eigen-value satisfies:

$$-B\frac{\lambda}{\nu}tanh(\sqrt{\frac{\lambda}{\nu}}(1-B)) = 1. \tag{114}$$

The above equations has no real solution for real λ, and the flow is linearly unconditional stable.

3.3 k finite mode

For finite k, we have $\psi_{yy} - \psi_{xy} \approx 0$, and $\psi_{xy} \approx 0$, which implies:

$$\psi = \psi_y = \psi_{yy} = 0, \tag{115}$$

inside the pseudo-plug. It reveals a very interesting phenomena of the flow: the plug in this case bahaves like a solid and seperate the flow completely. In fact, the pertubation in top part of the flow will not be transport to the bottom part of the flow! Both odd and even mode will exist and have the same eigenvalue, which is the same as the predicted by the regularized mode.([1])

4   Convection of Bingham fluid

Put the Bingham fluid between two plates with fixed temperatures: T_0 and T_1, with $T_0 > T_1$. The momentum equation will be:

$$\frac{Du}{Dt} = -\frac{1}{\rho_0}\frac{\partial p}{\partial x} + \frac{\partial \tau_{xx}}{\partial x} + \frac{\partial \tau_{xz}}{\partial z}, \tag{116}$$

$$\frac{Dw}{Dt} = -\frac{1}{\rho_0}\frac{\partial p}{\partial z} - g + \alpha g(T - T_0) + \frac{\partial \tau_{xz}}{\partial x} + \frac{\partial \tau_{zz}}{\partial z}. \tag{117}$$

the temperature equation is:

$$\frac{DT}{\partial t} = \kappa \nabla^2 T, \qquad (118)$$

with the continuity equation: $\nabla \cdot \boldsymbol{u} = 0$ and the following constitutive equation:

$$\begin{cases} \tau_{ij} = (\mu + \frac{\tau_Y}{\dot{\gamma}})\dot{\gamma}_{ij} & if \quad \tau > \tau_Y, \\ \dot{\gamma}_{ij} = 0 & if \quad \tau < \tau_Y, \end{cases} \qquad (119)$$

where τ_Y is the yield stress of the Bingham fluid, and ν is the viscosity. we scale the problem in the following way:

$$x \sim d, t \sim \frac{\kappa}{d^2}, u \sim \frac{d}{\kappa}, T \sim \frac{1}{\beta d}, p \sim \frac{d^2}{\rho \kappa}, \qquad (120)$$

where d is the spacing between two plates, and β is the inverse temperature gradient. Define the following dimensionless numbers: Rayleigh number R_a:

$$R_a = \frac{\alpha \beta g d^4}{\kappa \mu}, \qquad (121)$$

and define the Prandtle number Pr:

$$P_r = \frac{\mu}{\kappa}, \qquad (122)$$

and define the Bingham number: B

$$B = \frac{\tau_Y \rho \kappa}{d^2}, \qquad (123)$$

Then the scaled equations will be:

$$\frac{Du}{Dt} = -\frac{\partial p}{\partial x} + P_r \frac{\partial \tau_{xx}}{\partial x} + P_r \frac{\partial \tau_{xz}}{\partial z}, \qquad (124)$$

$$\frac{Dw}{Dt} = -\frac{\partial p}{\partial z} + P_r R_a T + P_r \frac{\partial \tau_{xz}}{\partial x} + P_r \frac{\partial \tau_{zz}}{\partial z}. \qquad (125)$$

the temperature equation is:

$$\frac{DT}{\partial t} - w = \kappa \nabla^2 T \qquad (126)$$

with the continuity equation: $\nabla \cdot \boldsymbol{u} = 0$ and the following constitutive equation:

$$\begin{cases} \tau_{ij} = (1 + \frac{B}{\dot{\gamma}})\dot{\gamma}_{ij} & if \quad \tau > B, \\ \dot{\gamma}_{ij} = 0 & if \quad \tau < B. \end{cases} \qquad (127)$$

We have the none-slip boundary condition at the top and the bottom surface: $u = w = 0$, also the temperature at the top is 1, and the temperature at the bottom is 0. At the equilibrium, the fluid has no motion: $u^* = w^* = 0$ and no stress: $\tau_{ij}^* = 0$. The equilibrium temperature structure will be: $T^* = 1 - z$ and the equilibrium pressure profile will be: $p^* = z - \frac{z^2}{2}$. Apply the small perturbations: u', w', θ, p', and drop the primes, then the perturbed momemtum equation will be:

$$\frac{Du}{Dt} = -\frac{\partial p}{\partial x} + P_r \frac{\partial \tau_{xx}}{\partial x} + P_r \frac{\partial \tau_{xz}}{\partial z}, \qquad (128)$$

$$\frac{Dw}{Dt} = -\frac{\partial p}{\partial z} + P_r R_a \theta + P_r \frac{\partial \tau_{xz}}{\partial x} + P_r \frac{\partial \tau_{zz}}{\partial z}. \qquad (129)$$

250

We conduct the linear stability analysis by assuming $u, w, \theta, p \propto exp(ikx + \lambda t)$. Since the fluid is heated from the below, the fluid is at the true equilibrium state in the beginning. The initial stress in the fluid is zero. Therefore, adding infinitesimal perturbation will not make the stress in the fluid larger than the yield stress (see equation 127). It can be easily shown that the only solution is $u = 0, w = 0$. Therefore, the fluid is linearly unconditional stable under the infinitesimal perturbation.

5 Conclusion

For Bingham fluid in the laboratory and in the nature, the fluid is likely to relaxed to a pseudo-plug state. In this case, the stress in the pseudo-plug is slightly above the yield stress and the fluid can be linearly unstable. However, for the thermal convection of the Bingham fluid, since the initial stress in the fluid is zero, adding infinitesimal perturbation will not make the stress in the fluid larger than the yield stress. The thermal convection of the Bingham fluid will be linearly unconditional stable.

6 Acknowledgement

References

[1] N.J. Balmforth and R.V. Craster A consistent thin-layer theory for Bingham plastics *J. Non-Newtonian Fluid Mech.*, 84(1):65–81, 1999.

[2] N.J. Balmforth and G.R. Ierley Stability of Poiseuille flow of viscoplastic fluid , 1998.

[3] T.B. Benjamin Wave formation in laminar flow down an inclined plane *J. Fluid Mech.*, 2(6):554–574, 1957.

[4] I.A. Frigaard, S.D. Howison and I.J. Sobey One the stability of Poiseuille flow of a Bingham fluid *J. Fluid Mech.*, 263:133–150, 1994.

[5] P.G. Hjorth Stability of free surface sediment flow *JGR*, 95:20,363–20,366, 1990.

[6] K.F. Liu and C.C. Mei Slow spreading of a sheet of Bingham fluid on an inclined plane *J. Fluid Mech.*, 207:505–529, 1989.

[7] K.F. Liu and C.C. Mei Approximate equations for the slow spreading of a thin sheet of Bingham plastic fluid *Phys. Fluids A*, 2(1):30–36, 1990.

[8] K.F. Liu and C.C. Mei Roll waves on a layer of a muddy fluid flowing down a gentle slope - a Bingham model *Phys. Fluids*, 6(8):2577–2590, 1994.

[9] C.C. Mei, K.F. Liu and M. Yuhi Mud Flow - slow and fast *Geomorphological Fluid Mechanics*, 548–577, 2001.

[10] C. Ng and C.C. Mei Roll waves on a shallow layer of mud modeled as a power-law fluid *J. Fluid Mech.*, 263:151–183, 1994.

[11] J.G. Oldroyd Two-dimensional plastic flow of a Bingham solid *Proc. Camb. Phil. Soc.*, 43:383–395, 1947.

[12] C. Ruyer-Quil and P. Manneville Modeling film flows down inclined planes *Eur. Phys. J. B*, 6:277–292, 1998.

[13] C. Ruyer-Quil and P. Manneville Improved modeling of flows down inclined planes *Eur. Phys. J. B*, 15:357–369, 2000.

[14] C. Ruyer-Quil and P. Manneville Further accuracy and convergence results on the modeling of flows down inclined planes by weighted-residual approximations *Phys. Fluids*, 14(1):170–183, 2002.

[15] C.S. Yih Stability of liquid flow down an inclined plane *Phys. Fluids*, 6(3):321–334, 1963.

A Novel Layered QG model

Neil Burrell

1 Introduction

The earth's ocean is a complicated fluid system. It is affected by the rotation of the earth, the density stratification due to temperature and salinity, and many other factors. These processes combine to act on an extremely wide range of length-scales, from centimeters to thousands of kilometers. One notable simplification is that the ocean is tremendously more shallow than it is wide. But the assumption that the ocean is two-dimensional is overly restrictive and does not capture important dynamical processes.

We concern ourselves here with the observation of a correlation in the energy-containing scales of the ocean with the first Rossby deformation radius. This correlation appears in observations of the sea surface using the TOPEX/POSEIDON satellite [1, 2] and also in models [3]. The processes which cause eddy energies in the ocean come to equilibrate at this horizontal scale are not well understood. It is the fully nonlinear development of ocean eddies (presumably created through wind stress forcing at the surface) that determines this scale. In addition, the effect of vertically non-uniform stratification on the downward propagation (barotropization) of energy are not clear. Typical models of ocean turbulence assume vertically homogeneous stratification, with correspondingly more uniform dynamics throughout the layer.

Smith and Vallis [4, 5] investigate these questions in the context of a non-uniformly stratified, three-dimensional ocean using quasigeostrophic (QG) dynamics. The surface-intensified stratification that they use leads to surface-localized potential vorticities. In an effort to create a simpler model for these processes, we consider a two-layer QG system in which the lower layer has no potential vorticity. In section 2 we review layered QG models in general. Then in sections 3 and 4 we examine the simplified two-layer model and its consequences for eddy evolution using numerical simulations. We present our conclusions in section 5.

2 Layered Quasigeostrophic Models

Consider a nearly incompressible, rotating, stratified fluid. All of the models that we consider here will neglect the meridional variation in the Coriolis parameter that is present
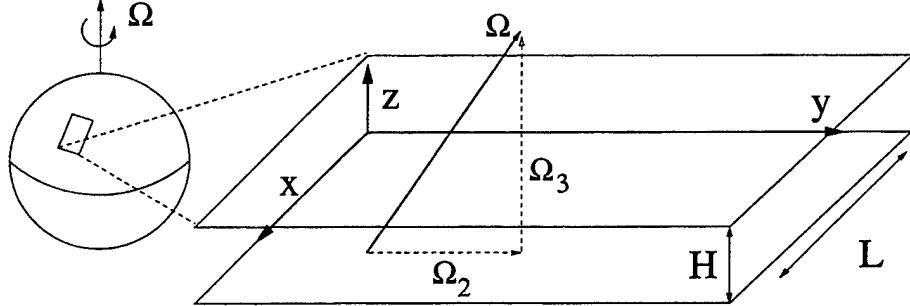
Figure 1: The f-plane geometry.

on a rotating sphere (see figure 1). On this f-plane, the Boussinesq equations are

$$D_t \boldsymbol{u} + 2\Omega(\hat{\Omega} \times \boldsymbol{u}) = -\frac{\nabla p}{\rho_0} + b\hat{z} + \frac{\mu}{\rho_0}\Delta\boldsymbol{u} \tag{1a}$$

$$D_t b + N^2(z)w = \kappa\Delta b \tag{1b}$$

$$\nabla \cdot \boldsymbol{u} = 0 \tag{1c}$$

where the dependent variables are the fluid velocity $\boldsymbol{u}$, the pressure p and the buoyancy anomaly $b = -g\rho/\rho_0$. The parameters are the rotation rate 2Ω, the typical background density ρ_0, the buoyancy frequency $N^2 = -(g/\rho_0)(\mathrm{d}\rho/\mathrm{d}z)$ for a background density $\bar{\rho}$ and the momentum and mass diffusivities, ν and κ respectively. Non-dimensionalizing these equations by $\boldsymbol{u} \sim U$, $\boldsymbol{x} \sim L$, , $b \sim B$, $p \sim P$ and $N^2(z) = N_0^2 S(z)$ we have

$$D_t \boldsymbol{u} + \frac{1}{\mathrm{Ro}}\hat{\Omega} \times \boldsymbol{u} = -\bar{P}\nabla p + \Gamma b\hat{z} + \frac{1}{\mathrm{Re}}\Delta\boldsymbol{u}, \tag{2a}$$

$$D_t b + \frac{S(z)}{\Gamma\mathrm{Fr}^2}w = \frac{1}{\mathrm{Pe}}\Delta b, \tag{2b}$$

$$\nabla \cdot \boldsymbol{u} = 0, \tag{2c}$$

where the Reynolds number $\mathrm{Re} = (UL)/\nu$ measures the strength of inertia relative to viscosity, the Peclet number $\mathrm{Pe} = (UL)/\kappa$ compares inertia to buoyancy diffusion, the Froude number $\mathrm{Fr} = U/(N_0 L)$ measures buoyancy relative to inertia and the Rossby number $\mathrm{Ro} = U/(2\Omega L)$ compares the rotational timescale to the dynamical timescale. There are two additional non-dimensional parameters $\bar{P} = P/(U^2\rho_0)$ and $\Gamma = (BL)/U^2$ that measure the strength of their respective terms of the equations.

Since the ocean is vastly shallower than it is wide, even at the horizontal scales considered here, we consider an asymptotic expansion in the aspect ratio $\epsilon = H/L$. In the ocean, the Rossby number is also small so we set $\mathrm{Ro} = \epsilon$. We neglect the effects of diffusion, by setting $\mathrm{Re} = \mathrm{Pe} = \infty$. Froude numbers in the ocean are smaller than the Rossby numbers, so we choose $\mathrm{Fr} = \epsilon^2$ and for the other two parameters we take $\Gamma = \epsilon^{-2}$ and $\bar{P} = \epsilon^{-1}$ to give the hydrostatic and geostrophic balances at leading order. Expanding the dependent variables in asymptotic series ($\boldsymbol{u} = \boldsymbol{u}_0 + \epsilon\boldsymbol{u}_1 + \epsilon\boldsymbol{u}_2 + \ldots$, etc.) and collecting terms of the same order

254

we have the following balances from the momentum equations,

$$O(\epsilon^{-2}): \quad -\partial_z p_0 + b_0 = 0 \tag{3a}$$

$$O(\epsilon^{-1}): \quad \hat{\Omega} \times \boldsymbol{u}_0 = -\nabla_\perp p_0 + \hat{\boldsymbol{z}}(b_1 - \partial_z p_1) \tag{3b}$$

$$O(1): \quad D_t^0 \boldsymbol{u}_0 + \hat{\Omega} \times \boldsymbol{u}_1 = -\nabla_\perp p_1 + \hat{\boldsymbol{z}}(b_2 - \partial_z p_2) \tag{3c}$$

the buoyancy equation,

$$O(\epsilon^{-2}): \quad S(z)w_0 = 0 \tag{3d}$$

$$O(\epsilon^{-1}): \quad w_0 \partial_z b_0 + S(z)w_1 = 0 \tag{3e}$$

$$O(1): \quad D_t^0 b_0 + w_1 \partial_z b_0 + S(z)w_2 = 0 \tag{3f}$$

$$\tag{3g}$$

and the continuity equation

$$O(1): \quad \nabla_\perp \cdot \boldsymbol{u}_0 = 0 \tag{3h}$$

$$O(\epsilon): \quad \nabla_\perp \cdot \boldsymbol{u}_1 + \partial_z w_2 = 0. \tag{3i}$$

From (3d) and (3e) we see that the fluid velocities are all horizontal. The hydrostatic balance is present at leading order in (3a) and the geostrophic balance in the x- and y-components of (3b). The incompressibility condition (3h) leads us to a streamfunction $\boldsymbol{u}_0 = \hat{\boldsymbol{z}} \times \nabla \psi_0$. The geostrophic and hydrostatic balances relate that streamfunction to the pressure and buoyancy fields at leading order: $p_0 = \Omega_3 \psi_0$ and $b_0 = \Omega_3 \partial_z \psi_0$. Taking the curl of (3c) and using (3i) to relate w_2 and $\boldsymbol{u}_1$ we have two closed equations for ψ and w_2

$$D_t^0 \nabla_\perp^2 \psi_0 - \Omega_3 \partial_z w_2 = 0 \tag{4a}$$

$$D_t^0 \Omega_3 \partial_z \psi_0 + S(z)w_2 = 0. \tag{4b}$$

Finally, eliminating w_2 and dropping the 0 subscripts we have the quasigeostrophic (QG) equations

$$D_t q = \partial_t q + J(\psi, q) = F \tag{5a}$$

$$q = \nabla^2 \psi + \Omega_3 \partial_z \left(\frac{1}{S(z)} \Omega_3 \partial_z \psi \right), \tag{5b}$$

where F represents any forcing or dissipation in the system.

We will use these equations as the starting point of our investigations. It is important to note that even in the three-dimensional case there is no vertical velocity; all fluid motion is in horizontal planes. If there is no dissipation, $F = 0$, then the QG equations express the conservation of the *potential vorticity* q on fluid elements. Additionally, there are two global conserved quantities: the *energy*

$$\mathcal{E} = -\frac{1}{2} \int_{\mathbb{R}^3} q\psi \, d\boldsymbol{x} \tag{6}$$

and the *enstrophy*

$$\mathcal{Z} = \int_{\mathbb{R}^3} q^2 \, d\boldsymbol{x}. \tag{7}$$

255

Related to the energy and enstrophy are the energy and enstrophy *spectra* defined by $\mathcal{E} = \int E(\kappa) \, \mathrm{d}k$ and $\mathcal{Z} = \int Z(\kappa) \, \mathrm{d}k$. We can define a mean wave number by the centroid of the energy spectrum

$$\kappa_m = \frac{1}{\mathcal{E}} \int \kappa E(\kappa) \, \mathrm{d}k. \tag{8}$$

In the absence of vertical variation, these are just the equations for two-dimensional fluid dynamics where q is the ordinary vorticity and ψ is the streamfunction of the flow. The dynamics of this type of flow are well known (see, for example [6, 7, 8, 9, 10, 11]). For the case of small F, energy is approximately conserved and moves to larger scales in an inverse cascade, enstrophy is not conserved and participates in a direct cascade to smaller scales and for unforced flow the evolution is dominated by the interaction of coherent vortices (which may be studied independently [12, 13, 14]). A quantitative scaling theory for the regime dominated by coherent vortices predicts algebraic evolution for many of the flow characteristics, including enstrophy, vortex number, vortex size and vortex amplitude [15, 9]. We will use these self-similarity properties later for our novel model.

The smallest amount of additional vertical variation that we can admit is a two-layer quasigeostrophic model. Considering two layers of fluid with different densities (see figure 2) the QG equations reduce to

$$\partial_t q_i + J(\psi_i, q_i) = 0, \tag{9a}$$

$$q_1 = \nabla^2 \psi_1 + F_1(\psi_2 - \psi_1), \tag{9b}$$

$$q_2 = \nabla^2 \psi_2 + F_2(\psi_1 - \psi_2) \tag{9c}$$

$$F_i = \frac{f^2}{g' H_i}, \quad f = 2\Omega_3, \quad g' = g \frac{\rho_2 - \rho_1}{\rho_2}.$$

(See [16] or [17] for a derivation of these equations.) In the interest of further simplicity, assume $H_2 \to \infty \Leftrightarrow F_2 = 0$. Then the motion in the lower layer is decoupled from that in the upper layer (although not vice-versa). If we assume that this infinitely deep lower layer was initially at rest, then it will always be at rest with $\psi_2 = 0$. This quiescent lower layer then has no effect on the upper layer and we get the *one-and-a-half layer* QG equations (also called the *equivalent barotropic* QG equations)

$$D_t q_1 = 0 \tag{10a}$$

$$q_1 = (\nabla^2 - F_1)\psi_1. \tag{10b}$$

The parameter F_1 is related to an intrinsic length scale of this flow, the *Rossby deformation radius*, $k_1^{-1} = F_1^{-1/2}$. The dynamics of this system in the case of unforced, decaying turbulence are similar to that of the one-layer equations for short times with the formation and interaction of coherent vortices. As the vortices grow to the size of the deformation radius, their motion begins to slow down [18, 19, 20]. This stops the inverse cascade of energy at that scale, in contrast to the one layer case where the inverse cascade continues to the largest scales in the problem.

Neither the one layer QG model nor the equivalent barotropic model can adequately explain the energetic distribution in the world's oceans. The inverse cascade in 2D turbulence moves to the largest available scales. In fact, there is no intrinsic length scale in
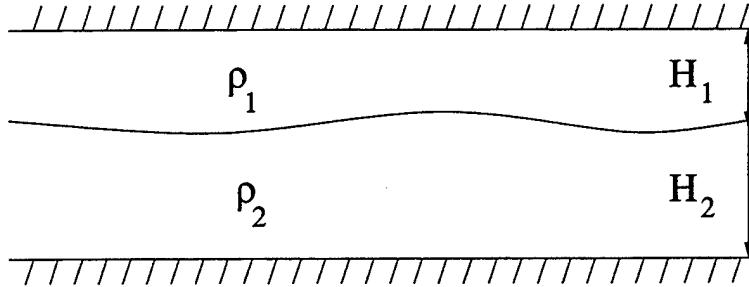
256

Figure 2: Two fluid layers.

the system. The one-and-a-half layer model does have a distinguished length scale, the deformation radius, but the energy cascade stops completely at that scale. The one layer model is overly simplistic, containing no contributions from rotation or stratification, nor any variation with depth. The addition of an infinitely deep lower layer contributes some of the dynamical features of the ocean, namely the rotational and stratification effects of the deformation radius, but at the cost of the long-time evolution of the flow. This limitation arises from the blatantly unrealistic assumption of infinite depth in the lower layer. For these reasons, we seek a slightly more complicated model that will retain essential features of the oceanic evolution, in particular the distinguished role of the first Rossby deformation radius.

3 The Finite-depth One-and-a-half Layer Model

In our derivation of the equivalent barotropic model, we assumed that the lower layer was infinitely deep. If we relax that assumption, then we cannot continue to insist that $\psi_2 = 0$ for all time. For any finite depth, any motion in the upper layer will induce a flow in the initially quiescent lower layer. Fundamentally, this is because the fluid velocity in the lower layer is not a materially conserved quantity: it may evolve with time. On the other hand, the potential vorticity in the lower layer q_2 is conserved, so if the flow initially has $q_2 = 0$ then it will for all time, irregardless of the motion of the upper or lower layers. This assumption is also consistent with observations [21] which show no potential vorticity signal below eddies in the North Atlantic. Finally, in the three dimensional calculations of Smith and Vallis [4, 5] they compute the eigenfunctions ϕ_i for the vertical structure of the 3D QG equations,

$$\partial_z \left(\frac{1}{S(z)} \partial_z \right) \phi_i = -\lambda_i^2 \phi_i, \tag{11}$$

for a surface-intensified stratification profile and they are quite small at large depths. One limitation of the assumption that $q_2 = 0$ for all time is that it there cannot be any bottom friction present in our model, because that would break the conservation of potential vorticity in the lower layer.

Proceeding with the assumption that $q_2 = 0$, (9c) just expresses a relation between the two streamfunctions

$$\nabla^2 \psi_2 + F_2(\psi_1 - \psi_2) = 0. \tag{12}$$

257

Thus, given ψ_1 we can solve this equation for ψ_2 in terms of $\hat{\psi}_1$ the Fourier transform of ψ_1

$$\psi_2(x,t) = \int \frac{F_2}{F_2 + \kappa^2} \hat{\psi}_1 e^{-ik \cdot x}\, dk \qquad (13)$$

where k is the horizontal wavenumber and $\kappa = |k|$. We will represent this solution schematically by

$$\psi_2 = \frac{F_2}{F_2 - \nabla^2}\psi_1 \qquad (14)$$

where (13) is meant by this symbol in all cases. Having solved for ψ_2 (9b) and (9a) are now a closed set of equations for the motion of the upper layer

$$D_t q_1 = 0, \qquad (15a)$$

$$q_1 = \left(\nabla^2 - F_1 + \frac{F_1 F_2}{F_2 - \nabla^2}\right)\psi_1. \qquad (15b)$$

We refer to these as the *finite-depth one-and-a-half layer* QG equations. Note that in contrast to the model with an infinitely-deep lower layer, the lower layer is not at rest in this model, but instead moves with exactly the relative vorticity $\nabla^2\psi_2$ necessary to cancel the vorticity added to the layer by stretching of the background planetary vorticity, $F_2(\psi_1 - \psi_2)$. These equations also contain both of the models talked about previously: if $F_1 = 0$ then we recover the one layer model and if $F_2 = 0$ we have the same equations as the one-and-a-half layer model. As far as we know, this model has not been studied for its turbulent cascade properties as we do here. Since it is a special case of the two-layer QG equations, solutions of this type have certainly appeared, most notably in studies of the merging of baroclinic vortices [22, 18, 23, 24].

4 Spin-down Simulations

The main component of this study is a series of numerical simulations of layered QG equations with a single active layer. The numerical code is pseudospectral in space and leapfrog in time. An isotropic truncation is applied with wavenumbers with $\kappa \le \kappa_{max} = 176$. When computing the nonlinear term, dealiasing is used, keeping wavenumbers up to $(3/2)\kappa_{max}$. Dissipation is present in the form of hyperdiffusion $F = -\nu\nabla^8 q$ (as in [4]). All of the simulations presented here use $\nu = 1.43 \times 10^{-17}$ which was chosen to absorb the direct cascade of enstrophy while dissipating as little energy as possible. The initial vorticity field is a random-phase realization with an initially narrow-band energy spectrum $E(\kappa) \propto \kappa^6/(\kappa + 2\kappa_0)^{18}$ with $\kappa_0 = 30$ and the normalization that $\mathcal{E}(t = 0) = 0.5$. The simulations continue up to $t = 80$.

Figure 3 shows representative evolutions of energy, enstrophy and κ_m for the one layer model. Over the length of the simulation, the energy falls to approximately 86% of its initial value while the enstrophy declines by a factor of over 60. The decrease in κ_m is evidence of the inverse cascade of energy to larger scales (lower wavenumbers). Figure 4 shows the vorticity field for the one layer model. As time progresses, there are fewer, larger coherent vortices. The same quantities are shown in figures 5 and 6 for the equivalent barotropic model with $k_1 = 15$. Here by comparison, the coherent vortices fill much more of the domain
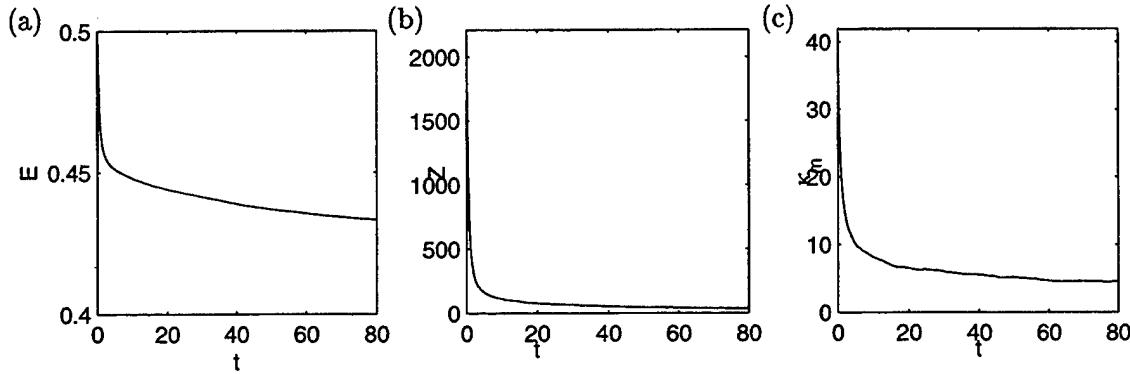
258

Figure 3: Time series of (a) $\mathcal{E}$, (b) $\mathcal{Z}$ and (c) κ_m for the one layer equations.

than in figure 4. The stopping of the inverse cascade of energy at a scale near the Rossby radius of deformation can be seen in the evolution of κ_m in figure 5.

For the finite-depth model, corresponding data are shown in figures 7 and 8 for $k_1 = 24$ and $k_2 = 12$. A number of notable features are present in these latter simulations. The inverse cascade of energy continues for the finite-depth case where it did not for the equivalent barotropic model ($\kappa_m(t = 80) = 7.5$ and $\kappa_m(t = 80) = 10.1$ respectively). Also, the coherent vortices for the finite-depth model fill more of the space than in the one layer model (figure 4) but less space than in the equivalent barotropic model (figure 6). For increasing values of $\lambda = 1 + F_1/F_2$ the vortices fill more of the domain and are less circular (see figure 9). This is consistent with the position of the finite-depth model as intermediate between the other two models (in the sense that the one layer model corresponds to $\lambda = 1$ and the equivalent barotropic model to $\lambda = \infty$). Finally, for the time evolution of this model: vortex dipoles are more active than in either of the other two models and vortex motions are slower than in the one-layer model but faster than in the equivalent barotropic model.

4.1 Vigorous Vortex Dipoles

To analyze the apparent vigor of close associations of two opposite signed vortices, we consider the induced velocity field for a point charge of potential vorticity. This profile is closely related to those of hetons [25]. Hogg and Stommel give the following solution in the special case $F_1 = F_2$. The azimuthal velocity field is

$$v_\theta(r) = \frac{1}{\lambda} \left(\frac{1}{r} + \frac{F_1}{F_2} k_R K_1 \left(k_R r \right) \right) \tag{16}$$

where $k_R = (F_1 + F_2)^{-1/2}$, $\lambda = 1 + F_1/F_2$ and $K_1(z)$ is the modified Bessel function of the second kind. While the vortices in our simulations are not point vortices, this solution should still hold outside of the cortex core, as in the case of the Rankine vortex for the one-layer model. For $r \ll 1/k_R$ the limiting behavior of this velocity is $v_\theta \sim (1/r)$ while for $r \gg 1/k_R$, $v_\theta \sim (1/\lambda)(1/r)$. Since $\lambda \geq 1$ the far-field velocity of a point vortex in
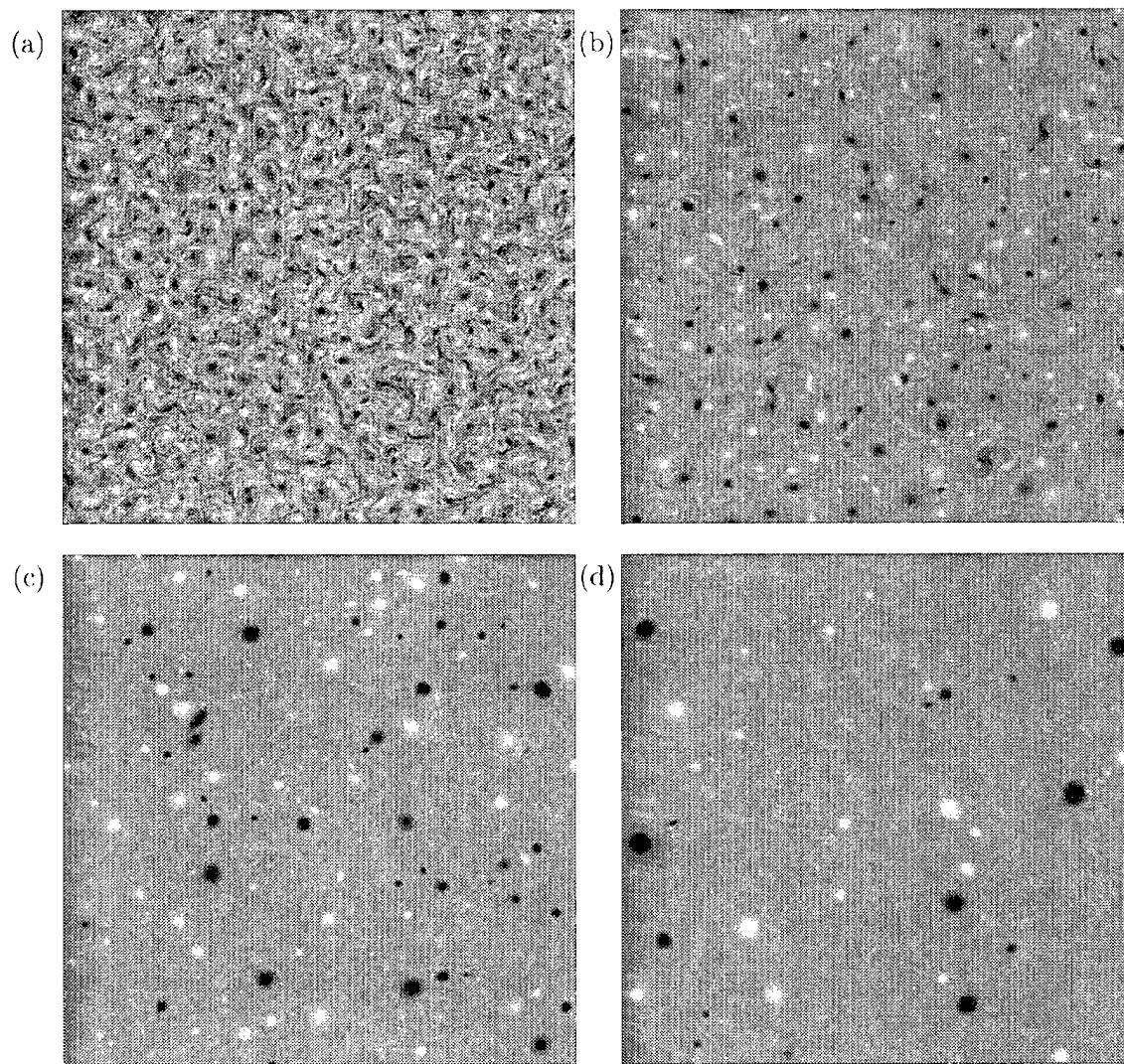
259

Figure 4: Vorticity field $q_1(x, y)$ at (a) $t = 1$, (b) $t = 5$, (c) $t = 20$ and (d) $t = 80$ for the one layer equations. Lighter colors represent higher vorticities.
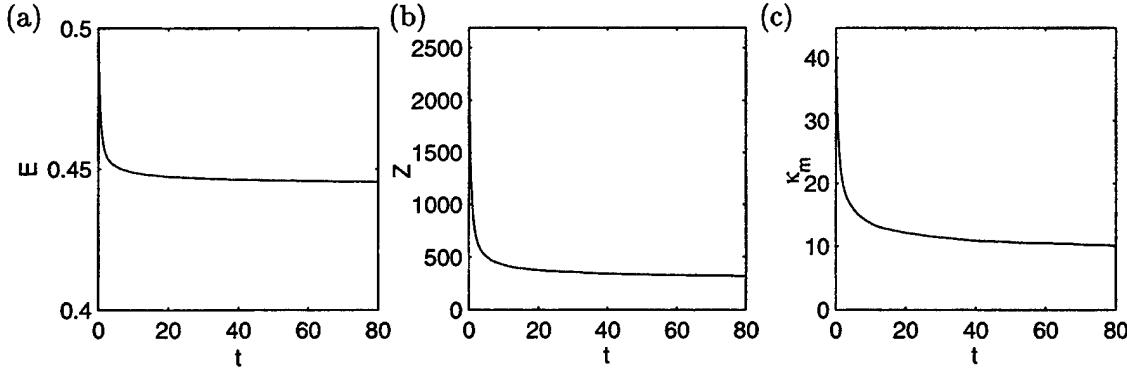
Figure 5: As in figure 3, but for the equivalent barotropic model with $k_1 = 15$.

the finite-depth one-and-a-half layer model is smaller than the near-field velocity. This explains the heightened activity of vortex dipoles in the simulations of these equations. When two opposite signed vortices come close together under the influence of the other vortices in the system, their mutual interaction is strengthened by a factor of λ, resulting in a (possibly dramatic) increase in their activity for the time of their close approach. The increased activity of vortex dipoles also leads to an increased number of dipole/dipole exchange interactions, where two dipoles collide and rebound having exchanged partners.

4.2 Vortex slowdown and self-similarity

A complementary view to the fundamentally physical space approach in section 4.1 is provided by examining the properties of the equations in Fourier space. We will see that there is an intimate connection between these two approaches in the form of the potential vorticity inversion operator. Acting between the Fourier transforms $\hat{q}_1(\boldsymbol{k})$ and $\hat{\psi}_1(\boldsymbol{k})$ this operator takes the form

$$\hat{q}_1 = \left(-\kappa^2 - F_1 + \frac{F_1 F_2}{F_2 + \kappa^2} \right) \hat{\psi}_1. \tag{17}$$

For short scales, when $\kappa \gg F_1^{1/2}$, $\hat{q}_1 \approx -\kappa^2 \hat{\psi}_1$ which is the same form of the operator as we would see in the one layer model where $q = \nabla^2 \psi$. At much larger scales, where $\kappa \ll F_2^{1/2}$, $\hat{q}_1 \approx -\kappa^2 \lambda \hat{\psi}_1$. The appearance of λ in the operator for the large scale interactions in spectral space is parallel to that of the factor of $1/\lambda$ in the velocity profile of a point vortex at large distances. To see this effect, note that if we rescale $q = l\psi \to q' = \gamma q = \gamma L\psi$, then the original equation for the material conservation of potential vorticity

$$\partial_t q + J(\psi, q) = 0$$

is invariant if we rescale time by $t' = t/\gamma$

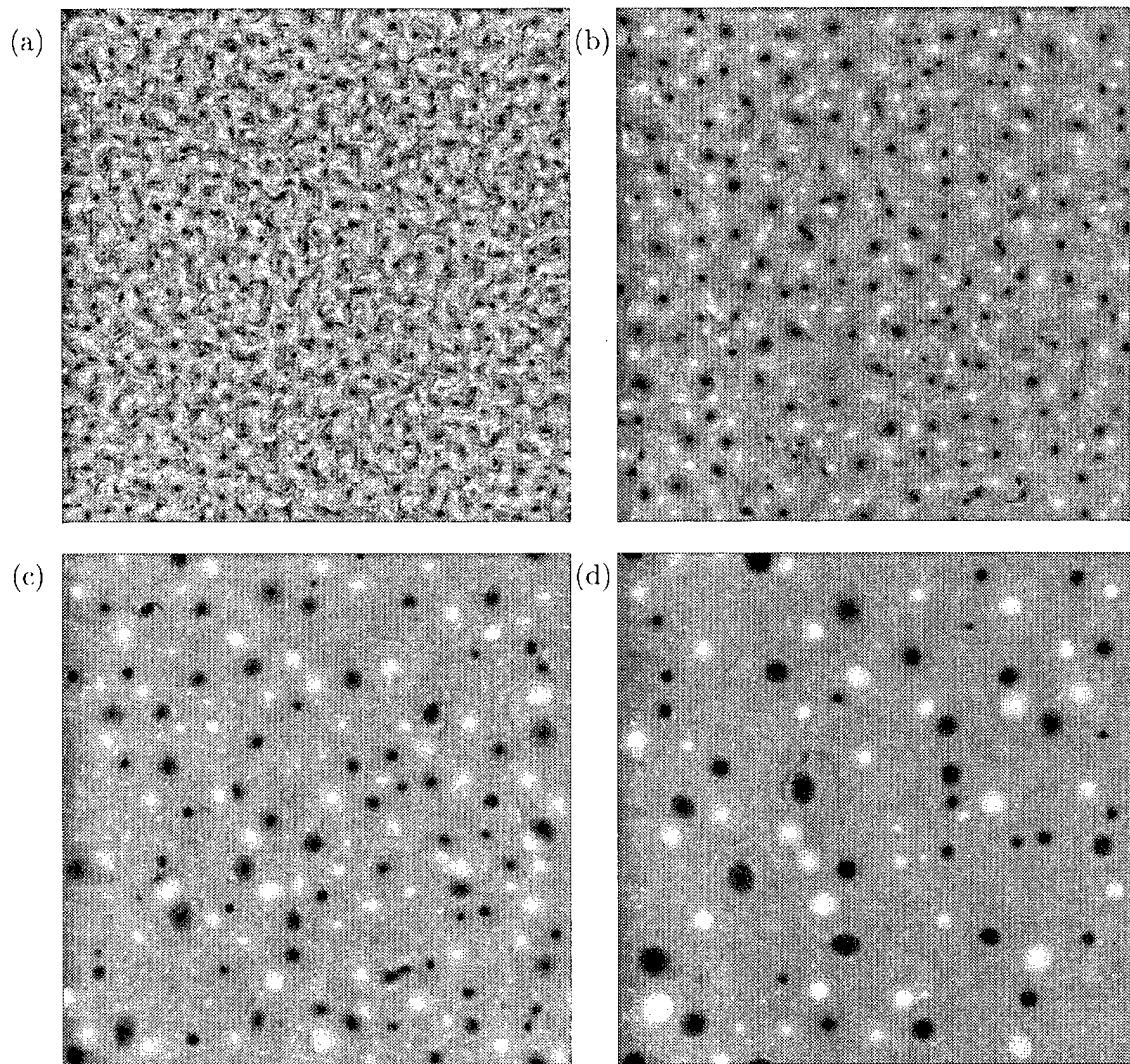$$\partial_{t'} q' + J(\psi, q') = 0.$$

261

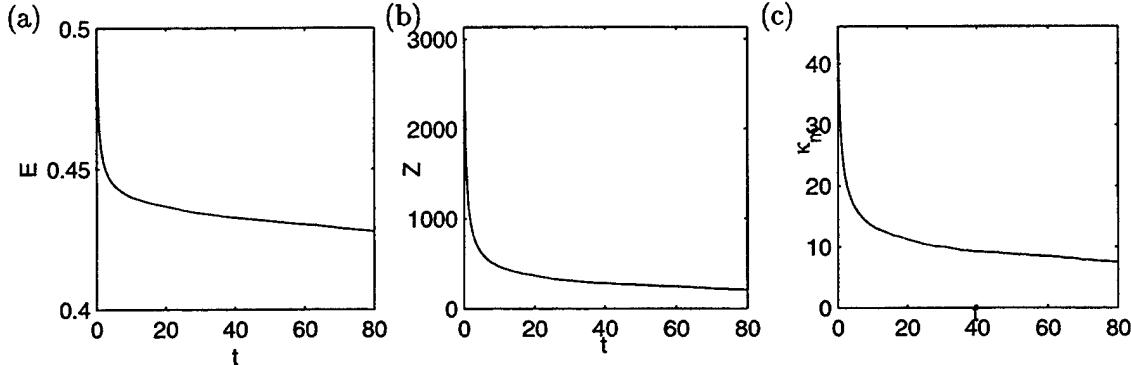Figure 6: As in figure 4, but for the equivalent barotropic model with $k_1 = 15$.

262

Figure 7: As in figure 3, but for the finite-depth model with $k_1 = 24$, $k_2 = 12$.

From this we can see that any factor that intrudes in the relationship between ψ and q acts analogously to slowing down time by that same factor. Time also slows down by that factor when we consider the reduction of velocity v_θ at large distances from a point vortex.

We can go further with the idea of rescaling time in our evolution equation by re-writing

$$\hat{q}_1 = -\kappa^2 \left(1 + \frac{F_1}{\kappa^2} - \frac{F_1 F_2}{\kappa^2 \left(F_2 + \kappa^2 \right)} \right) \hat{\psi}_1$$

$$= -\kappa^2 \gamma(\kappa) \hat{\psi}_1, \tag{18}$$

where $\gamma(\kappa)$ is the factor by which the finite-depth PV inversion operator differs from that of the operator for the one layer model. This function γ then determines a *scale-dependent* factor by which the evolution of the system should slow down. Note that $\lim_{\kappa \to \infty} \gamma(\kappa) = 1$, $\gamma(0) = \lambda$, consistent with what we saw earlier for small and large scales. This slowing down of time should be apparent in our modified system in the self-similar evolution of the flow. In this regime, $\kappa_m \sim (t/\bar{\gamma})^\alpha$ for some factor $\bar{\gamma}$. While it is not certain that such a self-similar regime exists, the apparent power-law behavior of κ_m for a range of values of λ (figure 10) suggest that it does. From a fit to this data we can determine a value for $\bar{\gamma}$ as a function of λ as shown in figure 11. If all of the energy of the flow were at the largest scales then we would expect $\bar{\gamma} = \lambda$ in accordance with the limit of $\gamma(\kappa)$ for small κ. Clearly this is not a good prediction for $\bar{\gamma}$, except for cases of small λ where most of the energy is at larger scales. A better prediction is given by considering the value of γ for the wavenumber that contains the most energy, as measured by κ_m at the end of the simulation. (κ_m changes by very little over the final half of the simulation.) In fact, the good agreement between these two measures of the slowing down of time is support for the interpretation of $\gamma(\kappa)$ that we gave earlier.

4.3 Reduced axisymmetrization

Another feature of the finite-depth one-and-a-half layer model that is seen in the simulations is a declining tendency for coherent vortices to become axisymmetric with increasing values of λ (figure 9). The process of axisymmetrization is important because it is thought to
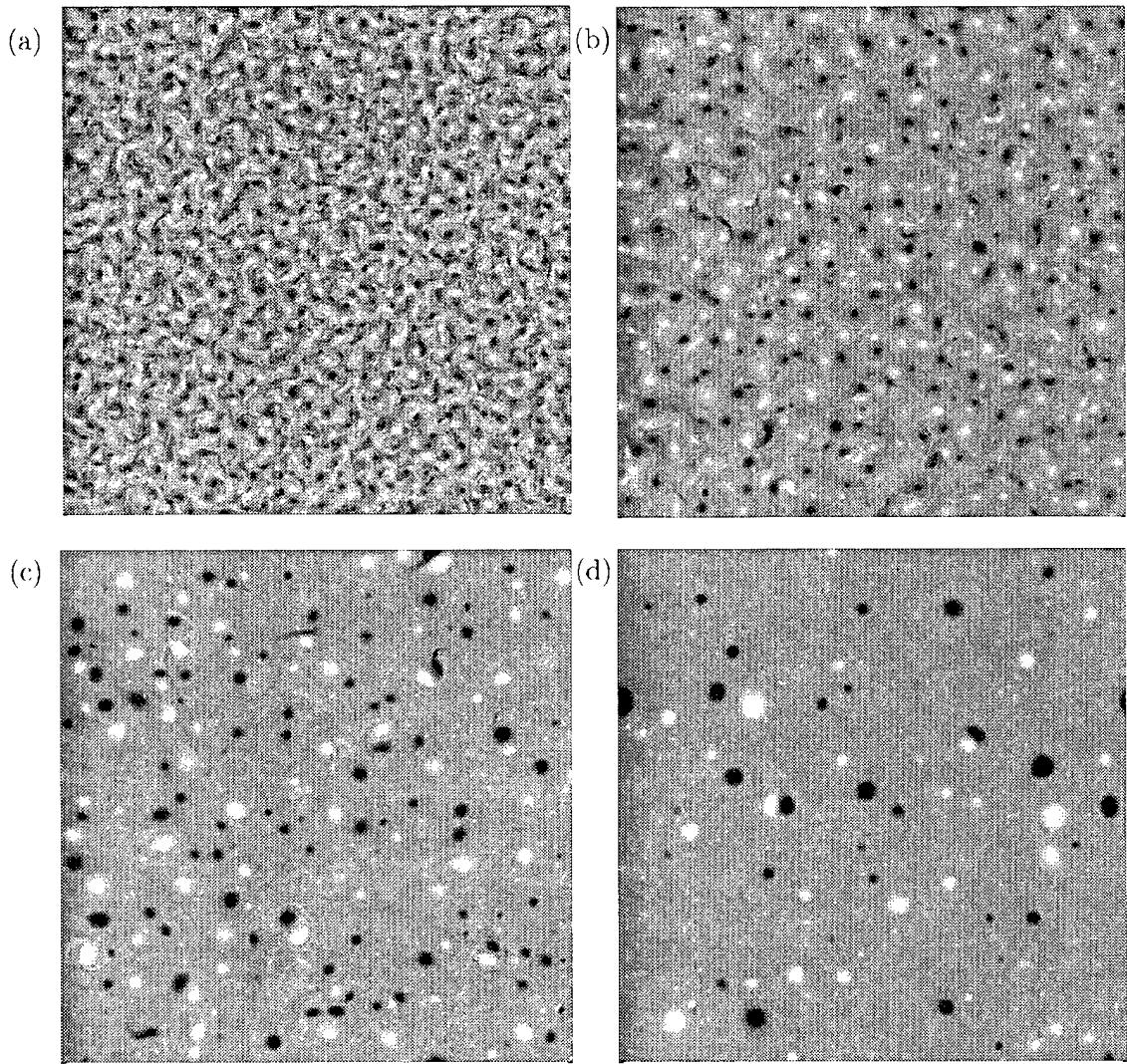
263

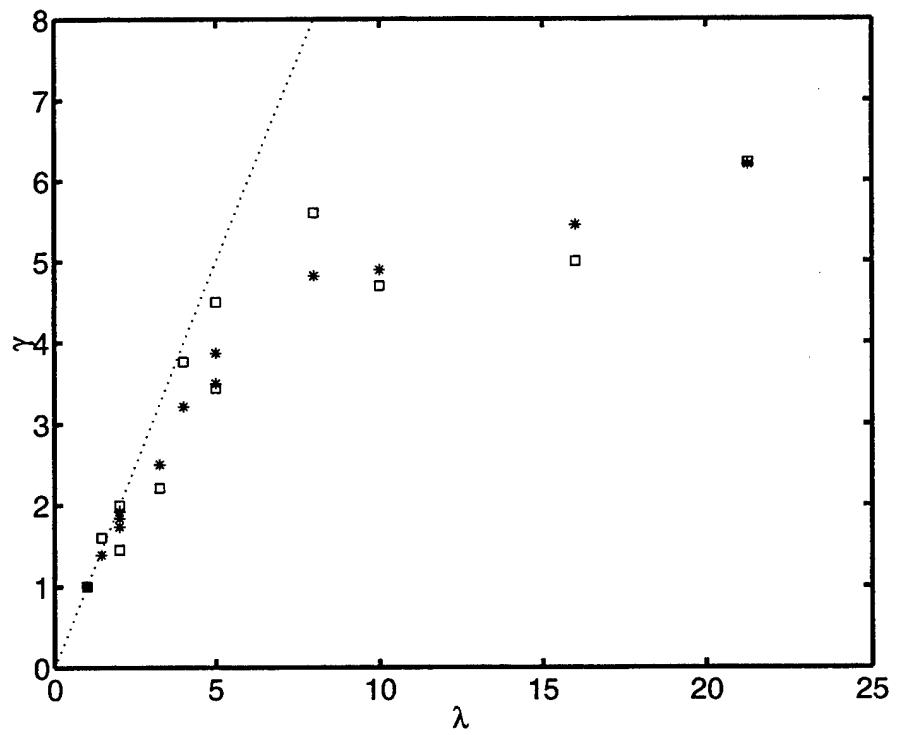Figure 8: As in figure 4, but for the finite-depth model with $k_1 = 24$, $k_2 = 12$.

264

Figure 11: $\bar{\gamma}$ vs. λ ($\square$). The dotted line is the prediction $\bar{\gamma} = \lambda$ and the stars are the prediction $\bar{\gamma} = \gamma\left(\kappa_m(t = 80)\right)$
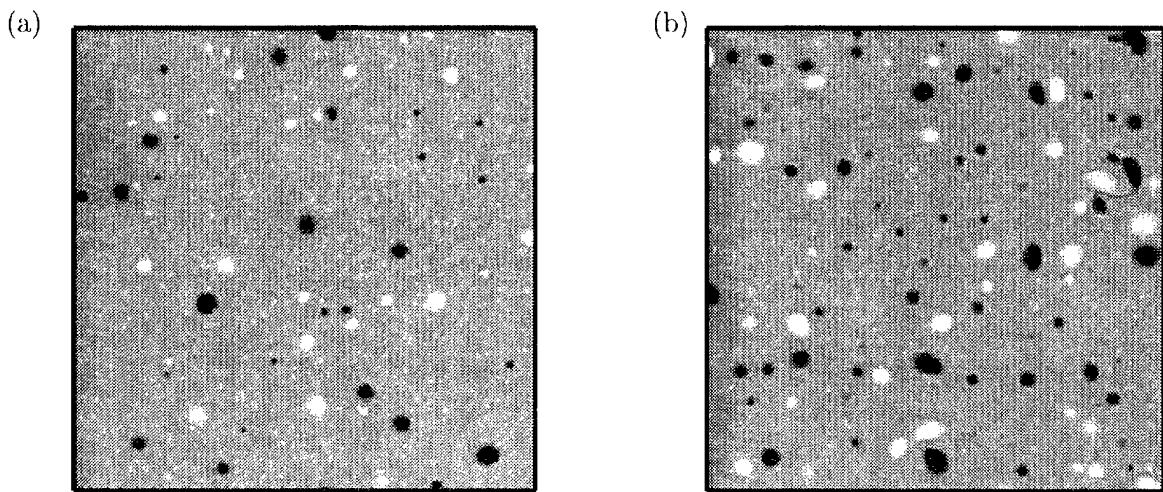
Figure 9: The final vorticity field for (a) $\lambda = 2$ and (b) $\lambda = 17$.
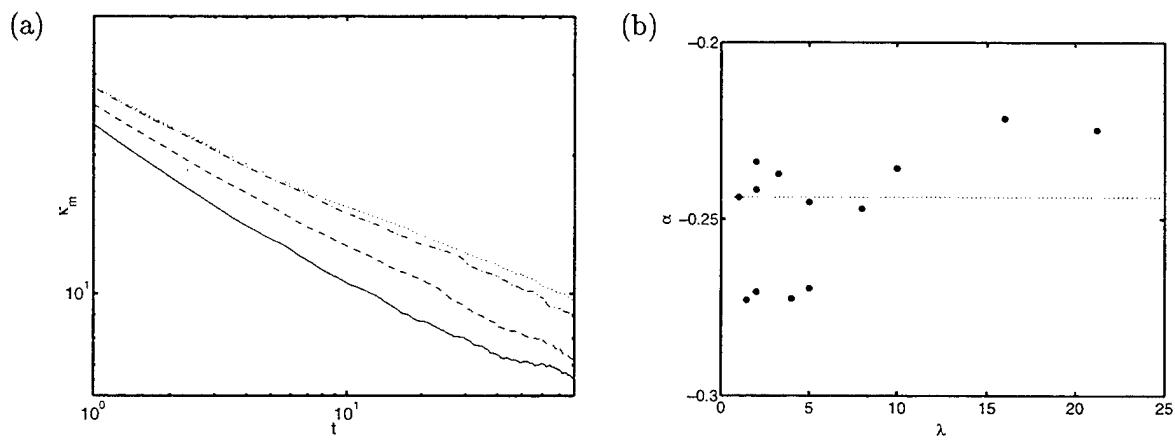
BEST AVAILABLE COPY

Figure 10: (a) κ_m vs time for $\lambda = 2$ (solid line), $\lambda = 4$ (dashed line), $\lambda = 9$ (dash-dotted line) and $\lambda = 17$ (dotted line). (b) Decay exponent α as a function of λ.
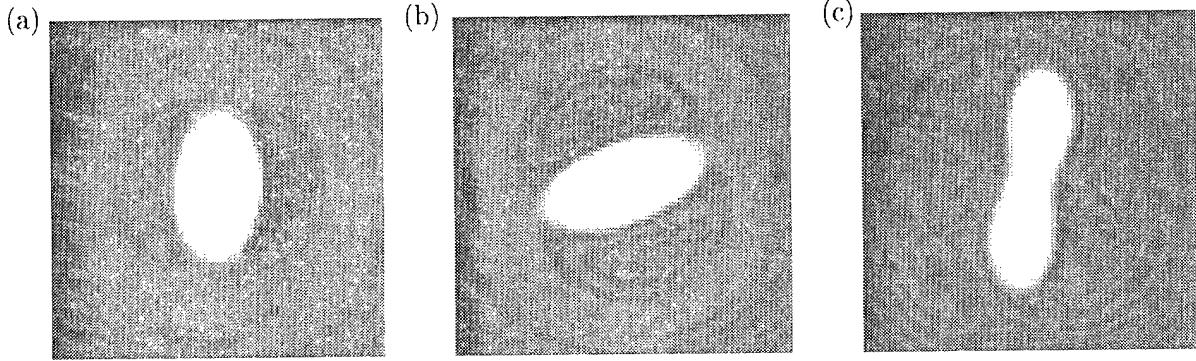
265

Figure 12: Vorticity field at $t = 20$ for an initially elliptical vortex with aspect ratio 8 for (a) one layer model, (b) $k_1 = 15$, $k_2 = 15$ and (c) $k_1 = 18, k_2 = 6$

be prototypical of the process of vortex merger [12]. Vortex merger is the major process controlling the evolution of a flow that is dominated by coherent vortices. We performed a series of simulations on the evolution of a single initially elliptical vortex in the model proposed here. While we have no quantitative results on the influence of finite-depth lower layers on vortex axisymmetrization, the qualitative differences are similar to those seen in the spin-down simulations. As λ increases, a given vortex undergoes less axisymmetrization, until for a critical value of λ there seems to be no trend at all to axisymmetrize, with wildly asymmetric vortex shapes persisting for long times (figure 12). Further characterization of the influence of k_R on the axisymmetrization process is also important.

5 Conclusion

The observation that initially motivated this investigation was of a correlation between the first Rossby deformation radius and the energy containing scales of the ocean circulation. Smith and Vallis showed that with surface-intensified stratification, such a correlation would be possible [4, 5]. Our model is much simpler, but can incorporate surface-intensified stratification by using deeper quiescent lower layers (i.e. $\lambda > 2$). We have shown that there is a scale-dependent slowing down of the evolution of this system. This slowing-down is a possible explanation for the build-up of energy at these scales in the ocean. In an equilibrium situation such as the ocean where input of energy at small scales is balanced by dissipation at large scales, retarded motion at a certain scale slows the inverse cascade of energy leading to an increased amount of energy at the retardation scale. To see quantitatively the effect of this in our model requires further simulations in the forced-dissipative equilibrium regime.

Further investigations of the evolution of the population of coherent vortices would give confirmation and additional understanding of the self-similar evolution and its slowdown at larger scales. To unify the spectral and physical space views of these equations, it would also be helpful to investigate the (physical space) interactions of individual vortices at a variety of length-scales. The study of the axisymmetrization of a single vortex and the

merger of two vortices would both be useful. Of particular interest is the effect of the finite lower layer depth on the critical merger separation for two vortices.

6   Acknowledgments

I would like to thank Oliver Bühler for the inspiration for and continual assistance with this work. Computational assistance was provided by Jeff Weiss, Keith Julien and Mark Petersen. The fellows of the 2003 GFD program also provided useful (and delicious) contributions.

References

[1] D. Stammer, "Global characteristics of ocean variability estimated from regional topex/poseidon altimeter measurements," J. Phys. Ocean. **27**, 1743 (1997).

[2] D. Stammer and C. Wunsch, in *Warm Water Sphere of the North Atlantic Ocean*, edited by W. Krauss (Gebrüder Bornträger, Berlin, 1996), pp. 159–194.

[3] A. Beckmann, C. W. Böning, B. Brügge, and D. Stammer, "On the generation and role of eddy variability in the central north atlantic ocean," J. Geophys. Res. **99**, 20381 (1994).

[4] K. S. Smith and G. K. Vallis, "The scales and equilibration of midocean eddies: Freely evolving flow," J. Phys. Ocean. **31**, 554 (2001).

[5] K. S. Smith and G. K. Vallis, "The scales and equilibration of midocean eddies: Forced-dissipative flow," J. Phys. Ocean. **32**, 1699 (2002).

[6] R. H. Kraichnan and D. Montgomery, "Two-dimensional turbulence," Reports on Progress in Physics **43**, 547 (1980).

[7] J. C. McWilliams, "The emergence of isolated coherent vortices in turbulent flow," J. Fluid Mech. **146**, 21 (1984).

[8] J. C. McWilliams, "The vortices of two-dimensional turbulence," J. Fluid Mech. **219**, 361 (1990).

[9] J. B. Weiss and J. C. McWilliams, "Temporal scaling behavior of decaying two-dimensional turbulence," Phys. Fluids A **5**, 608 (1993).

[10] A. Bracco, J. C. McWilliams, G. Murante, A. Provenzale, and J. B. Weiss, "Revisiting freely decaying two-dimensional turbulence at millenial resolution," Phys. Fluids **12**, 2931 (2000).

[11] A. Provenzale, "Transport by cooherent barotropic vortices," Ann. Rev. Fluid Mech. **31**, 55 (1999).

[12] M. V. Melander, N. J. Zabusky, and J. C. McWilliams, "Symmetric vortex merger in two dimensions: causes and conditions," J. Fluid Mech. **195**, 303 (1988).

[13] D. G. Dritschel and D. W. Waugh, "Quantification of the inelastic interaction of unequal vortices in two-dimensional vortex dynamics," Phys. Fluids A **4**, 1737 (1992).

[14] D. G. Dritschel, "A general theory for two-dimensional vortex interactions," J. Fluid Mech. **293**, 269 (1995).

[15] G. F. Carnevale, J. C. McWilliams, Y. Pomeau, J. B. Weiss, and W. R. Young, "Evolution of vortex statistics in two-dimensional turbulence," Phys. Rev. Lett. **66**, 2735 (1991).

[16] R. Salmon, *Lectures On Geophysical Fluid Dynamics* (Oxford University Press, New York, 1998).

[17] J. Pedlosky, *Geophysical Fluid Dynamics*, 2nd ed. (Springer Verlag, New York, 1987).

[18] L. M. Polvani, N. J. Zabusky, and G. R. Flierl, "Two-layer geostrophic vortex dynamics. part 1. upper v-states and merger," J. Fluid Mech. **205**, 215 (1989).

[19] V. D. Larichev and J. C. McWilliams, "Weakly decaying turbulence in an equivalent-barotropic fluid," Phys. Fluids A **3**, 938 (1991).

[20] N. Kukharkin, S. A. Orszag, and V. Yakhot, "Quasicrystallization of vortices in drift-wave turbulence," Phys. Rev. Lett. **75**, 2486 (1995).

[21] M. Arhan and A. Colin de Verdière, "Dynamics of eddy motion in the eastern north-atlantic," J. Phys. Ocean. **15**, 153 (1985).

[22] R. W. Griffiths and E. J. Hopfinger, "Coalescing of geostrophic vortices," J. Fluid Mech. **178**, 73 (1987).

[23] J. Verron, E. J. Hopfinger, and J. C. McWilliams, "Sensitivity to initial conditions in the merging of two layer baroclinic vortices," Phys. Fluids A **2**, 886 (1990).

[24] J. Verron and S. Valcke, "Scale-dependent merging of baroclinic vortices," J. Fluid Mech. **264**, 81 (1994).

[25] N. Hogg and H. Stommel, "The heton, an elementary interaction between discrete baroclinic geostrophic vortices and its implications concerning eddy heat-flow," Proc. Roy. Soc. London **397**, 1 (1985).

University of California, San Diego
SIO Library 0175C
9500 Gilman Drive
La Jolla, CA 92093-0175

Hancock Library of Biology & Oceanography
Alan Hancock Laboratory
University of Southern California
University Park
Los Angeles, CA 90089-0371

Gifts & Exchanges
Library
Bedford Institute of Oceanography
P.O. Box 1006
Dartmouth, NS, B2Y 4A2, CANADA

NOAA/EDIS Miami Library Center
4301 Rickenbacker Causeway
Miami, FL 33149

Research Library
U.S. Army Corps of Engineers
Waterways Experiment Station
3909 Halls Ferry Road
Vicksburg, MS 39180-6199

Marine Resources Information Center
Building E38-320
MIT
Cambridge, MA 02139

Library
Lamont-Doherty Geological Observatory
Columbia University
Palisades, NY 10964

Library
Serials Department
Oregon State University
Corvallis, OR 97331

Pell Marine Science Library
University of Rhode Island
Narragansett Bay Campus
Narragansett, RI 02882

Working Collection
Texas A&M University
Dept. of Oceanography
College Station, TX 77843

Fisheries-Oceanography Library
151 Oceanography Teaching Bldg.
University of Washington
Seattle, WA 98195

Library
R.S.M.A.S.
University of Miami
4600 Rickenbacker Causeway
Miami, FL 33149

Maury Oceanographic Library
Naval Oceanographic Office
Building 1003 South
1002 Balch Blvd.
Stennis Space Center, MS, 39522-5001

Library
Institute of Ocean Sciences
P.O. Box 6000
Sidney, B.C. V8L 4B2
CANADA

National Oceanographic Library
Southampton Oceanography Centre
European Way
Southampton SO14 3ZH
UK

The Librarian
CSIRO Marine Laboratories
G.P.O. Box 1538
Hobart, Tasmania
AUSTRALIA 7001

Library
Proudman Oceanographic Laboratory
Bidston Observatory
Birkenhead
Merseyside L43 7 RA
UNITED KINGDOM

IFREMER
Centre de Brest
Service Documentation - Publications
BP 70 29280 PLOUZANE
FRANCE

50272-101

REPORT DOCUMENTATION PAGE	1. REPORT NO. WHOI-2004-03	2.	3. Recipient's Accession No.

4. Title and Subtitle Conceptual Models of the Climate 2003 Program of Study: Non-Newtonian Geophysical Fluid Dynamics		5. Report Date February 2004
		6.

7. Author(s) Neil J. Balmforth, Director, John Hinch, Principal Lecturer	8. Performing Organization Rept. No. WHOI-2004-03

9. Performing Organization Name and Address Woods Hole Oceanographic Institution Woods Hole, Massachusetts 02543	10. Project/Task/Work Unit No.
	11. Contract(C) or Grant(G) No. (C) N00014-97-1-0934 (G) OCE 98-10647

12. Sponsoring Organization Name and Address Office of Naval Research	13. Type of Report & Period Covered Technical Report
	14.

15. Supplementary Notes

This report should be cited as: Woods Hole Oceanog. Inst. Tech. Rept., WHOI-2004-03

16. Abstract (Limit: 200 words)

Non-Newtonian fluids occur commonly in our world. These fluids, such as toothpaste, saliva, oils, mud and lava, exhibit a number of behaviors that are different from Newtonian fluids and have a number of additional material properties. In general, these differences arise because the fluid has a microstructure that influences the flow. In section 2 we will present a collection of some of the interesting phenomena arising from flow nonlinearities, the inhibition of stretching, elastic effects and normal stresses. In section 3 we will discuss a variety of devices for measuring material properties, a process known as rheometry.

17. Document Analysis   a. Descriptors

fluids
flow
Non-Newtonian

b. Identifiers/Open-Ended Terms

c. COSATI Field/Group

18. Availability Statement Approved for public release; distribution unlimited.	19. Security Class (This Report) UNCLASSIFIED	21. No. of Pages 306
	20. Security Class (This Page)	22. Price

(See ANSI-Z39.18)	See Instructions on Reverse	OPTIONAL FORM 272 (4-77) (Formerly NTIS-35) Department of Commerce